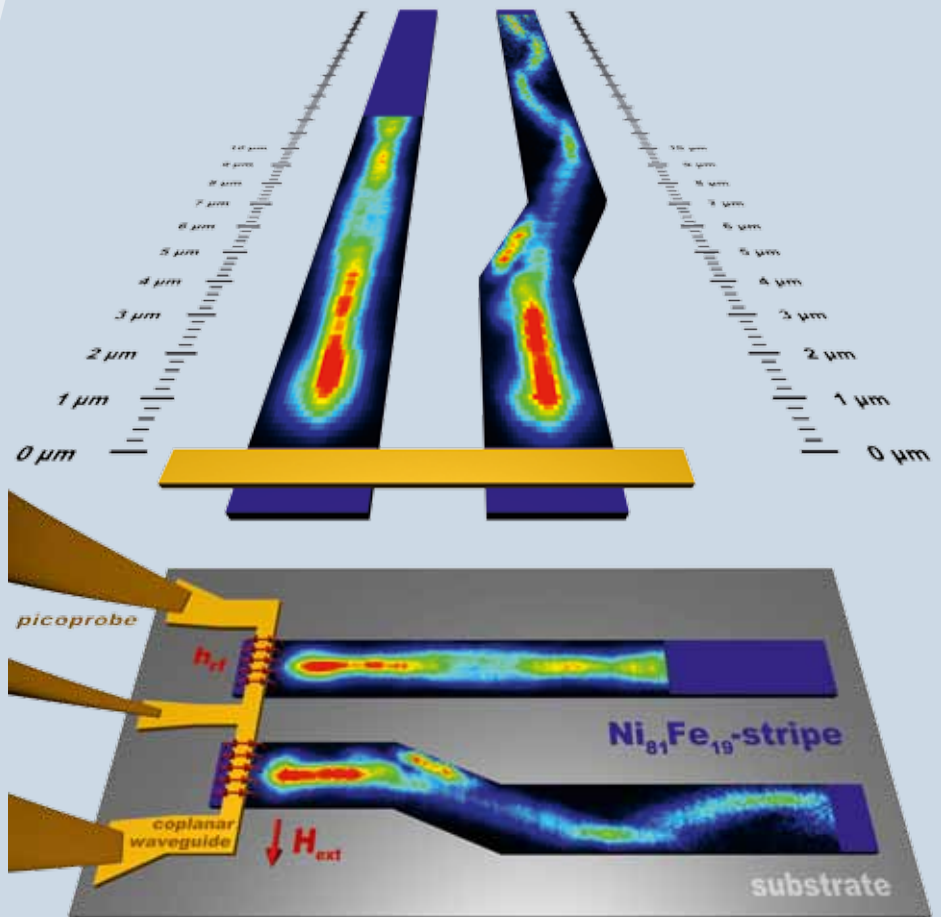


AG Magnetismus

Annual Report 2011



Front page: Spin-wave mode conversion in a waveguide exhibiting broken translational symmetry. The bottom image shows the experimental system. A microwave current flowing through the shorted end of a coplanar waveguide excites the magnetization in two micro-structured waveguides one of which includes a shift transverse to the propagation direction. The intensity distributions of the spin waves propagating in both stripes are recorded using space-resolved Brillouin light scattering microscopy and are illustrated in the upper image. For the straight waveguide, a symmetric mode profile can be observed which is related to the already known periodic self-focusing of spin wave width modes with odd mode numbers. In the second stripe containing a skew, a strong inhomogeneity in the magnetization distribution is generated leading to a conversion from a superposition of only symmetric modes before the skew into a mixed set of symmetric and antisymmetric spin-wave width modes behind it. For more details about this effect see Section 4.4 of this Report and P. Clausen et al. (Appl. Phys. Lett. **99**, 162505 (2011)).

Annual Report 2011

Address: Prof. Dr. Burkard Hillebrands
Fachbereich Physik
Landesforschungszentrum OPTIMAS
Technische Universität Kaiserslautern
Erwin-Schrödinger-Straße 56
67663 Kaiserslautern, Germany
Tel.: +49-(0)631-205-4228
Fax.: +49-(0)631-205-4095

Postal address: Postfach 3049
67653 Kaiserslautern, Germany

Internet: <http://www.physik.uni-kl.de/hillebrands/>
E-Mail: hilleb@physik.uni-kl.de

This Annual Report can be downloaded from:
<http://www.physik.uni-kl.de/hillebrands/publications/annual-reports/>

Our Group



From left to right:

Philipp Pirro, Dr. Vitaliy Vasyuchka, Thomas Brächer, Benjamin Jungfleisch,
Peter Clausen, Florin Ciubotaru, Milan Agrawal, Sibylle Müller, Thomas Langner,
Dr. Andrés Conca Parra, Thomas Sebastian, Björn Obry, Katrin Vogt,
Dieter Weller, Thomas Meyer, Jan Westermann, Roland Neb, Dr. Andrii Chumak,
Georg Wolf, Ana Ruiz Calaforra, Dr. Alexander Serga, Dr. Britta Leven,
Dmytro Bozhko (guest), Prof. Dr. Burkard Hillebrands,
Denis Slobodianiuk (guest).

This report contains unpublished results and should
not be quoted without permission from the authors.

Contents

| | | |
|------|--|----|
| 1 | Preface..... | 13 |
| 2 | Personnel..... | 17 |
| 2.1 | Members of the group | 17 |
| 2.2 | Visiting scientists, postdoctoral fellows and exchange students | 19 |
| 2.3 | Guest seminars | 22 |
| 2.4 | Visits of group members to other laboratories | 23 |
| 2.5 | Group member photo gallery | 24 |
| 3 | Methods | 27 |
| 3.1 | Brillouin light scattering spectroscopy (BLS) | 27 |
| 3.2 | Microwave techniques | 28 |
| 3.3 | Magneto-optic Kerr effect magnetometry and microscopy (MOKE) | 29 |
| 3.4 | Molecular beam epitaxy (MBE) | 31 |
| 4 | Reports on Experimental Results | 33 |
| A. | Magnon Gases and Condensates | 33 |
| 4.1 | Variable damping and coherence in a high-density magnon gas..... | 35 |
| 4.2 | Mode structure of parametrically excited magnons in a magnetic film | 42 |
| 4.3 | Transition processes in a highly excited multi-mode autonomous magnon system | 46 |
| B. | Magnon Spintronics | 51 |
| 4.4 | Mode conversion by symmetry breaking of propagating spin waves | 53 |
| 4.5 | Parallel parametric generation of spin waves in a $\text{Ni}_{81}\text{Fe}_{19}$ microstripe | 58 |
| 4.6 | Detection of parametrically excited exchange magnons by the inverse spin Hall effect..... | 64 |
| 4.7 | Spin-wave tunneling through a mechanical gap in a microstructured $\text{Ni}_{81}\text{Fe}_{19}$ -stripe | 69 |
| C. | Magnonic Crystals | 74 |
| 4.8 | Oscillatory energy exchange in a dynamic magnonic crystal..... | 76 |
| 4.9 | Magnonic band gap design by the edge modulation of micro-sized waveguides..... | 81 |
| 4.10 | Exact dipole-exchange theory for dynamic magnonic crystals | 86 |
| D. | Spin Caloric Transport | 90 |
| 4.11 | Spin-wave propagation and transformation in a thermal gradient | 91 |

| | | |
|-----------|---|-----|
| E. | New Materials and Heusler Compounds..... | 96 |
| 4.12 | Spin-wave propagation in Heusler waveguides | 99 |
| 4.13 | Magneto-optical characterization of single crystalline $\text{Co}_2\text{FeAl}_{0.4}\text{Si}_{0.6}$ thin films on MgO substrates | 104 |
| 4.14 | Ion beam patterning of antiferromagnetic elements in the submicron regime.. | 109 |
| 4.15 | Microscopic magnetic structuring of a spin-wave waveguide by ion implantation in a $\text{Ni}_{81}\text{Fe}_{19}$ layer | 115 |
| F. | Applied Spintronics..... | 120 |
| 4.16 | Determination of dynamic switching fields of TMR structures..... | 121 |
| 4.17 | Characterization of a TMR-based magnetic memory cell with elliptically shaped elements for moderate switching speed | 126 |
| 4.18 | Magnetic dynamics near vortex state nucleation in $\text{Ni}_{81}\text{Fe}_{19}$ dots..... | 132 |
| 5 | Publications | 137 |
| 6 | Conferences, Workshops, Schools, Seminars | 141 |
| 6.1 | Conferences | 141 |
| 6.2 | Workshops and Schools | 144 |
| 6.3 | Other meetings and trade fairs | 145 |
| 6.4 | Invited seminar talks and colloquia | 146 |
| 6.5 | Seminars | 146 |
| 6.6 | Awards and Fellowships | 146 |
| Appendix: | | |
| | Impressions from 2011..... | 147 |

Chapter 1: Preface

Dear Colleagues and Friends,

we are happy to present our Annual Report 2011 covering the period November 2010 to October 2011. A few highlights of our research in this period: In the field of magnon gases we progressed in investigating high-density magnon gases and their properties like variable damping and coherence. We succeeded in clarifying the autonomous behavior of highly populated magnon systems. We continued our work in the field of magnon spintronics and obtained fundamental results on the parametric generation of magnons in $\text{Ni}_{81}\text{Fe}_{19}$ microstripes. Another important milestone was the detection of parametrically excited short-wavelength exchange magnons via the inverse spin Hall effect in magnetic insulator-nonmagnetic metal heterostructures. The field of magnonic crystals is flourishing as well. We investigated experimentally the oscillatory energy exchange in a dynamic magnonic crystal and obtained new results in simulations of a shape-modulated magnonic crystal. A new field is the interaction of magnon currents with heat currents. We showed how a thermal gradient modifies the spin-wave propagation and transformation in a YIG waveguide, and we showed evidence for the magnon-based longitudinal Seebeck effect. In the field of new materials and Heusler compounds we succeeded to demonstrate that spin waves can propagate over a distance more than three times the propagation length in the reference material $\text{Ni}_{81}\text{Fe}_{19}$, opening this class of materials to new applications in spin-wave based data processing.

An important issue for us was the start of the new German DFG-funded Priority Programme 1538 “Spin Caloric Transport (SpinCaT)”. We work on two projects: “Magnon Seebeck effect” and “Magnon mediated heat and spin transport in magnetic insulators”. Equally important was the successful prolongation of our Sonderforschungsbereich / Transregio 49 “Condensed Systems with Variable Many-Body Interactions”. We can now continue our fruitful work on magnon gases and condensates for a second four-year period.

A highlight in the past year was the annual meeting of the ASPIMATT JST-DFG Research Unit in August in Villa Denis near Kaiserslautern chaired by my colleagues Koki Takanashi/Sendai, Claudia Felser/Mainz and myself, putting particular emphasis on student presentations and training. A large contribution to the organization was made by the ASPIMATT student representatives Thomas Sebastian and Yusuke Ohdaira. More than 60 persons took part, half of them from Japan.

Again, there have been several changes in our group. We are happy to welcome (in alphabetical order) Milan Agrawal, Thomas Meyer and Jan Westermann. Thomas Brächer and Thomas Langner started their Ph.D. research work, whereas Frederik Fohr and Christian Sandweg finished their Ph.D. successfully and continue their career in the private sector. Andreas Beck left us for a teaching position.

In 2011, one of our young researchers obtained two honorable awards: Helmut Schultheiss was awarded the “Promotionspreis der Kreissparkassen-Stiftung” and the “Auszeichnung an hervorragenden Nachwuchswissenschaftler durch die Prof. Dr. Jürgen Geiger-Stiftung” for his Ph.D. thesis “Coherence and damping of spin waves in magnetic microstructures”.

Our work would not have been possible without valuable collaborations with people all over the world. They are too many to list them here all. In particular we would like to thank, in alphabetical order, Johan Åkerman, Toshi An, Yasuo Ando, Christian Back, Gerrit Bauer, Giovanni Carlotti, Frederick Casper, John Chapman, Claude Chappert, Oksana Chubykalo-Fesenko, Russell Cowburn, Vincent Cros, Sergei Demokritov, Thibaut Devolder, Pallavi Dhagat, Bernard Dieny, Ursula Ebels, Hajo Elmers, Jürgen Fassbender, Gerhard Fecher, Claudia Felser, Albert Fert, Suzanna

and Paulo Freitas, Yasuhiro Fukuma, John Gregg, Natalia Grigoryeva, Hartmut Grützediek, Dirk Grundler, Gianluca Gubbiotti, Konstantin Gusliyenkov, Jarsolav Hamrle, Uwe Hartmann, Axel Hoffmann, Koichiro Innomata, Gerhard Jakob, Albrecht Jander, Xiaofeng Jin, Martin Jourdan, Gleb Kakazei, Boris Kalinikos, Alexy Karenowska, Sang-Koog Kim, Mathias Kläui, Peter Kopietz, Mikhail Kostylev, Andreas Kreisel, Jürgen Kübler, Takahide Kubota, Karen Liversey, Luis Lopez Diaz, Wolfram Maaß, Roland Mattheis, Gennadiy Melkov, Claudia and Tim Mewes, Hans Nembach, Takyuki Nozaki, Yoshichika Otani, Johannes Paul, Dorothée Petit, Günter Reiss, Bernhard Reuscher, Karsten Rott, Jürgen Rühl, Manfred Rührig, Eiji Saitoh, John R. Sandercock, Rudi Schäfer, Gerd Schönhense, Justin Shaw, Andrei Slavin, Bob Stamps, Yoshishige Suzuki, Koki Takanashi, Vasyl Tiberkevich, and Simon Trudel for their interactions with us and their strong input to our work.

Collaborations within the Fachbereich Physik at the University of Kaiserslautern (in particular Martin Aeschlimann, James Anglin, Sebastian Eggert, Michael Fleischhauer, Georg von Freymann, Herwig Ott, Hans-Christian Schneider, Volker Schünemann, and Arthur Widera and their groups), the Institut für Oberflächen- und Schichtanalytik, as well as the Nano Structuring Center have been very stimulating. We are very grateful to be a member of the State Research Center for Optics and Material Sciences OPTIMAS.

I would also like to thank all our sponsors, which are the Deutsche Forschungsgemeinschaft (DFG), the Bundesministerium für Bildung und Forschung (BMBF), the Deutscher Akademischer Austauschdienst (DAAD), the European Community, INTAS, the Carl Zeiss Foundation, the State of Rhineland Palatinate and the University of Kaiserslautern. Concerning our projects in applied research, I would like to express my gratitude to Prema GmbH, Sensitec GmbH, Siemens AG, and Singulus Technologies AG as our strong partners in R&D on spintronic sensors.

My special thanks go to Benjamin Jungfleisch, Britta Leven, and Sibylle Müller for their help in preparing this report and to Hubert Gerber from Photo-Repro-Druck, TU Kaiserslautern.

It is my special pleasure to greet all former group members. May this report help to stay in touch. If you are interested in our work I would be happy to hear from you. If you have any questions, comments or suggestions please contact us.

With all my best wishes for Christmas, and a Happy New Year,

Burkhard Hillebrands

Kaiserslautern, November 2011

Vorwort

Liebe Kolleginnen und Kollegen und Freunde unserer Arbeitsgruppe,

wir freuen uns Ihnen unseren Jahresbericht 2011, der die Zeit zwischen November 2010 und Oktober 2011 behandelt, präsentieren zu können. Zunächst einige besondere Höhepunkte unserer Forschung in dieser Zeitspanne: Auf dem Gebiet der Magnonengase konnten wir Fortschritte in der Beobachtung von Systemen hoher Dichte im Hinblick auf Eigenschaften wie variable Dämpfung sowie der Kohärenz erzielen. Es gelang uns das autonome Verhalten hoch angeregter Magnonensysteme zu klären. Wir setzten unsere Arbeit im Bereich der Magnon-Spintronik fort und erzielten fundamentale Resultate zur parametrischen Anregung von Magnonen in mikrostrukturierten $\text{Ni}_{81}\text{Fe}_{19}$ -Wellenleitern. Ein weiterer wichtiger Meilenstein war die Beobachtung von parametrisch angeregten, kurzwelligen, Austausch-dominierten Spinwellen in einer Heterostruktur aus einem magnetischen Isolator und einem nichtmagnetischen Metall mittels des inversen Spin-Hall- Effekts. Die Arbeit im Feld der magnonischen Kristalle gestaltet sich vielversprechend. Wir beobachteten den periodischen Energie-Transfer in einem dynamischen magnonischen Kristall experimentell und erzielten neue Resultate in der Simulation von räumlich modulierten magnonischen Kristallen. Ein neues Forschungsfeld ist die Wechselwirkung zwischen reinen Spinströmen und Wärmeströmen. Wir konnten zeigen, wie ein thermischer Gradient die Propagation und die Transformation von Spinwellen in einem YIG-Wellenleiter beeinflusst und präsentierten Hinweise auf den Magnon-basierten longitudinalen Seebeck Effekt. Auf dem Gebiet neuer Materialien und Heusler-Verbindungen konnten Propagationslängen beobachtet werden, die einer Verdreifachung der im Referenz-Material $\text{Ni}_{81}\text{Fe}_{19}$ beobachteten Längen entsprechen. Diese Beobachtung eröffnet die Möglichkeit diese Materialklasse in zukünftigen Anwendungen im Bereich von Spin-basierter Informationsverarbeitung erfolgreich einzusetzen.

Von großer Wichtigkeit für uns ist der Beginn des neuen, durch die DFG geförderten, Schwerpunktprogramms 1538 “Spin Caloric Transport (SpinCaT)”. Im Rahmen dieses Programms bearbeiten wir zwei Projekte: “Magnon Seebeck effect” und “Magnon mediated heat and spin transport in magnetic insulators”. Ebenso erfreulich ist die Verlängerung des Sonderforschungsbereiches / Transregio 49 “Condensed Systems with Variable Many-Body Interactions”. Damit kann unsere fruchtbare Arbeit zu Magnonen-Gasen und Kondensaten für weitere vier Jahre fortgesetzt werden.

Ein Höhepunkt im vergangenen Jahr war das jährliche Treffen der ASPIMATT JST- DFG-Forscherguppe in der Villa Denis nahe Kaiserslautern. Den Vorsitz bei diesem Treffen führten meine Kollegen Koki Takanashi/Sendai, Claudia Felser/Mainz und ich. Besonderes Augenmerk legten wir auf studentische Beiträge und deren Förderung. Einen großen Beitrag bei der Organisation dieses Treffens leisteten die ASPIMATT Studenten-Vertreter Thomas Sebastian und Yusuke Ohdaira. Es nahmen über 60 Personen, die Hälfte davon aus Japan, an dem Treffen teil.

Wieder gab es einige personelle Veränderungen in unserer Gruppe. Wir freuen uns Milan Agrawal, Thomas Meyer und Jan Westermann (in alphabetischer Reihenfolge) willkommen heißen zu können. Thomas Brächer und Thomas Langner begannen die Arbeit an ihren Promotionen, während Frederik Fohr und Christian Sandweg ihre Promotionen erfolgreich abschließen konnten und ihre Karrieren im privaten Sektor fortsetzen. Andreas Beck verließ die Gruppe, um eine Tätigkeit als Lehrer an einem Gymnasium anzutreten.

Im Jahr 2011 wurde einer unserer jungen Wissenschaftler mit zwei angesehenen Preisen ausgezeichnet: Helmut Schultheiß wurde der “Promotionspreis der Kreissparkassen-Stiftung” sowie die “Auszeichnung an hervorragende Nachwuchswissenschaftler durch die Prof. Dr. Jürgen Geiger-

Stiftung” für seine Dissertation “Kohärenz und Dämpfungsverhalten von Spinwellen in magnetischen Mikrostrukturen” verliehen.

Unsere Arbeit wäre nicht möglich gewesen ohne die vielen wertvollen Zusammenarbeiten mit Forscherkollegen rund um die Welt. Beispielhaft möchten wir uns bedanken bei (in alphabetischer Reihenfolge) Johan Åkerman, Toshu An, Yasuo Ando, Christian Back, Gerrit Bauer, Giovanni Carlotti, Frederick Casper, John Chapman, Claude Chappert, Oksana Chubykalo-Fesenko, Russell Cowburn, Vincent Cros, Sergei Demokritov, Thibaut Devolder, Pallavi Dhagat, Bernard Dieny, Ursula Ebels, Hajo Elmers, Jürgen Fassbender, Gerhard Fecher, Claudia Felser, Albert Fert, Suzanna and Paulo Freitas, Yasuhiro Fukuma, John Gregg, Natalia Grigoryeva, Hartmut Grützediek, Dirk Grundler, Gianluca Gubbiotti, Konstantin Guslienko, Jarsolav Hamrle, Uwe Hartmann, Axel Hoffmann, Koichiro Innomata, Gerhard Jakob, Albrecht Jander, Xiaofeng Jin, Martin Jourdan, Gleb Kakazei, Boris Kalinikos, Alexy Karenowska, Sang-Koog Kim, Mathias Kläui, Peter Kopietz, Mikhail Kostylev, Andreas Kreisel, Jürgen Kübler, Takahide Kubota, Karen Liversey, Luis Lopez Diaz, Wolfram Maaß, Roland Mattheis, Gennadiy Melkov, Claudia and Tim Mewes, Hans Nembach, Takyuki Nozaki, Yoshichika Otani, Johannes Paul, Dorothée Petit, Günter Reiss, Bernhard Reuscher, Karsten Rott, Jürgen Rühl, Manfred Rührig, Eiji Saitoh, John R. Sandercock, Rudi Schäfer, Gerd Schönhense, Justin Shaw, Andrei Slavin, Bob Stamps, Yoshishige Suzuki, Koki Takanashi, Vasyl Tiberkevich und Simon Trudel.

Zusammenarbeiten im Fachbereich Physik an der TU Kaiserslautern waren ebenfalls sehr wertvoll. Besonders bedanken möchten wir uns bei Martin Aeschlimann, James Anglin, Sebastian Eggert, Michael Fleischhauer, Herwig Ott, Hans-Christian Schneider, Volker Schünemann und Arthur Widera und ihren Gruppen, wie auch beim Institut für Oberflächen- und Schichtanalytik und dem Nano Structuring Center. Wir sind außerdem dankbar Mitglied im Landesforschungszentrum für Optik und Materialwissenschaften (OPTIMAS) zu sein.

Für finanzielle Unterstützungen danken wir der Deutschen Forschungsgemeinschaft (DFG), dem Bundesministerium für Bildung und Forschung (BMBF), dem Deutschen Akademischen Austauschdienst (DAAD), der Europäischen Gemeinschaft, INTAS, der Carl Zeiss-Stiftung, dem Land Rheinland-Pfalz und der TU Kaiserslautern. Ich möchte außerdem unseren Partnern in der angewandten Forschung an Spintronik-Sensoren, der Prema GmbH, der Sensitec GmbH, der Siemens AG und der Singulus Technologies AG danken.

Mein spezieller Dank geht an Benjamin Jungfleisch, Isabel Sattler und Sibylle Müller für ihre Hilfe in der Erstellung dieses Berichts, sowie an Hubert Gerber von Photo-Repro-Druck, TU Kaiserslautern.

Es ist meine besondere Freude, an dieser Stelle alle früheren Gruppenmitglieder zu grüßen. Vielleicht hilft dieser Bericht ein wenig, Kontakt zu halten. Wenn Sie/Ihr an unserer Arbeit interessiert sind, würden wir uns freuen von Ihnen/Euch zu hören. Das Gleiche gilt bei Fragen, Kommentare oder Anregungen.

Mit den besten Wünschen für ein frohes Weihnachtsfest und ein gutes Neues Jahr

Berhard Hillebrand

Kaiserslautern, im November 2011

Chapter 2: Personnel

2.1 Members of the group

Group leader:

Prof. Dr. Burkard Hillebrands

Senior scientists:

Dr. Britta Leven, Akad. Oberrätin

Dr. Andrii Chumak

Dr. Alexander Serga

Postdocs and long-term guest scientists:

Dr. Gerhard Baldsiefen (Rheinbreitbach) until 09/10

Dr. Andreas Beck until 01/11

Dr. Andrés Conca Parra

Dr. Thomas Schneider until 11/10

Dr. Vitaliy Vasyuchka

Ph.D. students:

Dipl.-Phys. Milan Agrawal since 11/10

Dipl.-Phys. Thomas Brächer since 12/10

Dipl.-Phys. Florin Ciubotaru

Dipl.-Phys. Peter Clausen

Dipl.-Phys. Frederik Fohr until 10/11

Dipl.-Phys. Benjamin Jungfleisch

Dipl.-Phys. Lisa Kleinen (Rheinbreitbach) until 09/11

Dipl.-Phys. Thomas Langner since 09/11

Dipl.-Phys. Roland Neb

Dipl.-Phys. Björn Obry

Dipl.-Phys. Philipp Pirro

Dipl.-Phys. Ana Ruiz Calaforra

Dipl.-Phys. Christian Sandweg until 06/11

Dipl.-Phys. Thomas Sebastian

Dipl.-Phys. Georg Wolf

Dipl.-Phys. Katrin Vogt

Diploma Students:

Thomas Brächer until 11/10

Thomas Langner until 05/11

Thomas Meyer since 04/11

Jan Westermann since 03/11

Engineers and Technicians

Eugen Momper (Rheinbreitbach) until 09/11

Dipl.-Ing. (FH) Dieter Weller

Administration:

Sibylle Müller
Dr. Isabel Sattler

2.2 Visiting scientists, postdoctoral fellows and exchange students

(sorted by date of first arrival in our group)

Alexy Karenowska, University of Oxford,
United Kingdom 02.01.2011 - 08.01.2011

This year Alexy Karenowska obtained a position of Junior Research Fellow in Clarendon Laboratory of University of Oxford. Her visit to Kaiserslautern has been supported by the State Research Center OPTIMAS of TU Kaiserslautern. We have spent a very useful week discussing the perspectives, trends and problems of magnon spintronics.

Prof. Toshu An, Institute for Solid State Physics,
University of Tokyo, Japan 18.01.2011 - 28.01.2011

The visit of Prof. An has been realized in the frame of our joint research on spin caloritronic transport. During his visit the joint experimental studies on the non-reciprocal magnon carried temperature flow and on the microwave cooling were performed.

Prof. Yoshichika Otani, Institute of Solid State Physics,
University of Tokyo, Japan 08.03.2011 - 11.03.2011

Prof. Otani visited our group in the framework of our JST/DFG collaboration project "Mapping of spin accumulation using Brillouin light scattering spectroscopy". During his stay, we discussed and analyzed our ongoing research work on spin dynamics in nonmagnetic metals and planned for future studies.

Dr. Natalia Grigoryeva, Electrotechnical University,
St. Petersburg, Russia 28.04.2011 - 09.06.2011

The stay of Dr. Grigoryeva was supported in the framework of our project "Coherent nonlinear spin-wave states in ferromagnetic films and ferromagnetic/ferroelectric layered structures" (DFG RUS 113/644/0). During her visit she continued the development of the exact dipole-exchange theory of spin-wave dynamics in magnonic crystals.

Olatz Idigoras, Nanoscience Cooperative Research Center,
CIC Nanogune, Donostia-San Sebastian, Spain 02.05.2011 - 30.06.2011

Olatz Idigoras is a Ph.D. student in the Nanomagnetism Group at CIC Nanogune. Her stay with us was possible due to a nanoICT exchange visit fellowship. The aim of her visit was to use Brillouin light scattering spectroscopy to study how the hard axis anomalous magnetization reversal in partially disordered Co thin films affects the spin wave spectrum. Additionally, she used the same technique to measure the exchange and anisotropy constants of a series of Co thin films with varying degree of disorder.

Dr. Sergiy Bunyayev, Universidade do Porto,
Portugal

17.06.2011 - 30.06.2011

The stay of Dr. Bunyayev was supported in the framework of our joint DAAD-FCT collaborative grant “Full metallic, nanoscale magnonic crystals”. He participated in BLS and MOKE studies of CrO₂ based magnonic crystals made in Portugal. He has also undergone a practical training in modern microwave measurement techniques.

Prof. Andrei Slavin, Oakland University,
USA

28.06.2011 - 24.07.2011

The visit of Prof. Slavin was supported by the Deutsche Forschungsgemeinschaft in the frame of the SFB/Transregio 49 “Condensed Matters Systems with Variable Many-Body Interactions”. During his visit he worked on transitional dynamics of a parametrically driven magnon gases and on the theory of nonlinear evaporative supercooling of a hot Bose-Einstein condensate of quasi-particles.

Prof. Johan Åkerman, University of Gothenburg,
Sweden

28.06.2011 - 02.07.2011

The research interests of Prof. Åkerman are focused on the area of spintronics where he works on developing of the next generation of MRAM and spintronic oscillators. We have thoroughly discussed our joint work on design and characterization of nano-contact spin-torque oscillators.

Dr. Hiroshi Naganuma, Tohoku Laboratory,
Tohoku University, Sendai, Japan

30.06.2011 - 05.07.2011

Dr. Naganuma visited our group in the framework of the JST-DFG project “Advanced spintronic materials and transport phenomena, ASPIMATT”. In the laboratory of Prof. Ando at the Tohoku University in Sendai, he is responsible for the project “Novel devices based on Heusler films with GMR and TMR nanocontacts”. His visit was focused on the observation of spin-wave propagation from a spin-torque nano-oscillator fabricated in Sendai via Brillouin light scattering spectroscopy.

Yuki Kawada, Tohoku Laboratory,
Tohoku University, Sendai, Japan

30.06.2011 - 05.07.2011

Yuki Kawada visited our group in the framework of the JST-project “Advanced spintronic materials and transport phenomena, ASPIMATT”. In the project “Novel devices based on Heusler films with GMR and TMR nanocontacts” he is responsible for the fabrication of spin-torque nano-oscillators. His visit was focused on the observation of spin-wave propagation from a spin-torque nano-oscillator fabricated in Sendai via Brillouin light scattering spectroscopy.

Prof. Gennadii Melkov, National Taras Shevchenko University,
University of Kiev, Ukraine 11.07.2011 - 24.08.2011

The visit of Prof. Melkov was supported by the Deutsche Forschungsgemeinschaft in the frame of the SFB/Transregio 49 “Condensed Matter Systems with Variable Many-Body interactions”. Prof. G. Melkov is ranked among the world’s leading specialists in nonlinear magnetic theory. During his stay Prof. Melkov was mainly working on the theoretical analysis of temporal dynamics of a condensate of photon coupled magnon pairs and spin pumping phenomena caused by parametric injection and nonlinear scattering of exchange and dipole-exchange magnons in magnetic insulator - non-magnetic metal bi-layer structures.

Denys Slobodianiuk, National Taras Shevchenko University,
University of Kyiv, Ukraine 12.09.2011 - 08.11.2011

Denys Slobodianiuk is a Ph.D. student working in the magnetism group of Prof. G. Melkov at the National University of Kyiv. Being an expert in the theory of parametrical instabilities in magnon gases, he spent his time with us on the development of the theory supporting the experimental studies performed in Kaiserslautern. Besides, jointly with Dmytro Bozhko, Denys Slobodianiuk has studied experimentally p-magnon phenomena in YIG thin films.

Dmytro Bozhko, National Taras Shevchenko University,
University of Kyiv, Ukraine 16.09.2011 - 15.11.2011

Dmytro Bozhko is a graduate student working in the magnetism group of Prof. G. Melkov at the National University of Kyiv. During his time with us, he has undertaken experimental work on spin-wave detection using inverse spin Hall effect and developed software for the automation of these measurements. Besides, he has developed special software for the analysis of the BLS data.

Dr. Gleb Kakazei, Universidade do Porto,
Portugal 26.09.2011 - 12.10.2011

The stay of Dr. Kakazei was supported in the framework of our joint DAAD-FCT collaborative grant “Full metallic, nanoscale magnonic crystals”. His visit was devoted to discuss the progress of the joint research on metallic magnonic crystals by means of BLS and FMR oriented microwave techniques. He participated in the preparation of novel metallic magnonic crystals and their initial characterization by CEM. Also a joint paper submitted to “Applied Physics Letters” on previously obtained results was prepared.

2.3 Guest seminars

| | |
|---|---|
| Prof. Dr. YoshiChika Otani 09.03.2011 | RIKEN, University of Tokyo, Japan <i>Strongly enhanced spin accumulation and long-distance spin manipulation in metallic lateral spin valves</i> Physics Colloquium |
| Dr. Axel Hoffmann 08.06.2011 | Argonne National Laboratory, Illinois, USA <i>Pure spin currents: discharging spintronics</i> Special seminar, IEEE Distinguished Lecture |
| Prof. Dr. Eric Fullerton 15.06.2011 | University of California, San Diego, USA <i>Controlled exchange in bit-patterned recording media</i> Special seminar |
| Prof. Dr. Andrew Kent 21.06.2011 | New York University, USA <i>Ultrafast spin-transfer driven magnetization reversal and exciting spin-waves</i> Special seminar |
| Dr. Vladimir L. Safonov 06.07.2011 | Mag & Bio Dynamics, Inc., Escondido, California, USA <i>Nonequilibrium magnetic excitations</i> Physics Colloquium |
| Prof. Dr. Peter Fischer 07.07.2011 | Lawrence Berkeley National Laboratory, USA <i>Magnetic soft X-ray microscopy: a path towards imaging magnetism down to fundamental length and time scales</i> Special seminar, IEEE Distinguished Lecture |
| Prof. Artur Widera 18.07.2011 | Technische Universität Kaiserslautern, Germany <i>Exploring quantum physics with single neutral atoms</i> Special group seminar |
| Prof. Dr. Arun Gupta 20.09.2011 | MINT, Alabama, USA <i>Ferromagnetic oxides for spintronics</i> Special seminar |

2.4 Visits of group members to other laboratories

| | |
|------------------|--|
| Katrin Vogt | Argonne National Laboratory, Argonne, USA 27.12.2010-07.02.2011 20.04.2011-21.06.2011 Host: Dr. Axel Hoffmann |
| | Colorado State University, Fort Collins, USA 22.06.2011-08.07.2011 Host: Prof. Kristen Buchanan |
| Peter Clausen | Faculdade de Ciencias da Universidade do Porto, Portugal 14.02.2011-18.02.2011 Host: Dr. Gleb Kakazei |
| Andrii Chumak | Faculdade de Ciencias da Universidade do Porto, Portugal 14.02.2011-18.02.2011 Host: Dr. Gleb Kakazei |
| Thomas Sebastian | Faculdade de Ciencias da Universidade do Porto, Portugal 14.02.2011-18.02.2011 Host: Dr. Gleb Kakazei |
| Oleksandr Serga | Faculdade de Ciencias da Universidade do Porto, Portugal 14.02.2011-18.02.2011 Host: Dr. Gleb Kakazei |
| Björn Obry | Helmholtz-Zentrum Dresden-Rossendorf 21.03.2011-25.03.2011 Host: Prof. Dr. J. Fassbender |

2.5 Group member photo gallery



Milan Agrawal
Ph.D. student



Dr. Gerhard Baldsiefen
Postdoc



Dr. Andreas Beck
Postdoc



Thomas Brächer
Ph.D. student



Dr. Andrii Chumak
Senior scientist



Florin Ciubotaru
Ph.D. student



Peter Clausen
Ph.D. student



Dr. Andrés Conca Parra
Postdoc



Frederik Fohr
Ph.D. student



Prof. Dr. Burkard Hillebrands
Group leader



Benjamin Jungfleisch
Ph.D. student



Lisa Kleinen
Ph.D. student



Thomas Langner
Diploma student



Dr. Britta Leven
Senior scientist



Thomas Meyer
Diploma student



Eugen Momper
Technician



Sibylle Müller
Secretary



Roland Neb
Ph.D. student



Björn Obry
Ph.D. student



Philipp Pirro
Ph.D. student



Ana Ruiz Calaforra
Ph.D. student



Christian Sandweg
Ph.D. student



Dr. Isabel Sattler
Administration



Thomas Schneider
Postdoc



Thomas Sebastian
Ph.D. student



Dr. Alexander Serga
Senior scientist



Dr. Vitaliy Vasyuchka
Postdoc



Katrin Vogt
Ph.D. student



Dieter Weller
Mechanical engineer



Jan Westermann
Diploma student



Georg Wolf
Ph.D. student

Chapter 3: Methods

3.1 Brillouin light scattering spectroscopy (BLS)

Brillouin light scattering (BLS) spectroscopy is one of the key techniques in our laboratory to investigate the dynamic properties of magnetic materials and devices. It is based on the interaction of photons with the fundamental excitations of a solid such as magnons, the quanta of magnetic excitations. The interaction can be understood as an inelastic scattering process of the incident photons with magnons, taking into account energy and momentum conservation as indicated in Fig. 1.

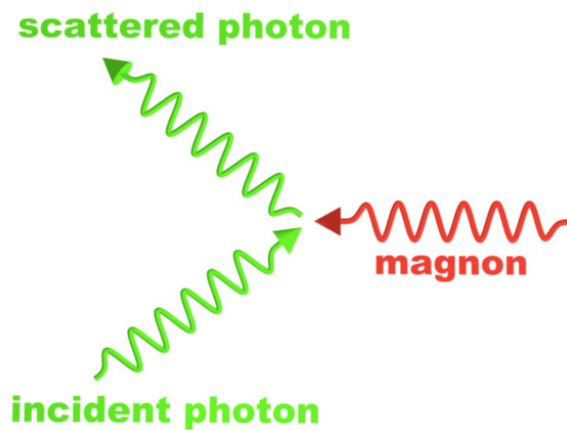


Fig. 1: Scheme of inelastic scattering of an incident photon by a magnon.

The detection of the inelastically scattered photons, i.e. the separation from the elastically scattered photons and the determination of the transferred energy, requires an interferometry technique with extremely high contrast and sensitivity. In our laboratory we implemented the (3+3) Tandem-Fabry-Perot-Interferometer, designed by John R. Sandercock and schematically shown in Fig. 2. It consists of two Fabry-Perot interferometers (FPI), each one passed three times by the inelastically scattered light. This approach results in a contrast better than 10^{10} for the separation of the elastically and inelastically scattered photons in a frequency range from 500 MHz up to 1 THz.

In the last decade we made significant progress in the improvement of BLS spectroscopy. The spatial resolution was pushed to the fundamental limit of classical optics by constructing a BLS-microscope (Fig. 3) with sophisticated active stabilization methods. Spin-wave transport phenomena can be investigated by time, phase- and wave-vector resolution. The following list gives an overview of the different BLS setups available in our group:

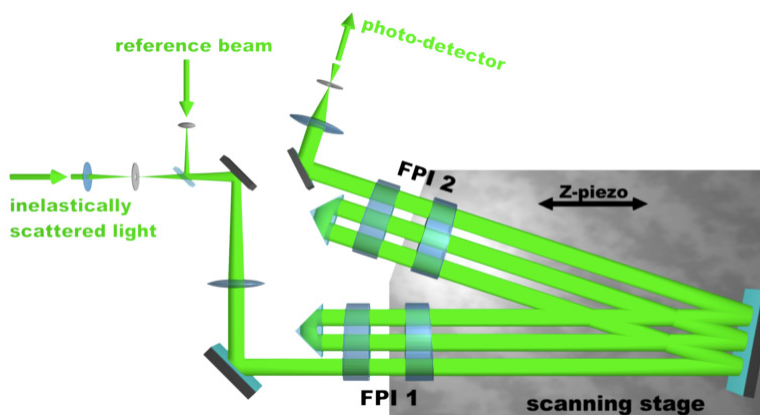


Fig. 2: Scheme of a (3+3) tandem Fabry-Perot interferometer, designed and build by John R. Sandercock (JRS Scientific Instruments, Zürich)

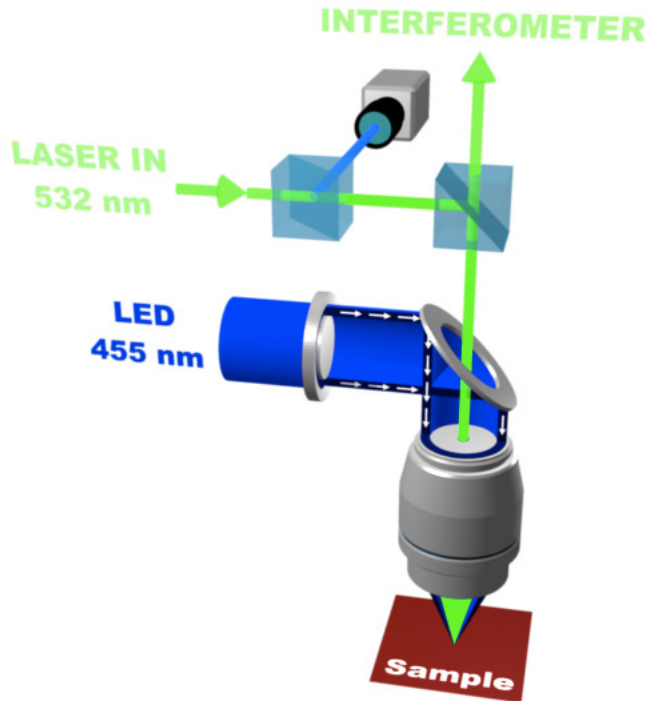


Fig. 3: Schematic setup of a BLS-microscope.

BLS1: High-field electromagnet (1.2 T), standard BLS spectroscopy equipment. Time resolution, phase resolution, space resolution (50 μm), wave-vector resolution.

BLS2: High-field electromagnet (1.2 T), standard BLS spectroscopy equipment. Microscope stage with 200 nm spatial resolution and build-in time and phase resolution.

BLS3: High-field electromagnet (1.2 T), standard BLS spectroscopy equipment. Microscope stage with 200 nm spatial resolution and build-in time and phase resolution.

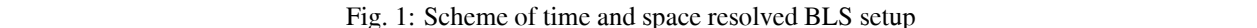
BLS4: Electromagnet (0.1 T), standard BLS spectroscopy equipment. Microscope stage with 200 nm spatial resolution and build-in time and phase resolution.

3.2 Microwave techniques

Various microwave techniques to study both linear and nonlinear dynamics of magnetization in nanostructured and in macroscopic samples are available in our laboratory.

We use continuous and pulsed microwave signals having powers of up to 100 Watt in a frequency range from 1 to 20 GHz. They are used for coherent excitation of long-wavelength dipolar-dominated spin waves and the ferromagnetic resonance. Thus, we are able to perform both continuous-wave measurements and to characterize travelling spin-wave packets. Spin waves are coupled to electromagnetic sources using different types of microstrip and coplanar antennas as well as wire loops and cavities. These devices induce microwave Oersted fields which force the precession of magnetic moments in the sample. Vice versa, the precession of macroscopic magnetic moments is converted by the same devices into microwave currents. These currents are amplified by high-sensitive low-noise amplifiers and rectified by crystal detectors. These signals are observed with an oscilloscope to reveal their temporal structure. Precise spin-wave amplitude and phase measurements in a wide frequency range are performed using spectrum and network analysers.

The parametric pumping process is another powerful microwave technique used in our laboratory.



This technique plays an important role in experiments on fundamental properties of magnetic excitations as well as in applications since it allows for the amplification, generation, and processing of spin-wave signals. Moreover, contrary to the forced excitation, this technique allows us to generate exchange-dominated spin waves with very short wavelength. In the case of spatially uniform parallel pumping (microwave magnetic field is parallel to the magnetization) each microwave photon of the pump field splits into two spin-wave quanta (i.e. magnons) having half the energy and propagating in opposite directions. As soon as the quantity of parametrically created magnons exceeds the quantity of magnons which disappear due to magnetic decay the intensity of the corresponding spin-wave mode starts to increase up to the level of nonlinear saturation. In this process a pumped magnon density of 10^{18} - 10^{19} cm $^{-3}$ can be reached, which is enough, for example, to cause the transition of the spin-wave system to a Bose-Einstein condensate state.

3.3 Magneto-optic Kerr effect magnetometry and microscopy (MOKE)

The magneto-optical Kerr effect (MOKE) is a well established technique to study magnetization properties. The effect is based on the fact, that the plane of polarization of light is rotated when the light is reflected from a magnetic material [1]. The physical origin of MOKE is the magnetic circular dichroism effect: exchange and spin-orbit coupling in a magnetic material lead to different absorption spectra for left- and right-circularly polarized light. Measuring the change of the polarization of the reflected beam (often referred to as Kerr angle Θ_{Kerr}) gives access to the magnetization state of the sample.

AG MAGNET/SMUS
TU KAISERSLAUTERN

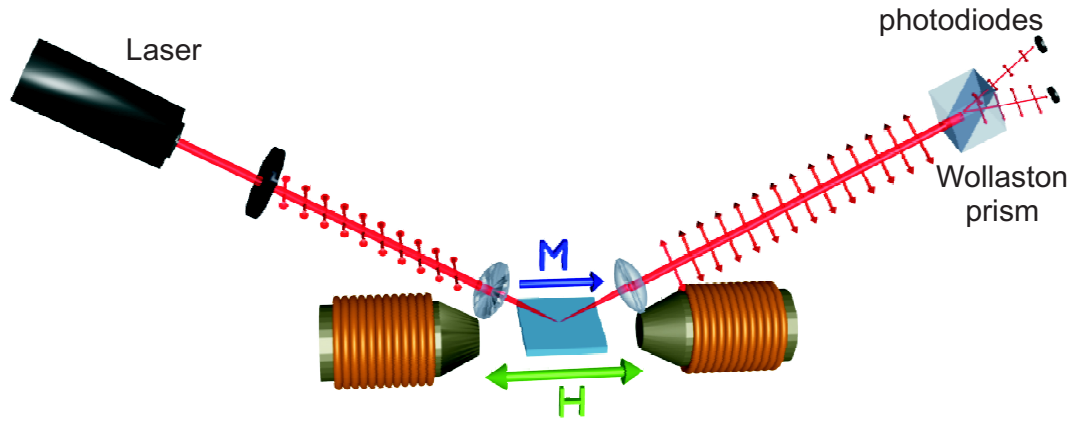


Fig. 1: Schematic setup of a longitudinal Kerr magnetometer.

resolution. Thus, we are able to study the static and dynamic properties of magnetic thin films and magnetic structures with lateral dimension down to $1\ \mu\text{m}$.

Our group uses four different MOKE setups, all of them using the same principle. The light of a laser source is s-polarized through a thin-film polarizer. The beam is focused onto the sample. The polarization of the reflected light is analyzed by a detector unit that was developed and is built in our laboratory. A Wollaston prism divides the beam into two orthogonally polarized beams, which are monitored by a pair of photodiodes. The detector works as an opto-electrical bridge circuit to increase the signal-to-noise ratio. The obtained normalized differential signal $(I_1 - I_2)/(I_1 + I_2)$ is directly proportional to the Kerr angle Θ_{Kerr} .

Four experimental setups are available to investigate different scientific aspects:

Longitudinal Kerr magnetometer: Longitudinal MOKE geometry to probe quasi-static properties of magnetic thin films. Optical resolution $\sim 100\ \mu\text{m}$, magnetic field up to 2 T, automated sample positioning and rotation.

Microfocused Kerr microscope with rotation unit: Longitudinal MOKE geometry to probe quasi-static properties of micro-structured magnetic elements. Optical resolution $< 1\ \mu\text{m}$, magnetic field up to 0.6 T, automated sample positioning, rotation and stabilization.

Dual MOKE magnetometer: Two combined MOKE magnetometers working in parallel, one in longitudinal and one in polar geometry to study the quadratic MOKE effects on magnetic thin films. Optical resolution $\sim 100\ \mu\text{m}$, two orthogonal pairs of magnet coils to provide any in-plane field direction up to 0.25 T, automated sample positioning and rotation.

Time resolved scanning Kerr microscope: Longitudinal or polar MOKE geometry to study dynamic magnetization reversal properties of micro-structured elements. Optical resolution $< 500\ \text{nm}$, time resolution $\sim 60\ \text{ps}$, magnetic field up to 150 mT, automated sample positioning and stabilization.

References

- [1] J. Kerr, *On rotation of the plane of polarization by reflection from the pole of a magnet*, Phil. Mag. **4**(5), 321 (1877).

3.4 Molecular beam epitaxy (MBE)

Molecular beam epitaxy (MBE) means the atomic layer specific (epitaxial) growth of a film on a substrate in ultra high vacuum (UHV). The particular advantage of this method of material deposition is the good controllability of the growth process, which has a significant influence on the physical properties of the specific layers [1]. The growth process takes place close to thermodynamic equilibrium.

For a typical MBE-deposition process the material that needs to be deposited is heated in UHV and forms a molecular beam. The atoms of the beam are then adsorbed by the sample surface (adatoms). During the deposition of the atoms the adatoms interact with the atoms of the surface (Fig. 1). This interaction depends on the type of adatoms, the substrate, and the temperature of the substrate. It is responsible for the nucleation and the subsequent growth in the form of thin layers on the substrate. To achieve good-quality film growth the growth rate must be small (typical growth rate: $0.05 \dots 1 \text{ \AA/s}$) and therefore the vacuum pressure in the ultrahigh vacuum regime is typically only a few 10^{-11} mbar .

Depending on the growth parameters one can generally distinguish between three different growth modes [2]:

1. Layer or Franck-van der Merwe growth mode: A new layer starts to grow only after the preceding one is finished (Fig. 2a).
2. Island or Vollmer-Weber growth mode: The deposited atoms cannot diffuse past the island boundaries. Already after a light coverage multiple monolayers can be formed as high islands (Fig. 2b).
3. Layer plus island or Stranski-Krastanov growth mode: This type is a combination of layer and island growth mode (Fig. 2c).

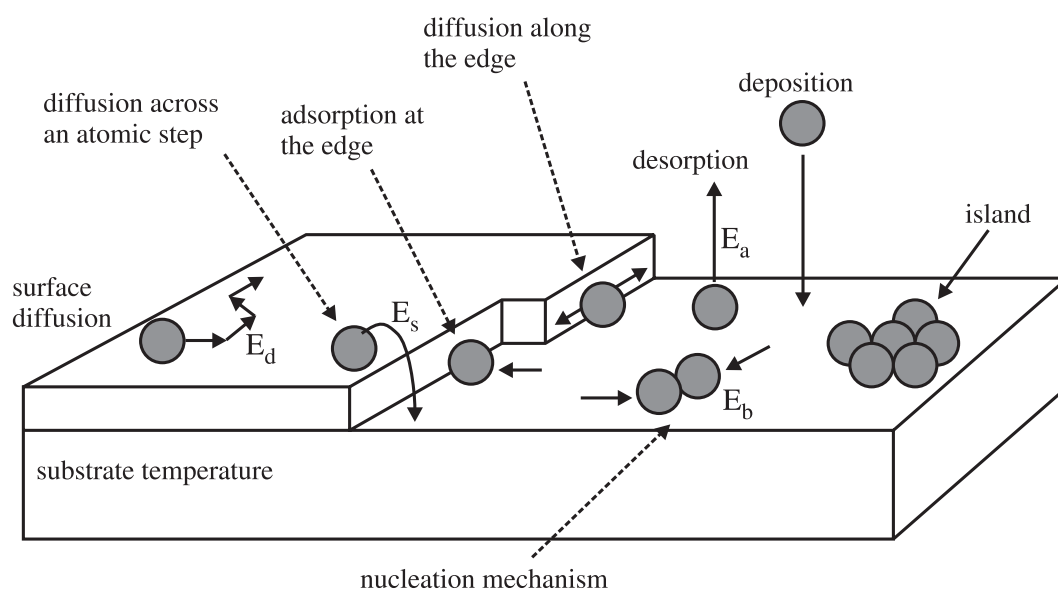


Fig. 1: Behavior of adatoms in the surface deposition process (diffusion until nucleation with other adatoms; deposition on edges).

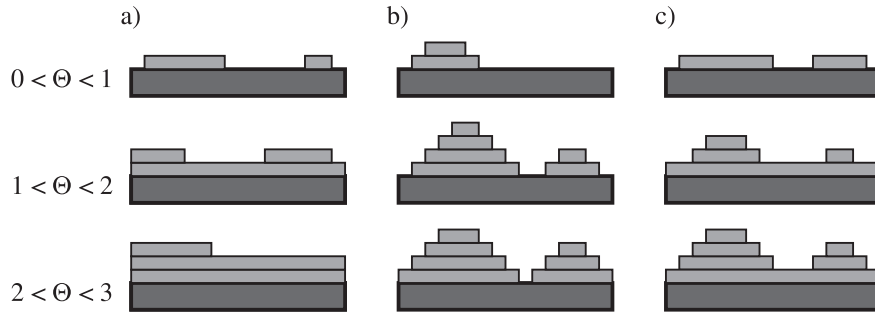


Fig. 2: Growth modes for layer development by MBE. θ - degree of coverage.

Two MBE machines are operated in our research group.

Multi-chamber UHV deposition system:

- deposition chamber (electron beam evaporator and Knudsen evaporation source) with RHEED, LEED, and Auger analytics for surface characterization
- scanning tunnelling microscopy chamber for *in situ* STM (Omicron)
- Brillouin light scattering and Kerr magnetometry chamber (magnetic field 1.2 T, temperature range 80-400 K)
- preparation chamber (optical coating, heating station 2300°C)
- plasma beam chamber

Two-chamber UHV multideposition system:

- deposition chamber (electron beam and Knudsen source evaporation, LEED and Auger analytics)
- ion beam chamber with fine-focus noble-gas keV ion source (Omicron), ion beam oxidation module

References

- [1] A.Y. Cho: Applied Physics Letters **19**, 467 (1971).
 [2] J.A. Venables, Reports on Progress in Physics **47**, 399 (1984).

Chapter 4: Reports on Experimental Results

A. Magnon Gases and Condensates

In ferromagnetic materials atoms having unpaired electrons act as individual magnets. Their magnetism is mostly caused by the magnetic moments of the uncompensated electron spins. Since these atomic magnets tend to be oriented in the same direction due to specific quantum-mechanical exchange interaction, a macroscopic magnetic moment appears. As the atoms strongly interact a reversal of a single atomic magnetic moment is not spatially localized but spreads through the solid as a wave of discrete magnetic momentum transfer. This wave is known as a spin wave, and in frame of the second quantization it is associated with a quasi-particle called magnon. Weakly interacting magnons can be considered as a gas of magnetic bosonic quasi-particles, and therefore this is called a magnon gas.

This gas may serve as a model system for the investigation of interacting bosonic particles and for correlated systems in general. Its potential is based on the wide controllability of the magnon density as well as on the spectral properties influencing the magnon-magnon interaction. The observation of Bose-Einstein condensation of magnons at room-temperature in the minimum of the spin-wave spectrum demonstrates this clearly (see *Nature* **443**, 430 (2006)).

The spectrum of a magnon gas can be easily controlled by change of orientation and strength of an external bias magnetic field. The most effective mechanism to inject magnons into the gas is microwave parametric pumping (see Gurevich and Melkov, *Magnetization Oscillation and Waves*, CRC, Cleveland, 1996). In the simplest case one photon of the pumping electromagnetic field excites two magnons with half the energy/frequency that propagate in opposite directions. Such mechanism creates a huge quantity of phase correlated magnons, called a condensate of photon-coupled magnon pairs. Among others, such magnon pairs serve as an energy source and as a strong disturbing factor for the entire spin-wave system. Formation, thermalization and disintegration of this condensate as well as its interaction with the other magnonic states and especially with the Bose-Einstein condensate (BEC) of magnons constitutes a hot topic of research. To investigate these processes we use time- and wavevector-sensitive Brillouin light scattering spectroscopy in combination with conventional microwave techniques.

In Report 4.1 “Variable damping and coherence in a high-density magnon gas” we demonstrate our recent results on the relaxation of a free evolving gas of parametrically pumped magnons. The experimental data show a clear deviation from the standard exponential spin-wave decay model. The results are in agreement with the model which accounts for variation of phase coherence for parametrically injected magnon groups during pump-free time intervals. In Report 4.2 “Mode structure of parametrically excited magnons in a magnetic film” we analyze the optically observed spectral distribution of a condensate of photon-coupled magnon pairs in a tangentially magnetized magnetic film. Finally, in Report 4.3 “Transition processes in a highly excited multi-mode autonomous magnon system”, processes of energy transfer between frequency-degenerated magnon groups in a highly excited multi-mode autonomous magnon system are studied both experimentally and theoretically.

A. Magnonengase und -kondensate

In ferromagnetischen Materialien treten Atome, die ungepaarte Elektronen haben, als einzelne Magnete auf. Ihr Magnetismus wird in der Regel durch die magnetischen Momente des nicht kompensierten Elektronenspins verursacht. Diese atomaren Magnete richten sich aufgrund der quantenmechanischen Austauschwechselwirkung in einem Ferromagneten parallel zueinander aus. Daher beobachtet man ein makroskopisches magnetisches Moment. Da die Atome stark miteinander wechselwirken, wird das Umklappen eines einzelnen atomaren Moments nicht räumlich lokalisiert sein, sondern breitet sich als Welle mit einem diskreten magnetischen Moment über den gesamten Festkörper aus. Diese Welle wird als Spinwelle bezeichnet und ist im Rahmen der zweiten Quantisierung mit einem Quasiteilchen, dem so genannten Magnon, verbunden. Schwach miteinander wechselwirkende Magnonen können als Gas von magnetischen bosonischen Quasiteilchen angesehen werden. Daher werden sie auch als Magnonengas bezeichnet.

Dieses Gas kann als Modellsystem für die Untersuchung von wechselwirkenden bosonischen Teilchen und von korrelierten Systemen im allgemeinen dienen. Sein Potenzial liegt dabei in der guten Kontrollierbarkeit der Magnondichte und den Eigenschaften des Spektrums, welche die Magnon-Magnon-Wechselwirkung beeinflussen. Die kürzlich erfolgte Beobachtung der Bose-Einstein-Kondensation von Magnonen bei Raumtemperatur im Minimum des Spinwellenspektrums zeigt dies deutlich (s. Nature **443**, 430 (2006)).

Das Spektrum des Magnonengases kann leicht durch eine Änderung der Richtung oder der Stärke eines externen Magnetfelds kontrolliert werden. Der wirkungsvollste Mechanismus, Magnonen in ein Magnonengas einzufüllen, ist parametrisches Pumpen mittels Mikrowellen (s. Gurevich and Melkov, Magnetization Oscillation and Waves, CRC, Cleveland, 1996). Im einfachsten Fall erzeugt ein Photon des elektromagnetischen Pumpfeldes zwei Magnonen mit je der Hälfte der Energie des Photons, die sich in entgegengesetzte Richtungen ausbreiten. Dieser Mechanismus erzeugt eine große Anzahl von phasenkorrelierten Magnonen, ein Kondensat von photonengekoppelten Magnonenpaaren. Unter anderem dienen solche Magnonenpaare als Energiequelle und als starke Störung des gesamten Spinwellensystems. Erzeugung, Thermalisierung und Zerfall dieses Kondensats sowie seine Wechselwirkung mit anderen Magnonenzuständen und besonders mit dem Bose-Einstein-Kondensat von Magnonen sind ein aktuelles Thema der Forschung. Zur Untersuchung dieser Prozesse verwenden wir zeit- und wellenvektoraufgelöste Brillouin-Lichtstreuungsspektroskopie in Verbindung mit konventioneller Mikrowellentechnik.

In Bericht 4.1 “Variable damping and coherence in a high-density magnon gas” stellen wir neue Resultate über die Relaxation eines sich frei entwickelnden Gases parametrisch gepumpter Magnonen vor. Die experimentellen Daten zeigen eine klare Abweichung vom üblichen exponentiellen Zerfallsmodell von Spinwellen. Die Resultate sind in Übereinstimmung mit dem Model, welches für die Veränderung der Phasenkohärenz von parametrisch injizierten Magnonengruppen während der pumpfreien Zeit herangezogen wird. Im Bericht 4.2 “Mode structure of parametrically excited magnons in a magnetic film” untersuchen wir optisch die spektrale Verteilung eines Kondensats von photonengekoppelten Magnonenpaaren in einem tangential magnetisierten magnetischen Film. Im Bericht 4.3 “Transition processes in a highly excited multi-mode autonomous magnon system” werden Energietransfer-Prozesse zwischen frequenzentarteten Magnonengruppen in einem hochangeregten, autonomen Multi-Mode Magnonensystem experimentell und theoretisch untersucht.

4.1 Variable damping and coherence in a high-density magnon gas

A.A. Serga, S. Schäfer, and B. Hillebrands¹

Several decades after the first phenomenological descriptions, the nature of spin-wave dissipation is still a subject of intense scientific research [1–5]. Recent developments in the study of energy transfer in magnon systems, including the discovery of Bose-Einstein condensation of magnons in a parametrically driven spin system of a low-damping Yttrium Iron Garnet (YIG) epitaxial film, have attracted particular interest to the problem of nonlinear damping and decoherence of densely populated magnon states, created by the effect of parametric pumping [6].

In this work we demonstrate that a free evolution of a dense group of parametrically injected magnons can be described neither by its monotonic exponential relaxation nor by possible nonlinear decay. The phase decoherence of the frequency smeared magnon group must be taken into account in order to understand the experimental data.

The experiment was carried out as follows. A 100ns-long traveling spin-wave packet is excited at a frequency of 7GHz by a microstrip input antenna in a 1.5mm-wide and 5 μ m-thick YIG stripe. An external magnetic field \vec{H}_0 of 143.64kA/m (1805Oe) is applied in the plane of the stripe, perpendicular to the spin-wave propagation (Fig. 1a), i.e. in the Damon-Eshbach (DE) geometry [7]. The excited spin-wave packet traverses the magnetic sample, is detected by the output antenna placed 12mm apart from the input one, amplified, and observed with an oscilloscope.

After 450ns since the passage by the wave packet of the central area of the YIG stripe ($\tau_0 = 450$ ns), a pumping microwave field \vec{h}_p at 14GHz produced by a dielectric resonator is applied parallel to the bias magnetic field. As a result of the pump action, an additional “recovered” pulse is observed at the output antenna at a frequency of 7GHz (see output waveform in Fig. 1a and dashed line in Fig. 2). Since the DE packet has already left the area of parametric interaction, this is not the

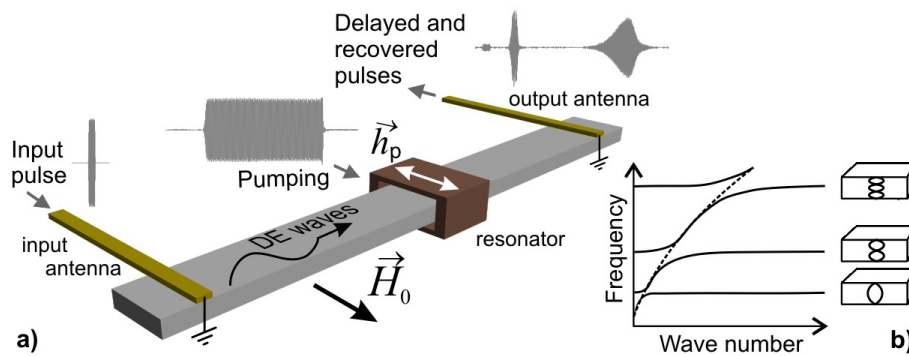


Fig. 1: a) Experimental setup, consisting of a single-crystal YIG waveguide, input and output antennas and a dielectric resonator for the application of the pumping microwave field. The waveforms are the shapes of the input, pumping and restored pulses as seen on the oscilloscope. b) Section of the spin-wave dispersion spectrum for a thin magnetic waveguide schematically showing the hybridization of Damon-Eshbach (dashed line) wave with standing spin wave modes.

¹In collaboration with M.P. Kostylev, School of Physics, M013, University of Western Australia, Crawley, WA 6009, Australia; S.S. is now at University of Alabama, Center for Materials for Information Technology, Department of Physics & Astronomy, Tuscaloosa, AL 35487, USA.

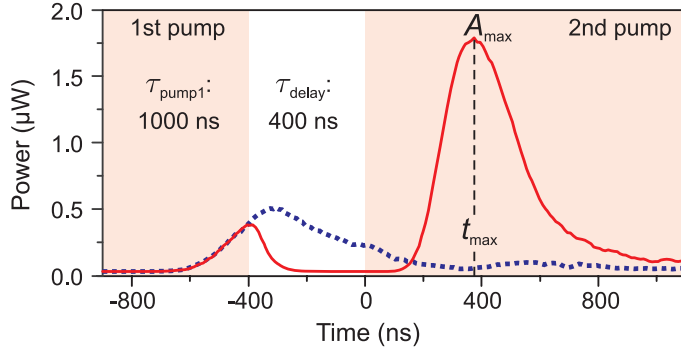


Fig. 2: Spin-wave power envelope as observed at the oscilloscope. The shaded areas show the time intervals when the pump is on. The continuous line represents the results of the two pump-pulse recovery. The first pump pulse is switched off before the recovered signal saturates. The dashed line represents the experimental result for the pumping not being interrupted.

result of the direct amplification of the signal pulse [8]. Rather, the parametric pumping acts on the standing spin-wave (SSW) modes (see Fig. 1b) which are excited across the film thickness by the traveling wave packet through a two-magnon scattering mechanism. These modes are then amplified by parametric pumping and are scattered back to form a new traveling DE wave, which is finally detected at an output antenna in a form of the “recovered” pulse (Fig. 1a).

Unlike in our previous studies [9–11], in the experiment reported here, two consecutive parametric pump pulses are used rather than one. The response of the magnonic system to the second pulse is utilized as a probing tool for extracting information about the free relaxation behavior of parametrically excited magnons during the pump-free pause. Therefore, we cut off the first recovered pulse by stopping the parametric pumping. After a certain delay time τ_{delay} , a second pumping pulse is applied and a second recovered pulse is observed (see continuous line in Fig. 2). We register the peak amplitude A_{max} and the arrival time t_{max} of the second recovered pulse. As one sees from Fig. 3, the behavior of the second recovered pulse strongly depends on the delay time τ_{delay} between two consecutive pumping pulses. It is remarkable that this dependence is non-monotonic: with an increase in τ_{delay} the pulse first grows, reaches a maximum, and then decreases in intensity. In particular, one observes a gain in the amplitude of the second recovered pulse compared to the experiment in which the pumping is uninterrupted ($\tau_{\text{delay}} \rightarrow 0$ in Fig. 3).

One easily finds that neither the initial increase in the amplitude nor the subsequent non-exponential decrease (note the logarithmic scale) in the peak amplitude can be explained in the framework of the standard approach based on association of a specific relaxation time with each decay process. For this reason we make an attempt to employ a more detailed model.

We start the description of the developed theory by noting that the recovered pulse has a pulse-like shape. This suggests that competition of two magnon groups for energy provided by the parametric pumping process [12] takes place in the magnon system, since a pulse-like shape of the observed signal is a typical result of this competition. This process can be understood in the following way. The parametric amplification is frequency selective: only magnon groups with eigenfrequencies ω_k which lie inside the narrow frequency band $\omega_p/2 - \nu < \omega(k) < \omega_p/2 + \nu$ whose width is equal to the parametric amplification gain $\nu = h_p V$ are amplified (V is the parametric coupling coefficient). They are driven at half the frequency $\omega_p/2$ of the applied microwave field. Importantly, there is no restriction on the magnitude and the direction of the magnon wavevector: the process allows creation of magnons with arbitrary wavevectors, provided their frequencies are inside this frequency band. Thus, given the large number of frequency-degenerate magnon dispersion branches, magnon groups over a large range of wavevectors are amplified. This includes externally excited oscillations, hereafter called the signal group, as well as thermally activated magnons with wavevectors up to 10^5 cm^{-1} . The latter magnons, which are considerably decoupled from structural defects of the YIG film because of their short wavelength, experience the lowest two-magnon decay and

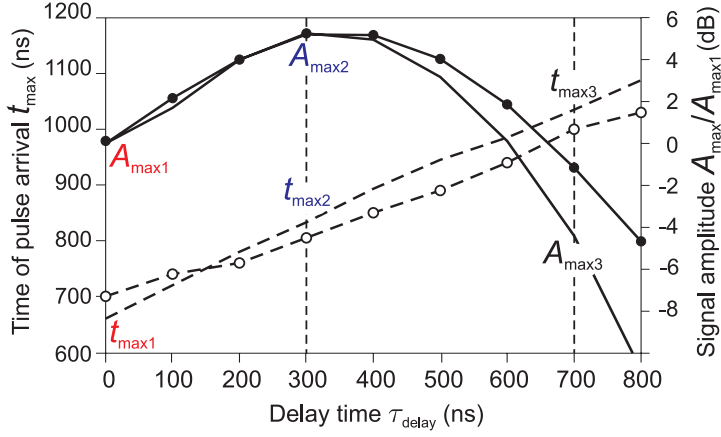


Fig. 3: Left axis: measured (circles connected by a dashed line) and simulated (dashed line) time t_{\max} at which the peak amplitude of the recovered pulse is observed as a function of τ_{delay} for $\tau_{\text{pump1}} = 400$ ns. Right axis: measured (dots connected by a solid line) and simulated (solid line) peak amplitudes of the recovered pulse for $\tau_{\text{pump1}} = 400$ ns.

consequently show the highest parametric gain [13]. Hence, we refer to this dominantly amplified magnon group as the dominant group. As the phase shift between the external pumping field \mathbf{h}_p and a microwave magnetic field induced by the parametrically pumped magnons (“internal pumping”) increases with increase in the total magnon density, the resulting effective pumping field inside the sample consecutively diminishes [11]. At some point in time the total magnon density reaches a critical threshold level A_{cr} at which the effective pumping becomes so small that it is able to further support just one magnon group, the one which has the lowest decay rate and the highest efficiency of parametric interaction: the dominant group. This leads to the suppression of the signal group, whilst the dominant group reaches saturation at A_{cr} . From this time on the system stays in a quasi-equilibrium state wherein the magnon density of the dominant group is saturated. The signal group is exposed to an effective pumping below the generation threshold, and thus should decay with time to the thermal level. As a result of this process, the signal group, and consequently the measured signal, acquire a pulse-like shape.

To obtain a quantitative description of the magnetic dynamics for the present case of two pump pulses, we perform numerical simulations based on the nonlinear model of the magnon group competition. We assume that the signal group represents a set of spin-wave oscillations (standing-wave modes) C_{ω}^s with resonance frequencies ω uniformly distributed across the frequency band $\delta\omega = \pm 1.5$ MHz around the half-pump frequency $\omega_p/2$. This frequency band corresponds to the spectral width of the dipole-exchange gaps in the spin-wave dispersion (Fig. 1b). Since the recovered pulse is only observed in these gaps, only magnons within this frequency band should contribute to the recovery process.

The standing-wave modes are excited through two-magnon scattering processes by the traveling-wave pulse on its way across the film. For simplicity we assume that the initial phase of magnetization precession for all the modes is the same. The output traveling-wave pulse is formed due to two-magnon back-scattering and thus represents an exact time replica of the dynamics of the signal group. Therefore it is sufficient to consider only the evolution of two immobile magnon groups: the signal and the dominant ones (The dominant group consists of magnons with complex amplitudes C_{ω}^d .)

The general dynamic equations are as follows:

$$\left[\partial/\partial t + \Gamma_s + i(\tilde{\omega}^s - \omega_p/2) \right] C_{\omega}^s - iP_{\omega}^s C_{\omega}^{s*} = 0, \quad (1)$$

$$\left[\partial/\partial t + \Gamma_d + i(\tilde{\omega}^d - \omega_p/2) \right] C_{\omega}^d - iP_{\omega}^d C_{\omega}^{d*} = 0, \quad (2)$$

where the stars denote complex conjugate, Γ_s and Γ_d are the relaxation parameters for the signal

and the dominant group respectively,

$$\tilde{\omega}^s = \omega + \Delta\omega^{ss} + \Delta\omega^{sd}, \quad (3)$$

$$\tilde{\omega}^d = \omega + \Delta\omega^{dd} + \Delta\omega^{ds} \quad (4)$$

are the eigenfrequencies of standing-wave oscillations with an account of nonlinear frequency shift for both signal and dominant groups respectively, and

$$P_\omega^s = \nu + P^{ss} + P^{sd}, \quad (5)$$

$$P_\omega^d = \nu + P^{ds} + P^{dd} \quad (6)$$

is the effective pumping for the signal and the dominant groups respectively. In Eqs. (3-6) and below the upper indices “s” and “d” denote the signal and the dominant group respectively. Double indices of type $\alpha\beta$ denote the action of the group β on the group α . If both indices are the same the respective coefficient or magnitude describes self-action.

In our calculations we use an usual assumption [11] that the nonlinear frequency shift is not important for the dynamics of the dominant group ($\Delta\omega^{dd} = 0$). Second, we do not need to take into account the contribution to the total nonlinear frequency shift by the signal group ($\Delta\omega^{ss} = \Delta\omega^{ds} = 0$), since its amplitude is considerably smaller than the amplitude of the dominant group at the time, when the effective pumping saturates. Thus, the only term we will account for is

$$\Delta\omega^{sd} = T \sum_{\omega', \omega'', \omega'''} C_{\omega'}^d C_{\omega''}^{d*} C_{\omega'''}^s \delta(\omega' - \omega'' + \omega''' - \omega), \quad (7)$$

where δ denotes the Kronecker Delta, and $T = T^{sd}$ is the respective nonlinear coefficient.

Similar considerations apply to the contributions to the total pumping which consists of the external pumping (ν) and the internal pumping given by the remainder of the terms in Eqs. (5, 6). We obtain: $P^{ss} = P^{ds} = 0$,

$$P^{sd} = S^{sd} \sum_{\omega', \omega'', \omega'''} C_{\omega'}^d C_{\omega''}^d C_{\omega'''}^{s*} \delta(\omega' - \omega'' + \omega''' - \omega), \quad (8)$$

$$P^{dd} = S^{dd} \sum_{\omega', \omega'', \omega'''} C_{\omega'}^d C_{\omega''}^d C_{\omega'''}^{d*} \delta(\omega' - \omega'' + \omega''' - \omega), \quad (9)$$

where $S^{\alpha\beta}$ are the respective nonlinear S -coefficients [11, 12].

Test numerical calculations show that calculation results do not qualitatively change with the variation in the difference $S^{dd} - S^{sd}$ in reasonable limits. Therefore, to minimize the number of degrees of freedom we set $S^{dd} = S^{sd} \equiv S$ and, as previously, we assume that $S > 0$ [11].

The last simplification we make is removing the frequency-mixing terms from Eqs. (7-9). This simplification does not lead to a qualitative change in the results of our numerical calculations, but enormously decreases the computation time. It reduces Eq. (5-6) to a simple formula for the effective pumping:

$$P_\omega^s = P_\omega^d \equiv P_\omega = \nu + S \sum_{\omega'} \left(C_{\omega'}^d \right)^2. \quad (10)$$

For the pump-free period the same equations (1-10) are valid, one just assumes $\nu = 0$, so that only the internal pumping is on during the pause.

Initial conditions for the dominant group are a random distribution of amplitudes for its frequency components. Initial conditions for the signal group follow from the expression for the frequency spectrum of a rectangular pulse

$$C_\omega(t = \tau_0) = C_0 \exp(i\omega\tau_0) F(\delta\omega) \frac{\sin(\omega\tau_{\text{input}}/2)}{\omega\tau_{\text{input}}/2}, \quad (11)$$

where τ_{input} is the length of the initial traveling wave pulse which generates the standing wave oscillations through the two-magnon scattering process, and τ_0 is the time interval between the the passage of the traveling wave pulse through the pump area and the begin of the first pump pulse, C_0 is some constant, and $F(\delta\omega)$ is equal to one within the dipole gap in the dipole exchange spectrum of travelling spin waves (Fig. 1), where the parametric signal recovery is usually observed ($F(\delta\omega) = 1$, for $-\delta\omega/2 < \omega < \delta\omega/2$) and vanishes outside the gap ($F(\delta\omega) = 0$, for $|\omega| > \delta\omega/2$).

The system of equations (1,2) was solved numerically. A number of simulation runs allows us to locate the area in the parameter space, where the simulated behavior is close to the experimental one. Figure 3 shows the best fit we obtain. One sees a fair agreement with the experiment of the simulated peak amplitudes of the restored pulse and of the times for the peak arrival t_{max} as a function of the pause length τ_{delay} . This calculation shows that the terms involving the S and T coefficients do not contribute to the dynamics during the pump-free pause, as the parametric amplification is quite far from saturation during this time interval. Note that analytical solutions exist for $S = T = 0$ and they are in full agreement with our simulations for the first two stages of the considered process ($t < 0$ in Fig. 4a-c). Figures 4a-4c show the behavior of the macroscopic amplitude of the signal group $A_s = 10 \log(|\sum_\omega C_\omega^s|^2)$ and of the strength of the internal pumping $A_d = 10 \log(|\sum_{\omega'} C_{\omega'}^d|^2)$. One sees that during the pump pause both magnitudes do not vary linearly on the logarithmic scale. The signal-group behavior is close to parabolic on this scale. Note the increase in the amplitude for the signal group during the first 200 ns after switching off the first pump in Fig. 4c. A careful analysis of this stage shows that the increase is due to phase reversal in a parametric-echo-like process [14, 15]. Recall that the coherence of the originally deterministic signal is lost due to dephasing during the time interval τ_0 between the passage of the traveling wave pulse and the application of the first pump pulse. In the phase reversal process the coherence is restored. The full phase restoration occurs for $\tau_{\text{delay}} = \tau_0$.

The behavior of A_d is more complicated: for the first 150 ns after the first pumping has been switched off, the internal pump decreases parabolically on the logarithmic scale, then its behavior switches to more or less linear on the same scale. This non-monotonic behavior of the internal pump also originates from dephasing. During the first pump pulse the frequency width of the dominant group reduces significantly due to the frequency selective amplification of the initially thermal signal. The phases of the waves which belong to this group are locked to the external pumping and the behavior of the internal pumping follows the linear behavior of the number of magnons, which is in full agreement with L'vov's S-theory. However, once the first pumping has been switched off, the phase coherence within the group is lost and the magnitude of A_d starts to decrease. As a result, at large times ($t > 300$ ns) the magnitude of A_d essentially follows the exponential decrease in the number of magnons, but deviates significantly from this law because of the dephasing for $t < 300$ ns.

Both echo-like behavior of the signal group and dephasing in the dominant group contribute to the non-monotonic behavior of the peak amplitude of the restored signal. From Fig. 4 one clearly sees that for $\tau_{\text{delay}} = 300$ ns (Fig. 4b) the amplitude of the signal at the end of the pause ($t = 0$ in this graph) is quite close to the amplitude of this group at $t = 0$ for the uninterrupted pump. However,

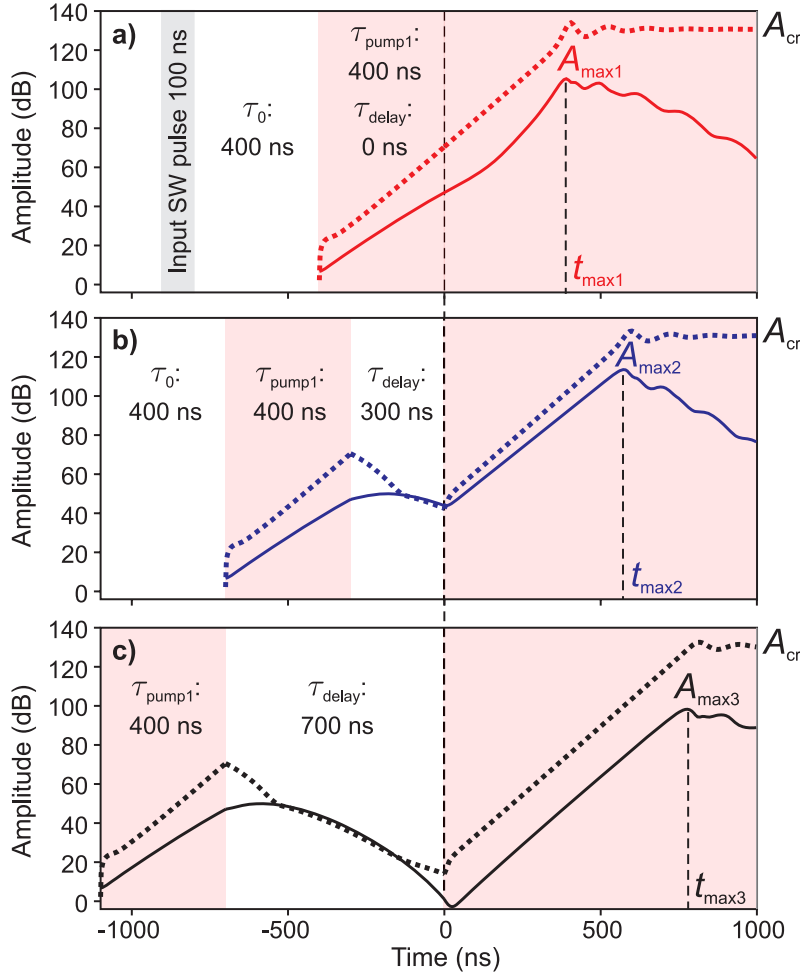


Fig. 4: Simulated time profiles of the signal (thin solid lines) and of the internal pumping (bold dashed lines). The shaded areas indicate the time intervals when the pump is on. a) Uninterrupted pumping ($\tau_{\text{delay}} = 0$). b) $\tau_{\text{delay}} = 300$ ns. c) $\tau_{\text{delay}} = 700$ ns. $t = 0$ corresponds to switching on the second pump. Duration of the first pump pulse $\tau_{\text{pump1}} = 400$ ns.

the internal pump by the dominant group at $t = 0$ for $\tau_{\text{delay}} = 300$ ns is smaller than for $\tau_{\text{delay}} = 0$ by 25 dB. This allows the recovered signal to develop a larger peak amplitude for $\tau_{\text{delay}} = 300$ ns than for $\tau_{\text{delay}} = 0$. Obviously, a larger τ_{delay} requires a larger time for the restored signal to peak, which results in a linear dependence of t_{max} on τ_{delay} in Fig. 3.

In addition we checked if nonlinear damping in the form of four-magnon scattering processes involving all spin waves existing at the half-pump frequency can contribute to the non-monotonic response. Our calculations for $\tau_{\text{pump1}} = 400$ ns have shown that the nonlinear damping is negligible during the pump pause for reasonable values of the nonlinear damping coefficient [16]. The amplitudes of both signal and dominant groups are just too small during the pause to develop the nonlinear damping. Accounting for the nonlinear damping during the second pump pulse does not lead to qualitative changes in the behavior either, unless one assumes that the coefficient of nonlinear damping is larger than T by several orders of magnitude, which is unreasonable.

In this work we have investigated the relaxation of a free evolving gas of previously parametrically pumped magnons. The experimental results show a clear deviation from the standard exponential spin-wave decay model. In particular, the inherent magnon damping is found to depend upon the presence of the parametric pumping field. The results are in agreement with the model which accounts for variation of phase coherence for parametrically injected magnon groups during the pump-free pause.

This work was recently published in Phys. Rev. B [17].

Financial support by the DFG within the *SFB/TRR49* and by the Australian Research Council is gratefully acknowledged.

References

- [1] H. Suhl, *Theory of the magnetic damping constant*, IEEE Trans. Mag. **34**, 1834 (1998).
- [2] T. Gilbert, *A phenomenological theory of damping in ferromagnetic materials*, IEEE Trans. Mag. **40**, 3443 (2004).
- [3] S. Rezende, A. Azevedo, M. Lucena, F. de Aguiar, *Anomalous spin-wave damping in exchange-biased films*, Phys. Rev. B **63**, 214418 (2001).
- [4] A.Y. Dobin and R. Victora, *Intrinsic nonlinear ferromagnetic relaxation in thin metallic films*, Phys. Rev. Lett. **90**, 167203 (2003).
- [5] K. Gilmore and M. D. Stiles, *Anisotropic damping of the magnetization dynamics in Ni, Co, and Fe*, Phys. Rev. B **81**, 174414 (2010).
- [6] S.O. Demokritov, V.E. Demidov, O. Dzyapko, G.A. Melkov, A.A. Serga, B. Hillebrands, A.N. Slavin, *Bose-Einstein condensation of quasi-equilibrium magnons at room temperature under pumping*, Nature **443**, 430 (2006).
- [7] R.W. Damon and J.R. Eshbach, *Magnetostatic modes of a ferromagnetic slab*, J. Appl. Phys. **31**, 104 (1960).
- [8] B.A. Kalinikos and M. P. Kostylev, *Parametric amplification of spin wave envelope solitons in ferromagnetic films by parallel pumping*, IEEE Trans. Mag. **33**, 3445 (1997).
- [9] A.A. Serga, A.V. Chumak, A. André, G.A. Melkov, A.N. Slavin, S.O. Demokritov, B. Hillebrands, *Parametrically stimulated recovery of a microwave signal stored in standing spin-wave modes of a magnetic film*, Phys. Rev. Lett. **99**, 227202 (2007).
- [10] S. Schäfer, A.V. Chumak, A.A. Serga, G.A. Melkov, B. Hillebrands, *Microwave spectral analysis by means of nonresonant parametric recovery of spin-wave signals in a thin magnetic film*, Appl. Phys. Lett. **92**, 162514 (2008).
- [11] A.V. Chumak, A.A. Serga, B. Hillebrands, G.A. Melkov, V. Tiberkevich, A.N. Slavin, *Parametrically stimulated recovery of a microwave signal using standing spin-wave modes of a magnetic film*, Phys. Rev. B **79**, 014405 (2009).
- [12] V.S. L'vov, *Wave Turbulence Under Parametric Excitation* (Springer, Berlin, 1994).
- [13] V.E. Zakharov, V.S. L'vov, S.S. Starobinets, *Spin-wave turbulence beyond the parametric excitation threshold*, Sov. Phys. Uspekhi **17**, 896 (1975).
- [14] G.A. Melkov, Y.V. Kobljanskyj, A.A. Serga, V.S. Tiberkevich, A.N. Slavin, *Reversal of momentum relaxation*, Phys. Rev. Lett. **86**, 4918 (2001).
- [15] G.F. Herrmann, R.M. Hill, D.E. Kaplan, *Instability and echo-pulse amplification in a ferrimagnetic spin system in an inhomogeneous field*, Phys. Rev. B **2**, 2587 (1970).
- [16] M.M. Scott, C.E. Patton, M.P. Kostylev, B.A. Kalinikos, *Nonlinear damping of high-power magnetostatic waves in yttrium-iron-garnet films*, J. Appl. Phys. **95**, 6294 (2004).
- [17] S. Schäfer, V. Kegel, A.A. Serga, B. Hillebrands, M.P. Kostylev, *Variable damping and coherence in a high-density magnon gas*, Phys. Rev. B **83**, 184407 (2011).

4.2 Mode structure of parametrically excited magnons in a magnetic film

V.I. Vasyuchka, A.A. Serga, M.B. Jungfleisch, C.W. Sandweg, and B. Hillebrands¹

The parametric excitation mechanism is well known as an effective method to inject magnons into a magnetic medium. This technique plays an important role in experiments on fundamental properties of magnetic excitations as well as in applications since it allows the amplification, shaping, and processing of microwave signals in different magnetic materials (see for example Review [1] and Ref. [2]). One of the most exciting applications of this technique was the observation of Bose-Einstein condensation of magnons at room temperature [3]. Currently much interest is attracted to experiments on spin pumping by parametrically excited magnons in ferrite-platinum bilayer structures [4–7].

Parametric excitation can be realized in different ways [8] and with various efficiencies for different magnon groups [9]. The first-order parametric process when one microwave photon of a pump electromagnetic field splits into two magnons at half of the pumping frequency is the simplest and in some cases [9] the most efficient excitation mechanism. In practice the first-order parametric process is realized in parallel pumping geometry when a pumping microwave magnetic field is arranged parallel to the bias magnetic field and interacts thus with an oscillating longitudinal magnetization. This oscillation occurs as a result of elliptical precession of a magnetization vector. Thus, the strongest coupling between the pump field and a spin-wave system appears in situations when the precession trajectory is heavily distorted due to a shape magnetic anisotropy or because of spin-wave propagation across to the magnetization direction. In particular, parallel pumping has the smallest threshold and, consequently, the highest efficiency if the short-wavelength magnons are injected in the exchange part of the magnon spectrum and propagate perpendicularly to the magnetization direction [8].

Considering the momentum conservation law and the fact that the photon wavenumber is negligibly small in comparison with the magnon wavenumbers, the parallel pumping process creates pairs of magnons with opposite wavevectors. In general, such pairs populate *all* spin-wave modes at half of the pumping frequency. However, if one increases the total density of the parametrically injected phase correlated magnons, which compete for the pump energy, a spectrally localized condensate of photon-coupled magnon pairs is formed [10]. The knowledge about the spectral position and mode structure of this condensate is of paramount importance for the interpretation of the experimental results on spin Hall and spin pumping effects caused by parametrically excited magnons [5–7]. Furthermore, this information is crucial for understanding the thermalization processes in magnon gases and the behavior of Bose-Einstein condensates of magnons.

Conventional microwave techniques give us no ability to directly determine the spectral positions of magnon groups involved in the parametric process. Fortunately, wavevector resolved Brillouin light scattering (BLS) spectroscopy is a powerful instrument for such studies. That is why a few attempts have been already made in order to characterize the wavevector distribution of parametric magnons in ferrite films of yttrium iron garnet (YIG) [11–15]. In works [11–14] the wavevector selectivity was realized using a movable diaphragm. However, this approach has low sensitivity and allows only to measure magnon wavevectors up to $k = 4.2 \text{ rad}/\mu\text{m}$. As a result it is not applicable for investigations of the most effectively excited exchange magnon branch with wavenumbers

¹In collaboration with A. Kreisel and P. Kopietz, Institut für Theoretische Physik, Universität Frankfurt, Germany.

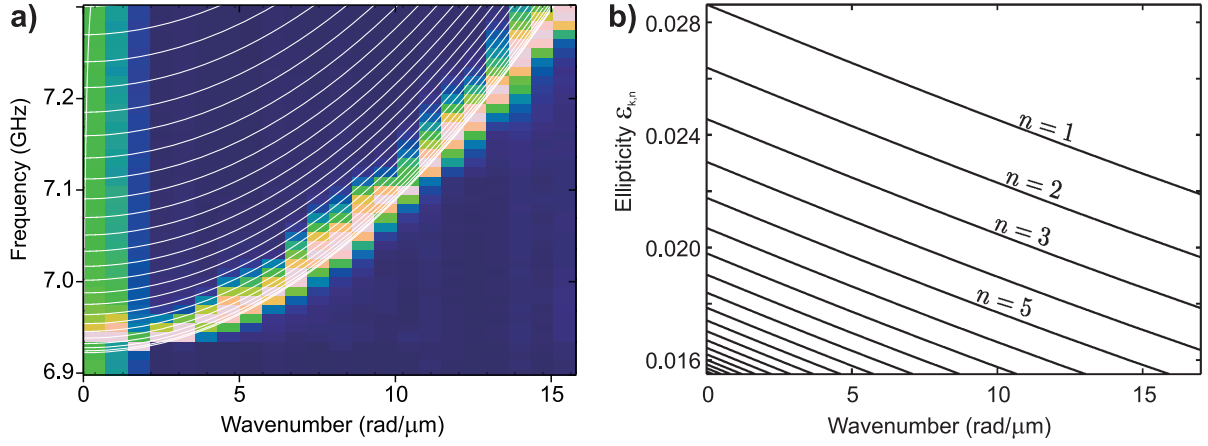


Fig. 1: a) Intensity map of the experimentally measured spectral position of parametrically excited magnons and the calculated spectrum of magnon modes propagating in YIG film plane under the angle $\vartheta_{\mathbf{k}} = \pi/2$ to the bias magnetic field H_0 . The broadening of the experimental curve results from four-magnon and two-magnon scattering processes to the adjacent spin-wave modes. b) Ellipticity of the corresponding magnon modes as a function of the wavenumber. YIG film thickness $d = 5\mu\text{m}$. $\mu_0 H_0 = 175\text{mT}$. Saturation magnetization $M_S = 138.6\text{kA/m}$.

$k \geq 5\text{rad}/\mu\text{m}$. The problem of bandwidth was overcome in our group through the development of a new k -resolved BLS sample stage in which spin-wave wavevectors oriented perpendicularly to the bias magnetic field are investigated by tilting the sample within the magnet gap. Wavevectors which are oriented parallel to the applied magnetic field are analyzed by turning the entire setup, including the magnet system, about the vertical axis. We have demonstrated the ability to select wavevectors up to $20.4\text{rad}/\mu\text{m}$ for both orientations [15].

In this Report we present the experimental data and theoretical analysis of the spectral distribution of parametrically injected exchange magnons in a tangentially magnetized YIG film. Our results give the first direct evidence that only one magnon group is excited by the parallel parametric pumping just above the threshold of parametric generation. Above the frequency of ferromagnetic resonance this group corresponds to the lowest volume spin-wave mode which propagates in a film plane perpendicularly to the bias magnetic field.

Experiments were performed using a $5\mu\text{m}$ thick tangentially magnetized YIG film placed on top of a non-resonant short-circuited microstrip antenna. A pumping pulse of $2\mu\text{s}$ duration and 100mW power was applied to the antenna. The pulse repetition time of $20\mu\text{s}$ was sufficiently long to avoid sample heating effects. The pumping power was chosen to be only 1dB over the threshold of spin-wave parametric generation. At this power level the magnon system was stably excited without developing of higher order nonlinear instabilities. In contrast with the conventional approach when a pumping frequency is fixed and the magnetic field is varied the external bias magnetic field $\mu_0 H_0 = 175\text{mT}$ was chosen to be constant in our experiment. The pumping frequency was varied from 13.6GHz up to 14.6GHz in steps of 20MHz and the scattered BLS signal from the YIG film was detected (see Fig. 1a). This scheme allows us to avoid the frequency shift of the magnon spectrum.

The measured dependence of the BLS signal on the wavenumber and on half of the pumping frequency is shown as an intensity map in Fig. 1a. The quadratic dependence of the frequency of the excited magnons on their wavenumber, which is typical for exchange magnons, is obvious. The calculated spectrum of magnon modes propagating perpendicularly to the bias field H_0 in the YIG film plane is shown over the experimental data. The used theoretical approach [16] takes

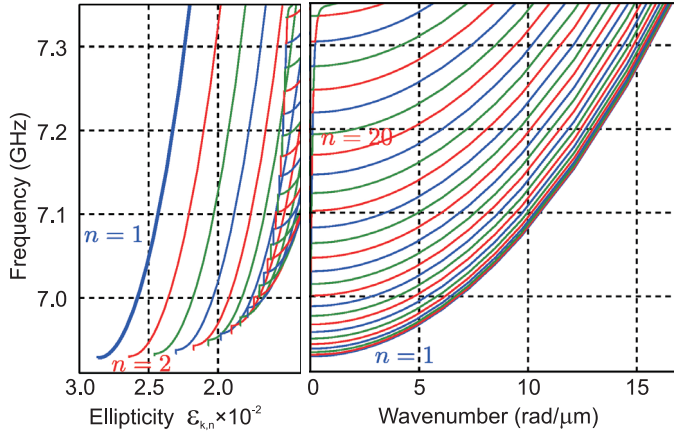


Fig. 2: The spin-wave spectrum (right) in comparison with the ellipticity of the corresponding magnon modes calculated as a function of the external pumping frequency (left). Since the ellipticity $\varepsilon_{k,n}$ is largest for the lowest magnon mode $n = 1$, pumping to this mode is expected to be dominant.

into account both dipole-dipole and exchange interactions and delivers the spectral positions of all volume magnon modes as well as a surface mode. The YIG film saturation magnetization M_S is assumed to be 138.6 kA/m. The 0.64 kA/m difference between this fitting value and the conventional YIG magnetization of 139.3 kA/m is caused by $\simeq 5$ degree tilting of the precessing magnetization vector. This angle perfectly corresponds with the equilibrium precession angle obtained from our previous measurements of temporally amplified spin-wave packets [17]. Furthermore, one can see a good agreement between the experimentally determined spectral positions of parametrically excited spin waves and the lowest volume mode in the calculated spectrum.

In order to understand this correspondence one should consider the connection between the precession ellipticity and the efficiency of parametric excitation.

The minimal threshold for the parallel pumping is [8]:

$$h_{\text{crit}} = \min \left\{ \frac{\omega_{rk}}{V_{k,n}} \right\} = \min \left\{ \frac{\omega_p \Delta H_k}{\omega_M \sin^2 \vartheta_k} \right\},$$

where $\omega_{rk} = \gamma \mu_0 \Delta H_k / 2$ and ΔH_k are dissipation parameters, $V_{k,n}$ is the coupling coefficient between the pumping microwave field and a magnon mode of number n and wavenumber k , $\omega_M = \gamma \mu_0 M_S$, gyromagnetic ratio $\gamma = 1.76 \cdot 10^{11} \text{ s}^{-1} \text{ T}^{-1}$, ϑ_k is the angle between the propagation direction of magnons and the bias field. Note that h_{crit} reaches the smallest possible value for $\vartheta_k = \pi/2$. Since the coupling coefficient $V_{k,n}$ is directly proportional to the ellipticity $\varepsilon_{k,n}$ of the corresponding mode, $V_{k,n} \propto \varepsilon_{k,n}$, we can identify the magnon mode that is dominantly populated by the pumping as a mode which possesses the highest precessional ellipticity under otherwise same conditions. The ellipticity can be defined as

$$\varepsilon_{k,n} = 1 - \frac{|m_{\min k,n}|^2}{|m_{\max k,n}|^2},$$

where $|m_{\min k,n}|$ and $|m_{\max k,n}|$ denote the large and the small axes of a precession ellipse. The calculated ellipticity $\varepsilon_{k,n}$ as a function of the wavenumber for the first twenty modes is shown in Fig. 1b. It decreases with increase of the wavenumber k and mode number n .

In our experiment the frequency of the pumped magnons crosses over many modes with different wavenumbers. In order to understand which mode is excited for the given pumping frequency, the dependence of the ellipticity of spin-wave modes on the frequency was calculated (left panel in

Fig. 2). This dependence is shown together with the spin-wave spectrum of the YIG film (right panel in Fig. 2). It is clearly seen that the maximal ellipticity, and accordingly the minimal parametric threshold, corresponds to the first ($n = 1$) spin-wave mode in the available range of magnon k -numbers. This result is in a good agreement with experimental data (Fig. 1a).

In addition, one can note the multiple intersections between ellipticity curves calculated for higher volume modes of the YIG film. Our calculations show the same behavior for all modes of a thin ($< 1 \mu\text{m}$) film. In this case an alternating parametric excitation of different modes is expected when the pumping frequency is changed [18].

In summary, we have observed the generation of parametric magnons under parallel pumping using the wavevector resolved BLS technique. A good agreement between the experimentally determined spectral position of photon-coupled magnon pairs in a tangentially magnetized YIG film and the lowest spin-wave mode in the YIG film spectrum was obtained. The dominant parametric excitation of this mode is understood as a result of its highest ellipticity in the range of accessible wavenumbers.

Support by the Deutsche Forschungsgemeinschaft within the *SFB/TR 49* is acknowledged.

References

- [1] A.A. Serga, A.V. Chumak, B. Hillebrands, *YIG magnonics*, J.Phys. D: Appl. Phys. **43**, 264002 (2010).
- [2] T. Brächer, P. Pirro, B. Obry, B. Leven, A.A. Serga, B. Hillebrands, *Mode selective parametric excitation of spin waves in a $\text{Ni}_{81}\text{Fe}_{19}$ microstripe*, Appl. Phys. Lett. **99**, 162501 (2011).
- [3] S.O. Demokritov, V.E. Demidov, G.A. Melkov, A.A. Serga, B. Hillebrands, A.N. Slavin, *Bose-Einstein condensation of quasi-equilibrium magnons at room temperature under pumping*, Nature **443**, 430 (2006).
- [4] G.E. Bauer, Y. Tserkovnyak, *Viewpoint: Spin-magnon transmutation*, Physics **4**, 40 (2011).
- [5] C.W. Sandweg, Y. Kajiwara, A.V. Chumak, A.A. Serga, V.I. Vasyuchka, M.B. Jungfleisch, E. Saitoh, B. Hillebrands, *Spin pumping by parametrically excited exchange magnons*, Phys. Rev. Lett. **106**, 216601 (2011).
- [6] H. Kurebayashi, O. Dzyapko, V.E. Demidov, D. Fang, A.J. Ferguson, S.O. Demokritov, *Controlled enhancement of spin-current emission by three-magnon splitting*, Nature Materials **10**, 660 (2011).
- [7] K. Ando, T. An, E. Saitoh, *Nonlinear spin pumping induced by parametric excitation*, Appl. Phys. Lett. **99**, 092510 (2011).
- [8] A.G. Gurevich, G.A. Melkov, *Magnetization oscillations and waves*, CRC Press, New York (1996).
- [9] T. Neumann, A.A. Serga, V.I. Vasyuchka, B. Hillebrands, *Field-induced transition from parallel to perpendicular parametric pumping for a microstrip transducer*, Appl. Phys. Lett. **94**, 192502 (2009).
- [10] V.S. L'vov, *Wave Turbulence under Parametric Excitations: Applications to Magnetism*, Springer, Berlin (1994).
- [11] V.E. Demidov, O. Dzyapko, M. Buchmeier, T. Stockhoff, G. Schmitz, G.A. Melkov, S.O. Demokritov, *Magnon kinetics and Bose-Einstein condensation studied in phase space*, Phys. Rev. Lett. **101**, 257201 (2008).
- [12] W.D. Wilber, W. Wuttling, P. Kabos, C.E. Patton, W. Jantza, *Light scattering from parallel-pump instabilities in yttrium iron garnet*, Phys. Rev. Lett. **51**, 1680 (1983).
- [13] P. Kabos, G. Wiese, C.E. Patton, *Measurement of spin wave instability magnon distributions for subsidiary absorption in yttrium iron garnet films by Brillouin light scattering*, Phys. Rev. Lett. **72**, 2093 (1994).
- [14] P. Kabos, M. Mendik, G. Wiese, C.E. Patton, *Spin-wave instability magnon distribution for parallel pumping in yttrium iron garnet films at 9.5 GHz*, Phys. Rev. B **55**, 11457 (1997).
- [15] C.W. Sandweg, M.B. Jungfleisch, V.I. Vasyucka, A.A. Serga, P. Clausen, H. Schultheiss, B. Hillebrands, A. Kreisel, P. Kopietz, *Wide-range wavevector selectivity of magnon gases in Brillouin light scattering spectroscopy*, Rev. Sci. Instrum. **81** 073902 (2010).
- [16] A. Kreisel, F. Sauli, L. Bartosch, P. Kopietz, *Microscopic spin-wave theory for yttrium-iron garnet film*, Eur. Phys. J. B **71**, 59 (2009).
- [17] A.A. Serga, T. Schneider, B. Hillebrands, M.P. Kostylev, A.N. Slavin, *Shaping of microwave pulses using phase-sensitive spin-wave amplifier*, Appl. Phys. Lett. **90**, 022502 (2007).
- [18] B.A. Kalinikos, N.G. Kovshikov, N.V. Kozhus, *Parametric excitation of a series of quasi - surface spin waves in thin ferromagnetic films*, Sov. Phys. Solid State **27**, 1681 (1986).

4.3 Transition processes in a highly excited multi-mode autonomous magnon system

V.I. Vasyuchka, A.A. Serga, C.W. Sandweg, and B. Hillebrands¹

A parametric process in a magnetic medium can be described using the corpuscular picture as a transformation of N quasi-particles of an electromagnetic pumping field into two coupled magnons (quanta of eigen spin-wave excitations), where N is the order of this process. It is the simplest method to excite magnons in a wide range of wavevectors, which are not accessible for the standard microstrip technique. The parametric pumping was widely used in many recent investigations such as spin pumping by parametrically excited magnons [1–3], Bose-Einstein condensation of magnons at room temperature [4,5], and excitation of exchange magnons in thin metallic structures [6, 7]. Usually experiments with parametric pumping are performed in a pulse regime and it is important to take into account possible transition processes.

Here we report on the experimental observation and theoretical description of transition processes in a magnon system after the pumping is switched off. First-order parallel parametric pumping was used to create a highly excited multi-mode magnon system with occupation numbers in a narrow spectral range exceeding the thermal level by many orders of magnitude [8]. The flow of external energy into the magnon system is stopped after the pumping is switched off, and an exponential decrease of the magnon density with characteristic decay time determined by the relaxation frequency is expected. In our experiments the energy transfer from parametrically excited magnons to the dipolar magnon group was observed. The amplitude of this group in the time period immediately after the pumping was switched off does not decrease but, instead, exceeds many times its initial level. The main condition to observe this effect is the existence of a highly excited parametrical magnon group which acts as an internal pumping source via four-magnon interactions after the external pump is switched off. Additionally, two-magnon scattering is necessary for the observed effect.

Experiments were carried out using an yttrium iron garnet (YIG) film of $5\mu\text{m}$ thickness placed on top of a microstrip antenna. The antenna of $50\mu\text{m}$ width, deposited on an aluminum nitride substrate, was used as a pumping exciter and, simultaneously, receiver of the microwaves emitted from the sample. The material for the substrate was chosen because of its good thermal conductivity (about $180\text{ W/m}\cdot\text{K}$). Therefore, any parasitic heat is effectively removed from the pumping region. A bias magnetic field was applied in the plane of the YIG waveguide and perpendicular to the antenna.

The input rectangular electromagnetic pumping pulse with carrying frequency of $\omega_p/2\pi = 14\text{ GHz}$ and duration of $\tau_p = 20\mu\text{s}$ was generated every $t_{\text{rep}} = 1.73\text{ ms}$ and applied to the microstrip transducer. Its power was controlled by an amplifier and attenuator up to the maximal value $P_p = 25\text{ W}$. A microwave stub tuner was used to adjust a minimum in the reflected pumping power from the antenna.

The parametric process exists only for pumping powers larger then a threshold value. The dependence of the threshold power on the bias magnetic field for $\tau_p = 20\mu\text{s}$ was measured using a kink at

¹In collaboration with Prof. G.A. Melkov and D.V. Slobodianiuk, Department of Radiophysics, National Taras Shevchenko University of Kiev, Ukraine.

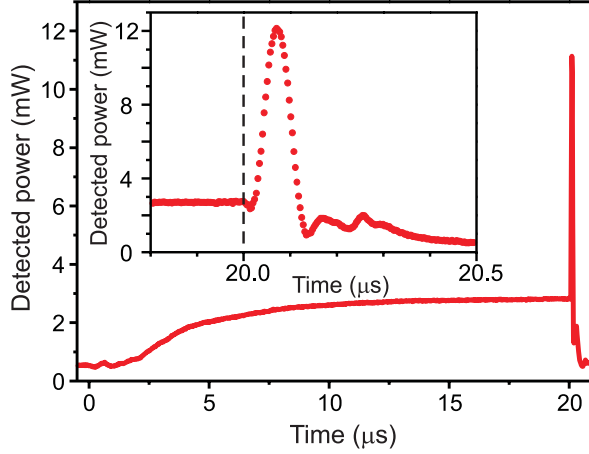


Fig. 1: Temporal evolution of the signal irradiated from the YIG film at half of the pumping frequency $\omega_p/4\pi = 7$ GHz for the bias magnetic field $\mu_0 H_0 = 173.86$ mT. Applied pumping power $P_p = 240$ mW and pumping pulse duration $\tau_p = 20$ μ s. Inset: Detailed time profile of the tail of the irradiated signal. The vertical dashed line indicates the moment when pumping is switched off.

the end of the reflected signal (see [9]). A critical field $\mu_0 H_C = 173$ mT corresponding to the minimal threshold, when a uniform resonance mode is excited, was found. We use the critical field below in order to find the position of half of the pumping frequency in the spin-wave spectrum.

Using the same antenna a signal irradiated from the YIG film at half of the pumping frequency was detected (see Fig. 1). A frequency splitter allows us to separate the reflected pumping signal at the pumping frequency from the one at half of the pumping frequency, irradiated by the excited magnon system. The peak at half of the pumping frequency was observed for a bias magnetic field $\mu_0 H_0 = 173.86$ mT, when the pumping power threshold was exceeded by 9.3 dB. Note, that the peak formation was found only in a narrow range of the bias fields (about 0.25 mT).

In order to understand the peak formation we have to consider the multi-mode spin-wave spectrum of a tangentially magnetized YIG film. It consists of discrete dispersion curves representing thickness modes of the film (see Fig. 2a). Since the applied bias field was larger than the critical one ($H_0 > H_C$), parametric excitation of dipole-exchange magnons with wavenumbers $k \sim 10$ rad/ μ m takes place [8]. The density of parametric magnons is at maximum near the dispersion minima due to the lowest relaxation parameter and zero group velocity, which prevents the magnon from flowing out of the pumping region. This explains the narrow bias range of the peak formation. Changing the bias magnetic field shifts the minimum frequencies and their intersections with half of the pumping frequency. This determines the magnetic field dependence of the observed effect (Fig. 2b). A good correspondence between the experimental field $\mu_0 H_0 = 173.86$ mT and the calculated value (the intersection between the mode minimum $m = 27$ and half of the pumping frequency in Fig. 2b) is clearly seen. Moreover, a similar peak was observed for the larger bias magnetic field which corresponds to the next intersection of the minimum frequency curves ($m = 26$) with half of the pumping frequency in Fig. 2b.

A theoretical description of the dynamics can be made in terms of the S-theory, developed in Ref. [10]. According to this theory, a magnon system can be described by the following equations:

$$\begin{aligned} \frac{dn_k}{dt} &= 2n_k \left[-\Gamma_k + \text{Im}(P_k^* e^{-i\psi_k}) \right] \\ \frac{d\psi_k}{dt} &= 2\tilde{\omega}_k - \omega_p + 2\text{Re}(P_k^* e^{-i\psi_k}) \end{aligned} \quad (1)$$

where n_k and ψ_k correspond to the density and phase of the magnon group of frequency ω_k with the wavenumber k , Γ_k is the magnon relaxation parameter. $P_k = \mu_0 h_z V_k + \sum_{k'} S_{kk'} n_{k'} e^{-i\psi_{k'}}$, $\tilde{\omega}_k =$

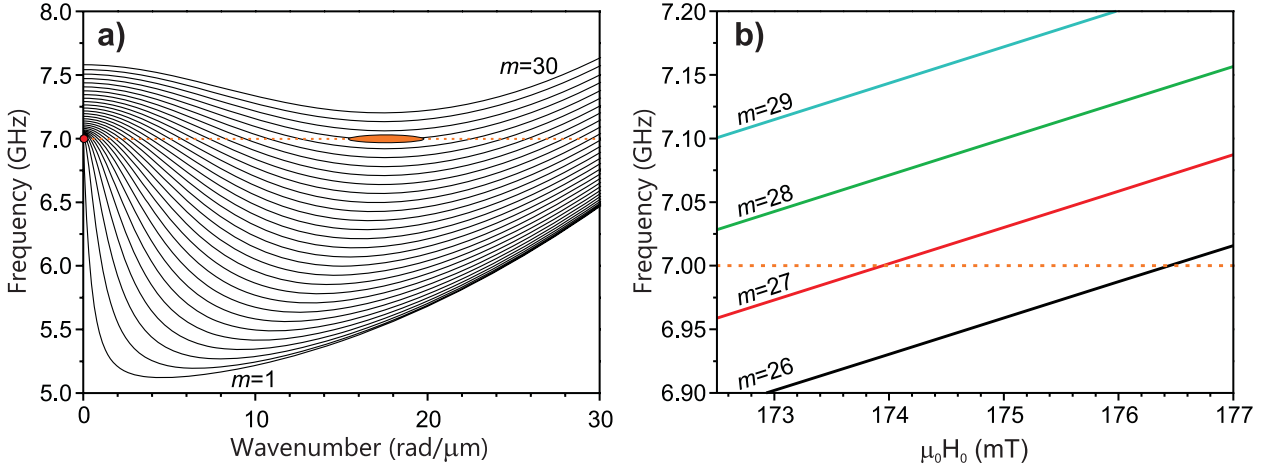


Fig. 2: a) Spin-wave spectrum of the tangentially magnetized 5 μm thick YIG film when spin waves propagate along the bias field. Dispersion curves of the first thirty modes calculated for $\mu_0 H_0 = 173.86 \text{ mT}$. An uniaxial anisotropy field $\mu_0 H_u = -6.67 \text{ mT}$ was used to fit the ferromagnetic resonance frequency equal to half of the pumping frequency for the experimental critical field $\mu_0 H_C = 173 \text{ mT}$. The spectral position of the parametrically excited dipole-exchange magnon group (ellipse) and dipolar magnons detected by the antenna (circle) are shown. b) Dependence of mode minimum frequencies on the magnetic field. Their intersections with half of the pumping frequency 7 GHz determines the magnetic field of the observed effect.

$\omega_k + 2 \sum_{k'} T_{kk'} n_{k'}$ describe the total pumping and renormalized frequency of the magnon group, respectively, where $\mu_0 h_z$ is an alternating pumping field, V_k is a coupling coefficient between the pumping and magnons, $S_{kk'}$ is the nonlinear coefficient describing a four-magnon interaction, and $T_{kk'}$ is the nonlinear frequency shift parameter. The first term in the total pumping corresponds to the external pumping, and the second one is the internal pumping which arises from magnon-magnon scattering processes in the magnetic system.

The set of equations (1) forms an infinite system describing the dynamics of all magnon spectra. However, in the most practical case the amplitudes of majority of spin waves are at thermal level n_0 and can be neglected. In this case one can take into consideration only waves with amplitudes much larger than n_0 . There are two magnon groups which satisfy this condition in our case. The first one is the parametric group which has the lowest threshold and is amplified by parallel pumping. When pumping is turned off ($t = 0$) it has the largest amplitude $n_1 = n_{\text{sat}} = \sqrt{(\mu_0 h_z V_k)^2 - \Gamma_1^2} / S$ [10]. This group has the lowest relaxation parameter Γ_1 . Another group of dipolar waves arises from two-magnon scattering processes in the system and its density is larger than the thermal level during the amplification process of the parametrical group. The amplitude of the dipolar group can be estimated to be about $n_2 = 10^{-2} n_{\text{sat}}$ and its relaxation parameter is larger than the one of the parametrical group $\Gamma_2 > \Gamma_1$.

It is important to stress here that, according to the S-theory in the stationary regime, only one magnon group with the lowest threshold can exist [10]. However, we remove this restriction taking into account two-magnon scattering processes, which also allows the energy transfer between groups before the pumping is turned off. Both groups are in a stationary non-equilibrium state while the external pumping is applied. However, when the external pumping is switched off only the internal pumping term remains. This leads to energy transfer between the two magnon groups which manifests in a formation of a sharp peak shown in Fig. 1.

Accordingly, the set of equations (1) can be written in a form:

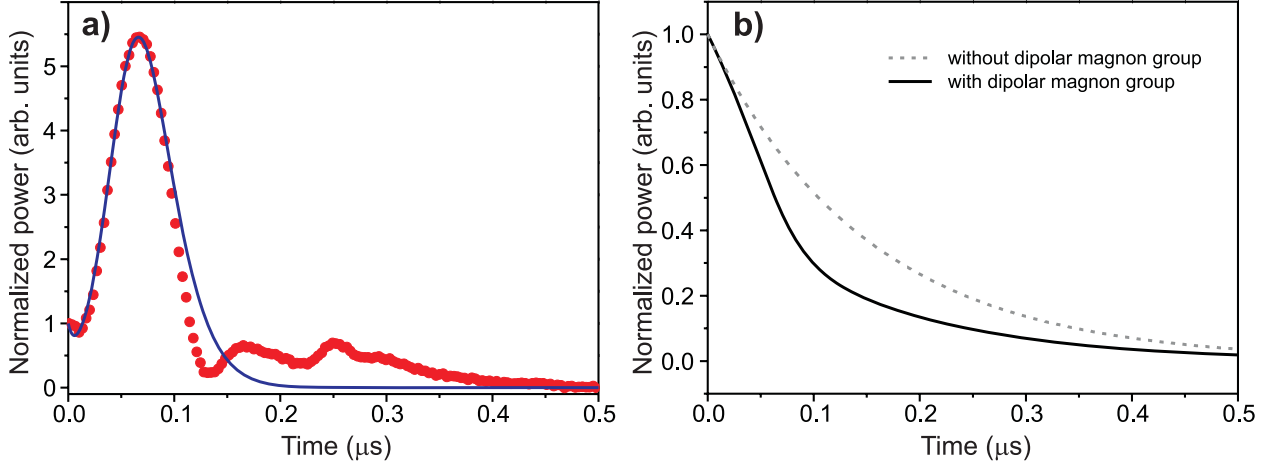


Fig. 3: Evolution of different magnon groups after the pumping is switched off. a) Dipolar magnon group evolution: points - experiment, solid line - theory. b) Parametrical magnon group evolution in the presence of dipolar magnons pumped by internal pumping (solid line) and without (dashed line).

$$\begin{aligned}
 \frac{dn_1}{dt} &= 2n_1[-\Gamma_1 + S_2 n_2 \sin(\psi_1 - \psi_2)] \\
 \frac{d\psi_1}{dt} &= 2S_1 n_1 + 2S_2 n_2 \cos(\psi_1 - \psi_2) \\
 \frac{dn_2}{dt} &= 2n_2[-\Gamma_2 + S_2 n_1 \sin(\psi_2 - \psi_1)] \\
 \frac{d\psi_2}{dt} &= 2S_1 n_2 + 2S_2 n_1 \cos(\psi_2 - \psi_1).
 \end{aligned} \tag{2}$$

Note that in the expression for the total pumping P_k only the second term is left after the external pumping field is switched off ($h_z = 0$). Also it is assumed that $\tilde{\omega}_1 = \tilde{\omega}_2 = \omega_p/2$ means that only resonant waves are taken into account. We choose the time scale such that the point $t = 0$ corresponds to the termination of the pumping. System (2) was solved numerically with the following initial conditions: $n_1(0) = n_{\text{sat}}$, $n_2(0) = 10^{-2}n_{\text{sat}}$, $\psi_1(0) = 2\pi$. The starting phase of the second group was chosen to best fit the experimental data.

Results of the modeling are shown in Fig. 3a. Good agreement with the experiment is obtained. The oscillations seen in the experimental curve at $t > 0.13 \mu\text{s}$ can be explained taking into account the fact that in the general case the internal pumping created by the parametrical magnon group can transfer its energy to numerous magnon groups with close wavevectors leading to an auto-oscillation regime [10].

To investigate the influence of the internal pumping on the parametrical group we have calculated the dynamics of this group in the presence and absence of the dipolar group. Figure 3b shows the results of this calculation. It is clearly seen that the dissipation rate of the parametric magnon group increases because it acts as the internal pumping source for other magnons. This is clear from Eq. (2): the term $2S_2 n_2 \sin(\psi_1 - \psi_2)$ can be regarded as an additional dissipation for the parametrical group. Also it is visible from Fig. 3b that on the late states of evolution the parametric group relaxation rate returns to normal values due to an amplitude decrease of the two-magnon group.

In conclusion, we have experimentally observed and numerically simulated the transfer of energy from the parametrically excited magnon group to dipolar magnons. During this process the ampli-

tude of the dipolar group detected by the antenna exceeds more than five times its initial level. The developed theoretical model provides a good qualitative description of the observed effect.

Support by the Deutsche Forschungsgemeinschaft within the *SFB/TR 49* is gratefully acknowledged.

References

- [1] C.W. Sandweg, Y. Kajiwara, A.V. Chumak, A.A. Serga, V.I. Vasyuchka, M.B. Jungfleisch, E. Saitoh, B. Hillebrands, *Spin pumping by parametrically excited exchange magnons*, Phys. Rev. Lett. **106**, 216601 (2011).
- [2] H. Kurebayashi, O. Dzyapko, V.E. Demidov, D. Fang, A.J. Ferguson, S.O. Demokritov, *Spin pumping by parametrically excited short-wavelength spin waves*, Appl. Phys. Lett. **99**, 162502 (2011).
- [3] K. Ando, T. An, E. Saitoh, *Nonlinear spin pumping induced by parametric excitation*, Appl. Phys. Lett. **99**, 092510 (2011).
- [4] S.O. Demokritov, V.E. Demidov, O. Dzyapko, G.A. Melkov, A.A. Serga, B. Hillebrands, A.N. Slavin, *Bose-Einstein condensation of quasi-equilibrium magnons at room temperature under pumping*, Nature **443**, 430 (2006).
- [5] A.V. Chumak, G.A. Melkov, V.E. Demidov, O. Dzyapko, V.L. Safonov, S.O. Demokritov, *Bose-Einstein condensation of magnons under incoherent pumping*, Phys. Rev. Lett. **102**, 187205 (2009).
- [6] T. Brächer, P. Pirro, B. Obry, B. Leven, A.A. Serga, B. Hillebrands, *Mode selective parametric excitation of spin waves in a $Ni_{81}Fe_{19}$ microstripe*, Appl. Phys. Lett. **99**, 162501 (2011).
- [7] H. Ulrichs, V.E. Demidov, S.O. Demokritov, S. Urazhdin, *Parametric excitation of eigenmodes in microscopic magnetic dots*, Phys. Rev. B **84**, 094401 (2011).
- [8] A.G. Gurevich, G.A. Melkov, *Magnetization oscillations and waves*, CRC Press, New York (1996).
- [9] T. Neumann, A.A. Serga, V.I. Vasyuchka, B. Hillebrands, *Field-induced transition from parallel to perpendicular parametric pumping for a microstrip transducer*, Appl. Phys. Lett. **94**, 192502 (2009).
- [10] V.S. L'vov, *Wave Turbulence under Parametric Excitations. Applications to Magnetism*, Springer-Verlag, (1994).

B. Magnon Spintronics

Spintronics is the field of spin-based data storage and processing. In conventional spintronics the electron is used as a carrier of spin. In particular, the manipulation of spin currents in nanostructures has potential applications in computing devices and magnetic memory. For the successful utilization of spin information, difficulties like the short distance over which an electron retains memory of its spin direction, the so-called spin diffusion length, have to be overcome. Here, a promising approach is the combination of standard spintronics with spin-wave dynamics resulting in “magnon spintronics”. A magnon, i.e. the quantum of a spin wave, carries an angular momentum or spin as well and can be used for storage, processing and transport of spin information, building on its outstanding properties such as long lifetime and potential for dissipationless transport. The field of “magnon spintronics” is currently emerging. Some building blocks such as magnon generators (spin wave emitters) and detectors have been realized, others are in development. The phase-resolved Brillouin light scattering (BLS) microscopy technique, which was developed in our group, opens new possibilities for the research on linear and nonlinear spin-wave dynamics in nanostructures. The BLS investigations of spin dynamics in nanostructures is supported by micromagnetic simulations. In Report 4.4 the mode conversion of propagating spin waves in $\text{Ni}_{81}\text{Fe}_{19}$ microstrips with specialized geometry is presented. In Report 4.5 the parallel parametric amplification of spin waves in a $\text{Ni}_{81}\text{Fe}_{19}$ microstripe is presented showing the potential to realize a spin-wave amplifier to open the opportunity for long information transfer routes. Report 4.6 addresses the detection of parametrically excited exchange magnons by the inverse spin Hall effect, a promising method in magnon spintronics to convert the spin-wave signal into electronic signals and vice versa. Report 4.7 demonstrates for the first time the tunneling of spin waves through a mechanical gap in $\text{Ni}_{81}\text{Fe}_{19}$ microstrips.

B. Magnon-Spintronik

Die Spintronik umfasst das Gebiet der Spin-basierten Informationsspeicherung und Verarbeitung. Bei der konventionellen Spintronik wird das Elektron als Träger des Spins verwendet. Ein besonderes Augenmerk im Hinblick auf potentielle Anwendungen in Computern oder magnetischen Speichern liegt auf der Manipulation von Spinströmen in Nanostrukturen. Für eine erfolgreiche Nutzung der Spininformationsübertragung ist es allerdings notwendig, Schwierigkeiten wie die vergleichbar kurze Länge der Spinkonservierung in Materialien, der sogenannten Spindiffusionslänge, zu überwinden. Ein sehr erfolgreicher Ansatz ist hier die Kombination der Spintronik mit der Spinwellendynamik, die “Magnon-Spintronik”. Ein Magnon, das Quant einer Spinwelle, trägt ebenfalls einen Drehimpuls oder Spin und kann analog zur konventionellen Spintronik für den Spin-basierten Datentransfer und die Datenverarbeitung genutzt werden, bietet aber zusätzlich herausragende Möglichkeiten wie z.B. lange Lebenszeiten und verlustfreien Transport. Das Feld der Magnon-Spintronik befindet sich noch in der Anfangsphase, erste Bausteine eines Anwendungsbaukastens, wie z.B. Magnongeneratoren (Spinwellenemitter) und Detektoren sind aber sehr vielversprechend. Die Technik der phasenaufgelösten Brillouin-Lichtstreuemikroskopie, die in unserer Gruppe entwickelt wurde, eröffnet hierbei besonders im Feld linearer und nichtlinearer Spinwellendynamik in Nanostrukturen neue Möglichkeiten. Die experimentellen Analysen mittels Brillouin-Lichtstreuenspektroskopie werden durch mikromagnetische Simulationen unterstützt. In Bericht 4.4 wird die Modenkonzersion propagierender Spinwellen in $\text{Ni}_{81}\text{Fe}_{19}$ -Mikrostreifen mit speziell angepasster Geometrie diskutiert. In Bericht 4.5 wird die parallel-parametrische Ver-

stärkung von Spinwellen in $\text{Ni}_{81}\text{Fe}_{19}$ Mikrostreifen präsentiert. Diese Methode zeigt ein großes Potential für die Realisierung von Spinwellenverstärkern in der Magnon-Spintronik, um größere Signaltransportstrecken auf einem Chip zu ermöglichen. In Bericht 4.6 wird die erfolgreiche Detektion parametrisch angeregter austauschdominierter Spinwellen mittels des inversen Spin-Hall-Effekts vorgestellt. Diese Methode stellt einen vielversprechenden Ansatz in der Magnon-Spintronik dar, da es die Konvertierung des Spinwellensignals in ein elektrisches Signal und umgekehrt erlaubt und so die Verbindung zur konventionellen Elektronik herstellt. Bericht 4.7 stellt die erstmalige Realisierung des Spinwellentunneleffekts in $\text{Ni}_{81}\text{Fe}_{19}$ -Mikrostreifen vor.

4.4 Mode conversion by symmetry breaking of propagating spin waves

P. Clausen, K. Vogt, H. Schultheiss, S. Schäfer, B. Obry, G. Wolf, P. Pirro, B. Leven and B. Hillebrands¹

For the excitation of spin waves on the micrometer length scale many mechanisms have been explored, e.g. excitation by uniform microwave fields [1], microstrip antennas [2, 3], spin-transfer torque [4, 5], or oscillating domain walls [6]. However, the transport of spin waves in waveguide structures was mainly focused on one-dimensional geometries [7, 8]. The implementation of spin waves for the transport and processing of information will require changes of the spin-wave propagation direction and will need to involve two-dimensional waveguides. Modifications in the shape of a magnetic waveguide often result in inhomogeneous demagnetizing fields and non-uniform magnetization distributions. However, the spin-wave dispersion as well as the mode profiles adiabatically adjust to the local variations in the internal field [9]. This makes the overall propagation and quantization pattern complex and difficult to predict.

A way out of this problem is a set of specific design rules for the layout of spin-wave waveguide structures. We demonstrate that such design rules exist and how specific mode properties can be utilized [10]. As an example the spin-wave transport in a waveguide with broken translational symmetry is considered. The waveguide is shifted transverse to the spin-wave propagation direction resulting in a parallel offset of the waveguide axis behind the skew section (see Fig. 1b). Despite being only a rather small deviation from a straight stripe, we show that this skew has a profound impact on the spin-wave modes propagating in the waveguide.

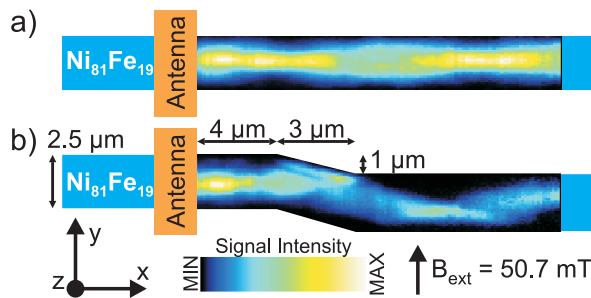


Fig. 1: Concept of the investigated spin-wave waveguides. a) Reference and b) spin-wave waveguide with a lateral skew. The distribution of the spin-wave intensity measured by Brillouin light scattering (BLS) microscopy is color coded where dark (bright) indicates minimum (maximum) intensity, respectively. The measured intensities have been normalized to compensate for damping.

The schematic layout of the investigated microstructure is shown in Fig. 1. Spin-wave waveguides with dimensions of $w = 2.5 \mu\text{m}$ and $l = 100 \mu\text{m}$ were fabricated from a 60 nm thick $\text{Ni}_{81}\text{Fe}_{19}$ film using electron-beam lithography and conventional lift-off techniques. Spin waves are excited by the magnetic Oersted field of a $2 \mu\text{m}$ wide and 500 nm thick Copper microstrip antenna driven with frequencies $\omega_{\text{rf}}/2\pi$ of up to 18 GHz.

A reference spin-wave waveguide with known spin-wave mode properties [8] is used for comparison of the measurement with the real two-dimensional spin-wave waveguide and is displayed in Fig. 1a. The two-dimensional waveguide is shown in Fig. 1b with a $3 \mu\text{m}$ long skew starting at a distance of $4 \mu\text{m}$ from the antenna resulting in a $1 \mu\text{m}$ parallel offset of the waveguide. A static magnetic field of $B_{\text{ext}} = 50.7 \text{ mT}$ is applied along the short axis of the waveguide (y-direction) to

¹H.S. is now at Materials Science Division, Argonne National Laboratory, Argonne, Illinois 60439, USA; S.S. is now at University of Alabama, Center for Materials for Information Technology, Department of Physics & Astronomy, Tuscaloosa, AL 35487, USA.

ensure the excitation of propagating spin waves travelling perpendicular to the magnetization direction with high group velocities, i.e. Damon-Eshbach spin-wave modes [11]. This allows for the investigation of propagation phenomena over large distances by means of Brillouin light scattering (BLS) microscopy [2, 12] as can be seen in the spin-wave intensity patterns overlaid in Fig. 1. A

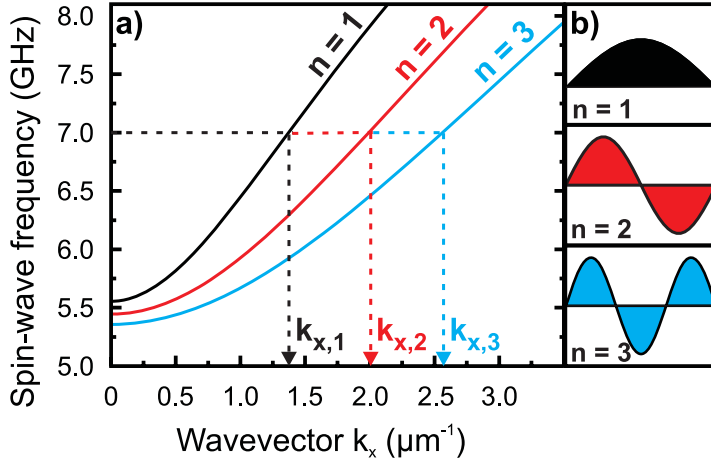


Fig. 2: a) Frequencies of lateral spin-wave modes with different mode numbers n as a function of the wavevector component along the waveguide (x -direction). The dashed lines depict the wavevectors for a fixed excitation frequency. b) Schematic spin-wave mode profiles in y -direction.

waveguide with a finite transversal width causes a discretization of the spin-wave wavevector in y -direction leading to a well-defined set of dispersion relations as shown in Fig. 2a. These dispersion relations display the frequency dependence of the spin-wave modes as a function of the wavevector component k_x in x -direction along the waveguide. The wavevector in y -direction, perpendicular to the waveguide, is quantized according to $k_{n,y} = n\pi/w_{\text{eff}}$, where the mode number n equals the number of anti-nodes in y -direction across the width of the stripe. In this geometry, the demagnetizing fields lead to a reduction of the effective quantization width w_{eff} smaller than the geometrical width w of the stripe. The calculation of the dispersion relations is made following the approach in [2] for an internal magnetic field of $B_{\text{int}} = 39.5 \text{ mT}$ and standard material parameters for $\text{Ni}_{81}\text{Fe}_{19}$ as summarized in [13]. The internal magnetic field is extracted from a micromagnetic simulation (oommf code, see [14]) and set to an averaged value over the assumed quantization width. The smaller value compared to the externally applied field is due to the demagnetizing fields originating from the magnetic charges at the boundaries of the waveguide.

In the further discussion, we assume a sinusoidal mode profile in y -direction, as schematically displayed in Fig. 2b for the three lowest width modes. This leads to an overall spatial spin-wave amplitude given by

$$\psi_n(x, y, t) = A_n e^{-i(k_x x - \omega_{\text{rf}} t)} \cdot \sin\left(\frac{n\pi}{w_{\text{eff}}} y\right), \quad (1)$$

where A_n is the maximum amplitude of the respective partial mode. For a given excitation frequency ($\omega_{\text{rf}}/2\pi = 7 \text{ GHz}$ in Fig. 2a) several modes with different n can be excited simultaneously. These modes interfere with each other and form a stationary intensity distribution [15, 16]. The resulting time-averaged interference pattern is the coherent superposition

$$I(x, y) = \left| \sum_n \psi_n(x, y) \right|^2 \quad (2)$$

of the amplitudes given in Eq. (1) and reflects the symmetry of the interfering modes. Only in the case when all spin-wave modes have an odd mode number n , the resulting intensity distribution is symmetric with respect to the center of the waveguide.

Since in our experiment the exciting field of the antenna is homogeneous across the waveguide's width, only spin-wave modes with a net component of the dynamic magnetization, i.e., odd modes with $n = 1, 3, 5, \dots$, can be directly excited. Therefore, only a symmetric spin-wave interference pattern is observed in the reference waveguide as can be seen in the measured BLS intensity in Fig. 1a. Such a symmetric spin-wave interference pattern is also visible in the $4\mu\text{m}$ long section between antenna and skew of the waveguide in Fig. 1b.

Inside the skew section, the spin-wave intensity distribution changes significantly compared to the reference waveguide. The incident spin-wave beam is not simply reflected at the edge of the skew section but rather attenuated. Furthermore, it excites a different mode which is strongly localized at the edge of the waveguide in a spin-wave well [17]. Calculations show, that the inhomogeneity of the internal magnetic field B_{int} , which is modified by the demagnetizing field of the stripe, traps the spin waves in a region extending only several hundred nanometers from the edge of the stripe which is comparable to the lateral dimensions of the edge mode in Fig. 1b.

Behind the skew section, in $7\mu\text{m}$ distance from the antenna, the interference pattern has an asymmetric component. This asymmetric spin-wave intensity distribution observed behind the skew can be described in good approximation as a superposition of the lowest even and odd mode with $n = 1$ and $n = 2$. This conversion from a purely symmetric system to a mixed set of symmetric and asymmetric spin-wave modes is caused by an asymmetric distribution of the dynamic magnetization, which originates from the originally excited modes ending up with their intensity maximum displaced from the center of the stripe by the skew. As a result, the asymmetric mode with $n = 2$ is excited.

To quantitatively analyze this effect, we consider the periodicity of the spin-wave intensity. For each stationary spin-wave intensity distribution, being either symmetric or asymmetric, its periodicity d_{per} in x -direction is determined by the difference $\Delta k_x(\omega_{\text{rf}})$ of the wavevector components k_x of the interfering spin waves and is a function of the excitation frequency ω_{rf} . In case the two lowest spin-wave modes are excited, this leads to a periodicity d_{per} given by:

$$d_{\text{per}}(\omega_{\text{rf}}) = \frac{2\pi}{(k_{x,1}(\omega_{\text{rf}}) - k_{x,2}(\omega_{\text{rf}}))} \quad . \quad (3)$$

In the experiment, the values of $k_{x,1}$ and $k_{x,2}$ are determined by the spin-wave dispersion relations shown in Fig. 2a. Consequently, the periodicity d_{per} can be controlled by either tuning the excitation frequency ω_{rf} or the externally applied magnetic field B_{ext} .

To support the stated interpretation of the asymmetric interference pattern being composed of the spin-wave modes with $n = 1$ and $n = 2$, we measured and calculated the intensity distributions of these two interfering modes for excitation frequencies $\omega_{\text{rf}}/2\pi$ ranging from 6.6 to 8.0GHz. For calculating the interference pattern we use Eq. (1) and Eq. (2) with $n = 1, 2$ and the wavevectors determined from the corresponding dispersion relations as in Fig. 2a for each excitation frequency. The amplitudes A_n are free parameters in the calculation and were set to match the measured intensity distributions. However, their specific values will not influence the periodicity of the interference pattern.

For three exemplary excitation frequencies, the intensity distributions measured behind the skew can be seen in Fig. 3a, both for experiment (left sub-panels) and calculations (right sub-panels).

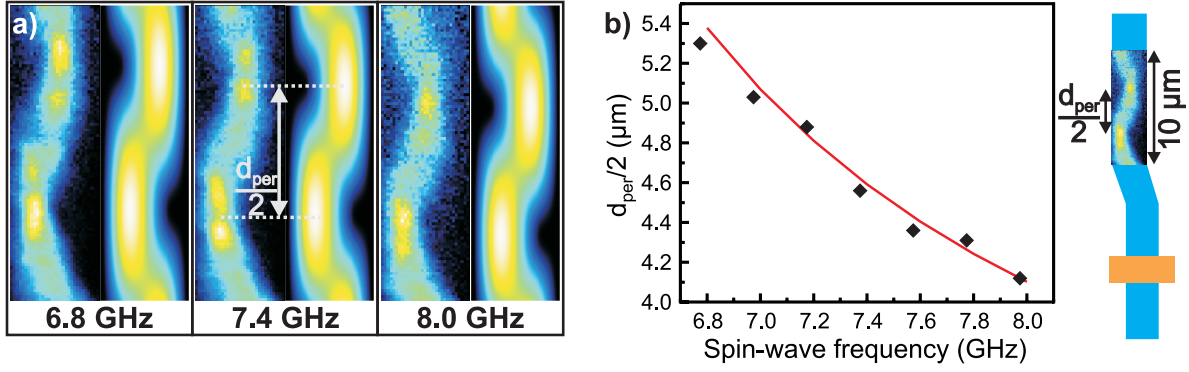


Fig. 3: a) Comparison of the measured (left sub-panels) and calculated (right sub-panels) spin-wave interference patterns for different frequencies. b) Black diamonds show the periodicity d_{per} extracted from the interference patterns as illustrated in a) as a function of the spin-wave frequency. The curve depicts calculated values.

The resulting change in the periodicity d_{per} of the snake-like mode pattern is evident in the experiment as well as in the calculations, showing an excellent agreement with each other.

Figure 3b summarizes the results obtained from BLS microscopy measurements (filled symbols) in direct comparison with the theoretical expectations (line), which are given by Eq. (3). For increasing excitation frequencies, the split in the dispersion relations becomes more pronounced leading to an increase of $\Delta k_x(\omega_{\text{rf}})$. Therefore, the periodicity d_{per} decreases in agreement with Eq. (3) as can be seen in Fig. 3a and b. The agreement between the measured data and calculations further supports our assumption of observing interference between the modes $n = 1$ and $n = 2$ behind the skew.

In conclusion, we were able to manipulate the spin-wave mode patterns of propagating spin waves in a microscopic waveguide from being a superposition of symmetric modes to a mixed system of symmetric/asymmetric spin-wave modes. This controlled mode conversion is achieved by a shift of the waveguide transverse to the propagation direction of the spin waves creating a variation in the magnetization distribution within the skew section and leading to a strong concentration of the spin-wave amplitude on one side of the waveguide. Ultimately, this inhomogeneity causes the excitation of asymmetric spin-wave modes behind the skew section.

This is not only an eminent chance to create spin-wave modes in microstructures which cannot be excited by antennas alone due to their homogeneous field. The study of spin-wave propagation and mode conversion in this structure may also lead to further insight into the interaction between spin waves and their excitation via the local dynamic magnetization. In addition, it is a first step to better understand and utilize spin-wave transport in truly two-dimensional microstructures, an essential step for the implementation of magnonics and magnon-spintronics into future devices.

This work has been recently published in Applied Physics Letters [10].

The authors thank Dr. P.A. Beck for deposition of the magnetic thin film and the Nano Structuring Center of the Technische Universität Kaiserslautern for assistance in sample preparation. Financial support by the Carl-Zeiss-Stiftung and the Graduiertenkolleg 792 is gratefully acknowledged.

References

- [1] Y. Au, T. Davison, E. Ahmad, P.S. Keatley, R.J. Hicken, V.V. Kruglyak, *Excitation of propagating spin waves with global uniform microwave fields*, Appl. Phys. Lett. **98**, 122506 (2011).

-
- [2] K. Vogt, H. Schultheiss, S.J. Hermsdoerfer, P. Pirro, A.A. Serga, B. Hillebrands, *All-optical detection of phase fronts of propagating spin waves in a $\text{Ni}_{81}\text{Fe}_{19}$ microstripe*, Appl. Phys. Lett. **95**, 182508 (2009).
 - [3] V.E. Demidov, M.P. Kostylev, K. Rott, P. Krzysteczko, G. Reiss, and S.O. Demokritov, *Excitation of microwaveguide modes by a stripe antenna*, Appl. Phys. Lett. **95**, 112509 (2009).
 - [4] J. Slonczewski, *Current-driven excitation of magnetic multilayers*, J. Magn. Magn. Mater. **159**, L1 (1996).
 - [5] V.E. Demidov, S. Urazhdin, V.V. Tiberkevich, A. Slavin, S.O. Demokritov, *Control of spin-wave emission from spin-torque nano-oscillators by microwave pumping*, Phys. Rev. B **83**, 060406 (2011).
 - [6] S. Hermsdoerfer, H. Schultheiss, C. Rausch, S. Schäfer, B. Leven, S. Kim, B. Hillebrands, *A spin-wave frequency doubler by domain wall oscillation*, Appl. Phys. Lett. **94**, 223510 (2009).
 - [7] O. Büttner, S.O. Demokritov, V. Grimalsky, Yu. Rapoport, A.N. Slavin, B. Hillebrands, *Observation of spatiotemporal self-focusing of spin waves in magnetic films*, Phys. Rev. Lett. **81**, 3769 (1998).
 - [8] V.E. Demidov, J. Jersch, K. Rott, P. Krzysteczko, G. Reiss, S.O. Demokritov, *Nonlinear propagation of spin waves in microscopic magnetic stripes*, Phys. Rev. Lett. **102**, 177207 (2009).
 - [9] C. Bayer, J.P. Park, H. Wang, M. Yan, C.E. Campbell, P.A. Crowell, *Spin waves in an inhomogeneously magnetized stripe*, Phys. Rev. B **69**, 134401 (2004).
 - [10] P. Clausen, K. Vogt, H. Schultheiss, S. Schäfer, B. Obry, G. Wolf, P. Pirro, B. Leven, B. Hillebrands, *Mode conversion by symmetry breaking of propagating spin waves*, Appl. Phys. Lett. **99**, 162505 (2011).
 - [11] R.W. Damon and J.R. Eshbach, *Magnetostatic modes of a ferromagnet slab*, J. Phys. Chem. Solids **19**, 308 (1961).
 - [12] V.E. Demidov, S.O. Demokritov, B. Hillebrands, M. Laufenberg, P.P. Freitas, *Radiation of spin waves by a single micrometer-sized magnetic element*, Appl. Phys. Lett. **85**, 2866 (2004).
 - [13] The material parameters used for calculating the spin-wave dispersions are:
 Saturation magnetization: $M_s = 800 \text{ kA/m}$
 Gyromagnetic ratio: $|\gamma|/2\pi = 28 \text{ GHz/T}$
 Exchange stiffness constant: $A = 1.6 \cdot 10^{-11} \text{ J/m}$
 - [14] M.J. Donahue and D.G. Porter, *OOMMF User's Guide, Version 1.0*, Interagency Report NISTIR 6376, National Institute of Standards and Technology, Gaithersburg, MD (1999).
 - [15] O. Büttner, M. Bauer, C. Mathieu, S.O. Demokritov, B. Hillebrands, P. Kolodin, M. Kostylev, S. Sure, H. Dotsch, V. Grimalsky, Y. Rapoport, A.N. Slavin, *Mode beating of spin wave beams in ferrimagnetic $\text{Lu}_{2.04}\text{Bi}_{0.96}\text{Fe}_5\text{O}_{12}$ films*, IEEE Trans. Magn. **34**, 1381 (1998).
 - [16] V.E. Demidov, S.O. Demokritov, K. Rott, P. Krzysteczko, G. Reiss, *Mode interference and periodic self-focusing of spin waves in permalloy microstripes*, Phys. Rev. B **77**, 064406 (2008).
 - [17] J. Jorzick, S.O. Demokritov, B. Hillebrands, M. Bailleul, C. Fermon, K.Y. Guslienko, A.N. Slavin, D.V. Berkov, N.L. Gorn, *Spin wave wells in nonellipsoidal micrometer size magnetic elements*, Phys. Rev. Lett. **88**, 047204 (2002).

4.5 Parallel parametric generation of spin waves in a $\text{Ni}_{81}\text{Fe}_{19}$ microstripe

T. Brächer, P. Pirro, B. Obry, A.A. Serga, B. Leven, and B. Hillebrands

Parallel parametric amplification [1, 2] is a versatile technique to modulate, save and recover information in a spin-wave signal [3–5]. The usability of this technique was widely demonstrated in Yttrium Iron Garnet (YIG) [6]. The key aspect of parallel parametric amplification is that it acts opposite to the intrinsic damping of a given spin-wave mode by creating magnon pairs out of microwave photons. In metallic ferromagnets like the nickel-iron compound Permalloy ($\text{Ni}_{81}\text{Fe}_{19}$) this feature becomes very interesting, since the spin-wave lifetime in this material is limited to a few nanoseconds leading to typical propagation distances on the micrometer scale in microstructured elements. Parallel parametric amplification promises to enhance the spin-wave lifetime tremendously, which might be very helpful for devices based on spin waves as information carriers. This is of major interest since $\text{Ni}_{81}\text{Fe}_{19}$ and other ferromagnetic metals offer compatibility with CMOS technology, are well eligible for microstructuring and comparably affordable.

Another key feature of parallel parametric amplification is the amplification of all existing spin-wave modes - i.e. all populated modes - at half the pumping frequency that show a finite coupling to the pumping field. However, there will be a set of modes having the highest amplification gain, the so called dominant group. In general, the dominant group is not coinciding with the signal group i.e. the externally excited magnons carrying the signal. In most experiments performed in YIG this puts a strong limitation on the amplification gain for the signal group as the dominant group will be the only amplified mode after a certain time. The exact processes limiting the final amplification gain can however not be fully explained [7]. Since microstructured systems offer a tailored mode spectrum due to quantization [12] the investigation of parametric processes in microstructures might also be helpful to understand the interaction between the different amplified modes and the processes limiting the amplification.

In this Report we demonstrate that parallel parametric amplification can be used to amplify thermal spin waves in a $\text{Ni}_{81}\text{Fe}_{19}$ microstripe and investigate the nature of the amplified modes [9]. We have found that these modes include the ones that can be externally excited by a microstrip antenna as well as even eigenmodes of the stripe and modes confined to its edges.

As mentioned above, parallel parametric amplification describes the extinction of one microwave photon of frequency f_{MW} by creating a pair of magnons with $f = f_{\text{MW}}/2$ and opposite wavevector. The number of magnons $n_j(t)$ of the magnon group j can then be described by [10]

$$n_j(t) = n_{j0} \exp(-2(\Gamma_j - V_j \tilde{h})t) \quad , \quad (1)$$

where n_{j0} denotes the (thermal) starting population of the magnon group, Γ_j the relaxation frequency and V_j the coupling parameter of the alternating microwave field \tilde{h} - which is pointing parallel to the static magnetization - to the magnon group. Following Eq. 1 the amplification acts oppositely to the damping, and if the product $V_j \tilde{h}$ compensates Γ_j the number of magnons will increase exponentially in time. Hence parallel parametric amplification is a threshold process.

The experimental observation of parametrically amplified spin waves in a micron-sized stripe of $\text{Ni}_{81}\text{Fe}_{19}$ is performed by means of Brillouin light scattering microscopy (BLS) [11]. Since the BLS intensity is proportional to the spin-wave intensity, it provides a space- and frequency-resolved analysis of the amplified spin waves. The investigated structure (scheme see Fig. 1)

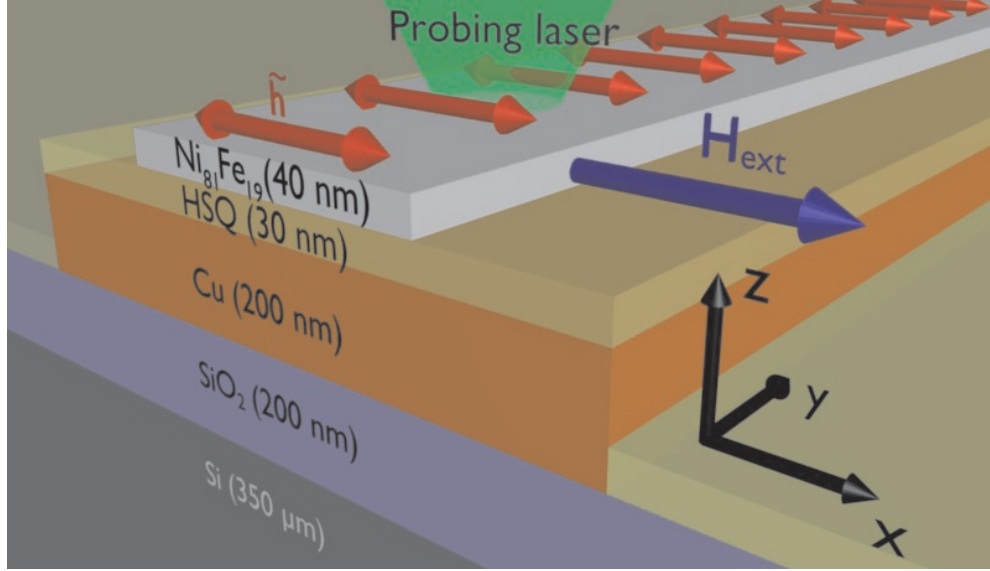


Fig. 1: Schematic sample design: A $\text{Ni}_{81}\text{Fe}_{19}$ microstripe (width $w_s = 2.5\mu\text{m}$, thickness $t_s = 40\text{nm}$, length $l_s = 75\mu\text{m}$) is placed on top of a Cu waveguide (width $w_a = 6\mu\text{m}$, thickness $t_a = 200\text{nm}$) which is connected to a microwave generator. The Cu and the $\text{Ni}_{81}\text{Fe}_{19}$ layers are separated by an insulation layer (HSQ) (thickness $t = 30\text{nm}$) and the $\text{Ni}_{81}\text{Fe}_{19}$ is capped with a $t_c = 2\text{nm}$ thick layer of aluminum oxide (not shown). As substrate an oxidized Si sample is used ($t_{\text{Oxide}} = 200\text{nm}$). An alternating current is passed through the Cu waveguide, creating an alternating Oersted field \tilde{h} parallel to the externally applied field H_{ext} .

has been patterned by electron beam lithography and lift-off technique. The $\text{Ni}_{81}\text{Fe}_{19}$ stripe is deposited by molecular beam epitaxy, capped with 2nm of alumina and placed onto a copper (Cu) waveguide. The $\text{Ni}_{81}\text{Fe}_{19}$ and the Cu layers are separated by an insulation layer of hydrosilsequioxane (HSQ).

In order to understand the response of the spin system to the microwave pumping field one should consider the available spin-wave modes. The finite dimensions of the $\text{Ni}_{81}\text{Fe}_{19}$ stripe lead to a quantization of the existing spin-wave eigenmodes across its height and width. These modes are characterized by the mode numbers $(p;n)$ which correspond to the number of anti-nodes across the height and width [12]. Figure 2a shows a spin-wave spectrum recorded at an external static magnetic field of $\mu_0 H_{\text{ext}} = 55\text{mT}$ without any applied microwave field, revealing the eigenmodes of the system. The bottom of the spin-wave band can be seen at $f \approx 6\text{GHz}$. The corresponding spin-wave dispersion relations for the modes $n = 1, 2, 3, 8, 9$ for $p = 0$ are shown in Fig. 2b. As can be seen from Fig. 2b the frequency $f_{0,n} = f(k_y = 0, n)$, i.e. the origin of the spin-wave band n , decreases with increasing n for $n \leq 8$. For $n > 8$ the exchange energy originating from the tilt of neighboring spins overcomes the gain in dipolar energy and f_0 increases. For increasing frequency the BLS intensity starts to decrease (see Fig. 2a). This effect can be assigned to the decrease in BLS detection efficiency with increasing wavevector of the observed spin waves [11]. At $f \approx 16\text{GHz}$ a second peak is observed which corresponds to the set of perpendicular standing spin waves (PSSW) with $p = 1$.

In order to amplify the thermal spin-wave manifold with $p = 0$ a microwave current was passed through the Cu waveguide. To exclude direct excitation of the set of modes with $p = 1$ the frequency of this current was chosen to $f_{\text{MW}} = 12\text{GHz}$ leading to the amplification of spin waves with an eigenfrequency $f = 6\text{GHz}$. The current was pulsed with a pulse length of $t_{\text{pulse}} = 50\text{ns}$ and with a repetition rate of $\tau = 200\text{ns}$ to avoid heating effects. During the measurement the external field

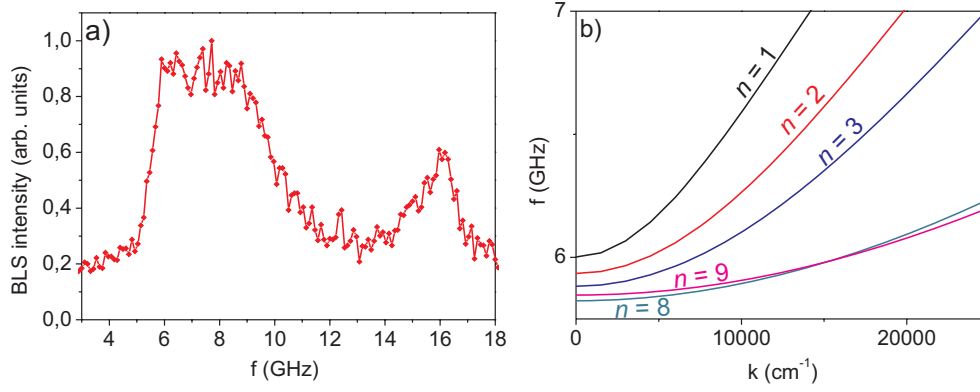


Fig. 2: a) Normalized thermal BLS spectrum recorded at an applied external field of $\mu_0 H_{\text{ext}} = 55$ mT without applied pumping. b) Calculated dispersion relations (according to [13]) for the transverse spin-wave modes (0; 1, 2, 3, 8, 9).

H_{ext} was varied in the range from $\mu_0 H_{\text{ext}} = 30$ mT to 70 mT. This also ensures that the spin-wave dispersion relations of the set of modes with $p = 1$ always lie at frequencies above $f = 12$ GHz.

In Fig. 3a the BLS-intensity at $f = 6$ GHz in dependence of the magnetic field $\mu_0 H_{\text{ext}}$ and the applied microwave power is shown color coded. The signal is recorded in the middle of the short axis of the $\text{Ni}_{81}\text{Fe}_{19}$ stripe. Figure 3b shows exemplarily a power sweep recorded at $\mu_0 H_{\text{ext}} = 54$ mT and Fig. 3c shows the dependence of k_y on the applied magnetic field. As can be seen from Fig. 3b for a given magnetic field there is no notable spin-wave intensity below a certain threshold power. If the applied power overcomes this threshold, thermal spin waves are amplified and the measured spin-wave intensity increases drastically. From Figs. 3a and b it can be seen that close to an external applied field of 54 mT this threshold power reaches a minimum value of 21 dBm. If the external field is increased from this point, the threshold power increases rapidly, and if the field is decreased the threshold power increases slowly.

To obtain a better understanding of this behavior and to associate the threshold characteristics (butterfly curve) with the spin-wave modes of the $\text{Ni}_{81}\text{Fe}_{19}$ stripe, the BLS intensity across the $\text{Ni}_{81}\text{Fe}_{19}$ stripe and thus the transverse mode profiles of the amplified modes are recorded. The profiles measured at the external fields and microwave powers marked by the black dots in Fig. 3a are shown in Fig. 4. Note that the recorded profiles correspond to a convolution of the real mode profiles with the finite intensity distribution of the laser spot.

For field values lower than or equal to 54 mT the profiles show one maximum across the stripe width, hence the dominant group is the mode $n = 1$ (Fig. 4i - ii). Here, with a decrease of $\mu_0 H_{\text{ext}}$, the threshold power increases. To understand this, one should consider the dependence of the ellipticity of precession [14] ε on the magnetic field, since the coupling parameter [15] V of the microwave pumping field to the magnetization increases with ε . For a fixed frequency a decrease of the field leads to an increase of the wavevector k_y (see Fig. 3c). This is connected to a decrease of the ellipticity of this mode which can be explained by simple arguments [16]:

The ellipticity is highest for $\mathbf{k} = 0$. If one of the in-plane components of \mathbf{k} increases the resulting finite wavelength leads to magnetic moments pointing in opposite z -directions which reduce the dipolar stray field and thus favor the out-of-plane precession. On the other hand in a transversally magnetized stripe the dipolar interaction of the in-plane components of the precession reduces the in-plane precession amplitude compared to $\mathbf{k} = 0$. Both effects lead to a decrease of ε with increasing k . This reduction of ε and thus of the coupling parameter V can explain the increase of

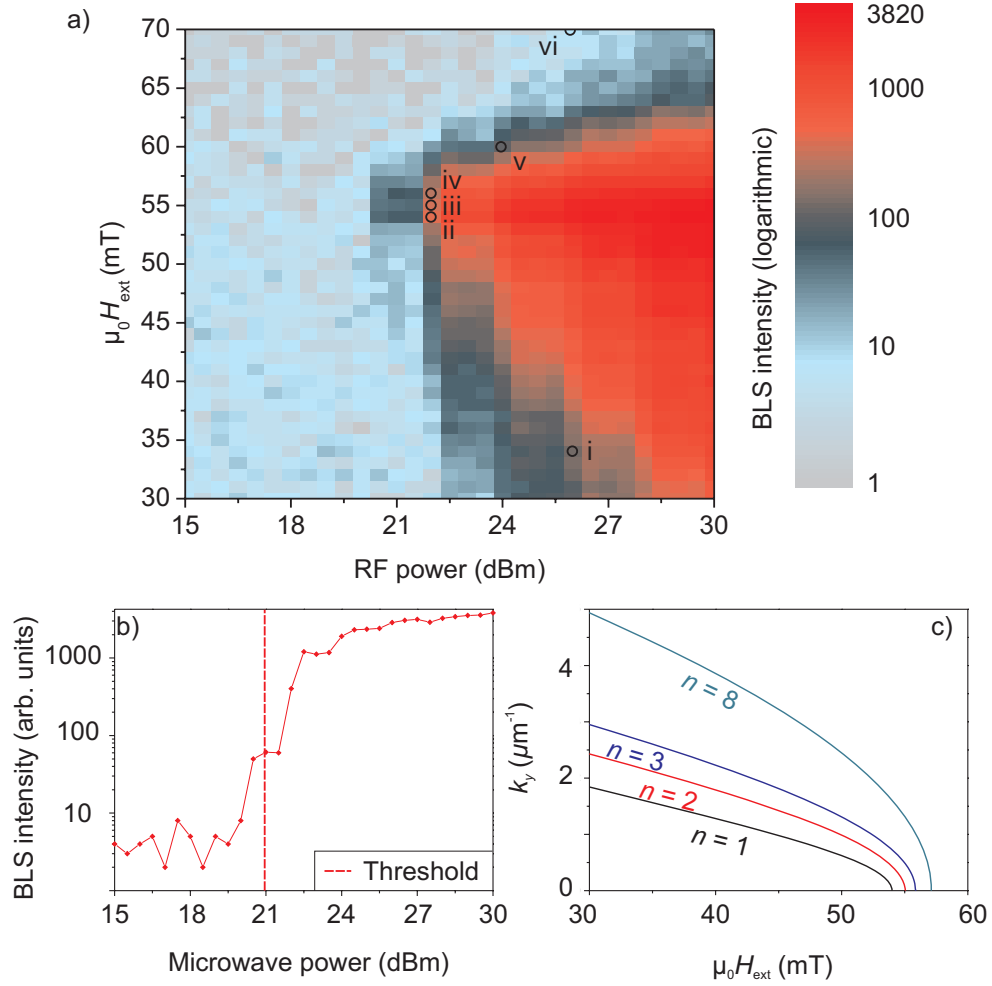


Fig. 3: a) Color coded BLS intensity at $f = 6$ GHz for different magnetic fields in a range from 30 mT to 70 mT and different applied microwave powers (15 – 30 dBm). The black dots (i - vi) mark the fields and powers at which transverse mode profiles are recorded. b) Exemplary cut of Fig. 3a for a fixed field of $\mu_0 H_{\text{ext}} = 54$ mT. c) Calculated wavevectors [13] k_y for the modes (0; 1, 2, 3, 8) vs. $\mu_0 H_{\text{ext}}$ for a fixed frequency of 6 GHz.

the threshold power for this mode with increasing k_y . As a further consequence, the preferably amplified mode for a fixed frequency is the mode with the lowest available n since for higher n either the larger k -vector in y - or in x -direction leads to a smaller ε (see Fig. 3c).

If the field is increased to 55 mT the mode profile changes and two anti-nodes are visible (Fig. 4iii). This is identified as the point where $f_{0,1}$ is shifted above $f = 6$ GHz by increasing the magnetic field and the next available mode is the mode $n = 2$. Since modes with even n have no net dynamic magnetic moment they cannot be excited with conventional microstripe antennas [8]. Hence parallel parametric amplification offers a unique way of exciting these modes.

A further increase to 56 mT will also shift $f_{0,2}$ above 6 GHz yielding three anti-nodes across the stripe width, resembling the mode $n = 3$ (Fig. 4iv). For higher field values even higher transversal modes are observed (not shown) up to the field where no transversal mode exists in the stripe anymore ($f_{0,8}$ shifted above 6 GHz). From this field value on the observed mode profiles show a confinement to the stripe edges (Fig. 4v - vi). This can be explained by the internal field distribution in the transversally magnetized stripe: Since the internal field drops towards the edges, there exists a region where the internal field allows for a mode at a frequency of 6 GHz localized at the stripe edges (named “edge modes” [12]). For higher field values only these edge modes can be amplified

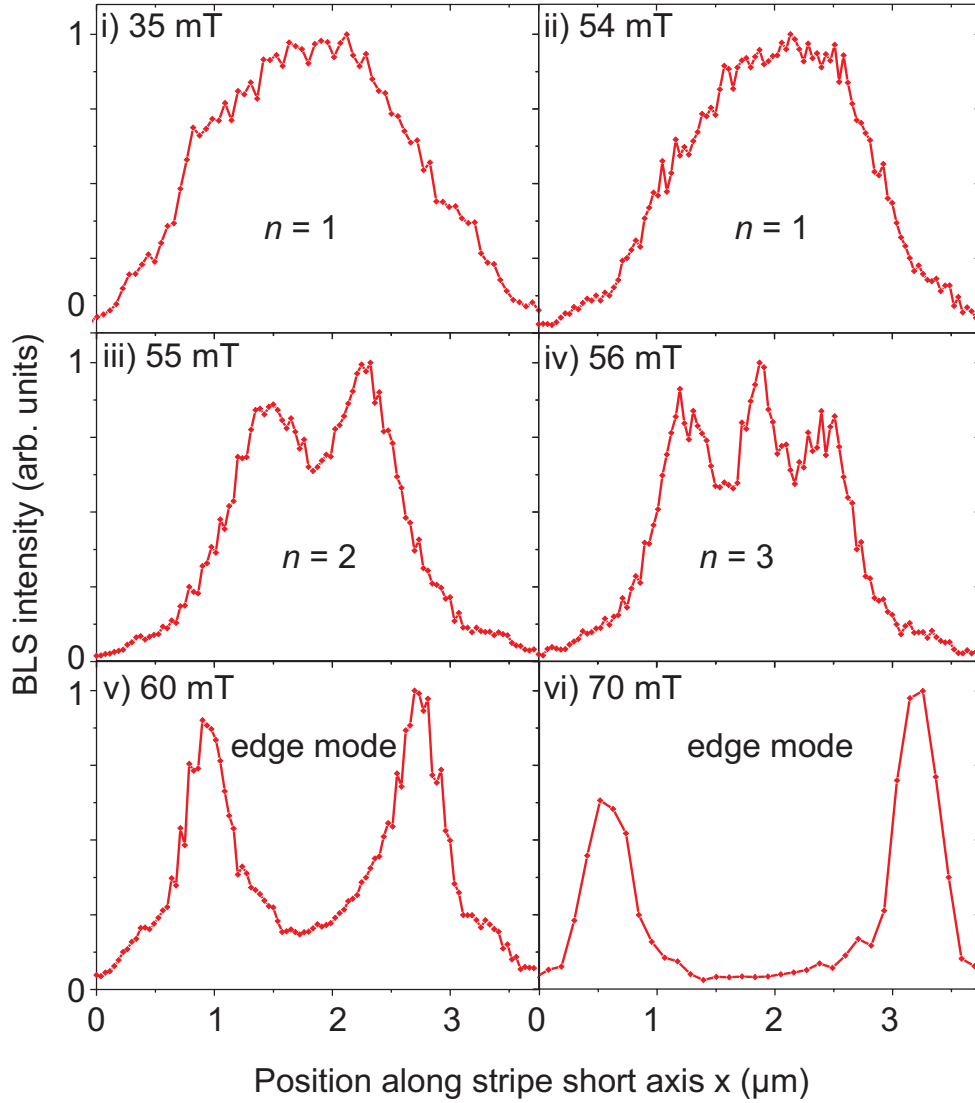


Fig. 4: Individually normalized mode profiles recorded along the stripe short axis (see Fig. 1) at the fields and powers indicated by the black dots in Fig. 3a.

at 6 GHz. The sharp decrease of the measured BLS intensity for increasing magnetic field is connected to the fact that no transversal eigenmode can be excited anymore and the amplified modes are increasingly confined to the stripe edges.

In conclusion we observed that parallel parametric amplification allows for the selective amplification of spin-wave modes in $\text{Ni}_{81}\text{Fe}_{19}$ microstrips and that in a large region the mode $n = 1$ is preferably amplified. As this mode has a comparably high group velocity and the largest detection efficiency for microstripe receivers of all transverse eigenmodes, it is the preferred mode in terms of applications for spin-wave information processing. This makes parallel parametric amplification a promising candidate to overcome the spin-wave damping losses in $\text{Ni}_{81}\text{Fe}_{19}$ because in this system the dominant group can be tuned to be the mode that carries the signal. By tuning the field also the k -vector of this mode can be selected. In addition, it is possible to selectively amplify other modes by choosing the right applied magnetic field and frequency. Especially, this gives access to even spin-wave modes which cannot be excited with regular microstripe antennas, and, furthermore, this allows for the amplification of edge modes.

This work has been published recently in Applied Physics Letters [9].

The authors thank P.A. Beck and the Nano+Bio Center of the Technische Universität Kaiserslautern for their assistance in sample preparation and A. Chumak and M.P. Kostylev for helpful discussion. Financial support by the DFG and the OPTIMAS Carl-Zeiss doctoral program funded by the Carl-Zeiss Foundation is gratefully acknowledged.

References

- [1] E. Schlömann, J.J. Green, and U. Milano, *Recent developments in ferromagnetic resonance at high power levels*, J. Appl. Phys. **31**, p. 386S (1960).
- [2] S.M. Rezende and F.M. de Aguiar, *Spin-wave instabilities, auto-oscillations, and chaos in yttrium-iron-garnet*, IEEE Proc. **78**, 6 (1990).
- [3] K.R. Smith, V.I. Vasyuchka, M. Wu, G.A. Melkov, C.E. Patton, *Cloning and trapping of magnetostatic spin-wave pulses by parametric pumping*, Phys. Rev. B **76**, 054412 (2007).
- [4] G.A. Melkov, A.A. Serga, A.N. Slavin, V.S. Tiberkevich, A.N. Oleinik, A.V. Bagada, *Parametric interaction of magnetostatic waves with a nonstationary local pump*, JETP **89** (6), 1189-1199 (1999).
- [5] A.A. Serga, A.V. Chumak, A. André, G.A. Melkov, A.N. Slavin, S.O. Demokritov, B. Hillebrands, *Parametrically Stimulated Recovery of a Microwave Signal Stored in Standing Spin-Wave Modes of a Magnetic Film*, Phys. Rev. Lett. **99**, 227202 (2007).
- [6] A.A. Serga, A.V. Chumak, B. Hillebrands, *YIG magnonics*, J. Phys. D: Appl. Phys. **43**, 264002 (2010).
- [7] S. Schäfer, V. Kegel, A.A. Serga, B. Hillebrands, M.P. Kostylev, *Variable damping and coherence in a high-density magnon gas*, Phys. Rev. B **83**, 184407 (2011).
- [8] V.E. Demidov, M.P. Kostylev, K. Rott, P. Krzysteczko, G. Reiss, S.O. Demokritov, *Excitation of microwaveguide modes by a stripe antenna*, Appl. Phys. Lett. **95**, 112509 (2009).
- [9] T. Brächer, P. Pirro, B. Obry, B. Leven, A.A. Serga, B. Hillebrands, *Mode selective parametric excitation of spin waves in a $\text{Ni}_{81}\text{Fe}_{19}$ microstripe*, Appl. Phys. Lett. **99**, 162501 (2011).
- [10] S. Schäfer, A.V. Chumak, A.A. Serga, G.A. Melkov, B. Hillebrands, *Microwave spectral analysis by means of nonresonant parametric recovery of spin-wave signals in a thin magnetic film*, Appl. Phys. Lett. **92**, 162514 (2008).
- [11] V.E. Demidov, S.O. Demokritov, B. Hillebrands, M. Laufenberg, P.P. Freitas, *Radiation of spin waves by a single micrometer-sized magnetic element*, Appl. Phys. Lett. **85**, 2866 (2004).
- [12] J. Jorzick, S.O. Demokritov, B. Hillebrands, D. Berkov, N.L. Gorn, K. Guslienko, A.N. Slavin, *Spin wave wells in nonellipsoidal micrometer size magnetic elements*, Phys. Rev. Lett. **88**, 047204 (2002).
- [13] B.A. Kalinikos, A.N. Slavin, *Theory of dipole-exchange spin wave spectrum for ferromagnetic films with mixed exchange boundary conditions*, J. Phys. C: Solid State **19**, 7013 (1986).
- [14] Due to dipolar stray fields that are created during the magnetization precession in thin film geometry the precession in this system is elliptic. The ellipticity ϵ is defined as the amplitude of the in-plane precession over the amplitude of the out-of-plane precession.
- [15] A.G. Gurevich and G.A. Melkov, *Magnetization Oscillations and Waves* (CRC, New York, 1996).
- [16] M.P. Kostylev, J.G. Hu, R.L. Stamps, *Confinement quantization of parallel pump instability threshold in a metallic ferromagnetic stripe*, Appl. Phys. Lett. **90**, 012507 (2007).

4.6 Detection of parametrically excited exchange magnons by the inverse spin Hall effect

M.B. Jungfleisch, C.W. Sandweg, A.V. Chumak, A.A. Serga, V.I. Vasyuchka, and B. Hillebrands¹

The emerging field of spintronics has become of great interest in the last decade. Spintronics is concerned with the development of devices which exceed the performance and energy efficiency of conventional charge-based electronics by exploiting the electron's spin degree of freedom [1, 2]. It has been demonstrated recently that it is possible to use magnons, the quanta of spin waves, instead of spin-polarized electrons to transfer information in magnetic insulators [1]. The spin pumping effect and the inverse spin Hall effect (ISHE) turned out to be the two fundamental physical mechanisms in the prospering field of magnon spintronics. Spin currents in a nonmagnetic metal can be generated by the spin pumping effect [3], while the inverse spin Hall effect can subsequently be used to transform this spin current into a measurable charge current [4].

To excite magnons one can use mainly two different ways. Firstly, a force excitation of a microwave magnetic field with the same frequency as the spin wave and secondly, parametric pumping where the spin waves are excited with a microwave magnetic field with twice the frequency [5, 6, 12]. In the first case, mostly dipolar-dominated spin waves, i.e. with small wavenumbers (and long wavelengths; restricted by the lateral size of the antenna) and frequencies near the ferromagnetic resonance (FMR), can be excited. In the latter case, there is no upper limit for the wavenumbers of the excited spin waves, which allows for the excitation of exchange-dominated spin waves with small wavelengths. The spin pumping mechanism and the ISHE has been investigated so far only for FMR excitation or dipolar-dominated spin waves with large wavelengths [1, 4, 8]. The present experiment is the first one, in which spin pumping by parametric pumping from a magnetic material to a nonmagnetic metal was investigated.

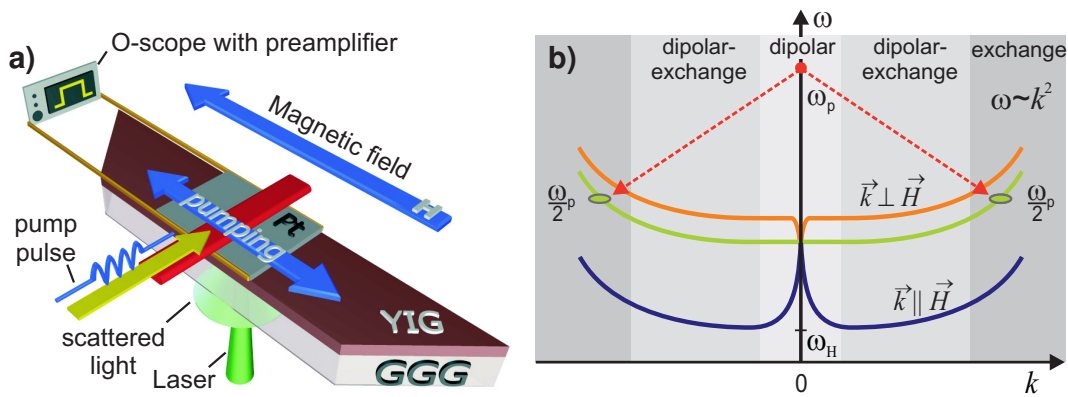


Fig. 1: a) Schematic illustration of the experimental setup. b) The magnon spectrum and the mechanism of the parametric pumping process.

In this Report we present spin pumping by exchange magnons and its detection by the ISHE voltage. These magnons were pumped into the magnon system in a parallel pumping process: by varying the bias magnetic field H and the pumping power P we were able to change the wavenumber

¹In collaboration with Y. Kajiwara and E. Saitoh, Institute for Materials Research, Tohoku University, Sendai 980-8577, Japan.

of the injected magnons and we observe contributions to the spin pumping from different magnon groups. It turned out that exchange magnons have a significant contribution to the spin pumping process.

Figure 1a shows a sketch of the experimental setup. The sample used in the present study comprises a $2.1\mu\text{m}$ thick (111)-single-crystal $\text{Y}_3\text{Fe}_5\text{O}_{12}$ (YIG) film grown on a $\text{Gd}_3\text{Ga}_5\text{O}_{12}$ single-crystal substrate by liquid phase epitaxy. On top, a 10nm thick $3 \times 3\text{mm}^2$ Pt layer is deposited directly onto the YIG film. Two electrodes are directly attached to the Pt pad and wired to a FEMTO DHPVA-200 voltage preamplifier and an oscilloscope in order to detect the electromotive force V_{ISHE} generated by the ISHE. Magnons were pumped by a microwave Oersted field which was guided to a microstrip antenna of $50\mu\text{m}$ width placed on top of the Pt pad transverse to the long side of the YIG stripe. The antenna was insulated from the Pt by a thin non-magnetic dielectric coating of cyan-acrylate. Both parallel and perpendicular (relative to \mathbf{H}) components of the Oersted field contribute to the parametric pumping process [9]. The magnetizing field \mathbf{H} is applied perpendicular to the electron-carried spin current and the ISHE-induced charge current, which are also perpendicular to each other. The spin current propagates into the Pt layer, perpendicular to the film surface [1, 4]. During the experiments, the pumping frequency was held constant at 14GHz and the pumping power was varied. $5\mu\text{s}$ -long microwave pulses with $50\mu\text{s}$ repetition time were applied. At the same time, the bias magnetic field H was varied from -300mT to 300mT in a step size of 5mT .

Figure 1b shows the schematic illustration of the dispersion relation of spin waves in a YIG film and the parallel pumping process. The dispersion relation can be separated in three different parts. The area, where spin waves have long wavelengths and short wavenumbers, is dipolar dominated. In a region from 10^6rad/m to 10^7rad/m the spin waves are influenced by both dipolar and exchange interactions. The third area (above 10^7rad/m) is purely exchange dominated and no dipolar interaction contributes to the dispersion relation ($\omega \propto k^2$).

The parallel pumping process can be described in terms of energy quanta, where a single microwave photon with the frequency ω_p splits into two magnons with $\omega_p/2$ and opposite wavevectors \mathbf{k} and $-\mathbf{k}$. Different magnon groups with the same frequency $\omega_p/2$ are pumped at the same time, but only the one with the lowest damping survives [6]. This magnon group, the dominant group, is characterized by the highest coupling to the pumping field [6, 9]. By variation of the magnetic field at constant pumping frequency, the whole spectrum as shown in Fig. 1b is shifted up or down respectively. Thus, the wavenumber of the excited magnons can be tuned up to the exchange part.

The signal of the electromotive force V_{ISHE} for $P = 8.9\text{W}$ at $H = 275\text{mT}$ is shown in Fig. 2a. On the right hand-side the sketch of the corresponding pumping process demonstrates that $\omega_p/2$ lies below the spin-wave spectrum and no parametric excitation can take place. Despite of this fact, a V_{ISHE} -signal is detected and can be recognized as the longitudinal spin-Seebeck effect which has recently been discovered in magnetic insulators [10]. The longitudinal spin-Seebeck effect is independent of the value of the bias magnetic field H and changes its polarity at $H = 0\text{mT}$. The temperature gradient ∇T is parallel to the magnon-induced spin current perpendicular to the YIG surface. The reason for the presence of this temperature gradient ∇T is the heating of the Pt layer due to eddy currents created by the microwave pumping field. Due to the higher conduction electron temperature in the Pt layer thermal fluctuations are present and lead to an ejection of spins from the Pt into the YIG [10, 11].

At $H = 185\text{mT}$, as shown in Fig. 2b, the situation is different since magnons can be parametrically excited for this magnetic field. The $\omega_p/2$ -frequency lies above the minimum of the magnon

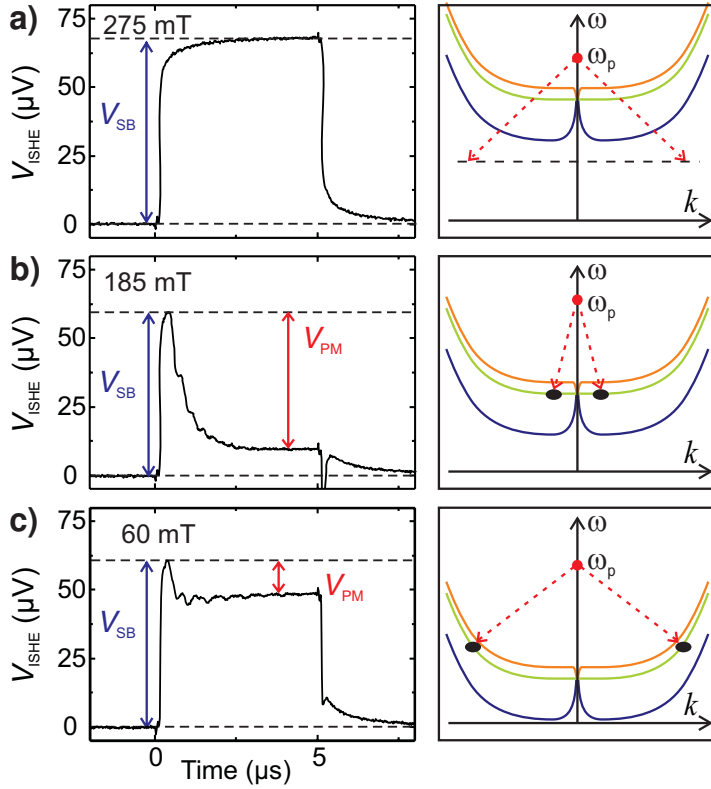


Fig. 2: a)-c) Waveforms of the V_{ISHE} voltage (left panels) and pumping schemes for different magnetizing fields (right panels). Two signals contribute to V_{ISHE} . Firstly, the recently discovered longitudinal spin-Seebeck effect (V_{SB}) [10], which can be understood by an imbalance between an effective magnon temperature in YIG and an effective conduction electron temperature in the attached Pt layer. The second contribution V_{PM} can be attributed to the spin pumping process by parametrically excited magnons.

spectrum ω_H in the dipolar area (see Fig. 1b). The time-profile of V_{ISHE} shows two counteracting contributions which compensate each other partially. The first contribution V_{SB} belongs to the longitudinal spin-Seebeck effect, as in the former case. However, the second contribution V_{PM} can be attributed to the spin pumping by parametrically excited magnons. The polarity of V_{PM} is determined by the direction of the bias magnetic field H . In this process, spins are injected into the Pt layer, while in the case of the longitudinal spin-Seebeck effect, spins are ejected from the Pt layer to the YIG film. Thus, these two effects show different polarities in the signal of the electromotive force V_{ISHE} . It is important to note, that the voltage V_{PM} of the parametrically excited magnons is temporarily retarded since the equilibrium needs time to be established after the pumping pulse is switched on. By subtracting the two contributions to the V_{ISHE} -signal, the pure V_{PM} signal can be extracted (as shown in the inset in Fig. 3b). Figure 2c shows the situation for $H = 60\text{ mT}$, where only magnons in the exchange area are pumped. The corresponding V_{ISHE} -profile shows again the two contributions V_{PM} and V_{SB} to the electromotive force V_{ISHE} , but the contribution of the parametrically pumped magnons is not as prominent as in the dipolar case.

The extracted normalized V_{PM} -signal for each measured magnetic field H from -300 mT to 300 mT is presented in Fig. 3b. The curve is antisymmetric with respect to the field polarity. For small fields, the voltage goes to zero because of the sample demagnetization and the formation of domains. For fields larger than 240 mT , the voltage is zero as $\omega_p/2$ lies below the magnon spectrum and no parametric excitation can take place. The voltage maximum is observed around $H_c = \pm 178\text{ mT}$, where the minima of the parametric pumping threshold lies and the magnon injection is most effective. This field H_c corresponds to the situation when $\omega_p/2$ is in the vicinity of the ferromagnetic resonance frequency. In order to check this, a second experiment has been performed. This time, the spin waves have been excited directly by forced excitation with a microwave frequency $\omega_s = \omega_p/2 = 7\text{ GHz}$ using the same antenna as before and the ISHE voltage was measured. The maxima of both dependencies coincide very well (see Fig. 3b).

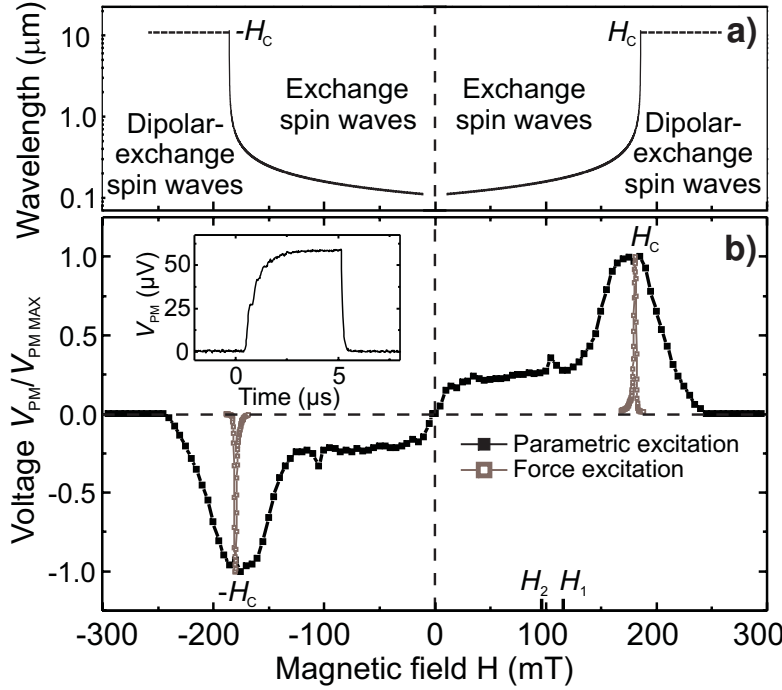


Fig. 3: a) Calculated wavelength of the parametrically injected magnons. b) Spin pumping induced voltage dependencies $V_{PM}(H)$ for parametrically pumped magnons (black filled squares) and force excited magnons (gray empty squares). The inset shows the time profile of the pure signal V_{PM} .

In order to explain the small voltages V_{PM} in the exchange region ($|H| < 130\text{mT}$) in comparison to the dipolar region ($130\text{mT} < |H| < 240\text{mT}$) we need to analyze the spatial localization of the dominant group taking the interface nature of the spin pumping effect into account. The dominant group is characterized by the smallest spin-wave damping, which is mostly determined by two-magnon scattering on impurities and inhomogeneities [6]. The impurities are mainly localized close to the film surface and thus, we can conclude, that the dominant group is located in the center of the YIG film, where the scattering is the smallest. The localization of the magnons depend on their wavelengths and defines the strength of the magnetization precession on the interface. The shorter the wavelength, the higher the localization, and consequently the spin pumping is smaller due to the decreasing of the magnetization precession at the YIG-Pt interface.

Figure 3a shows the calculated magnon wavelengths dependent on the applied bias magnetic field. It is obvious that the curve follows the voltage dependence shown in Fig. 3b quantitatively: while the increase of the field in the region $130\text{mT} < |H| < |H_c|$ results in a increase of the magnon wavelength as well as the observed voltage, the wavelength and the ISHE-voltage does not change much in the exchange region. Thus, the magnon wavelength and localization are of crucial importance for the spin pumping efficiency. A slight increase of the parametric pumping threshold can also partially contribute to the measured voltage decrease in the exchange region. However, for $H > H_c$ the threshold increases rapidly to infinity at $\omega_p/2 = \omega_H$ [6]. This effect determines the voltage fall in the high field region.

ISHE-induced voltage measurements for different pumping powers showed, that an increase of the pump power and consequently an increase of the density of the parametrically excited magnons does not change the qualitative voltage behavior. Only a small increase of the voltage slope in the exchange region was observed. This can be associated with nonlinear damping caused by three-magnon scattering which is allowed for fields smaller than a critical field $H_1 = 115\text{Oe}$ in our case [7, 12]. Small peaks in the ISHE voltage (see Fig. 3b) appear just below this critical field H_1 . They can be associated with the confluence of two parametrically injected magnons. This process occurs for our experimental conditions at a second critical field $H_2 = 97\text{mT}$ [7, 12]. For

one of the confluent magnons is the angular momentum conservation not fulfilled: the angular momentum must be passed to the entire lattice. It may be directly passed to a free electron in the Pt layer what results in an increase of the spin polarization of the electron gas leading to an increase of the ISHE voltage.

In conclusion, we demonstrate that exchange magnons of submicron wavelengths significantly contribute to the spin pumping in magnetic insulator - nonmagnetic metal bilayers. The spin pumping efficiency is mainly defined by localization of the injected magnons relative to the interface. The results may be useful for the understanding of the physics of the spin pumping effect and are of great importance for miniaturization of magnon-based spintronic devices because only short-wavelength exchange magnons allow signal processing on the nanometer scale distance. Furthermore, the results show, that the combination of the spin pumping effect and the ISHE is an effective detection instrument for magnons beyond the wavenumber limitation of most existing methods including Brillouin light scattering spectroscopy.

This work was recently published in Physical Review Letters [13].

Financial support by the DFG within the *SFB/TRR 49*, a Grant-in-Aid MEXT/JSPS, a Grant for Industrial Technology Research from NEDO, and Fundamental Research Grant from TRF, Japan is acknowledged.

References

- [1] Y. Kajiwara, K. Harii, S. Takahashi, J. Ohe, K. Uchida, M. Mizuguchi, H. Umezawa, H. Kawai, K. Ando, K. Takanashi, S. Maekawa, E. Saitoh, *Transmission of electrical signals by spin-wave interconversion in a magnetic insulator*, Nature **464**, 262 (2010).
- [2] S.A. Wolf, D.D. Awschalom, R.A. Buhrman, J.M. Daughton, S. von Molnar, M.L. Roukes, A.Y. Chtchelkanova, D.M. Treger, *Spintronics: A spin-based electronics vision for the future*, Science **294**, 5546 (2001).
- [3] Y. Tserkovnyak, A. Brataas, G.E.W. Bauer, *Enhanced Gilbert damping in thin ferromagnetic films*, Phys. Rev. Lett. **88**, 117601 (2002).
- [4] E. Saitoh, M. Ueda, H. Miyajima, G. Tatara, *Conversion of spin current into charge current at room temperature: inverse spin-Hall effect*, Appl. Phys. Lett. **88**, 182509 (2006).
- [5] A.A. Serga, A.V. Chumak, B. Hillebrands, *YIG Magnonics*, J. Phys. D: Appl. Phys. **43**, 264002 (2010).
- [6] A.G. Gurevich and G.A. Melkov, *Magnetization Oscillations and Waves* (CRC Press, New York, 1996).
- [7] V.S. L'vov and G.E. Fal'kovich, *On the interaction of parametrically excited spin waves with thermal spin wave*, Sov. Phys. JETP **55**, 904 (1982).
- [8] S. Mizukami, Y. Ando, T. Miyazaki, *Effect of spin diffusion on Gilbert damping for a very thin permalloy layer in Cu/permalloy/Cu/Pt films*, Phys. Rev. B **66**, 104413 (2002).
- [9] T. Neumann, A.A. Serga, V.I. Vasyuchka, B. Hillebrands, *Field-induced transition from parallel to perpendicular parametric pumping for a microstrip transducer* Appl. Phys. Lett. **94**, 192502 (2009).
- [10] K. Uchida, T. Ota, H. Adachi, H. Nakayama, S. Maekawa, E. Saitoh, *Observation of longitudinal spin-Seebeck effect in magnetic insulators*, Appl. Phys. Lett. **97**, 172505 (2010).
- [11] J. Xiao, G.E.W. Bauer, K. Uchida, E. Saitoh, S. Maekawa, *Theory of magnon-driven spin Seebeck effect*, Phys. Rev. B **81**, 214418 (2010).
- [12] V.S. L'vov, *Wave Turbulence under Parametric Excitations: Applications to Magnetism* (Springer, Berlin, 1994).
- [13] C.W. Sandweg, Y. Kajiwara, A.V. Chumak, A.A. Serga, V.I. Vasyuchka, M.B. Jungfleisch, E. Saitoh, B. Hillebrands, *Spin pumping by parametrically excited exchange magnons*, Phys. Rev. Lett. **106**, 216601 (2011).

4.7 Spin-wave tunneling through a mechanical gap in a microstructured $\text{Ni}_{81}\text{Fe}_{19}$ -stripe

T. Langner, B. Obry, P. Pirro, T. Brächer, K. Vogt, B. Leven and B. Hillebrands

The investigation of spin waves in microstructured magnetic materials has attracted a lot of interest in recent research. The propagation of spin waves in simple systems like continuous films or stripes is well understood [1]. Spin waves and their quanta, the magnons, are good candidates to develop magnetic logic circuits [2]. Magnonic crystals [3–7] and the propagation through tunnel barriers are examples for building blocks, which selectively transmit a spin-wave signal. Tunnel barriers can be realized either by magnetic barriers using a wire with an electrical current flow [8,9] or simply by a mechanical air gap. The propagation through such a gap has recently been investigated by Kozhanov et al. in CoTaZr [10] and Schneider et al. in YIG [11].

In the work presented here the tunneling of spin waves through a mechanical gap was investigated in microstructured stripes made of $\text{Ni}_{81}\text{Fe}_{19}$ (permalloy). To avoid direct measurements of the electromagnetic leakage the investigations were done by using the microfocus Brillouin light scattering technique [12] allowing for the investigation of the spatial distribution of tunneling spin waves in a microstripe. We present an investigation of spin waves tunneling through a mechanical gap in the MSSW geometry. The focus of this work is on the investigation of the transmission of spin waves through a tunnel barrier with respect to the position of the gap. We will show that quantization effects play an important role in the behavior of tunneled spin waves in microscaled systems.

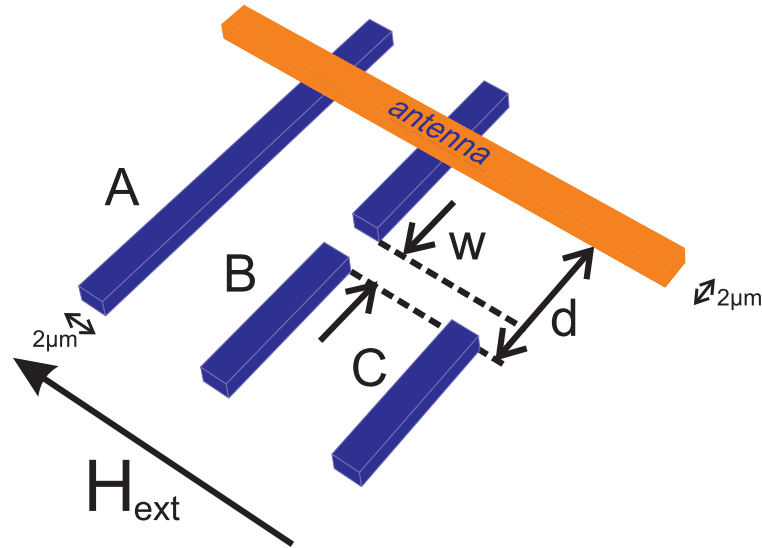


Fig. 1: Schematic design of the sample. The three $\text{Ni}_{81}\text{Fe}_{19}$ -stripes are shown. Stripe A is the reference stripe, B the stripe containing the gap and C the shortened stripe. The width of the gap is marked by w and the distance of the shortened stripe to the antenna is given by d . The excitation antenna made by a copper stripe has a width of $2\mu\text{m}$ and a thickness of 500nm .

The investigated samples consist of groups of three stripes made of $\text{Ni}_{81}\text{Fe}_{19}$, as shown in Fig. 1. All stripes have a width of $2\mu\text{m}$, a thickness of 40nm and a length of $75\mu\text{m}$. Two stripes (A,B) are positioned below the $2\mu\text{m}$ wide shortened end of a coplanar waveguide made of copper. By

applying a microwave current spin waves can be excited that propagate along the long axis of the stripes. A reference signal is measured on a stripe without any modification (A) that has the same orientation to the antenna as the stripe with the gap (B) in the middle of the structure. The gaps in different samples have a width w ranging from 80 nm to 510 nm. They are patterned by using the focused ion beam (FIB) technique. The third stripe (C) is a shortened stripe that is not elongated towards the antenna but begins at a distance d from the antenna where the back edge of the mechanical tunneling gap for stripe B is positioned. This shorter stripe C is used to investigate to which degree the far field of the antenna directly excites any spin wave behind the gap. In addition to the width of the gap w the distance d of the back edge of the gap from the antenna is varied between 2 μm and 3 μm . An external in plane magnetic field can be applied perpendicular to the long axis of the stripes. Hence spin waves propagating along the stripe will have a wavevector \mathbf{k} perpendicular to the magnetization vector \mathbf{M} , which corresponds to the MSSW geometry. In order to excite spin waves with different wavevectors the frequency of the applied microwave current was changed while keeping the external magnetic field constant.

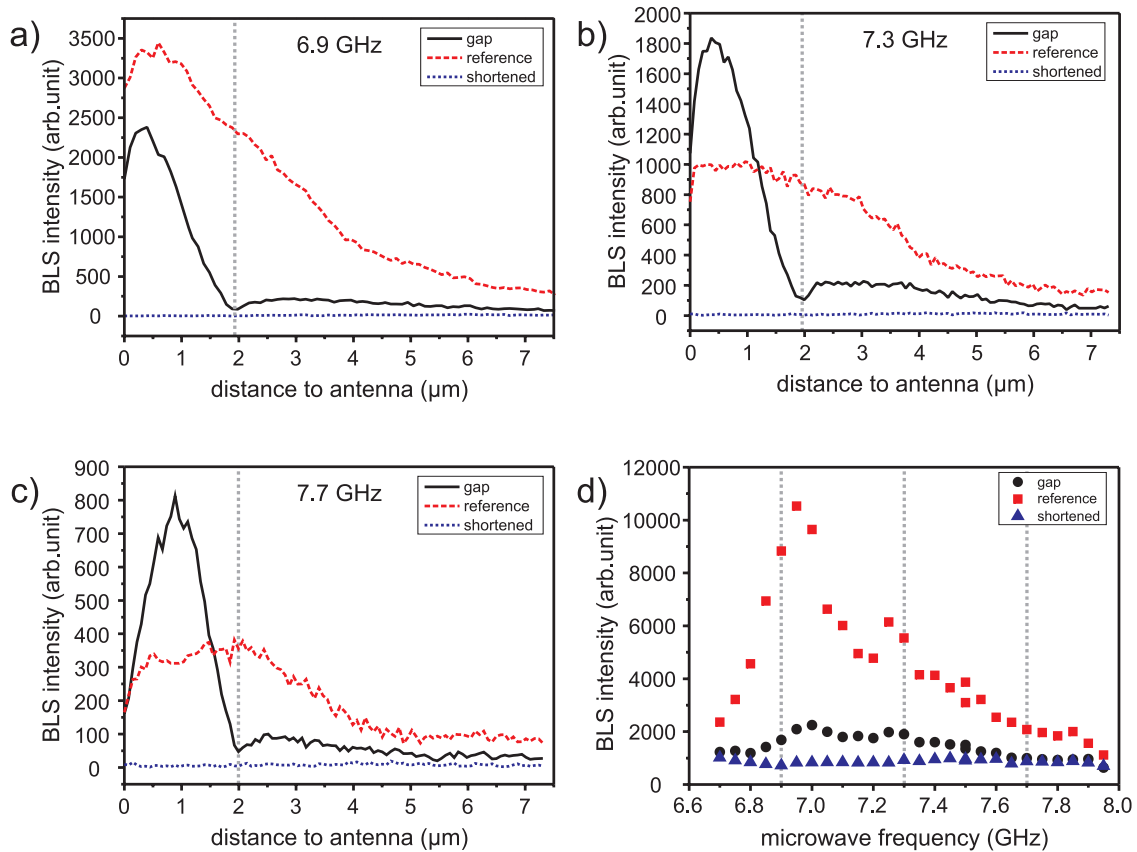


Fig. 2: Space resolved measurements of the BLS intensity along the three stripes for three different microwave frequency values a) 6.9 GHz, b) 7.1 GHz and c) 7.3 GHz. The dashed lines show the position of the gap. The excitation spectra for the three stripes with respect to the microwave frequency are shown in d). The microwave frequencies used in a), b) and c) are marked with dashed vertical lines.

First the spatial distribution of the spin-wave intensities was investigated by scanning along a line in the center of the stripe parallel to the propagation direction on each stripe beginning at the edge of the antenna. For the chosen magnetic field of 65 mT the ferromagnetic resonance can be found close to the microwave frequency 6.9 GHz (see Fig. 2d). Figure 2a shows the dependence of the spin-wave intensity on the distance to the excitation antenna for $w = 80$ nm and $d = 2$ μm

and for an excitation frequency of 6.9 GHz. Being close to the FMR this frequency corresponds to a wavelength that is large compared to the distance from the gap to the antenna. The intensity measured on the reference stripe is higher than the intensity measured on the stripe with the gap at each corresponding position. At the position of the gap the intensity is minimal. When increasing the microwave frequency to excite spin waves with a shorter wavelength (see fig. 2b,c) the intensity of the signal between the antenna and the gap is significantly higher on the stripe with the gap (B) than the reference signal (A) at the corresponding position. The signal on the shortened stripe (C) is only at noise level. The results show that the area between the antenna and the gap acts like a resonator for spin waves. If the wavelength is larger than twice the distance between the antenna and the gap it is hardly possible to excite magnons inside this resonator. The observed signal is merely to be seen as non-resonant excitation of spin waves by the antenna. If the wavelength is comparable to twice the resonator length, the excitation efficiency becomes higher and a standing spin wave is formed inside the resonator. This standing spin wave is a result of the constructive interference of the propagating spin waves excited by the antenna and the spin waves partially reflected from the gap. The excitation of standing spin waves can be seen by the fact that for higher microwave frequencies the maximum of the spin-wave excitation moves to the center between antenna and gap. At a frequency of 7.86 GHz the wavelength of the spin wave is exactly twice the length of the resonator in that case.

The transmission properties of spin waves through a mechanical gap are now investigated as follows: The spin-wave intensity on each stripe was measured under the same conditions on the corresponding position of each stripe by scanning along the short axis of all stripes. By summarizing over the whole width of the stripe the influence of the superposition of different transversal spin-wave excitation modes [13] can be neglected. The measurements are done at about $2\mu\text{m}$ behind the gap. This distance was chosen to avoid the influence of pinning effects which might occur at the gap edges. The transmission of the spin wave through the air gap is given by the ratio of the intensity measured on the stripe with the gap I_g (B) and the one measured on the reference stripe I_r (A). The noise intensity that can be measured on the shortened stripe I_0 (C) as mentioned above is subtracted from both other measured intensities. Finally the transmission T can then be defined as

$$T = \frac{I_g - I_0}{I_r - I_0}. \quad (1)$$

Transmission spectra using Eq. (1) are shown in Fig. 3. The transmission is given as a function of the spin-wave wavevector, which can be calculated from the applied microwave frequency using the theoretical dispersion relation [14] for an effective magnetic field of $\mu_0 H_{\text{eff}} = 63.6\text{ mT}$, a thickness of 40 nm , a saturation magnetization $M_s = 720\text{ kA/m}$, an effective width of the stripe of $w_{\text{eff}} = 1.95\mu\text{m}$, a gyromagnetic ratio of $\gamma = 176\text{ GHz/T}$ and an exchange constant of $A = 1.6 \cdot 10^{-11}\text{ J/m}$. The typical transmission spectrum shows a very low value for small wavevectors, that means close to the ferromagnetic resonance. The transmission calculated with Eq. (1) increases up to a maximum at a wavevector of about $0.8\mu\text{m}^{-1}$ and starts to decrease afterwards. These results are in conflict to those measured in [11] for a YIG system with sizes in the range of several millimeters. As already mentioned above the area between the antenna and the gap can be seen as a spin-wave resonator. For small wavevector values according to wavelengths larger than twice the length of the resonator the excitation efficiency inside this resonator is very low. If the wavelength is exactly twice the length of the resonator the excitation efficiency for spin waves on the stripe with the gap is maximal. But in this case the magnetic moments at the edges of the resonator have zero precession amplitude suppressing the transmission through the gap. The points corresponding to this wavelength can be identified in the transmission spectra in Fig. 3 and are marked by a dashed

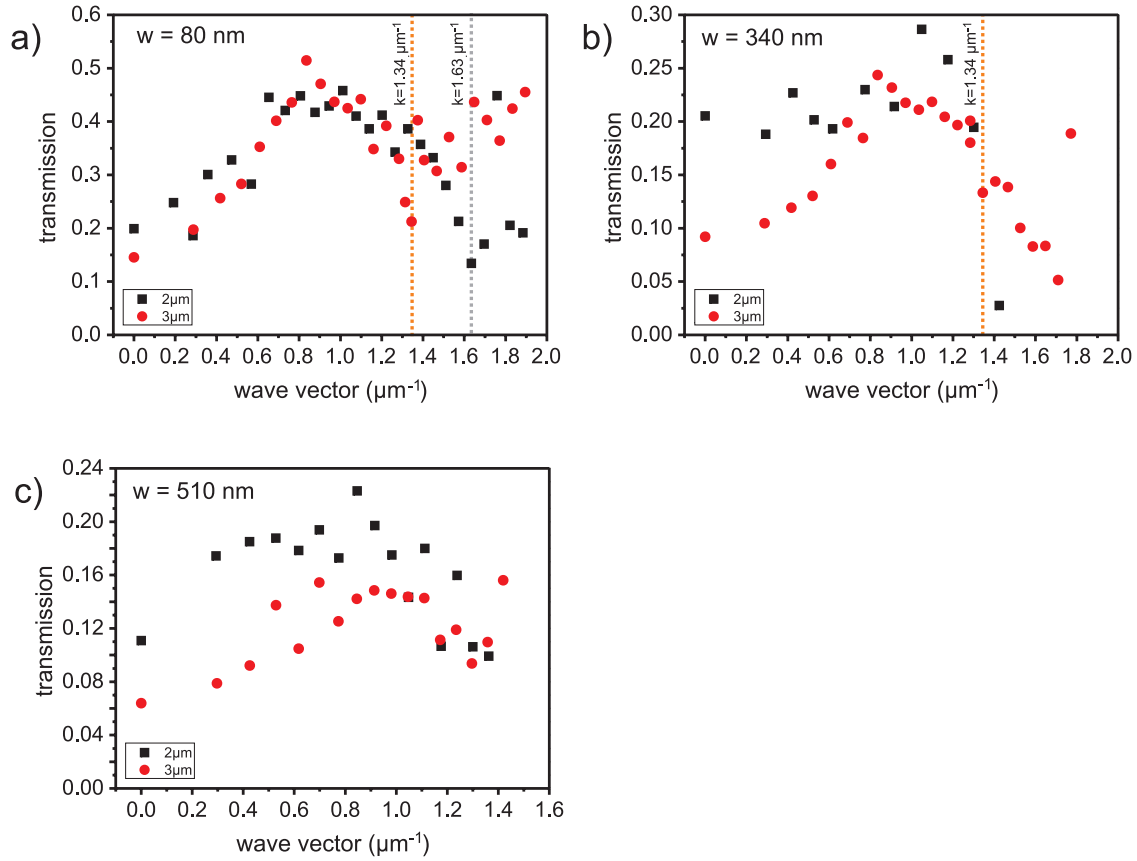


Fig. 3: Transmission spectra for different nominal gap widths a) $w = 80 \text{ nm}$, b) $w = 340 \text{ nm}$, c) $w = 510 \text{ nm}$. The squares are the transmission values for $d = 2 \mu\text{m}$, the circles for $d = 3 \mu\text{m}$. The dashed lines show the wavevector whose corresponding wavelength is twice the resonator length as mentioned in the text.

vertical line. The best transmission can be found when the wavelength is close to twice the resonator length, but long enough not to have strong pinning effects. For large wavevector values the transmission efficiency decreases as for shorter wavelengths magnetic dynamic dipole moments with opposite sign are closer to each other and extenuate each other. There is less excitation of magnetic moments behind the gap.

In this work the tunneling of spin waves through a mechanical gap in permalloy has been investigated. It has been shown that in microstructured systems quantization effects play an important role in the properties of tunneling spin waves. Those quantization effects make a comparison to previous measurements in macroscopic systems difficult. However these effects are of high importance for the development of micro-sized logic elements.

Acknowledgement Preparation of the samples was done by P. Pirro, T. Brächer and Dr. P.A. Beck in collaboration with the Nano+Bio Center (NBC) of Technische Universität Kaiserslautern and the Institut für Oberflächen- und Schichtanalytik (IFOS).

References

- [1] K. Vogt, H. Schultheiss, S.J. Hermsdoerfer, P. Pirro, A.A. Serga, B. Hillebrands, *All-optical detection of phase fronts of propagating spin waves in a $\text{Ni}_{81}\text{Fe}_{19}$ microstripe*, Appl. Phys. Lett. **95**, 182508 (2009).
- [2] A.A. Serga, A.V. Chumak, B. Hillebrands *YIG magnonics*, J. Phys. D **43**, 264002 (2010).

-
- [3] A.V. Chumak, A.A. Serga, S. Wolff, B. Hillebrands, M.P. Kostylev, *Design and optimization of one-dimensional ferrite-film based magnonic crystals*, J. Appl. Phys. **105**, 083906 (2009).
 - [4] A.V. Chumak, T. Neumann, A.A. Serga, B. Hillebrands, M.P. Kostylev, *A current-controlled, dynamic magnonic crystal*, J. Phys. D **42**, 205005 (2009).
 - [5] A.V. Chumak, P. Pirro, A.A. Serga, M.P. Kostylev, R.L. Stamps, H. Schultheiss, K. Vogt, S.J. Hermsdoerfer, B. Laegel, P.A. Beck, B. Hillebrands, *Spin-wave propagation in a microstructured magnonic crystal*, Appl. Phys. Lett. **95**, 262508 (2009).
 - [6] G. Gubbiotti, S. Tacchi, M. Madami, G. Carlotti, A.O. Adeyeye, M. Kostylev *Brillouin light scattering studies of planar metallic magnonic crystals*, J. Phys. D **43**, 264003 (2010).
 - [7] Z.K. Wang, V.L. Zhang, H.S. Lim, S.C. Ng, M.H. Kuok, S. Jain, A.O. Adeyeye, *Observation of frequency band gaps in a one-dimensional nanostructured magnonic crystal*, Appl. Phys. Lett. **94**, 083112 (2009).
 - [8] S.O. Demokritov, A.A. Serga, A. André, V.E. Demidov, M.P. Kostylev, B. Hillebrands, A.N. Slavin, *Tunneling of dipolar spin waves through a region of inhomogeneous magnetic field*, Phys. Rev. Lett. **93**, 047201 (2004).
 - [9] A.A. Serga, T. Neumann, A.V. Chumak, B. Hillebrands, *Generation of spin-wave pulse trains by current-controlled magnetic mirrors*, Appl. Phys. Lett. **94**, 112501 (2009).
 - [10] A. Kozhanov, D. Oulette, M. Rodwell, S.J. Allen, A.P. Jacob, D.W. Lee, S.X. Wang, *Dispersion and spin wave “tunneling” in nanostructured magnetostatic spin waveguides*, J. Appl. Phys. **105**, 07D311 (2009).
 - [11] T. Schneider, A.A. Serga, A.V. Chumak, B. Hillebrands, R.L. Stamps, M.P. Kostylev, *Spin-wave tunneling through a mechanical gap*, Europhys. Lett. **90**, 27003 (2010).
 - [12] S.O. Demokritov, V.E. Demidov, *Micro-Brillouin light scattering spectroscopy of magnetic nanostructures*, IEEE Trans. Magn. **44**, 6 (2008).
 - [13] T. Brächer, P. Pirro, B. Obry, B. Leven, A.A. Serga, and B. Hillebrands, *Mode selective parametric excitation of spin waves in a $\text{Ni}_{81}\text{Fe}_{19}$ microstripe*, Appl. Phys. Lett. **99**, 162501 (2011).
 - [14] B.A. Kalinikos, A.N. Slavin, *Theory of dipole-exchange spin wave spectrum for ferromagnetic films with mixed exchange boundary conditions*, J. Phys.: Condens. Matter **19**, 7013 (1986).

C. Magnonic Crystals

A magnonic crystal is a wave transmission medium which features an artificial lattice created by a wavelength-scale modulation in its material properties. Such systems belong to the class of so-called meta-materials: synthetic media with properties derived from an engineered, mesoscopic (rather than atomic-scale or molecular) structure. The wave transmission spectra of artificial crystals typically include band gaps: frequency intervals over which propagation is prohibited.

The simplest type of a magnonic crystal is a one-dimensional diffraction grating created in a spin-wave waveguide by modulating periodically the internal magnetic field along the propagation direction. The waveguide typically has the form of a thin and narrow strip of a magnetically ordered material. When the spin wave is channeled along the main axis of such a waveguide, this grating behaves like a one-dimensional magnonic crystal. Report 4.8 is devoted to this kind of artificial crystal. It is made of a single crystalline ferrimagnetic yttrium-iron-garnet (YIG) waveguide. The internal magnetic field is modulated using a dynamically controlled Oersted field of the electric current flowing near the YIG film surface in meander-type fashion. In the previous Annual Report 2010 we have shown that time reversal and frequency inversion can be realized using such a dynamic magnonic crystal. In this Report we study the effect of counter-propagating waves coupled by the crystal and the oscillatory energy exchange between these coupled waves. As well as representing a fundamental development in the understanding of wave dynamics in meta-material systems, the studied effect potentially might find a technological application in the context of signal processing. The dipole-exchange theory of the studied dynamic magnonic crystal is shown in Report 4.10.

The possibility to control the number and characteristics of the rejection bands of a magnonic crystal is discussed in Reports 4.9 and 4.10. It is suggested to control them via a tuning of the function describing the variation of the magnetic properties: spin-wave waveguide width modulation (Report 4.9) and the magnetic field (Report 4.10). A permalloy-based planar magnonic crystal studied by means of micromagnetic simulations is especially interesting due to the micron size of the structure. The influence of the demagnetizing field and waveguide width variations, as well as of the probing point position on the band-gaps characteristics are studied in Report 4.9. Besides, both Reports point out the potential to design single band-gap magnonic crystals using a sinusoidal variation of the magnetic properties and multi-band magnonic crystals using a meander-like variation of the biasing magnetic field or the waveguide width.

C. Magnonische Kristalle

Magnonische Kristalle sind Wellenleiterstrukturen, die eine periodische Modulation ihrer Materialeigenschaften aufweisen, wobei die Periodizitätslängen in der Größenordnung der Wellenlängen der propagierenden Wellen liegen. Solche Systeme, wie auch die eng verwandten photonischen Kristalle, gehören zur Klasse der sogenannten Metamaterialien: künstliche Materialien mit Eigenschaften, die von einer gezielt entworfenen mesoskopischen Struktur hervorgerufen werden. Die Transmissionsspektren dieser künstlichen Kristalle weisen typischerweise Bandlücken auf, also Frequenz-Bereiche, in denen die Wellenpropagation unterdrückt ist.

Der einfachste Typ eines magnonischen Kristalls ist ein eindimensionales Beugungsgitter, das durch die periodische Änderung des effektiven Feldes in Propagationsrichtung der Spinwellen in einem Wellenleiter erzeugt wird. Ein solcher Wellenleiter hat in der Regel die Form eines dün-

nen, schmalen Streifens aus einem magnetisch geordneten Material. Bei Propagation einer Spinwelle entlang des Wellenleiters fungiert dieses Gitter als eindimensionaler magnonischer Kristall. Bericht 4.8 widmet sich dieser Art eines magnonischen Kristalls. Er wird von einem monokristallinen ferrimagnetischen Yttrium-Eisen-Granat (YIG)-Wellenleiter gebildet. Die Modulation des effektiven Feldes wird durch dynamisch veränderliche Oersted-Felder erzeugt, welche durch mäanderförmige elektrische Ströme nahe der Oberfläche des YIG Filmes hervorgerufen werden. Im Jahresbericht 2010 haben wir bereits gezeigt, dass Zeitumkehr sowie Frequenzinversion mit Hilfe einer solchen Struktur realisiert werden können. Im vorliegenden Beitrag untersuchen wir die durch einen magnonischen Kristall vermittelte Kopplung zweier entgegengesetzt propagierender Wellen und den damit verbundenen Energiefluss zwischen ihnen. Neben der Vertiefung des grundlegenden Verständnisses der Wellenpropagation in Metamaterialien sind die Ergebnisse dieser Studie sehr interessant im Hinblick auf technische Anwendungen im Gebiet der Signalverarbeitung. Die Beschreibung des untersuchten dynamischen magnonischen Kristalls im Rahmen einer Dipol-Austausch-Theorie wird in Beitrag 4.10 präsentiert. Mit Hilfe dieser Arbeit können die Eigenschaften der Bandlücke in magnonischen Kristallen, die auf der Modulation des externen Feldes beruhen, nun präziser beschrieben werden.

Die Möglichkeit, Eigenschaften und Anzahl der Bandlücken in einem magnonischen Kristallen zu kontrollieren, wird in den Beiträgen 4.9 und 4.10 diskutiert. Hier wird vorgeschlagen, diese Kontrolle durch periodische Variation der Breite des Spinwellen-Wellenleiters (Bericht 4.9) und des Magnetfeldes (Bericht 4.10) zu realisieren. Ein auf Permalloy basierender, planarer magnonischer Kristall, der im zweiten Fall mittels mikromagnetischer Simulation untersucht wurde, ist aufgrund der Strukturgröße im Mikrometer-Bereich von besonderem Interesse. In diesem Beitrag wird der Einfluss diskutiert, den das Entmagnetisierungsfeld sowie die Variation der Breite des Wellenleiters an verschiedenen Positionen auf der Struktur hervorrufen. Zudem zeigen beide Artikel Möglichkeiten auf, magnonische Kristalle mit nur einer einzigen Bandlücke - mittels einer sinusförmigen Veränderung relevanter Eigenschaften - sowie Kristalle mit mehreren Bandlücken - mittels mäanderförmiger Änderungen des externen Feldes oder der Wellenleiter-Geometrie - zu realisieren.

4.8 Oscillatory energy exchange in a dynamic magnonic crystal

A.V. Chumak, A.A. Serga, and B. Hillebrands¹

Originally, the study of artificial crystals was directed exclusively toward time-invariant structures. However, considerable attention is now focussed on an emerging class of dynamic artificial crystals [1–8] which have properties that can be modified whilst waves propagate through them. Particularly interesting is a subset of dynamic artificial crystals which has a lattice that can be turned “on” and “off”. Recently, we used an experimental dynamic magnonic crystal (DMC) to demonstrate that if such a crystal undergoes a rapid transition from “off” to “on” whilst a wave mode lying within the band gap is excited inside it, this mode becomes coupled to a secondary counter-propagating wave, generally of a different frequency [8]. Here, we report on findings that the underlying physics of this coupling mechanism reveals a fundamental result of general wave dynamics. It is shown that the process is one of oscillatory inter-modal energy exchange which can be described by modeling the waves as interacting harmonic oscillators.

Figure 1a shows the experimental spin-wave system. Our one-dimensional DMC comprises a planar metallic meander structure (period $a = 300\text{ }\mu\text{m}$) situated close to the surface of an yttrium iron garnet (YIG) thin-film spin-wave waveguide [6, 9]. An antenna is positioned at each end, and a static bias magnetic field $B_0 = 180\text{ mT}$ is applied along the spin-wave propagation direction. In the absence of a current in the meander structure, the transmission characteristics and spin-wave dispersion relationship $\omega(k)$ for the system are as shown by the dotted lines in Figs. 1c and 1d, and the DMC is “off” (note that we consider positive values of k to correspond to waves propagating from the input antenna to the output antenna). If a current $I_0(t)$ is applied to the meander structure the magnetic field it creates spatially modulates the waveguide’s magnetic bias (Fig. 1b). Under these conditions, the DMC is “on” and has a band gap corresponding to the wavevectors $\pm k_a = \pm\pi/a = \pm 105\text{ rad}\cdot\text{cm}^{-1}$ which appears as a discontinuity in the spin-wave dispersion relationship centered on the resonance frequency $\omega(\pm k_a) = \omega_a = 2\pi \cdot 6.5\text{ GHz}$ (solid lines, Fig. 1d) [10] and creates a valley in the transmission characteristic (solid line, Fig. 1c). The band-gap width is determined by ΔB_0 .

If a spin wave with wavevector $k_s \approx +k_a = +\pi/a$ is incident on the crystal whilst it is in the “on” state, it is simply reflected (Fig. 1c). However, if the crystal is switched from “off” to “on” whilst such a wave is inside, a coupling between the incident mode and secondary modes with wavevectors $k_r = k_s \pm 2k_a$ is brought about. This coupling is pronounced when the eigenfrequencies of the waves $\omega_s = \omega(k_s)$ and $\omega_r = \omega(k_r)$ are similar, i.e. for $k_s \approx k_a$ and thus counter-propagating waves $k_r = k_s - 2k_a \approx -k_a$. The dynamics of the complex amplitudes c_s and c_r of the two interacting waves can be modeled by a pair of coupled equations

$$\frac{dc_s}{dt} = i\omega_s c_s + i\Omega_a c_r \quad , \quad (1\text{-a})$$

$$\frac{dc_r}{dt} = i\omega_r c_r + i\Omega_a c_s \quad . \quad (1\text{-b})$$

¹In collaboration with A.D. Karenowska, Department of Physics, Clarendon Laboratory, University of Oxford, OX1 3PU Oxford, United Kingdom; V.S. Tiberkevich, A.N. Slavin Department of Physics, Oakland University, Rochester, USA

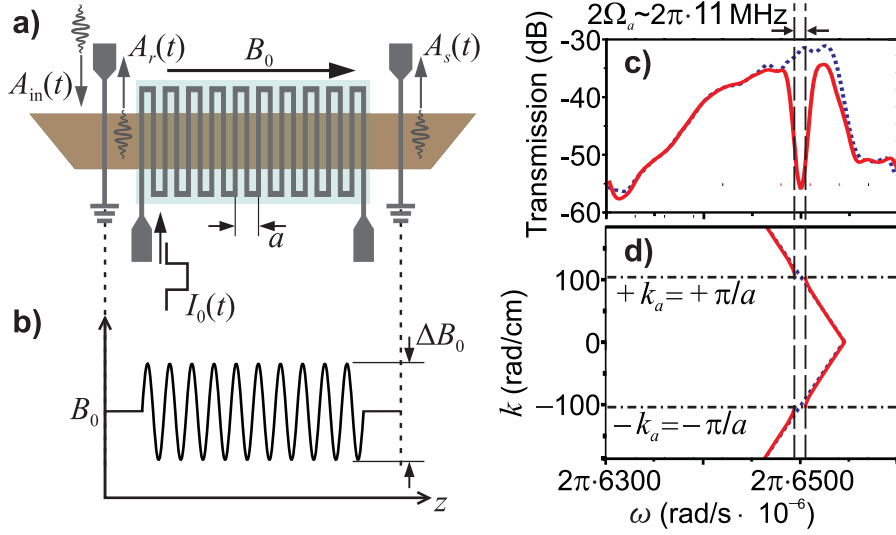


Fig. 1: a) The dynamic magnonic crystal (DMC) comprises a metallic meander structure with 20 periods of lattice constant a (10 shown) situated close to the surface of a spin-wave waveguide. Microstrip input and output antennas are arranged on the surface of the film and a bias magnetic field B_0 is applied along the spin-wave propagation direction. b) When a current $I_0(t)$ is applied to the meander structure, the magnetic field it creates (amplitude ΔB_0) spatially modulates the waveguide's magnetic bias and the DMC is "on". c) Spin-wave transmission characteristics with the DMC "off" (dotted) and "on" ($I_0 = 1$ A, solid) d) Calculated spin-wave dispersion relationship for the "off" (dotted) and "on" ($I_0 = 1$ A, solid) states of the DMC system.

where Ω_a is the coupling constant (with units of angular frequency), numerically equal to the half-width of the crystal band gap. Oscillatory solutions to Eqs. (1-a) and (1-b) have frequencies

$$\omega_{1,2} = \bar{\omega} \pm \sqrt{\Omega_a^2 + \delta\omega^2} = \bar{\omega} \pm \Omega \quad , \quad (2)$$

where $\bar{\omega} = (\omega_s + \omega_r)/2$ is the average eigenfrequency of the waves, and $\delta\omega = (\omega_s - \omega_r)/2$ is their frequency mismatch. Equation (2) describes the dispersion relation for a static magnonic crystal in the "on" state with a band gap of width $2\Omega_a$ centered on $\omega_s = \omega_r = \omega_a$ (see Fig. 1d).

In a dynamic experiment, at the moment when the crystal is switched "on" ($t = 0$) the amplitude of the incident wave takes a maximum value ($c_s = 1$), whilst the coupled secondary wave is absent ($c_r = 0$). Solving Eqs. (1-a) and (1-b) with these initial conditions, one can find how the power $P_{s,r} = |c_{s,r}|^2$ of each wave changes with time:

$$P_s(t) = \cos^2(\Omega t) + \frac{\delta\omega^2}{\Omega^2} \sin^2(\Omega t) \quad , \quad (3-a)$$

$$P_r(t) = \frac{\Omega_a^2}{\Omega^2} \sin^2(\Omega t) \quad . \quad (3-b)$$

The equations above describe periodic energy exchange at frequency Ω (see Eq. (2)) between confined incident (k_s) and secondary (k_r) modes. The maximum power fraction transferred to the k_r mode is close to unity for waves within the band gap and is achieved after a characteristic energy exchange time

$$T = \frac{\pi}{2\Omega} = \frac{\pi}{2\sqrt{\Omega_a^2 + \delta\omega^2}} \quad , \quad (4)$$

or odd integer multiples thereof (see Fig. 2a). If the dynamic crystal is switched "off" at $t = \tau$, eliminating the coupling, the waves, which have powers given by the instantaneous solutions of

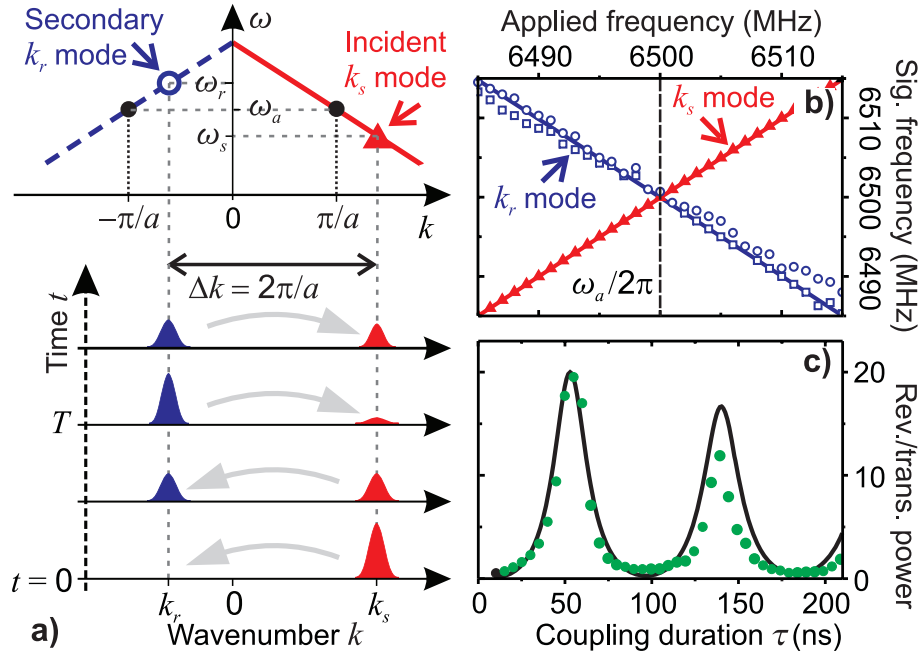


Fig. 2: (a) If the DMC is switched “on” at $t = 0$ whilst an incident mode $k_s \approx +k_a$, frequency ω_s (triangle) is inside, this mode is coupled to a secondary mode $k_r = k_s - 2k_a$, frequency ω_r (open circle). The heights of the peaks in the lower panel represent the power in the incident (k_s , red) and secondary modes (k_r , blue). Almost complete energy exchange occurs every T seconds for as long as the coupling persists. (b) Reversed (k_r , open symbols) and transmitted (k_s , triangles) signal frequencies as a function of the applied spin-wave carrier frequency. Reversed signal data is shown for $\tau = 25$ ns (circles) and $\tau = 20$ ns (squares). Transmitted signal datapoints for both values of τ are represented by a single triangular symbol. Solid lines show the theory of Eq. 6. (c) Ratio of reversed to transmitted signal powers as a function of τ for $\omega_s = \omega_r = \omega_a$; circular symbols are experimental datapoints, the solid line shows the theory.

Eqs. (3-a) and (3-b) travel in opposite directions. Experimentally, the oscillatory energy exchange process may be studied by recovering the ratio of the powers of these waves:

$$\kappa(\tau) = \frac{P_r(\tau)}{P_s(\tau)} = \frac{\Omega_a^2 \tan^2(\Omega\tau)}{\Omega^2 + \delta\omega^2 \tan^2(\Omega\tau)} \quad , \quad (5)$$

which is independent (up to a constant factor) of their damping. Since this process is efficient only over a narrow range of wavevectors $k_s \approx k_a$, the dispersion relation can be approximated using Taylor expansions: $\omega_s = \omega(k_s) = \omega_a + v_g(k_s - k_a)$, $\omega_r = \omega(k_r) = \omega_a - v_g(k_r + k_a)$, where $v_g = d\omega(k)/dk$ is the spin-wave group velocity at $k = k_a$, and we assume a symmetric dispersion law $\omega(k) = \omega(-k)$:

$$\omega_r = 2\omega_a - \omega_s \quad , \quad (6)$$

i.e. the detuning of the incident and secondary mode frequencies is inverted about ω_a .

Experimental investigations into the geometrical mode coupling mechanism were undertaken using a current pulse $I_0(t)$ of duration τ to briefly switch the DMC “on” whilst an incident spin-wave signal packet of center frequency ω_s and duration 200 ns excited by a signal (A_{in} , Fig. 1a) was contained within it. When the DMC is switched “on” ($t = 0$), transfer of energy from the incident k_s mode into the secondary k_r mode initiates (see Fig. 2a), both modes being confined to the crystal. At $t = \tau$ when the coupling is deactivated, the k_s mode propagates to the output antenna, producing a transmitted signal of power $A_s \propto P_s(\tau)$, whilst the k_r mode travels to the input antenna, originating a “reversed” signal of power $A_r \propto P_r(\tau)$ (see Fig. 1a).

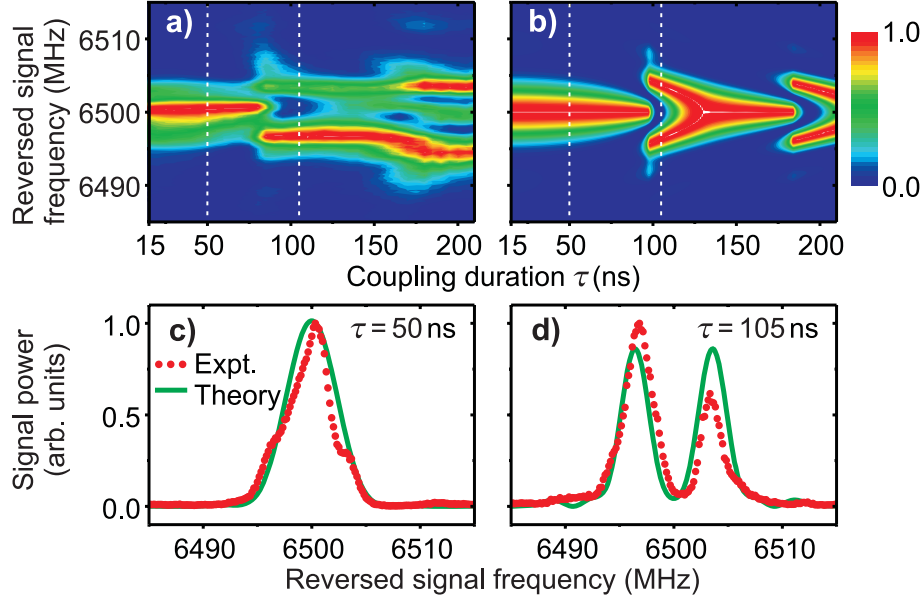


Fig. 3: a) Reversed ($A_r \propto P_r(\tau)$, Fig. 1a) signal spectra for varying τ (input spin-wave signal duration 150 ns, carrier frequency $\omega_s = \omega_a = 2\pi \cdot 6.5$ GHz). Each spectrum is individually normalized to compensate for damping. b) Theoretical calculation of the data of (a) using experimentally derived parameters. Panels c) and d) show sections of the experimental data of a) (circular symbols) and b) (solid curves) at $\tau = 50$ ns and $\tau = 105$ ns respectively (vertical dashed lines in a) and b)).

Measured frequencies of the transmitted (k_s) and reversed (k_r) signals are plotted in Fig. 2b for two values of the coupling duration τ . The frequency of the transmitted signal remains unchanged after interaction with the crystal. The reversed frequency, as predicted by Eq. (6), is determined solely by the geometry of the DMC and is independent of τ . The data are a near-perfect fit to the theory (solid lines on the same axes), providing strong evidence for its validity. Figure 2c shows experimentally measured ratios of reversed (P_r) to transmitted signals (P_s) (circular symbols) for the resonance case $\omega_s = \omega_r = \omega_a$ and the corresponding theory ($\kappa = P_r/P_s$, solid line). The theoretical curve assumes $\Omega_a = 2\pi \cdot 5.53$ MHz, a small detuning $\delta\omega = 0.03\%$, and an effective coupling duration $\tau_{\text{eff}} = \tau - 2\Delta\tau$ where $2\Delta\tau = 12.5$ ns to account for the effect of the finite rise and fall times of the DMC current pulse. The plot is also scaled to match the experimental and theoretical maximum ratios. The difference in heights of the two peaks in Fig. 2c is due to the finite spectral width of the input signal (the total power of the reversed signal is the integral of Eq. (3-b) over all frequency components of the input signal). The value of the coupling constant $\Omega_a = 2\pi \cdot 5.53$ MHz derived from the dynamic experiments corresponds to the -20 dB width of the static DMC band gap (i.e. the width of the gap measured -20 dB down on the spin-wave transmission through the system with the DMC “off”). This is consistent with the fact that the coupling mechanism requires strong rejection of waves from the crystal.

For a fixed incident mode power, Eqs. (3-a) and (3-b) predict that the frequency dependence of the secondary mode power varies with the coupling duration τ . In order to observe this dependence experimentally, the power spectrum of the reversed signal ($A_r(t)$, Fig. 1a) produced from an input spin-wave packet of duration 150 ns and carrier frequency $\omega_s = \omega_a = 2\pi \cdot 6.5$ GHz was recovered for varying τ . Results are plotted in Fig. 3a. Figure 3b shows the corresponding theory. As can be seen, the theory accurately predicts the key features of the data. Figures 3c and 3d are sections through the data of Figs. 3a (circular symbols) and 3b (solid curves) at $\tau = 50$ and 105 ns, respectively. The deviation between theory and experiment at long coupling times in Figs. 3a and

3b occurs as a result of leakage of energy from the DMC during the coupling interval; an inevitable feature of any experiment using an artificial crystal of finite length.

In summary, we have described—and demonstrated using spin waves—a mode coupling phenomenon in a dynamic artificial crystal. The mechanism, which is a principle of application to waves of any nature, involves oscillatory energy exchange between two counter-propagating wave modes, generally of different frequencies. The repeated spontaneous reversal of energy flow direction which characterizes the effect distinguishes it from all other known methods of inter-modal energy transfer in wave systems (see for example [9, 10]). As well as representing an interesting development in the understanding of wave dynamics in metamaterial systems, the effect potentially finds widespread technological application in the context of magnon spintronic signal processing.

This work has been accepted for publication in Physical Review Letters.

Financial support from the Deutsche Forschungsgemeinschaft (Grant No. SE 1771/2), from the *ECCS* and *DMR* Programs of the USA National Science Foundation, and from the Defense Advanced Research Projects Agency (DARPA) is gratefully acknowledged. A.D.K. is grateful for the support of Magdalen College, Oxford.

References

- [1] Y. Tanaka, J. Upham, T. Nagashima, T. Sugiya, T. Asano, S. Noda, *Dynamic control of the Q factor in a photonic crystal nanocavity*, Nature Mater. **6**, 862 (2007).
- [2] J. Bravo-Abad, M. Soljačić, *Photonic crystals go dynamic*, Nature Mater. **6**, 799 (2007).
- [3] S. Longhi, *Stopping and time reversal of light in dynamic photonic structures via Bloch oscillations*, Phys. Rev. E **75**, 026606 (2007).
- [4] E.J. Reed, M. Soljačić, J.D. Joannopoulos, *Color of shock waves in photonic crystals*, Phys. Rev. Lett. **90**, 203904 (2003).
- [5] A. Khorshidahmad and A.G. Kirk, *Wavelength conversion by interband transition in a double heterostructure photonic crystal cavity*, Opt. Lett. **34**, 3035 (2009).
- [6] A.V. Chumak, T. Neumann, A.A. Serga, B. Hillebrands, M.P. Kostylev, *A current-controlled, dynamic magnonic crystal*, J. Phys. D **42**, 205005 (2009).
- [7] A.V. Chumak, P. Dhagat, A. Jander, A.A. Serga, B. Hillebrands, *Reverse Doppler effect of magnons with negative group velocity scattered from a moving Bragg grating*, Phys. Rev. B **81**, 140404(R) (2010).
- [8] A.V. Chumak, V.S. Tiberkevich, A.D. Karenowska, A.A. Serga, J.F. Gregg, A.N. Slavin, B. Hillebrands, *All-linear time reversal by a dynamic artificial crystal*, Nature Commun. **1**, 141 (2010).
- [9] A.A. Serga, A.V. Chumak, B. Hillebrands, *YIG magnonics*, J. Phys. D **43**, 264002 (2010).
- [10] D.D. Stancil, *Theory of Magnetostatic Waves* (Springer-Verlag, New York, 1993).

4.9 Magnonic band gap design by the edge modulation of micro-sized waveguides

F. Ciubotaru, A.V. Chumak, A.A. Serga and B. Hillebrands¹

The linear and nonlinear magnetization dynamics in magnonic crystals [1–10] is a motivating topic of investigation due to their potential use in the signal processing in the microwave frequency range [9, 11–14].

Many studies were concentrated on magnonic crystals (MC) based on yttrium-iron-garnet (YIG) ferrite films due to the extremely small spin-wave attenuation in this material [1, 2, 4–6, 10]. In particular, two types of magnonic crystals attracted attention: crystals designed as a spin-wave waveguide of periodically variable thickness and crystals designed as a plane spin-wave waveguide placed in a dynamically controlled modulated magnetic field. The first type (grooves-based crystal) represents probably the easiest and the most efficient design of a one-dimensional magnonic crystal [2, 15]. The second one, the field controlled crystal, allows for a fast dynamic control of the crystal properties [6, 10]. The important difference between these two structures is the function describing the spatial variation of the magnetic properties of the waveguide. In the first case it is a step function (expressing the variation of the thickness with nearly rectangular profile), while the second function (giving the variation of the magnetic field) is practically sinusoidal. Taking into account that the reflection coefficient for a wave with wavenumber k incident on the periodic structure is proportional to the Fourier component of the magnetic inhomogeneity with Fourier wavenumber $2k$ [6], the grooves-based magnonic crystal reveals multiple band gaps (frequency regions where spin waves are not allowed to propagate) while the current controlled crystal reveals a single band gap. Thus, the proper choice of the function describing the variation of the magnetic properties allows us to control the rejection bands characteristics and, in consequence, to control the properties of microwave filters and phase shifters based on MCs. Nevertheless, modern microwave devices require micro-sized patterned elements which are extremely hard to be produced from YIG. Moreover, a possibility to control the band gaps of the planar MCs within micron and submicron sizes is demanded.

Here we present a proposal to control the transmission band gap characteristics of a microstructured Permalloy (Py) magnonic crystal. Using micromagnetic simulations [16] we analyzed and compared the transmission characteristics of two different magnonic crystals realized as spin-wave waveguides with variable width and different edge profiles. In the first case, the MC width is changing abruptly in the form of rectangular notches. This magnonic crystal has been studied experimentally in [14]. In the second case, the width is changing monotonously following a sinusoidal function. We show that substituting the sharp notches with a harmonical variation of the waveguide width one can change the MC operational transmission characteristic from multiple rejection band state to a single band state. The advantage is that both structures are planar and can be integrated on a chip at the same time within a single process allowing for fully identical preparation conditions.

The two types of magnonic crystals under investigation are presented in Fig. 1a and Fig. 1b. The length of the permalloy waveguides is $7.25\mu\text{m}$ and the thickness is 40nm . The variation of the width has a period $\Lambda = 1\mu\text{m}$ with a modulation depth of $0.5\mu\text{m}$. The standard material param-

¹In collaboration with N. Grigoryeva and B. Kalinikos, St. Petersburg Electrotechnical University, Russia.

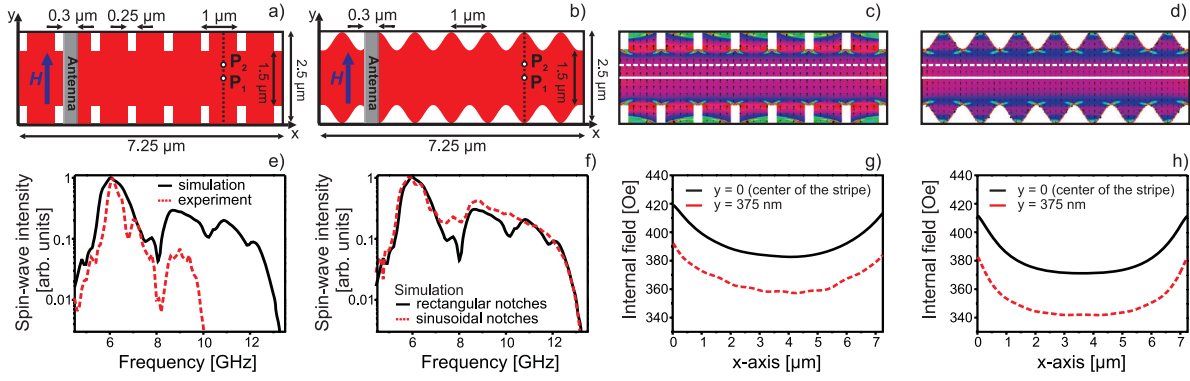


Fig. 1: Sketch of the simulated structures: MCs with rectangular a) and sinusoidal notches b). c) and d) Distribution of the magnetic internal field (H_y component) for the simulated structures. Comparison of spin-wave transmission characteristics extracted from: e) experiment [14] and simulation of MC with rectangular notches and f) simulated structures. g) and h) H_y component of the internal field extracted along the magnetic stripes in the center ($y = 0$, white lines from e) and f)) and at $y = 375$ nm (dashed lines in e) and f)).

eters of Py used to simulate the dynamic of magnetization are: saturation magnetization $\mu_0 M_s = 1$ T, exchange stiffness constant $A = 1.3 \times 10^{-11}$ J/m and zero magnetocrystalline anisotropy was assumed. The damping constant in the Landau-Lifshitz-Gilbert equation was considered $\alpha = 0.01$. Damping boundary conditions were used to avoid spin-wave reflection at the lateral edges of the simulated structure ($x = 0$ and $x = 7.25 \mu\text{m}$). In the boundary area ($\sim 1 \mu\text{m}$ on each side) the damping parameter is gradually increased more than fifty times at the structure edges, thus the spin-wave intensity decays strongly towards the boundaries.

In order to excite spin waves within a wide frequency range we have applied a video pulse (70 ps length) to a 300 nm wide antenna. The frequency cut-off limit given by the pulse duration is ~ 13.5 GHz while the used antenna can excite spin-waves with wavenumbers up to $21 \text{ rad}/\mu\text{m}$. The static magnetic field (500 Oe) has been applied in the film plane transverse to the width in order to satisfy the conditions for the excitation and detection of the magnetostatic surface spin waves (MSSW). We have chosen this type of spin waves and these sizes of the magnonic crystal in order to ensure large spin-wave free paths of order of several microns.

Both the modulation of the internal field and the modulation of the width structure can contribute to the formation of the band gaps. The calculated distributions of the internal field for both MCs configuration are displayed in Fig. 1c and Fig. 1d, respectively. One may observe that the two distributions are similar over a quite large area centered inside the waveguides, practically the spin-wave propagation channel. Furthermore, different cuts of the distribution made along the structure (x -axis) within this area (see Fig. 1g and Fig. 1h) have shown that there is virtually no modulation of the internal field, but a gradual decay towards the edges of the channel. Later we will show how the decay influences the magnonic crystal operational characteristics.

The transmission characteristics extracted from the simulated data at a distance $x = 4 \mu\text{m}$ from the antenna are presented in Fig. 1e and Fig. 1f. In addition, the experimentally measured transmission [14] is shown in Fig. 1e. One can see that the results of numerical simulations of the MC with rectangular notches are in agreement with the experiment taking into account the following: 1) in the experiment the antenna width is equal to $1 \mu\text{m}$ and limits the wavenumbers of the excited spin waves to $k_{\text{max}} = 6.28 \text{ rad}/\mu\text{m}$. This value coincides with the wavenumber of the second rejection band, thus in the experiment the second band gap is absent. Nevertheless, the results of the simulations clearly show the existence of the second band gap. 2) The depth, width and the

slight shift of the first rejection band was recorded in the experiment after 8 structure periods while in the simulation after 4 periods.

If we compare now the transmission characteristics extracted from both simulated structures (see Fig. 1f) one sees that the second band gap does not exist for the sinusoidal magnonic crystal. Moreover, the band gap is not so pronounced for the sinusoidal structures. Since there is no true modulation of the internal field, the width variation is mainly responsible for the formation of the band gaps via the modulation of the spin-wave transversal wavevector. We can express the variation of the width in terms of wavenumbers as follows. Generally, the total wavevector of the propagating wave is given by: $|\vec{k}| = k_L^2 + k_W^2 + k_T^2$, in which k_L represents the longitudinal wavevector, $k_W = (n\pi/w)$ and $k_T = (m\pi/t)$ are the transverse quantized wavenumbers due to the finite width (w) and finite thickness (t), respectively. The integer parameters n and m represent the width and the thickness mode numbers. In our case $k_T = 0$ due to the small thickness. Moreover, k_W becomes a function of the coordinate along the structure, and for sinusoidal and step function modulation we will have the corresponding relations:

$$k_{w,\text{sinus}}^2(x) = \left(\frac{n\pi}{w}\right)^2 \left[1 - 2\frac{2\delta}{w} \sin\left(\frac{2\pi}{\Lambda}x\right) + o\left(\frac{2\delta}{w}\right) \right] ; \quad (1)$$

$$k_{w,\text{step}}^2(x) = \left(\frac{n\pi}{w}\right)^2 \left[1 - 2\frac{2\delta}{w} \sum_{p=1}^{\infty} \left(\frac{1 - (-1)^p}{\pi p} \right) \times \sin\left(\frac{2p\pi}{\Lambda}x\right) + o\left(\frac{2\delta}{w}\right) \right] . \quad (2)$$

where δ is the modulation amplitude, x is the spatial coordinate along the structure, Λ is the period of the modulation and p is the number of space harmonic in the Fourier series. $o(2\delta/w)$ represents the higher space harmonics of the parameter $2\delta/w$ with amplitudes orders smaller than the first term. One can observe that both equations predict multiple rejection bands. However, the amplitudes given by the higher order terms $o\left(\frac{2\delta}{w}\right)$ are negligible in comparison with the ones given by the first term. To prove this fact we performed an additional simulation in which we considered a sinusoidal structure with the width modulation depth of $0.75\mu\text{m}$ (50% increase in the modulation amplitude), the other parameters being kept constant. Yet, the results have shown a single band gap in the spin-wave operational transmission characteristics. Moreover, the Fourier analysis of the width function of the sinusoidal structure shows only one harmonic. Therefore, the second band gap is practically invisible for the structure with sinusoidal notches.

The frequency and the depth of the rejection bands depend on the distance from the excitation antenna (the number of periods of the MC modulation magnetic parameter). From Fig. 2a and Fig. 2b one may observe that the spin waves must pass at least two periods of the structure in order to form band gaps in their operational transmission characteristics. Furthermore, the simulation data shows that the depth of the rejection band depends also on the probing position across the MCs width. In Figs. 2c and 2d the transmission characteristics extracted in two points are presented: P_1 in the center of the structure (see Fig. 1a), and P_2 at the half distance between the center and the edge of the spin-wave propagation channel ($y = 375\text{nm}$). One may observe that the depth of the rejection bands is increased for both simulated structures. The full dependence of the alternative component of the magnetization (or spin-wave amplitude) as a function of the position across the MC structures are shown in Fig. 2e and Fig. 2f. Several features are clearly visible: (1) the band gaps are more pronounced at the regions close to the edges of the waveguide rather than in the center; (2) the band gap frequency is slightly varied with the position; (3) the absence of

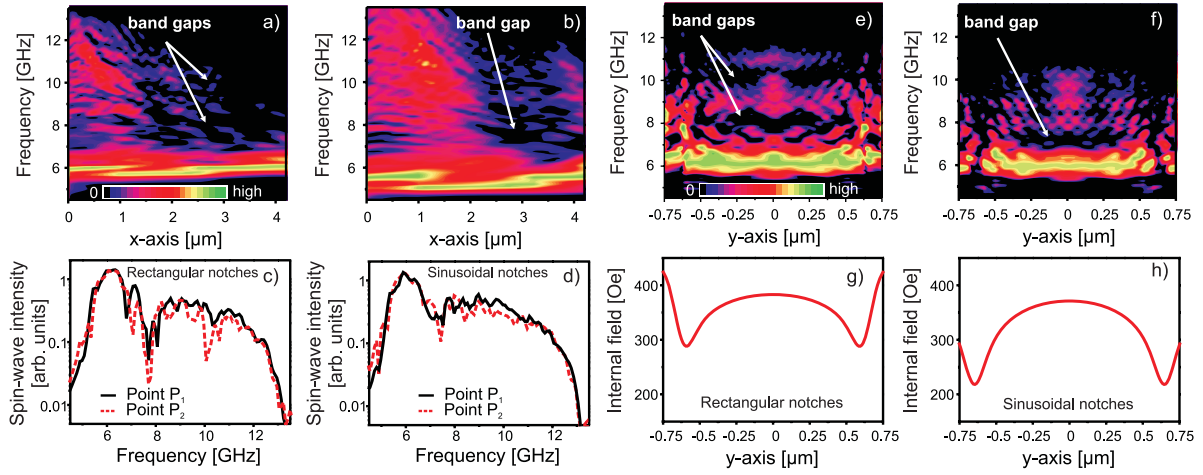


Fig. 2: Spin-wave transmission characteristics as a function of propagation distance (x) from the antenna, extracted in the center of the magnetic stripes with a) step function and b) sinusoidal edge profile. c) and d) Transmission characteristics extracted locally in the points P_1 (in the center) and P_2 (at $y = 375$ nm) (see Fig. 1a and Fig. 1b) inside the MC. Transmission characteristics as a function of the probing position across the spin-waves propagation channel for the e) step function and f) sinusoidal structures at a distance $x = 4$ μm from antenna. g) and h) H_y component of the magnetic internal field across the simulated structures.

the rejection bands just near the waveguide edges. To understand the first feature one should consider that beside the modulation of the transversal wavevector there is a weak variation of the internal field closer to the notches. The propagating spin waves in this region start to be sensitive to the modulation of the internal field. In consequence, the rejection efficiency is increased and, therefore, the band gap is more pronounced. The second feature is related to the decay of the internal field distribution towards the notches (see Fig. 2g and 2h). The changes of the internal field produce a shift of the spin-wave dispersion characteristics triggering the shift of the band gap frequency. Moreover, the temporal evolution of the spatial distribution of the magnetization shows a complicated behavior at the edge of the structure. Standing waves formed inside the anti-notches are mixed with secondary higher-order width modes generated due to the scattering of the originally excited one at the edges. As a consequence, the band gaps are vanishing at the edges of the spin-wave propagation channel (third feature).

In conclusion, we performed a micromagnetic study of the spin-wave transmission in microstructured Permalloy magnonic crystals with variable widths. Two kinds of waveguides were investigated: with a step function and a sinusoidal edge profile. Band gaps in the spin-wave transmission characteristics have been clearly observed and studied in the space and frequency domain. The formation of the band gaps is related to the modulation of the transversal wavevectors of the spin waves. It was demonstrated that the number of the band gaps can be controlled by the proper choice of the magnonic crystal geometry. It is shown that both the band gap frequency and its depth depend strongly on the probing position inside the MC due the internal magnetic field distribution. Hence, the internal field plays an important role in the shape design of a magnonic crystal as well.

Financial support by the DFG SE-1771/1-2 is gratefully acknowledged.

References

- [1] S.L. Vysotskii, S.A. Nikitov, and Yu.A. Filimonov, *Magnetostatic spin waves in two-dimensional periodic structures (Magnetophoton crystals)*, JETP **101**, 636 (2005).

-
- [2] A.V. Chumak, A.A. Serga, B. Hillebrands, and M.P. Kostylev, *Scattering of backward spin waves in a one-dimensional magnonic crystal*, Appl. Phys. Lett. **93**, 022508 (2008).
 - [3] M. Krawczyk and H. Puzkarski, *Plane-wave theory of three-dimensional magnonic crystals*, Phys. Rev. B **77**, 054437 (2008).
 - [4] A.V. Chumak, A.A. Serga, S. Wolff, B. Hillebrands, and M.P. Kostylev, *Scattering of surface and volume spin waves in a magnonic crystal*, Appl. Phys. Lett. **94**, 172511 (2009).
 - [5] A.B. Ustinov, N.Yu. Grigoreva, and B.A. Kalinikos, *Observation of spin-wave envelope solitons in periodic magnetic film structures*, JETP Lett. **88**, 31 (2009).
 - [6] A.V. Chumak, T. Neumann, A.A. Serga, B. Hillebrands, and M.P. Kostylev, *A current-controlled, dynamic magnonic crystal*, J. Phys. D: Appl. Phys. **42**, 205005 (2009).
 - [7] G. Gubbiotti, S. Tacchi, G. Carlotti, N. Singh, S. Goolaup, A.O. Adeyeye, and M. Kostylev, *Collective spin modes in monodimensional magnonic crystals consisting of dipolarly coupled nanowires*, Appl. Phys. Lett. **90**, 092503 (2007).
 - [8] M. Kostylev, P. Schrader, R.L. Stamps, G. Gubbiotti, G. Carlotti, A.O. Adeyeye, S. Goolaup, and N. Singh, *Partial frequency band gap in one-dimensional magnonic crystals*, Appl. Phys. Lett. **92**, 132504 (2008).
 - [9] Z.K. Wang, V.L. Zhang, H.S. Lim, S.C. Ng, M.H. Kuok, S. Jain, and A.O. Adeyeye, *Observation of frequency band gaps in a one-dimensional nanostructured magnonic crystal*, Appl. Phys. Lett. **94**, 083112 (2009).
 - [10] A.V. Chumak, V.S. Tiberkevich, A.D. Karenowska, A.A. Serga, J.F. Gregg, A.N. Slavin, and B. Hillebrands, *All-linear time reversal by a dynamic artificial crystal*, Nat. Commun. **94**, 141 (2010).
 - [11] K.S. Lee, D.S. Han, and S.K. Kim, *Physical origin and generic control of magnonic band gaps of dipole-exchange spin waves in width-modulated nanostrip waveguides*, Phys. Rev. Lett. **102**, 127202 (2009).
 - [12] S.K. Kim, K.S. Lee, and D.S. Han, *A gigahertz-range spin-wave filter composed of width-modulated nanostrip magnonic-crystal waveguides*, Appl. Phys. Lett. **95**, 082507 (2009).
 - [13] V.V. Kruglyak, R.J. Hicken, A.N. Kuchko, and V.Y. Gorobets, *Spin waves in a periodically layered magnetic nanowire*, J. Appl. Phys. **98**, 014304 (2005).
 - [14] A.V. Chumak, P. Pirro, A.A. Serga, M.P. Kostylev, R.L. Stamps, H. Schultheiss, K. Vogt, S.J. Hermsdoerfer, B. Laegel, P.A. Beck, and B. Hillebrands, *Spin-wave propagation in a microstructured magnonic crystal*, Appl. Phys. Lett. **95**, 262508 (2009).
 - [15] A. V. Chumak, A. A. Serga, S. Wolff, B. Hillebrands, and M. P. Kostylev, *Design and optimization of one-dimensional ferrite-film based magnonic crystals*, J. Appl. Phys. **105**, 083906 (2009).
 - [16] The simulations were performed using the OOMMF open code: M.J. Donahue, and D.G. Porter, Report NISTIR 6376, National Institute of Standards and Technology, Gaithersburg, MD (1999).

4.10 Exact dipole-exchange theory for dynamic magnonic crystals

A.A. Serga, A.V. Chumak, and B. Hillebrands¹

Extensive studies of the magnonic crystals (MC) formed by a periodic variation of static external magnetic field were started more than two decades ago [1, 2]. A renewed interest to this type of MCs is associated with the opened possibility of the dynamical tuning of the parameters of such waveguiding structure during the spin-wave propagation. In the experiments [3, 4] a dynamic MC was formed by a current meander structure near the surface of the ferromagnetic film, which can be switched on and off during the spin-wave propagation. Such a dynamical tuning allows one to obtain several interesting physical effects such as all-linear time reversal of pulsed microwave signals, propagated in ferromagnetic film, frequency inversion [4], and oscillatory energy exchange between two counter-propagating wave modes (see report “Oscillatory energy exchange between wave modes coupled by a dynamic magnonic crystal”).

It is well-known that the MCs as a magnetic counterpart of photonic and sonic crystals have a considerably modified spectrum of spin-wave excitations, which contains full band gaps, where spin waves are not allowed to propagate [5]. The form of this spectrum determines the behaviour of propagating spin waves in such structures. Thus, a consistent dipole-exchange spin-wave theory is needed to describe the processes in dynamic MCs.

Previously elaborated theory of dynamic MCs [3] takes into account only a sinusoidal form of the Oersted field produced by a conducting array of stripes. However, it is well-known that an Oersted field, produced by a current-carrying stripe structure, has a complicated non-sinusoidal profile. Its Fourier spectrum consists of more than one space harmonics. Thus, the first Born approximation cannot be applied in this case. Here we report on the theoretical investigation of the dipole-exchange spin-wave spectrum of the dynamic MC formed by a non-sinusoidal periodic external magnetic field.

The theory is based on a general spin-wave modes approach together with a method of tensorial Green’s functions [6]. The influence of the periodic variation of the bias magnetic field is described according to the Floquet theorem [7]. The exact dispersion relation is obtained in the form of an infinite determinant, which can be easily reduced to a finite one for each particular problem according to common perturbation theory. The presented theory takes into account an arbitrary periodic character of the external magnetic field as well as arbitrary spin pinning boundary conditions on the surfaces of the ferromagnetic waveguide.

Such structure (see Fig. 1) is usually patterned by means of photolithography on an aluminium nitride substrate with high thermal conductivity in order to avoid heating. When a current is applied to the conducting structure, a periodic magnetic Oersted field is produced. In order to minimize the electromagnetic coupling between the current carrying, metallic stripes and the spin waves, a nonmagnetic dielectric spacer with thickness d is placed between the ferromagnetic film and the conducting structure. The static bias magnetic field is applied in the configuration, when the backward volume magnetostatic spin waves (BVMSW) are propagating in the structure.

To describe the considered model structure a linearized Landau-Lifshitz equation of motion is used. The dipole-dipole and exchange interactions in the ferromagnetic structure are taken in account as well as an arbitrary surface magnetic anisotropy, and retardation effects are assumed

¹In collaboration with N.Yu. Grigoryeva and B.A. Kalinikos, St. Petersburg Electrotechnical University, Russia.

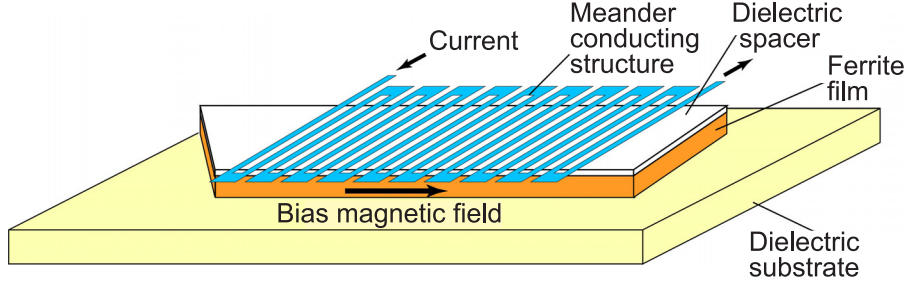


Fig. 1: Considered structure of the magnonic crystal.

to be negligible. We search for a solution of the linearized Landau-Lifshitz equation of motion together with Maxwell's equations in the magnetostatic limit corresponding to monochromatic spin waves. To take into account the spatial periodicity of the internal static magnetic field we use the Floquet theorem for differential equation with periodic coefficients. In the frames of this method a solution for the dynamic magnetization $\mathbf{m}(\mathbf{r})$ and the expression for the dynamic dipole field $\mathbf{h}(\mathbf{r})$ can be represented as a product of a plane-wave envelope function and a corresponding periodic function. Then the periodic function is expanded in a Fourier series. Thus the result is written as:

$$\mathbf{m}(\mathbf{r}) = \sum_{m=-\infty}^{+\infty} e^{-iK_m z} \mathbf{m}(x; K_m), \quad \mathbf{h}(\mathbf{r}) = \sum_{m=-\infty}^{+\infty} e^{-iK_m z} \mathbf{h}(x; K_m) \quad . \quad (1)$$

As far as we are interested in the solutions in the form of plane waves the dynamic magnetization and the dynamic dipole field are the functions of only two spatial coordinates: x , directed perpendicularly to the ferromagnetic film plane, and z , which is directed along the spin-wave propagation direction. In Eq. (1) $K_m = k_z + 2m\pi/\Lambda$ represents physically the propagation wavenumbers of the space harmonic contributions, so called Bloch wavevectors. Now k_z lies in the first Brillouin zone $0 \leq k_z < 2\pi/\Lambda$ and $k_m = 2m\pi/\Lambda$ denotes a reciprocal lattice vector, Λ is the period of the structure.

The Fourier transform that maps the space-periodic part of the bias magnetic field to the reciprocal space is as follows:

$$\mathbf{H}^0(\mathbf{r}) = \sum_{m'=-\infty}^{+\infty} \mathbf{H}_{m'}^0 e^{-ik_{m'} z} \quad . \quad (2)$$

Here we assume that the static magnetic field is spatially inhomogeneous only in the direction of the periodic variation, i.e. in our case in the direction of spin-waves propagation. The Fourier coefficients $\mathbf{H}_{m'}^0$ can be found from the inverse transform, and in the case of a trapezoidal field modulation, it is:

$$\mathbf{H}_{m'}^0 = i \frac{\delta H \Lambda}{2a\pi^2 m'^2} \sin\left(\frac{2m'a\pi}{\Lambda}\right) \left(1 - (-1)^{m'}\right) \quad . \quad (3)$$

Here δH is the amplitude of the bias magnetic field modulation and a/Λ is the degree of keystoneing (at $a/\Lambda \rightarrow 0$ we arrive to meander-type of modulation). In the general case these coefficients can be calculated either by integration over the period or determined numerically by means of fast Fourier transform.

Finally we arrive at an infinite system of pairs of integro-differential equations for the vector space

harmonic amplitudes $\mathbf{m}(x; K_m)$:

$$i2\pi f m_m^x(x; K_m) = -|g| \mu_0 \sum_{m'} H_{m-m'}^0 m_{m'}^y(x; K_{m'}) + |g| \mu_0 M^S \alpha \left(\frac{\partial^2}{\partial x^2} - k_z^2 \right) m_m^y(x; K_m) \\ + |g| \mu_0 M^S \int_{L/2}^{L/2} [G^{yx}(x, x'; K_m) m_{m'}^x(x'; K_m) + G^{yy}(x, x'; K_m) m_{m'}^y(x'; K_m)] dx' \quad (4-a)$$

$$i2\pi f m_m^y(x; K_m) = |g| \mu_0 \sum_{m'} H_{m-m'}^0 m_{m'}^x(x; K_{m'}) - |g| \mu_0 M^S \alpha \left(\frac{\partial^2}{\partial x^2} - k_z^2 \right) m_m^x(x; K_m) \\ - |g| \mu_0 M^S \int_{L/2}^{L/2} [G^{xx}(x, x'; K_m) m_{m'}^x(x'; K_m) + G^{xy}(x, x'; K_m) m_{m'}^y(x'; K_m)] dx' \quad (4-b)$$

Here $G^{\alpha\beta}(x, x'; K_m)$ are the components of the tensorial Green's function, which are derived from a solution of Maxwell's equations with appropriate electrodynamic boundary conditions [6].

Making use of a standard procedure of a spin-wave modes approach, described in detail in Ref. [6], we arrive at a system of linear equations for the spin-wave mode amplitudes. Zeroing the determinant of this system we obtain the dispersion relation in the form:

$$\det \left[D_{nn}^{mm} + \sum_{n'} R_{nn'}^{mm} + \sum_{n'} \sum_{m'} L_{nn'}^{mm'} \right] = 0 \quad , \quad (5)$$

where D_{nn}^{mm} , $R_{nn'}^{mm}$, $L_{nn'}^{mm'}$ - are square matrices 2×2 ; the matrix elements in D_{nn}^{mm} and $R_{nn'}^{mm}$ can be found from corresponding matrices in [6] with substitution $k_\zeta \rightarrow K_m$, and matrix $L_{nn'}^{mm'}$ corresponding to the form of perturbation (3) have the following form:

$$L_{nn'}^{mm'} = \frac{\delta H}{M^S} \frac{i\Lambda}{2a\pi^2(m-m')^2} \sin \left(\frac{2(m-m')a\pi}{\Lambda} \right) \left(1 - (-1)^{m-m'} \right) \quad . \quad (6)$$

The results of the numerical calculations of the spin-wave spectrum in the field induced MC according to Eq. (5) are presented in Fig. 2. Here three types of static magnetic field perturbation are shown: sinusoidal, meander and trapezoidal. Three cases are compared for the same set of the parameters taken from the experimental data [3] (see Fig. 2). For all cases it was assumed that the YIG film has free surface spins on both surfaces. The parameter of keystoneing for the third case was taken $a = 45 \mu\text{m}$. For the meander and the trapezoidal perturbation only the first five space harmonics are taken into account.

It is well seen from Fig. 2a, that a sinusoidal perturbation of the external magnetic field produces a very narrow band gap. The comparison with the corresponding experimental data of Fig. 2c in Ref. [3] shows that it does not suffice to produce the effect observed in the experiment. On the other hand, the meander perturbation, as it can be seen from Fig. 2b, produces several large bandgaps in the spin-wave spectrum. This fact is also contrary to the experimental data [3], where higher order band gaps are not observed. Finally, only a trapezoidal type of the external magnetic field modulation fits well with the results reported in Ref. [3] (Fig. 2(c) in Ref. [3]). The obtained parameters of the first band gap are: central frequency of the band gap $f_c = 6.516 \text{ GHz}$ and a gap width of $\Delta f \simeq 13 \text{ MHz}$. The next three band gaps are too small to be detected in the experiment.

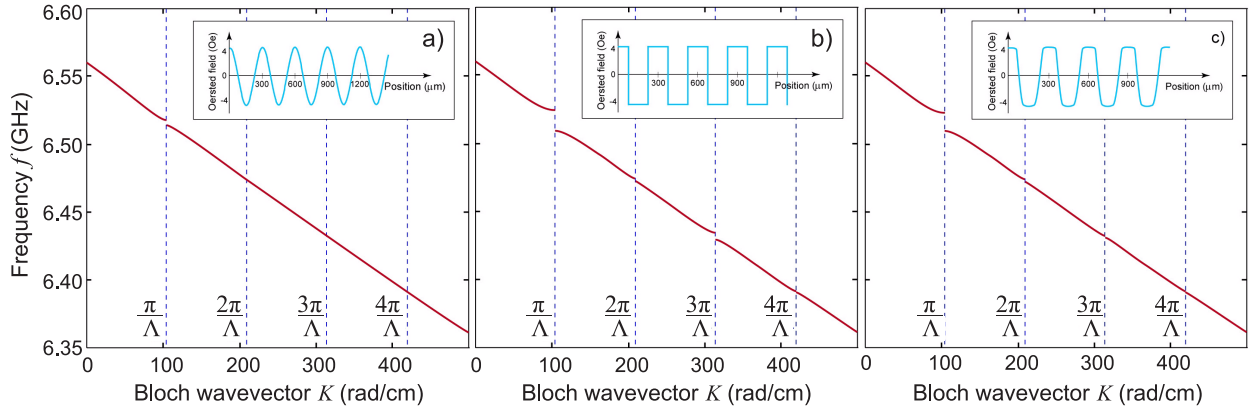


Fig. 2: Dispersion characteristics for three types of dynamic magnonic crystals. Parameters of calculations are taken from Ref. [3]: $4\pi M_S = 1750 \text{ G}$, $H_0 = 1625 \text{ Oe}$, $L = 5 \mu\text{m}$, $\Lambda = 300 \mu\text{m}$, $\delta H = 4 \text{ Oe}$ (which corresponds to a current in the meander structure of $I = 0.5 \text{ A}$).

In conclusion, the exact dipole-exchange theory for dynamic magnonic crystals produced by the arbitrary periodic variation of the external magnetic field is elaborated. It is shown that both the band gap frequency and its depth depend strongly on the form of the external perturbation. The performed numerical calculations show that the periodic Oersted field produced by the conducting meander structure in the experiments [3] is not sinusoidal. A comparison to theory shows that the form of the periodic perturbation is most likely of trapezoidal shape. Thus it was demonstrated that the number of band gaps and their width can be controlled by the proper choice of the form of the Oersted field.

Support by the Deutsche Forschungsgemeinschaft within German-Russian collaborative project 436 RUS 113/644/0-3 is gratefully acknowledged.

References

- [1] A.V. Voronenko, S.V. Gerus, *Interaction of surface magnetostatic waves with spatially-periodic magnetic field*, JTP Letters **10**, 746 (1984).
- [2] A.V. Voronenko, S.V. Gerus, V.D. Kharitonov, *Bragg diffraction of surface magnetostatic waves from magnetic lattices*, Russian Physics Journal **31**, 915 (1988).
- [3] A.V. Chumak, T. Neumann, A.A. Serga, B. Hillebrands, M.P. Kostylev, *A current-controlled, dynamic magnonic crystal*, J. Phys. D **42**, 205005 (2009).
- [4] A.V. Chumak, V.S. Tiberkevich, A.D. Karenowska, A.A. Serga, J.F. Gregg, A.N. Slavin, B. Hillebrands, *All-linear time reversal by a dynamic artificial crystal*, Nat. Commun. **94**, 141 (2010).
- [5] S.L. Vysotskii, S.A. Nikitov, Yu.A. Filimonov, *Magnetostatic spin waves in two-dimensional periodic structures (magnetophoton crystals)*, JETP **101**, 547 (2005).
- [6] B.A. Kalinikos, A.N. Slavin, *Theory of dipole-exchange spin wave spectrum for ferromagnetic films with mixed exchange boundary conditions*, J. Phys. C: Solid State Phys. **19**, 7013 (1986).
- [7] L. Brillouin, M. Parodi, *Propagation des ondes dans les milieux périodiques* (Paris: Masson-Dunod, 1956).

D. Spin Caloric Transport

Spin Caloric Transport is a new field of research, which investigates the interplay between spin- and heat-based transport phenomena. The recent observation of the spin Seebeck effect in a magnetic insulator demonstrates the crucial role of collective magnetization excitations, i.e. spin waves and their quanta, magnons, in spin caloric transport processes, and illustrates the conceptual distinction between this phenomenon and conventional thermoelectric generation. Most interesting and important is the conversion of a heat flow into magnon currents and vice versa in a magnetic insulator. On a long-time scale this may bring to the utilization of heat currents to support the transfer and processing of spin information.

Spin waves may travel and transport the spin over macroscopic distances, which can reach into several centimeters in yttrium iron garnet (YIG). Their properties are known to be strongly dependent on the temperature of the magnetic material. The magnon-phonon interaction as well as the dependence of the saturation magnetization on the temperature are the most pronounced mechanisms. Report 4.11 is devoted to the investigation of spin wave propagation in a thermally non-uniform magnetic medium, as a first step in studies of the interaction between magnon currents and heat currents created by thermal gradients. The transformation of the spin-wave wavelength during the propagation of spin waves in the YIG waveguide with thermal gradients is demonstrated.

D. Spin-kalorischer Transport

Der spin-kalorische Transport ist ein neues Forschungsfeld, das das Zusammenspiel zwischen Spin-basierten und Wärme-basierten Transportphänomenen untersucht. Die ersten Untersuchungen des Spin-Seebeck-Effekts in magnetischen Isolatoren zeigen dabei die wichtige Rolle auf, welche die kollektiven Anregungen des magnetischen Systems - also Spinwellen - in spin-kalorischen Transport-Prozessen spielen. Weiterhin verdeutlichen diese Beobachtungen die konzeptuelle Unterscheidung zwischen diesen Phänomenen auf der einen sowie konventionellen thermoelektrischen Effekten auf der anderen Seite. Von größtem Interesse und von größter Wichtigkeit in diesem Forschungsgebiet ist die Untersuchung der Umwandlung von Wärmeströmen in reine Spinströme in Isolatoren. Perspektivisch kann das Verständnis dieser Prozesse zur Nutzung von Wärmeströmen für den Transport sowie die Verarbeitung von Spin-Information beitragen.

Spinwellen in Yttrium-Eisen-Granat (YIG) zeigen makroskopische Propagationslängen von bis zu mehreren Zentimetern. Die Eigenschaften dieser Spinwellen werden dabei stark von der Temperatur des magnetischen Materials beeinflusst. Hierbei spielen die Magnon-Phonon-Wechselwirkung und die Temperaturabhängigkeit der Sättigungsmagnetisierung eine entscheidende Rolle. Bericht 4.11 widmet sich der Untersuchung der Spinwellenpropagation in einem magnetischen Material, das einen Temperaturgradienten aufweist. Dies stellt einen ersten Schritt in der Erforschung der Wechselwirkung zwischen reinen Spinströmen und dem Wärmetransport in Temperaturgradienten dar. Dabei konnte die Änderung der Spinwellen-Wellenlänge bei Propagation der Spinwellen in einem YIG-Wellenleiter mit Temperaturgradient beobachtet werden.

4.11 Spin-wave propagation and transformation in a thermal gradient

B. Obry, V.I. Vasyuchka, A.V. Chumak, A.A. Serga, and B. Hillebrands

The discovery of the spin Seebeck effect by Uchida et al. [1] has launched a series of investigations on the influence of temperature gradients on the spin system of magnetic materials. It has been shown that a thermal gradient applied between the two sides of a magnetic material gives rise to a spin voltage between the hot and the cold area. Pure spin currents can thus be established over long distances and are detected utilizing the inverse spin Hall effect. A variety of experimental and theoretical work has been carried out to gain a deeper insight into the microscopic origin of the creation of a spin voltage due to thermal gradients and to understand phenomena like the regular and longitudinal spin Seebeck effect, respectively [2, 3]. Especially intriguing is the observation that the creation of a spin voltage in a thermal gradient is not connected to the magnetic material being electrically conducting [4]. Consequently, the spin voltage in an electrical insulator must be mediated by magnetization dynamics. For the case of yttrium iron garnet (YIG) the flow of a pure spin current is maintained by spin waves [5]. Therefore, spin waves play an important role in spin caloric processes being a means to transport heat from a hot to a cold reservoir.

Considered in another way, a thermal gradient acts as a new way of creating, amplifying or manipulating spin waves. In a thermal gradient the magnetic properties like anisotropy fields, exchange constant, saturation magnetization and hence the dispersion relation of the material are changed locally. Since a spin wave represents the collective motion of a magnet's spin system and stands out due to its high coherence length, it is instructive to study its behavior in a region with inhomogeneous temperature and thus varying magnetic properties.

In this Report the influence of a thermal gradient on externally excited propagating spin waves is investigated. It is shown that a spin wave continuously adapts its wavelength upon propagation along a YIG waveguide with linearly changing temperature. The reason for that can be found in the change in saturation magnetization and hence in the shift of the dispersion relation according to the local temperature. Furthermore a reflection of a spin wave can be observed in a positive temperature gradient. This is attributed to an unaccessible region in the waveguide, where no spin waves with given frequency can exist, which is created due to the large downshift of the dispersion relation by the temperature increase.

The experiments are performed using Brillouin light scattering spectroscopy (BLS) on a YIG waveguide with a thickness of $t = 6.7\mu\text{m}$ and a width of $w = 1.2\text{mm}$. Each end of the stripe is mounted on a Peltier element (see Fig. 1) allowing for the application of a temperature gradient along the stripe axis of up to 50°C . In between the Peltier elements and the YIG stripe, a heat conducting aluminum nitride interlayer containing a lithographically produced microstrip line serving as a microwave antenna is used. BVMSW spin waves are excited by the antenna in an external magnetic field $\mu_0\mathbf{H}$ along the stripe's long axis. The direction of the thermal gradient can be reversed by changing the polarity of the current applied to the Peltier elements. Figure 1 shows two thermal images of the experimental setup, where the spin waves propagate in a negative (Fig. 1a) and positive (Fig. 1b) thermal gradient, respectively.

As can be seen from Fig. 1, the excitation antenna is placed on top of the left Peltier element. The antenna structure on the right Peltier element (see shadow in Fig. 1) is disconnected. Hence spin waves can solely be excited from the left antenna. Changing the magnitude of the thermal gradient thus yields different temperatures at the position of the antenna. As a consequence the

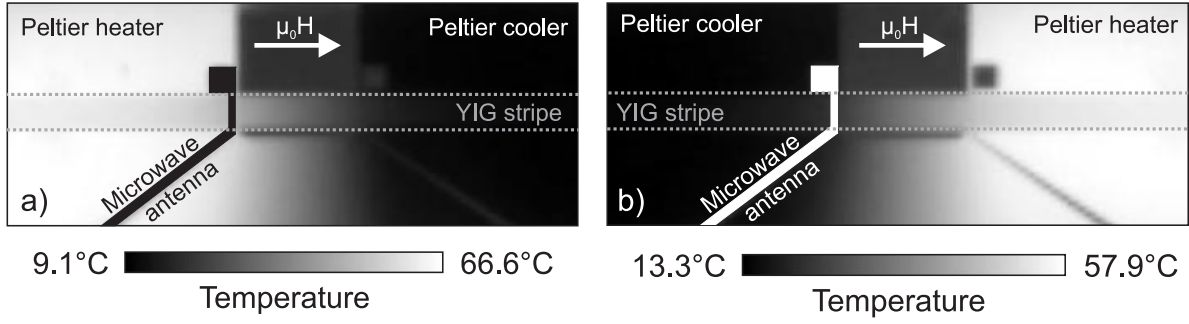


Fig. 1: Thermal images and schematic setup of the sample in a negative (a) and positive (b) thermal gradient, respectively. White (black) indicates a hot (cold) region. Displayed is the temperature of the YIG stripe with the two Peltier elements, which are attached to each end of the stripe. A microwave antenna excites spin waves in the YIG, which then propagate along the thermal gradient. The microwave antennas are shown only schematically.

saturation magnetization M_s as well as the dispersion relation will be changed, too. This can easily be observed using a scalar network analyzer. Figure 2a shows measurements of the microwave signal that is absorbed by the YIG film. A minimum in the return loss curve indicates maximum absorption by the YIG waveguide. Consequently, the spin-wave absorption spectrum at the position of the microwave antenna can be mapped. For an external magnetic field of $\mu_0 H = 187 \text{ mT}$ an increase in temperature by 16°C yields a reduction of the absorption spectrum in frequency by about 65 MHz . For a reliable comparison between spin-wave propagation in a homogeneous waveguide and in a thermal gradient, this shift of the resonance is undesirable. This means that spin waves are excited at a different position of the spin-wave dispersion and hence with different wavevectors, depending on the respective temperature. The discrepancy in starting conditions can be avoided by compensating the shift of the absorption spectrum by means of the magnetic field. The dependence of the magnetic field needed for a constant absorption spectrum as a function of the temperature at the antenna is shown in Fig. 2b. An increase in temperature will decrease M_s and results in a shift of the dispersion relation to smaller frequencies. This can be compensated by increasing the external magnetic field $\mu_0 \mathbf{H}$.

The results of Fig. 2b allow for a quantitative analysis of the decrease in saturation magnetization as a function of temperature. Since the frequency of the ferromagnetic resonance ν is kept constant by changing the magnetic field by $\mu_0 \Delta H$, the change in M_s can be calculated using Kittel's formula [6]

$$\nu(T_0) = \mu_0 \gamma \sqrt{H_0(H_0 + M_s^0)} = \mu_0 \gamma \sqrt{(H_0 + \Delta H)[(H_0 + \Delta H)(M_s^0 - \Delta M_s)]} = \nu(T_0 + \Delta T) \quad . \quad (1)$$

Here, $\gamma = 28 \text{ GHz/T}$ is the gyromagnetic ratio. In agreement with Algra et al. [7] a decrease of the saturation magnetization by $\Delta M_s / \Delta T = 0.38 \text{ kA}/(\text{m} \cdot \text{K})$ can be determined.

The behavior of spin waves propagating in a negative thermal gradient, i.e. into a region with decreasing temperature, has been investigated utilizing the settings shown in Fig. 1a. Using Brillouin light scattering the interference between light scattered from spin waves and reference light with the same frequency but constant phase has been recorded, the latter being created by an electro-optic modulator [8,9]. By mapping the spatial distribution of the interference signal it is possible to visualize the spin-wave wavelength, which is the distance between two adjacent interference minima. The result is depicted in the lower part of Fig. 3a. It shows the radiation of spin waves from the antenna at $x = 0 \text{ mm}$ along the YIG waveguide for a magnetic field of $\mu_0 H = 192.7 \text{ mT}$ and a temperature difference of $\Delta T = 25^\circ\text{C}$. Interference minima are marked by white dashes.

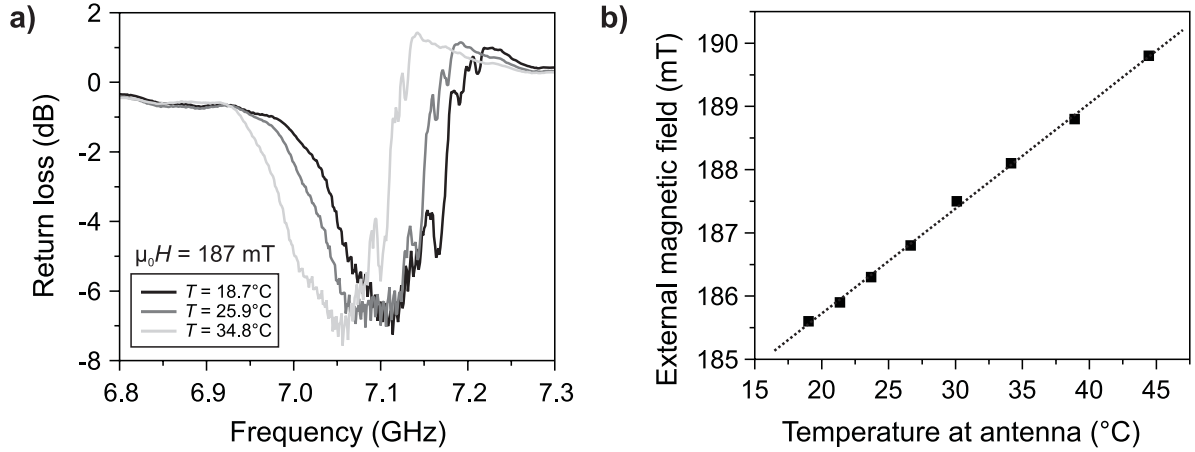


Fig. 2: a) Scalar network analyzer measurements of the microwave signal being reflected at the excitation antenna for an external field of $\mu_0 H = 187$ mT and different temperatures. A minimum in the return loss curve indicates maximum absorption by the YIG stripe. b) Dependence of the external magnetic field which is needed to compensate the dispersion shift in a) on the temperature measured at the position of the antenna. Squares indicate experimental values, the dashed line represents the best linear fit.

For comparison, the upper part of Fig. 3a displays an interference measurement of spin waves propagating in the YIG waveguide with homogeneous temperature. In order to compensate the dispersion shift (see Fig. 2a), the magnetic field has been changed to $\mu_0 H = 188.5$ mT. It can be seen that the interference minima for the case of homogeneous temperature are equidistant. As expected, the spin-wave wavelength remains constant for spin waves propagating along a regular waveguide. In case the spin waves propagate in a negative thermal gradient, it is apparent that the distance between the interference minima decreases along the YIG waveguide indicating a wavelength reduction.

This reduction of the spin-wave wavelength for the spin-wave propagation from a hot into a cold region can be understood by taking into account the change in saturation magnetization M_s . For a homogeneous magnet and temperatures below the Curie point, M_s is given by averaging the total magnetic moment over the magnet's volume. Heating the magnet will reduce its saturation magnetization by inducing molecular motion. In the case of a linear temperature gradient the saturation magnetization, though being a macroscopic quantity, has to be defined locally in an infinitely small volume element. Thus the spin waves, which are propagating into a colder region as shown in Fig. 3, will experience an increasing value of M_s . This is reflected in the spin waves' dispersion relation. Schematically, Fig. 3b describes the shift of the dispersion relation from a point close to the antenna with temperature T_1 (black line) to higher frequencies at a point farther away from the antenna with $T_2 < T_1$ (grey line). As the spin-wave frequency is conserved, the shift of the dispersion causes an increase in wavevector from k_1 to k_2 and hence a reduction of the spin-wave wavelength.

The complementary experiment of spin waves travelling in a positive temperature gradient has been realized in the configuration shown by the thermal image in Fig. 1b. Here, the same waveguide is used with the direction of the DC current at the Peltier elements reversed. Spin waves which are excited by the microwave antenna propagate along the waveguide into regions of increasing temperature. Figure 4a shows BLS measurements of the spin-wave intensity along the YIG waveguide with the antenna at the position $x = 0$ mm and an external magnetic field of $\mu_0 H = 183.5$ mT. A temperature difference between $x = 0$ mm and $x = 4$ mm of $\Delta T = 23^\circ\text{C}$ is realized. The result

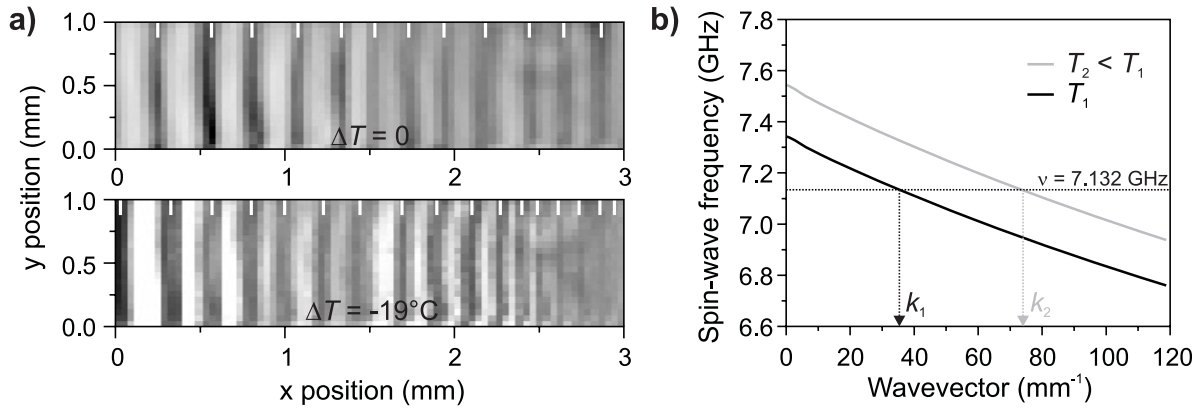


Fig. 3: Demonstration of the wavelength reduction of spin waves in a negative thermal gradient. a) Brillouin light scattering interference measurements of the spin-wave phasefronts in a 1 mm wide and 3 mm long region. Spin waves are excited by the antenna at $x = 0$ mm. The white dashes indicate points with the same spin-wave phase. While the wavelength remains constant for homogeneous temperature (upper panel), a decrease is observed for spin waves in a negative thermal gradient (lower panel). b) Calculation of the dispersion relations for two different positions on the waveguide. By increasing the distance from the antenna, the temperature decreases from T_1 to $T_2 < T_1$. As a result the saturation magnetization is increased which causes a shift of the dispersion relation to higher frequency values. Hence the spin-wave wavevector increases from k_1 to $k_2 > k_1$.

can be seen in Fig. 4a. An exponential decay for the spin-wave intensity along the waveguide with homogeneous temperature can be observed (black line) with an overlaid periodic oscillation. The situation changes when switchig on the thermal gradient (grey line). Compared to the stripe with homogeneous temperature, the spin-wave intensity is much larger close to the antenna position, while a drastic decrease of the spin-wave signal is obtained beyond a critical point at $x = 1.5$ mm indicating a reflection of the spin waves at this point. Also in the case of an applied temperature gradient an oscillating spin-wave intensity can be observed in front of the reflection point. The reason for those oscillations is not yet clear and requires further investigation.

The reflection of spin waves in a positive thermal gradient can be understood by taking into account the calculated dispersion relations for different positions on the waveguide. With increasing distance from the antenna, the saturation magnetization decreases due to the higher temperature resulting in a downshift of the dispersion relation to smaller frequencies (Fig. 4b). If the temperature at the antenna is T_1 (black line), spin waves with a wavevector k_1 will be excited by the excitation frequency $\nu = 7.132$ GHz. Eventually, there will be a critical point at a distance from the antenna, where the temperature has increased to $T_2 > T_1$ (grey line). At this temperature the dispersion shift is large enough that it is no longer possible to excite any spin waves with an excitation frequency of ν . This is indicated in Fig. 4b by the fact that the horizontal line at 7.132 GHz has no intercept with the dispersion relation at T_2 (grey line). This means that spin waves cannot access the region with temperatures that are higher than T_2 . As a consequence, the spin wave is reflected at the critical point. The result of Fig. 4a can now be interpreted as the superposition of incoming and reflected spin waves in the region between $x = 0$ mm and $x = 1.5$ mm, resulting in an increased spin-wave intensity. Beyond $x = 1.5$ mm the spin-wave intensity drastically decreases. This marks the ‘forbidden’ region, where spin waves are unable to exist for this frequency.

The presented results demonstrate that it is possible to effectively manipulate spin waves by the application of a thermal gradient. Thereby, a propagation into regions of lower temperature results in a reduction of the spin-wave wavelength to half of its original value. This is especially promising for small wavenumbers, as the antenna size sets a lower limit for the excitation of small

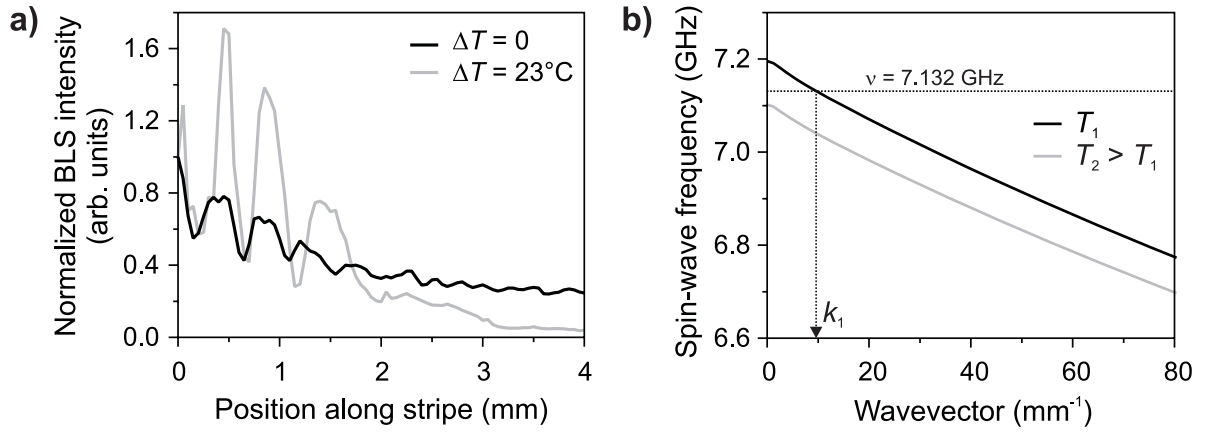


Fig. 4: Reflection of spin waves in a positive thermal gradient. a) Brillouin light scattering intensity measurements along the YIG waveguide for homogeneous temperature (black line) and in case of a positive thermal gradient (grey line). The temperature gradient results in an increased spin-wave intensity in front of a critical point at $x = 1.5 \text{ mm}$ and a rapid drop in intensity beyond. b) Calculated dispersion relations for two different positions of the waveguide in a positive thermal gradient. At the antenna (temperature T_1) spin waves with a frequency of 7.132 GHz and a wavevector k_1 are excited. At a critical point the temperature has increased to $T_2 > T_1$ and caused a downshift of the dispersion relation. The given frequency now is above the accessible spin-wave band. Hence spin waves cannot propagate into a region with a temperature $T > T_2$.

wavelengths. Moreover, spin waves can experience a reflection upon travelling into warmer regions. Thermal gradients thus are a good tool for influencing the propagation direction of spin waves. These effects show that there is a large potential in thermal gradients, which needs to be explored and exploited for application in spintronic or magnon logic devices.

The authors would like to thank E. Saitoh for fruitful discussions. Financial support by the Deutsche Forschungsgemeinschaft (DFG, VA 735/1-1) within Priority Program 1538 "Spin Caloric Transport" is gratefully acknowledged.

References

- [1] K. Uchida, S. Takahashi, K. Harii, J. Ieda, W. Koshibae, K. Ando, S. Maekawa, E. Saitoh, *Observation of the spin Seebeck effect*, Nature **455**, 778-781 (2008).
- [2] K. Uchida, H. Adachi, T. Ota, H. Nakayama, S. Maekawa, E. Saitoh, *Observation of longitudinal spin-Seebeck effect in magnetic insulators*, Appl. Phys. Lett. **97**, 172505 (2010).
- [3] J. Xiao, G.E.W. Bauer, K. Uchida, E. Saitoh, S. Maekawa, *Theory of magnon-driven spin Seebeck effect*, Phys. Rev. B **81**, 214418 (2010).
- [4] K. Uchida, J. Xiao, H. Adachi, J. Ohe, S. Takahashi, J. Ieda, T. Ota, Y. Kajiwara, H. Umezawa, H. Kawai, G.E.W. Bauer, S. Maekawa, E. Saitoh, *Spin Seebeck insulator*, Nature Materials **9**, 894-897 (2010).
- [5] Y. Kajiwara, K. Harii, S. Takahashi, J. Ohe, K. Uchida, M. Mizuguchi, H. Umezawa, H. Kawai, K. Ando, K. Takanashi, S. Maekawa, E. Saitoh, *Transmission of electrical signals by spin-wave interconversion in a magnetic insulator*, Nature **464**, 262-266 (2010).
- [6] C. Kittel, *On the theory of ferromagnetic resonance absorption*, Phys. Rev. **73**, 155-161 (1948).
- [7] H.A. Algra, P. Hansen, *Temperature dependence of the saturation magnetization of ion-implanted YIG films*, Appl. Phys. A **29**, 83-86 (1982).
- [8] A.A. Serga, T. Schneider, B. Hillebrands, S.O. Demokritov, M.P. Kostylev, *Phase-sensitive Brillouin light scattering spectroscopy from spin-wave packets*, Appl. Phys. Lett. **89**, 063506 (2006).
- [9] K. Vogt, H. Schultheiss, S.J. Hermsdoerfer, P. Pirro, A.A. Serga, B. Hillebrands, *All-optical detection of phase fronts of propagating spin waves in a $\text{Ni}_{81}\text{Fe}_{19}$ microstripe*, Appl. Phys. Lett. **95**, 182508 (2009).

E. New Materials and Heusler Compounds

Heusler compounds are promising as a new class of materials due to their possible use in the novel field of spin-dependent or spintronic devices, such as non-volatile memories with low energy consumption and new types of magnetic sensors. The interest in Heusler compounds is mainly due to the half-metallic character of their spin-split band structure. Half-metallic character means that the material provides metallic behavior for electrons with one spin component (e.g. for electrons with spins oriented 'up'), and insulating behavior for the other spin orientation (e.g. for electrons with spins oriented 'down'). These materials may exhibit a 100% spin polarization at the Fermi level, which would make them ideal candidates for e.g. spin polarizers or spin detectors. Heusler compounds are materials with the very general composition X_2YZ (with X, Y being a transition metal and Z an element from the III-V groups), where each element X, Y, Z can be chosen from about 10 different candidates. Hence, the desired properties of the Heusler compounds can be tuned by adjusting their composition. The most well-known example is the group of Co_2YZ compounds showing a high Curie temperature and a large magnetic moment for some of its compounds.

Our group is part of the Japanese-German Research Program "Advanced Spintronic Materials and Transport Phenomena" ASPIMATT, an international project which is devoted to develop the foundation for future spintronics. The Heusler compounds play a key role in spintronics in order to overcome some drawbacks of conventional 3d ferromagnets, in particular when combining spintronics with standard industrial CMOS technologies. Our contribution to ASPIMATT is to explore fundamental issues of nonlinear spin dynamics and spin-wave radiation in Heusler-based microstructures. In this context, an additional property present in some of the Heusler compounds, becomes very attractive. A low damping, smaller than for most of the standard 3d ferromagnets ($Ni_{81}Fe_{19}$, CoFe or CoFeB) has been observed. This allows for increased spin-wave propagation distances and opens the way for the design of new functionalities.

Developing new materials is not the only possible approach in order to generate properties of interest in basic or applied research. A promising alternative is also to modify well-known materials to adjust them to the desired characteristics. This course of action has the advantage of using well-established *know-how* in the preparation and characterization of these materials. The resulting properties of this refashion can produce such new attributes that it can be seen as a completely new material. One common way to achieve this is ion implantation. Typically, a sample of the standard material is bombarded by moderate energetic ions which induce changes in the crystalline lattice and stay embedded in it. The new properties are a result of both the changes induced by the bombardment and the presence of the new atoms which act as a dopant.

In Report 4.12 we report on the first observation of spin-wave propagation in a microstructured spin-wave waveguide made of the Heusler compound $Co_2Mn_{0.6}Fe_{0.4}Si$ (CMFS). We have demonstrated propagation distances of more than 75 μm employing Brillouin light scattering microscopy. This represents an increase by a factor of three compared to the commonly used material $Ni_{81}Fe_{19}$ what qualifies CMFS as a very promising candidate for future devices.

In Report 4.13 a study on the influence of the seed layer on the magnetic properties of epitaxial $Co_2FeAl_{0.4}Si_{0.6}$ thin films deposited on MgO substrates is presented. The in-plane angular dependence of the coercive field is measured using the magneto-optical Kerr effect revealing a rotation of the magnetic easy axes with respect to the crystalline axes.

Report 4.14 discusses the magnetic behavior of embedded ferromagnetic elements at remanence in an antiferromagnetic environment. The elements have been fabricated by ion beam irradiation of Fe/Cr/Fe trilayers. Both Fe layers are antiferromagnetically coupled. The ion irradiation destroys

the Cr interlayer and thus generates a ferromagnetic coupling. We show that, contrary to previous findings, the irradiated ferromagnetic areas can be located very close to each other (200 nm) without evident interaction. This opens the way for new applications.

In Report 4.15 we describe the fabrication of a fully planar spin-wave waveguide by Cr ion implantation in a $\text{Ni}_{81}\text{Fe}_{19}$ layer. We find that the ion implantation induces a reduction of the saturation magnetization of the $\text{Ni}_{81}\text{Fe}_{19}$ film. Additionally, the experiments reveal that spin-wave propagation is limited to the non-irradiated areas, demonstrating the realization of a spin-wave waveguide without a topographically patterning of the system.

E. Neue Materialien und Heusler-Legierungen

Heusler-Verbindungen sind eine vielversprechende Materialklasse aufgrund ihrer möglichen Verwendung für neuartige, den magnetischen Spin nutzende (*spintronische*) Bauteile, z.B. für nicht-flüchtige Computerspeicher mit geringem Energiebedarf oder für neue magnetische Sensoren. Aufgrund ihrer spinaufgespaltenen Bandstruktur zeigen diese synthetischen anorganischen Verbindungen ein halbmetallisches Verhalten: Für eine der beiden Spinorientierungen (z.B. Spin “up”) verhält sich das Material wie ein Metall, für die entgegengesetzte Orientierung (z.B. Spin “down”) wie ein Isolator. Diese Verbindungen können daher eine vollständige Spinpolarisation an der Fermi-Kante aufweisen. Damit sind Heusler-Verbindungen ideale Kandidaten für Spinpolarisatoren oder Spindetektoren. Heusler-Verbindungen haben die generelle chemische Struktur X_2YZ , wobei für jedes X, Y, Z aus etwa zehn verschiedenen Elementen des Periodensystems gewählt werden kann. Die gewünschten Eigenschaften der Heusler-Verbindungen können daher durch die geeignete chemische Zusammensetzung eingestellt werden. Die am besten untersuchten Beispiele sind Kobalt-basierende Verbindungen (Co_2YZ). Viele dieser Verbindungen zeigen eine hohe Curie-Temperatur und ein großes magnetisches Moment.

Unsere Arbeitsgruppe ist Mitglied der deutsch-japanischen Forschergruppe ASPIMATT “Advanced Spintronic Materials and Transport Phenomena”, deren Hauptziel es ist, die Grundsteine für die Spintronik der Zukunft zu legen. Heusler-Verbindungen spielen eine sehr wichtige Rolle in dieser Initiative, da einige Nachteile der konventionellen 3d-Ferromagnete sich damit überwinden lassen. Insbesondere können Heusler-Verbindungen helfen, die Spintronik mit der etablierten CMOS-Technologie zu kombinieren. Der Beitrag unserer Arbeitsgruppe in ASPIMATT ist die Untersuchung von grundlegenden Fragestellungen der nichtlinearen Spindynamik und der Spinwellenausbreitung in Heusler-basierten Strukturen. In dieser Hinsicht ist eine zusätzliche Eigenschaft der Heusler-Verbindungen sehr interessant: in einigen Heusler-Verbindungen wurde eine reduzierte magnetische Dämpfung im Vergleich zu typischen 3d-Ferromagneten (z.B. Permalloy, CoFe oder CoFeB) beobachtet. Dies könnte die Ausbreitung von Spinwellen auf größeren Längenskalen erlauben und so eine Vielfalt von neue Anwendungen und Forschungsrichtungen eröffnen.

Die Entwicklung neuer Materialien ist nicht der einzige Weg, neue Eigenschaften von Interesse für Grundlagen- oder angewandte Forschung zu generieren. Eine Alternative liegt darin, bekannte Materialien so zu modifizieren, dass sie die gewünschten Eigenschaften zeigen. Diese Vorgehensweise hat einen großen Vorteil: die Erfahrung und das *Know-how* in der Präparation und Charakterisierung dieser Materialien ist schon vorhanden. Modifizierungen dieser Art können so viele neue Eigenschaften produzieren, dass das Ergebnis als neues Material betrachtet werden kann. Ein übliches Verfahren ist die Ionenimplantation. Eine Probe wird mit mittlereenergetischen Ionen bombardiert, die schließlich Änderungen in der Kristallstruktur verursachen und danach in dem Material eingebunden bleiben.

Im Bericht 4.12 wird die erste Beobachtung von Spinwellenausbreitung in einem mikrostrukturierten Spinwellenleiter aus einer Heusler-Verbindung präsentiert. Es handelt sich um die Verbindung $\text{Co}_2\text{Mn}_{0.6}\text{Fe}_{0.4}\text{Si}$. Ausbreitungslängen von bis $75\text{ }\mu\text{m}$ konnten mittels der Brillouin-Lichtstreuungsspektroskopie nachgewiesen werden. Dieser Wert ist um einen Faktor drei größer als der für Permalloy, was diese Verbindung als sehr guten Kandidaten für zukünftige spintronische Bauteile qualifiziert.

In Bericht 4.13 wird eine Untersuchung des Einflusses der Pufferschicht auf die magnetischen Eigenschaften epitaktischer $\text{Co}_2\text{FeAl}_{0.4}\text{Si}_{0.6}$ -Schichten auf MgO -Substraten vorgestellt. Die Winkelabhängigkeit des Koerzitivfeldes wurde mittels des magneto-optischen Kerr-Effektes gemessen. Eine Drehung der magnetisch leichten Achse gegenüber den kristallinen Achsen in Abhängigkeit von der verwendeten Pufferschicht wurde beobachtet.

Das Verhalten von ferromagnetischen Elementen in Remanenz welche in eine antiferromagnetische Umgebung eingebettet sind, wird in Bericht 4.14 diskutiert. Die Elemente wurden mittels Ionenimplantation im dreilagigen System Fe/Cr/Fe erzeugt. Ohne Bestrahlung sind die Fe Schichten antiferromagnetisch gekoppelt; der Ionenbeschuss zerstört die Cr Zwischenschicht und generiert eine ferromagnetische Kopplung zwischen den Fe-Schichten. Wir zeigen, dass für moderate Ionendosen die ferromagnetischen Regionen in deutlich geringerem Abstand erzeugt werden können als vorher für hohe Ionendosen angenommen, ohne dass eine starke Wechselwirkung stattfindet.

In Bericht 4.15 wird erstmals die Herstellung eines planaren Spinwellenleiters aus Permalloy ($\text{Ni}_{81}\text{Fe}_{19}$) mit Cr-Ionenbeschuss beschrieben. Eine reduzierte Sättigungsmagnetisierung für Permalloy in den bestrahlten Regionen führt zu einer Eingrenzung der Spinwellenausbreitung im unbestrahlten Bereich und so zur Realisierung des planaren, d.h. nicht-topographisch definierten Wellenleiters.

4.12 Spin-wave propagation in Heusler waveguides

T. Sebastian, P. Pirro, T. Brächer, A.A. Serga, and B. Hillebrands¹

The main concept of *spintronics* is not only to use the charge of the electron but also the spin of the electron to transfer and process information. The development of technical applications based on magneto-resistive elements is a well developed and growing field in data storage and sensor technology. These devices - like read-heads for hard disk drives or the magnetic random access memory - use the spin-dependent scattering of electrons in spin valves to encode the information and still rely on the flow of electrons.

In contrast to this approach, in the emerging field of *magnon spintronics*, it is singly the spin of the electron that is needed to transfer information. In this concept, the carriers of information are spin waves, the excitations of the magnetic system. The quanta of these excitations are called magnons. One advantage of using magnons is their collective nature that could lead to less power consumption in possible applications compared to the diffusive transport of conduction electrons. In addition, the potentials offered by the use of waves, e.g. interference, could enable the use of new concepts in data processing.

To obtain a basic understanding of the physics of spin waves, films made of yttrium iron garnet (YIG) are commonly used as spin-wave waveguides. The reason for this choice is that YIG shows the lowest magnetic Gilbert damping of all known materials. Unfortunately, YIG has several disadvantages regarding technical applications. Structures of YIG have comparatively large sizes in the range of hundreds of microns and the growing process of the material is incompatible with complementary metal oxide semiconductor (CMOS) technologies. Furthermore, since YIG is an insulator, the material cannot be used in applications using the spin-transfer-torque effect.

Among the possible candidates of magnetic materials that are compatible with the demands of industrial growth- and micro-/nano-structuring processes, Heusler compounds look very promising. Cobalt-based Heusler materials show sufficiently high Curie temperature as well as a lower magnetic Gilbert damping and a higher spin polarization than most conventional metallic 3d-ferromagnets [1]. Therefore new Heusler materials are developed and optimized to be used in magnetic tunneling junctions in both the industrial and the scientific environment.

In this Report, we document on the first observation of spin wave propagation in a micro-structured spin-wave waveguide made of a Heusler compound, which is $\text{Co}_2\text{Fe}_{0.4}\text{Mn}_{0.6}\text{Si}$ (CMFS). The film with a thickness of 30nm has been prepared by our Japanese co-workers in the framework of the ASPIMATT collaboration² at the Tohoku University in Sendai. After the deposition, the film was annealed at a temperature of 500 °C to improve the crystal structure. This procedure yields a dominating L2_1 order. Further details about the growth of the film and the influence of the composition and the annealing temperature on the band structure and the magnetic losses of the material can be found in Ref. [2].

In a first set of measurements the material properties were characterized using the magneto-optical Kerr effect (MOKE) and ferromagnetic resonance (FMR) utilizing a vector network analyzer (VNA). The results are displayed in Fig. 1. Figure 1a shows the polar plot of the coercive field H_C

¹In collaboration with Y. Ohdaira, H. Naganuma, M. Oogane, and Y. Ando, Department of Applied Physics, Tohoku University, Sendai, Japan.

²JST-DFG Research Unit *Advanced spintronic materials and transport phenomena*.

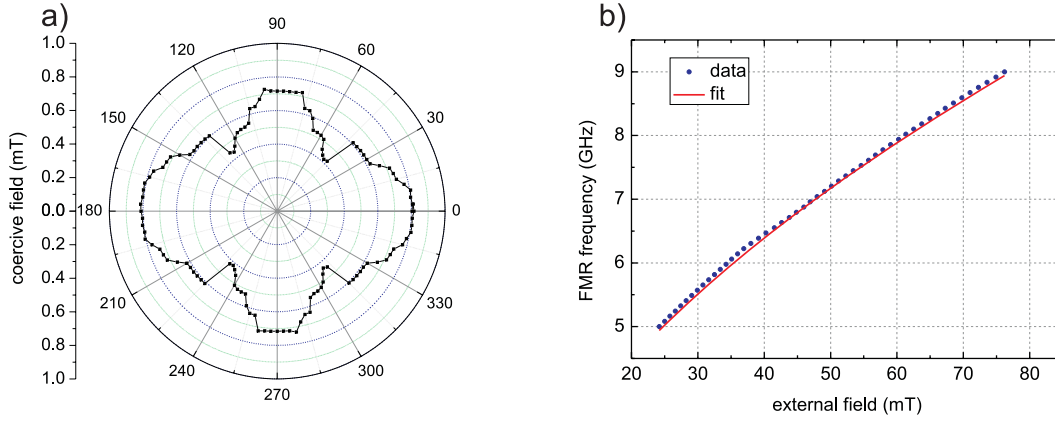


Fig. 1: Measurements to characterize the material parameters of the unstructured CMFS thin film. a) shows a polar plot of the coercive field H_C as a function of the sample orientation. The coercive field was extracted from hysteresis loops taken on a MOKE setup. b) shows the results of an VNA-FMR measurement and the fit corresponding to the Kittel Eq. 1. The fit yields the values $M_s = 1003 \text{ kA/m}$ and $H_{\text{ani}} < 1 \text{ kA/m}$.

as a function of the magnetization direction. The comparatively low values of the coercive field of up to $H_C \approx 0.8 \text{ mT}$ indicate a soft magnetic material. Lowest coercive fields can be found at a value of $H_C \approx 0.4 \text{ mT}$. These values are almost negligible compared to the values of the externally applied field in typical Brillouin light scattering (BLS) spectroscopy measurements, which are in the range of 50 mT . Figure 1b shows the results of the VNA-FMR measurements and the corresponding fit according to the Kittel equation [3]:

$$f_{\text{FMR}} = -\frac{\gamma}{2\pi} \mu_0 \sqrt{(H_{\text{ext}} + H_{\text{ani}})(H_{\text{ext}} + H_{\text{ani}} + M_s)} \quad . \quad (1)$$

The fit is in good accordance with the experimental data and yields the values $M_s = 1003 \text{ kA/m}$ and $H_{\text{ani}} < 1 \text{ kA/m}$. This indicates again that the magneto-crystalline anisotropy of the soft magnetic CMFS is comparatively small and can be neglected in the following considerations.

After these preliminary measurements, the thin film was microstructured using electron beam lithography and ion milling. The investigated structures are stripes of different widths ranging from 1 to $10 \mu\text{m}$ with a length of $80 \mu\text{m}$. In order to excite spin waves in these magnetic microstructures, the shortened end of a coplanar waveguide (CPW) made of copper was placed on top of them. The Oersted fields created by microwave currents flowing in the CPW are suitable to excite spin dynamics in the Gigahertz range. The external magnetic field was applied transverse to the stripe in all cases. This results in a magnetization direction perpendicular to the wavevector of the propagating spin waves and, thus, Damon-Eshbach geometry [4]. A sketch of the sample layout is shown in Fig. 2.

To directly evaluate the damping of the Heusler compound CMFS by the observation of propagating spin waves in the waveguide, the spin-wave intensity was observed at different distances from the exciting antenna on a $4 \mu\text{m}$ wide stripe. To avoid any influence caused by the effect of mode beating [5], the intensity was measured and integrated over the entire width of the stripe for each distance from the antenna. Figure 3 shows the results of the integrated BLS intensity as a function of the distance from the antenna. The externally applied field in this measurement was $H_{\text{ext}} = 50 \text{ mT}$, and the excitation frequency was $f = 6.9 \text{ GHz}$. As can be seen in Fig. 3a, a non-vanishing intensity can still be observed for a distance of $22 \mu\text{m}$. Without further detailed evaluation of the data, this first result shows an important advantage of the CMFS material over

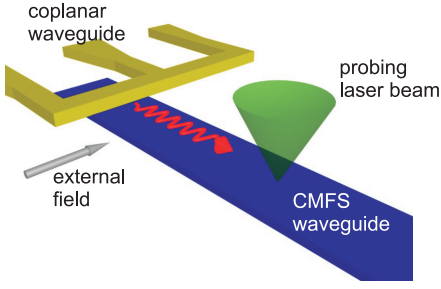


Fig. 2: Scheme of the sample layout. A 4 μm wide CMFS waveguide is magnetized transverse to the stripe by the external field. The shortened end of a coplanar waveguide serves to excite spin dynamics in the GHz range. The probing laser light of the BLS microscope is used to detect the spin-wave intensity.

the commonly used Permalloy ($\text{Ni}_{81}\text{Fe}_{19}$), in which propagation distances of 25 μm can hardly be observed. The signal-to-noise ratio as well as the excitation efficiency of spin dynamics in the Heusler waveguides seem to be improved compared to the situation in Permalloy waveguides. The improved excitation efficiency may be caused by the higher saturation magnetization of the Heusler compound leading to a higher torque of the dynamic Oersted fields of the antenna. By changing the applied microwave frequency, different spin-wave modes can be excited and their group velocity changes according to the spin-wave dispersion. Changing the excitation frequency in order to get a higher group velocity of the propagating spin waves results in even larger propagation distances than reported above. Even for distances of more than 75 μm the spin-wave signal was clearly observable on the background of the noise level. To get a more quantitative picture, the data in Fig. 3 was further evaluated. The observed decay of the spin-wave intensity can be described using an exponential equation:

$$I(x) = I_0 \exp\left(-\frac{2x}{\delta}\right) + b \quad , \quad (2)$$

where x is the distance from the antenna and δ is the decay length of the spin-wave amplitude. Equation 2 includes the factor 2 in the exponent to take into account the relation between the experimentally observed quantity - the intensity - and the quantity commonly used in theoretical deductions, namely the amplitude. Figure 3b shows the spin-wave intensity on a logarithmic scale to justify the assumption of an exponential decay. As expected the data points show a linear behavior and the fitting procedure according to Eq. 2 - as shown in Fig. 3a by the straight line - finally yields the decay length δ as a parameter. As described in Ref. [6], the magnetic Gilbert damping α can be calculated using the following equations:

$$\tau = \delta/v_G, \quad \alpha = \frac{1}{\tau\gamma\mu_0(H_{\text{eff}} + \frac{M_s}{2})} \quad , \quad (3)$$

where τ is the decay time of the spin-wave amplitude, v_G is the group velocity of the spin waves, γ is the gyromagnetic ratio of the free electron, μ_0 is the vacuum permeability, and H_{eff} is the effective field. The effective field $H_{\text{eff}} = H_{\text{ext}} + H_{\text{ani}} + H_{\text{demag}}$ for known material parameters, given the externally applied field and the waveguide geometry, can be calculated using the *object-oriented micromagnetic framework* (OOMMF). This package is open source software.³ The only parameter still missing in Eq. 3 is the group velocity v_G . The dispersion relation of spin waves in magnetic thin films and, thus, their group velocity can be calculated by using the analytical equation derived by B.A. Kalinikos and A.N. Slavin in 1986 [7].

³<http://math.nist.gov/oommf>

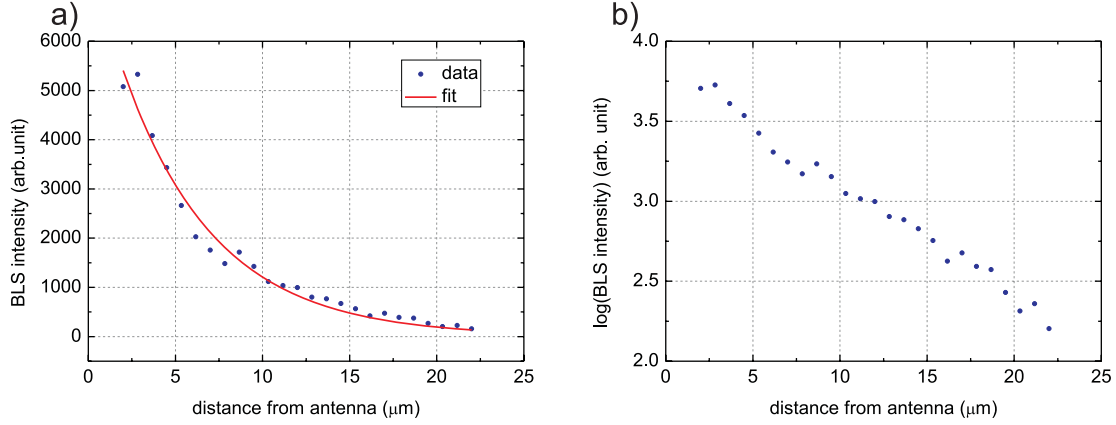


Fig. 3: BLS intensity integrated over the width of a 4 μm wide CMFS waveguide in dependence on the distance from the exciting antenna. The external field was $H_{\text{ext}} = 50 \text{ mT}$ and the excitation frequency was $f = 6.9 \text{ GHz}$. a) Directly measured BLS intensity and fit according to Eq. 2. b) Intensity on a logarithmic scale.

The results of these calculations according to Eqs. 2 and 3 for different measurements and experimental parameters are shown in Table 1. The two measurements with the excitation frequency of 6.0 GHz and the two measurements with the excitation frequency of 6.2 GHz have been performed in the same experimental situation to check the reproducibility of our experimental approach. All resulting Gilbert damping parameters α show values close to our expectations. The literature value for the intrinsic magnetic losses in CMFS is $\alpha = 3 \times 10^{-3}$ as reported by our Japanese co-workers [2]. All values presented here are slightly larger than the intrinsic damping of the material. A reason for this deviation is the fact that our BLS measurements do not only yield the intrinsic damping but also extrinsic contributions. Since we cannot exclude magnon-scattering processes - especially near the edges of the microstructured waveguides - we have to take into account a flow of energy from the observed spin-wave modes to the rest of the spin-wave spectrum and, thus, additional losses for the observed spin-wave modes. To avoid further losses due to non-linear effects, all measurements presented in Table 1 have been performed at microwave powers sufficiently low to ensure spin dynamics in the linear regime.

| frequency (GHz) | external field (mT) | decay length (μm) | group velocity (μm/ns) | decay time (ns) | $\alpha \times 10^{-3}$ |
|--------------------|------------------------|----------------------|---------------------------|--------------------|-------------------------|
| 6.0 | 40 | 8.38 | 4.22 | 1.98 | 4.3 |
| 6.0 | 40 | 8.65 | 4.22 | 2.05 | 4.2 |
| 6.2 | 40 | 11.85 | 7.24 | 1.64 | 5.2 |
| 6.2 | 40 | 11.23 | 7.24 | 1.55 | 5.5 |
| 7.5 | 40 | 9.05 | 9.05 | 1.12 | 7.7 |
| 6.9 | 50 | 10.64 | 5.90 | 1.80 | 4.7 |
| 7.2 | 50 | 16.72 | 7.68 | 2.18 | 3.9 |

Table 1: Summary of the results on the damping in the CMFS Heusler compound.

Besides the increase of these values with regard to the publication by T. Kubota et al. [2], there are variations of the resulting Gilbert damping parameters between measurements with different experimental parameters. Since the reproducibility of our experimental approach was shown and assuming the same intrinsic magnetic Gilbert damping for different spin-wave modes, there has to be another reason for these variations. One reason could be different possibilities for magnon-

scattering processes for different spin-wave modes and, thus, different extrinsic contributions to the net magnetic losses. For measurements with an externally applied field of $H_{\text{ext}} = 40 \text{ mT}$ the values increase with increasing applied microwave frequency. Since the inelastic magnon scattering caused by surface or edge roughness of the waveguide should decrease the magnon energy, it is depending on the density of states for modes with frequencies smaller than the applied microwave frequency. The increased density of states energetically below the directly excited mode could enhance the extrinsic contribution to the damping and serve as an explanation in this case.

However, since this explanation does not hold true in the case of an applied field $H_{\text{ext}} = 50 \text{ mT}$, there has to be an additional reason for the observations. First measurements (not shown here) using the phase-resolved BLS technique [8] indicate that the actual dispersion relation could deviate from the calculated one. This would lead to different group velocities which play an important role in the calculation of the damping parameter. Unfortunately, the electro-optical modulator (EOM) used to create a reference beam in our setup does not cover the full frequency range necessary for a thorough investigation of the dispersion relation according to the experimental parameters presented above. A promising approach for the estimation of the spin-wave wavelength for given frequency and, thus, the dispersion relation is the investigation of spin-wave interference. This technique has been demonstrated recently by P. Pirro et al. [9]. Samples according to this approach are in preparation.

In summary, we present the first observation of spin-wave propagation in a micro-structured Heusler waveguide. Propagation distances of more than $75 \mu\text{m}$ are observed. This increase of the observable propagation distance by a factor of three compared to the commonly used Permalloy qualifies CMFS as a very promising candidate for future *magnon spintronic* devices. The magnetic losses in the micro-structured waveguide could be evaluated using BLS spectroscopy with reasonable agreement to literature values. To get a more complete and accurate picture and to solve open questions regarding our experimental results, new samples have been designed and are in preparation.

We want to gratefully acknowledge financial support by the *DFG Research Unit 1464: ASPIMATT* and by the Graduate School of Excellence: Materials Science in Mainz. We thank our colleagues from the Nano+Bio Center of the TU Kaiserslautern for their assistance in sample preparation.

References

- [1] S. Trudel, O. Gaier, J. Hamrle, B. Hillebrands, *Magnetic anisotropy, exchange and damping in cobalt-based full-Heusler compounds: an experimental review*, J. Phys. D: Appl. Phys. **43**, 193001 (2010).
- [2] T. Kubota, S. Tsunegi, M. Oogane, S. Mizukami, T. Miyazaki, H. Naganuma, *Half-metallicity and Gilbert damping constant in $\text{Co}_2\text{Fe}_x\text{Mn}_{1-x}\text{Si}$ Heusler alloys depending on the film composition*, Y. Ando, Appl. Phys. Lett. **94**, 122504 (2009).
- [3] C. Kittel, *On the Theory of Ferromagnetic Resonance Absorption*, Phys. Rev. **73**, 155 (1948).
- [4] R.W. Damon, J.R. Eshbach, *Magnetostatic modes of a ferromagnet slab*, J. Phys. Chem. Solids **19**, 308 (1961).
- [5] V. Demidov, S. Demokritov, K. Rott, P. Krzysteczko, G. Reiss, *Mode interference and periodic self-focusing of spin waves in permalloy microstripes*, Phys. Rev. B **77**, 064406 (2008).
- [6] D.D. Stancil, *Phenomenological propagation loss theory for magnetostatic waves in thin ferrite films*, J. Appl. Phys. **59**, 218 (1986).
- [7] B. Kalinikos, A. Slavin, *Theory of dipole-exchange spin wave spectrum for ferromagnetic films with mixed exchange boundary conditions*, J. Phys.-Condens. Mat. **19**, 7013 (1986).
- [8] K. Vogt, H. Schultheiss, S.J. Hermsdoerfer, P. Pirro, A.A. Serga, B. Hillebrands, *All-optical detection of phase fronts of propagating spin waves in a $\text{Ni}_{81}\text{Fe}_{19}$ microstripe*, Appl. Phys. Lett. **95**, 182508 (2009).
- [9] P. Pirro, T. Brächer, K. Vogt, B. Obry, H. Schultheiss, B. Leven, B. Hillebrands, *Interference of coherent spin waves in micron-sized ferromagnetic waveguides*, Phys. status solidi B **248**, 2404 (2011).

4.13 Magneto-optical characterization of single crystalline $\text{Co}_2\text{FeAl}_{0.4}\text{Si}_{0.6}$ thin films on MgO substrates

A. Conca Parra, A. Ruiz Calaforra, B. Leven, and B. Hillebrands¹

In spite of the large research efforts of the last decade and the large number of publications related to Heusler compounds, the interest of the magnetism community in this family of materials is far from being decaying. The original promise of a 100% spin polarization predicted by theoretical studies has been partially corroborated (at least for some compounds) by the high tunneling magnetoresistance (TMR) values [1]. However, in this case, the large decrease of the TMR ratio with increasing temperature is still an open issue. Furthermore, there is still a long way to understand why certain systems are not showing the expected high polarization.

Some additional properties make Heusler thin films good candidates in other fields. For instance, the low damping values that had been reported for certain compounds [2–6], make them suitable for spinwave experiments where propagation with reduced attenuation is required. For some compounds, the measured Gilbert damping constants are smaller than for permalloy, the standard material for many experiments. A strong anomalous Hall effect is also present in Heusler films [7] with a remarkable low temperature dependence which is of interest for high temperature magnetic sensors. Here we report on results obtained in collaboration with T. Graf, F. Casper and C. Felser in the framework of the BMBF-project MultiMag. We present investigations on epitaxial thin films of the full Heusler compound $\text{Co}_2\text{FeAl}_{0.4}\text{Si}_{0.6}$ (CFAS). The films were deposited at room temperature on MgO (100) substrates using dc magnetron sputtering and annealed *ex-situ* at 500 °C for 30 min in a nitrogen atmosphere. The CFAS films are 30 nm thick and capped by 4 nm Al. The films were prepared using an industrial deposition tool at the fabrication plant of Sensitec GmbH [13]. The films were deposited directly on the MgO substrate and with different seed layer materials. The influence of the seed layer composition on the magnetic properties of the films is analyzed. Four different alternatives were studied: CFAS films directly on the native MgO substrate (type A), with MgO seed layer (type B), with Cr seed layer (type C), and with MgO/Cr double seed layer (type D). The Cr and MgO layers were grown by an ion beam deposition process.

The X-Ray diffraction (XRD) measurements of the films carried out by T. Graf show that CFAS grows epitaxially in all the cases but with different crystalline properties. The (111) superstructure

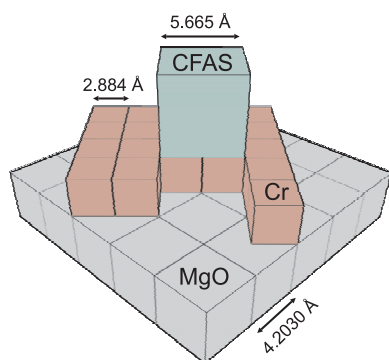


Fig. 1: Schematic representation of the epitaxial relationship of CFAS on a Cr buffer layer on MgO (100).

¹In collaboration with T. Graf (1)(2), F. Casper (1), C. Felser (1), (1) Institut für Anorganische Chemie und Analytische Chemie, Johannes Gutenberg-Universität, Staudinger Weg 9, D-55099 Mainz, Germany. (2) IBM Almaden Research Center, 650 Harry Rd., San Jose, CA 95120, USA

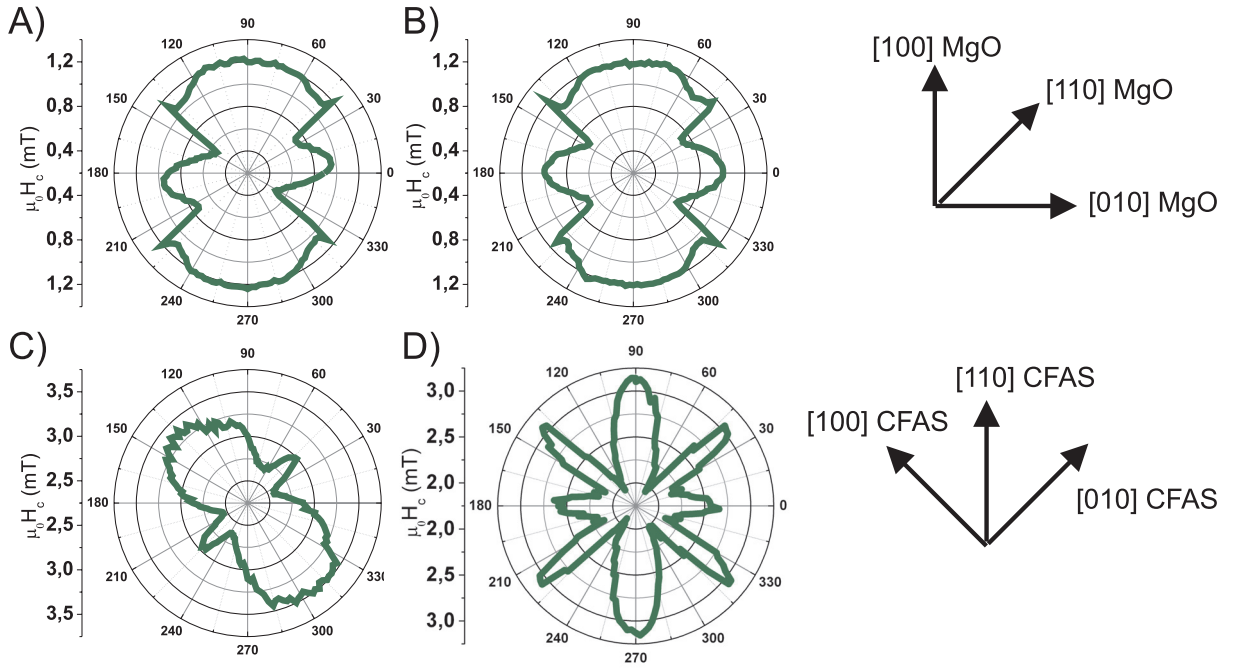


Fig. 2: Angular dependence of the in-plane coercive field of CFAS samples deposited directly on a MgO (100) substrate (a), with an additional 10.5 nm MgO seed layer (B), with a 20 nm Cr seed layer (C) and with a double seed layer 10.5 nm MgO/20 nm Cr (D).

reflection is visible in the Cr-seeded film (type C), proving $L2_1$ order. It is absent in the other films, nonetheless, the presence of the (220) reflections assures at least B2 order. In all cases the CFAS and Cr unit cells are rotated 45° with respect to the unit cell of MgO, as schematically shown in Fig. 1. Thus, the MgO [110] axis is parallel to the CFAS [100] axis. This epitaxial relationship is also valid when no Cr seed layer is used.

To study the magnetocrystalline anisotropy of the CFAS samples magneto-optical Kerr effect (MOKE) magnetometry was employed. The MOKE setup corresponds to the longitudinal geometry with an angle of incidence of 45° . A rotational stage allows for magnetization reversal measurements for any in-plane orientation of the sample with respect to the applied field. In this way, hysteresis loops were recorded every 2° and the coercive field H_C was obtained. The spatial resolution is about $100\mu\text{m}$.

Figure 2 shows the polar representation of the angular dependence of the coercive field. The top graphs correspond to CFAS samples deposited directly on crystalline MgO (100) substrates (type A) and with an additional 10 nm MgO seed layer (type B). The angular dependence of H_C is very similar for both samples, exhibiting a dominant uniaxial anisotropy with a small biaxial contribution. The easy axis is parallel to the [110] direction in CFAS (and therefore parallel to the [100] direction in MgO). A similar behavior was recently reported for the related compound $\text{Co}_2\text{FeAl}_{0.5}\text{Si}_{0.5}$ [10]. However, there is a small difference visible when comparing graphs (a) and (B). While in (B), both easy axes are perpendicular oriented, in (A) the angle between the easy axes differs from 90° , resulting in an asymmetric polar plot. The previously discussed XRD measurements show a better crystalline order for sample (A) deposited directly on the MgO substrate. For this reason, the reason for this asymmetry remains unclear.

In both of the previous cases (types A and B), sharp peaks with increased H_C values can be recognized at 40° , 140° , 220° , and 320° . Similar structures have also been observed before in

Cr-seeded $\text{Co}_2\text{Cr}_{0.6}\text{Fe}_{0.4}\text{Al}$ samples [12]. The interpretation of this peaks will be discussed later in this Report.

The bottom graphs of Fig. 2 show the results for the samples deposited on 20nm Cr seed layer (type C) and a 10.5 nm MgO / 20nm Cr seed layer (type D). The sample in (C) presents a dominant uniaxial magnetic anisotropy. The easy axis is rotated by 45° in comparison with samples (A) and (B) and is now parallel to the [100] CFAS axis ([110] MgO axis). This change of the orientation of the easy axis with respect to the crystalline axes of the CFAS is quite remarkable. Similar behavior has also been published for the Heusler compound $\text{Co}_2\text{Cr}_{0.6}\text{Fe}_{0.4}\text{Al}$ [12]. There, a rotation of the easy axis with respect to the crystalline axis of $\text{Co}_2\text{Cr}_{0.6}\text{Fe}_{0.4}\text{Al}$ was observed when comparing films deposited with Fe and Cr seed layer.

The type D sample, deposited on a double MgO/Cr seed layer, shown in Fig. 2D, has a peculiar anisotropy which differs substantially from the expected behavior. It has to be remembered first, that the crystallographic order of this sample is B2 instead of the $L2_1$ of the film in (C). Nevertheless, the use of a Cr seed layer should also induce that the easy axis lays parallel to the [100] CFAS axis, resulting in a behavior similar to (C). However, the easy axis is again parallel to the [110] CFAS direction as in (A) and (B). Furthermore, additional structures appear which can be interpreted as an extreme development of the peaks observed in (A) and (B).

The type C and D samples prove that the orientation of the easy axis is not only dependent on the material of the seed layer but also of its detailed growth conditions. We believe that the rotation of the easy axis, for CFAS as well as for the reported $\text{Co}_2\text{Cr}_{0.6}\text{Fe}_{0.4}\text{Al}$ case [12], is stress-mediated. It must be noted that the relative misfit between the lattice constants of CFAS and the underlying layer is not only material dependent but may also vary for the same material. Let us consider first the case of the system Cr seed layer/MgO substrate. The lattice mismatch is of $(2a_{\text{Cr}} - \sqrt{2}a_{\text{MgO}})/a_{\text{MgO}} = 3.1\%$ ($a_{\text{MgO}} = 4.2030 \text{ \AA}$, $a_{\text{Cr}} = 2.8840 \text{ \AA}$) [9]. This value is large and produces a large stress in the first atomic layers of Cr. Ideally, this stress should relax with the subsequent layers and vanish at the interface with the CFAS film. However, as shown by the XRD measurements, this is not the case and the relaxation is incomplete. The Cr seed is 0.7% compressively strained. Consequently, the actual misfit at the interface Cr/CFAS varies depending on the thickness of the seed layer and the growth conditions. The fact that the Cr-seeded film has the smallest lattice constant which also deviates the most from the bulk value (5.665 \AA [8]), is a hint of the possible role of the stress in the rotation of the easy axis orientation. However, in any case, further investigations are required to confirm this point.

For a deeper understanding of the magnetic behavior occurring at the angles where the sharp structures appear on the CFAS samples from panels (A) and (B) in Fig. 2, scanning MOKE microscopy imaging was performed. For this purpose, a microfocused laser spot (size $\approx 1 \mu\text{m}$) was scanned over the sample and the Kerr rotation for each point was measured. This technique permits the visualization of magnetic domain formation occurring during the magnetization reversal process. The experimental setup is described in [11]. The scanned area comprises $500 \mu\text{m} \times 500 \mu\text{m}$. From the experimental values the orientation of magnetization was deduced. A series of field values in the region where the switching of magnetization takes place was chosen.

In Fig. 3, three sets of MOKE images are presented in accordance to three different orientations of the MgO-seeded CFAS film. For each of them, the corresponding hysteresis curve is shown at the left. Figure 3a displays the case in which the field is applied at 60° from the easy axis direction; this is the 'out-of-peak' configuration. The circles on the hysteresis curve represent the field values for which the MOKE imaging was carried out. By applying a field of 0.53 mT, which coincides with the jump in the hysteresis loop, the image shows how the magnetization in a large percentage

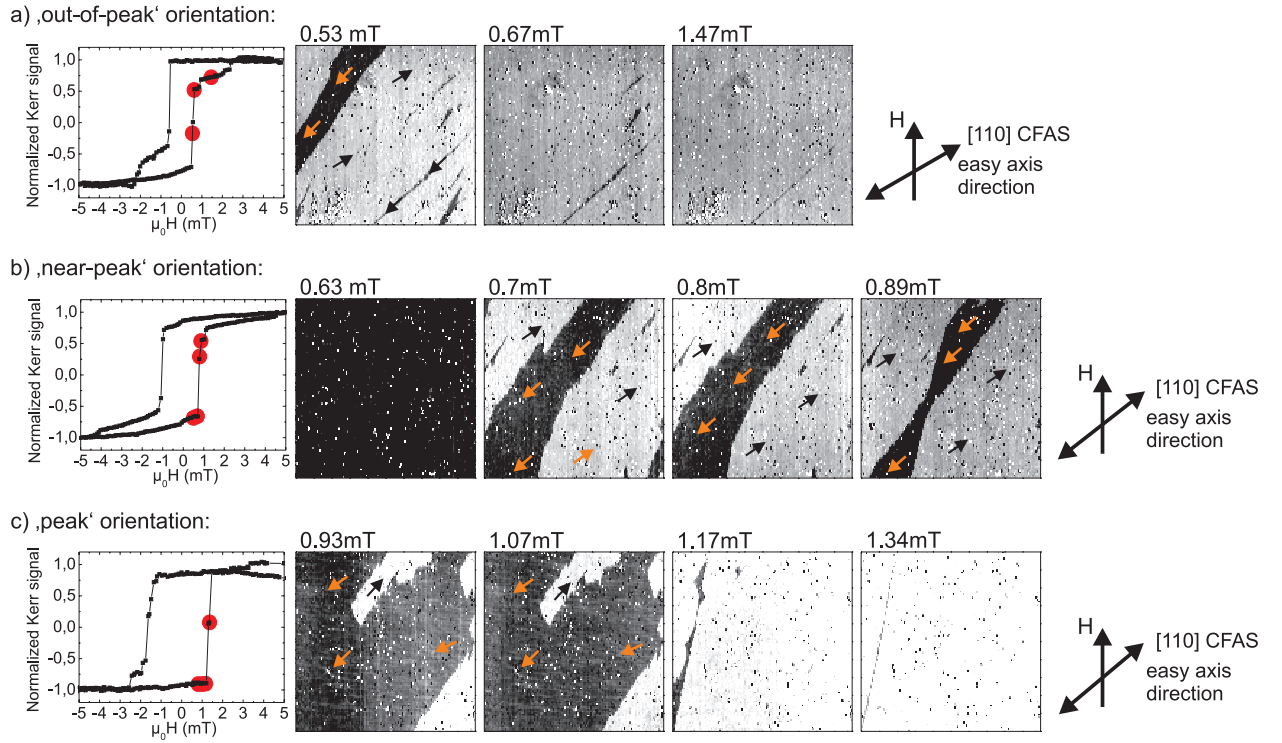


Fig. 3: Scanning Kerr-microscope imaging of the magnetization reversal process in a MgO-seeded CFAS film at different orientations of the applied field respect to the easy axis of the film. The circles on the corresponding hysteresis curve represent the field values for which the MOKE imaging was carried out. The size of the scanned regions is $500\mu\text{m} \times 500\mu\text{m}$.

of the scanned area has already switched, although strip-shaped domains of $75\mu\text{m}$ width are still in the process of switching their magnetization. Arrows pointing in the direction of magnetization have been introduced for a better comprehension of the images. For an increased field of 0.67 mT the resulting image shows a nearly fully switched magnetization state, except for thin domain structures. In the third image, taken for a field of 1.47 mT , the magnetization configuration in the scanned area shows hardly any change.

In the case of Fig. 3b the field is applied at an angle of 52° with respect to the easy axis direction, 2° apart from the peak orientation (i.e. 'near-peak' orientation). An homogeneously magnetized state can be seen in the first image, corresponding to a field of 0.63 mT . By increasing the field, the magnetization starts to switch forming stable domains oriented in the easy axis direction with similar width as the ones in the 'out-of-peak' configuration. Also, thin stripe domains appear for this configuration.

A similar behavior can be seen for the 'on-peak' configuration in Fig. 3c. Here, the easy axis direction forms an angle of 50° with the external applied field direction. For fields of 0.93 mT and 1.07 mT the magnetization has started to switch, but a sharp change of the magnetization occurs for fields above 1.17 mT . This is consistent with the resulting rectangularly shaped loop in the corresponding hysteresis.

As mentioned before, such peak structures in the angular dependence of the coercive field have also been observed in CCFA/Cr samples [12]. In the referred case, the sample presented a four-fold symmetry and the sharp peaks pointed in the hard axis orientations. Also via MOKE imaging (non-scanning), the peaks were described as a result of a special checker-board domain configuration

taking place during the magnetic reversal process [12]. In contrast, our results reveal that the peaks exhibited for CFAS thin films deposited on MgO substrates are not a consequence of any special or metastable domain configuration. The increase of H_C at the peaks positions may be a result of a magnetic frustration at certain orientations between two easy axes.

In summary, CFAS thin films were epitaxially grown on MgO substrates. L2₁-order was achieved for samples deposited on 20nm Cr buffer layers and annealing at 500°C. Films grown on MgO-buffer layers show B2-type order. The magneto-optical characterization shows the presence of an overall uniaxial anisotropy in all CFAS films with a biaxial contribution with a strong dependence on the nature of the used seed layer. A rotation of the easy axis orientation with respect to the crystalline axis has been observed when using Cr as single seed layer but not in combination with MgO. This rotation is tentatively explained by the presence of stress in the films. Additional research is needed to confirm this point.

Financial support by the BMBF *MultiMag* (VDI- TZ 13N9913) project is gratefully acknowledged. The authors also thank Sensitec GmbH for the technical support and fruitful discussions.

References

- [1] Y. Sakuraba, M. Hattori, M. Oogane, Y. Ando, H. Kato, A. Sakuma, T. Miyazaki, H. Kubota, *Giant tunneling magnetoresistance in Co₂MnSi/Al-O/Co₂MnSi magnetic tunnel junctions*, Appl. Phys. Lett. **88**, 192508 (2006).
- [2] S. Trudel, O. Gaier, J. Hamrle, B. Hillebrands, *Magnetic anisotropy, exchange and damping in cobalt-based full-Heusler compounds: an experimental review*, J. Phys. D **43**, 193001 (2010).
- [3] R. Yilgin, Y. Sakuraba, M. Oogane, S. Mizumaki, Y. Ando, T. Miyazaki, *Anisotropic intrinsic damping constant of epitaxial Co₂MnSi Heusler alloy films*, Japan. J. Appl. Phys. **46**, L205 (2007).
- [4] M. Oogane, T. Wakitani, S. Yakata, R. Yilgin, Y. Ando, A. Sakuma, T. Miyazaki, *Magnetic damping in ferromagnetic thin films*, Japan. J. Appl. Phys. **45**, 3889 (2006).
- [5] T. Kubota, S. Tsunegi, M. Oogane, S. Mizukami, T. Miyazaki, H. Naganuma and Y. Ando, *Half-metallicity and Gilbert damping constant in Co₂Fe_xMn_{1-x}Si Heusler alloys depending on the film composition*, Appl. Phys. Lett. **94**, 122504 (2009).
- [6] S. Mizukami, D. Watanabe, M. Oogane, Y. Ando, Y. Miura, M. Shirai, T. Miyazaki, *Low damping constant for Co₂FeAl Heusler alloy films and its correlation with density of states*, J. Appl. Phys. **105**, 07D306 (2009).
- [7] E. Vilanova Vidal, H. Schneider, G. Jakob, *Influence of disorder on anomalous Hall effect for Heusler compounds*, Phys. Rev. B **83**, 174410 (2011).
- [8] B. Balke, G.H. Fecher, C. Felser, *Structural and magnetic properties of Co₂FeAl_{1-x}Si_x*, Appl. Phys. Lett. **90**, 242503 (2007).
- [9] *Pearson's Handbook of crystallographic data for intermetallic phases*, ASM International, (1996).
- [10] S. Trudel, G. Wolf, J. Hamrle, B. Hillebrands, P. Klaer, O. Gaier, M. Kallmayer, H.J. Elmers, H. Sukegawa, W. Wang, K. Inomata, *Effect of annealing on Co₂FeAl_{0.5}Si_{0.5} thin films: A magneto-optical and x-ray absorption study*, Phys. Rev. B **83**, 104412 (2011).
- [11] T. Sebastian, A. Conca, G. Wolf, H. Schultheiß, B. Leven, B. Hillebrands, *Magneto-optical investigation of the shape anisotropy of individual micron-sized magnetic elements*, J. Appl. Phys. , **110**, 083909 (2011).
- [12] J. Hamrle, S. Blomeier, O. Gaier, B. Hillebrands, R. Schäfer, M. Jourdan, *Magnetic anisotropies and magnetization reversal of the Co₂Cr_{0.6}Fe_{0.4}Al Heusler compound*, J. Appl. Phys. **100**, 103904 (2006).
- [13] www.sensitec.com

4.14 Ion beam patterning of antiferromagnetic elements in the submicron regime

R. Neb, T. Sebastian, P. Pirro, and B. Hillebrands¹

Ion beam irradiation is an established tool to locally modify the properties of a system. There are two common ways to realize this: By using a focused ion beam (FIB) tool, modifications can be created in the micron and sub-micron regime, limited by the finite spatial size of the beam (see [1] and [2] for an introduction). Also, a resist mask can be patterned and then broad beam irradiation can be applied. We use both techniques to pattern an antiferromagnetically coupled Fe/Cr/Fe-trilayer. These trilayers consist of two 10nm thick Fe layers, separated by a 0.7nm thick Cr interlayer. Without the interlayer the two Fe layers will couple ferromagnetically, but due to interlayer exchange coupling the Fe layers of the trilayer couple antiferromagnetically. Ion beam irradiation leads to a partial destruction of the interlayer, and thus to appearance of a ferromagnetic coupling of the two Fe layers in the irradiated areas. For a detailed description of the fabrication process see [3]. In the FIB process 30keV Ga⁺-ions were used; for the mask technique we employed a broad beam source with 5keV He⁺-ions and a resist mask of 400nm thick PMMA. With this irradiation procedure we are able to create elements of ferromagnetic coupling in an antiferromagnetic environment. The main advantage is that it can be realized without altering the topography. Thus the interaction between two elements is also governed by exchange interaction instead of solely dipolar interaction. In an earlier approach, a large ion dose was applied (see [2]

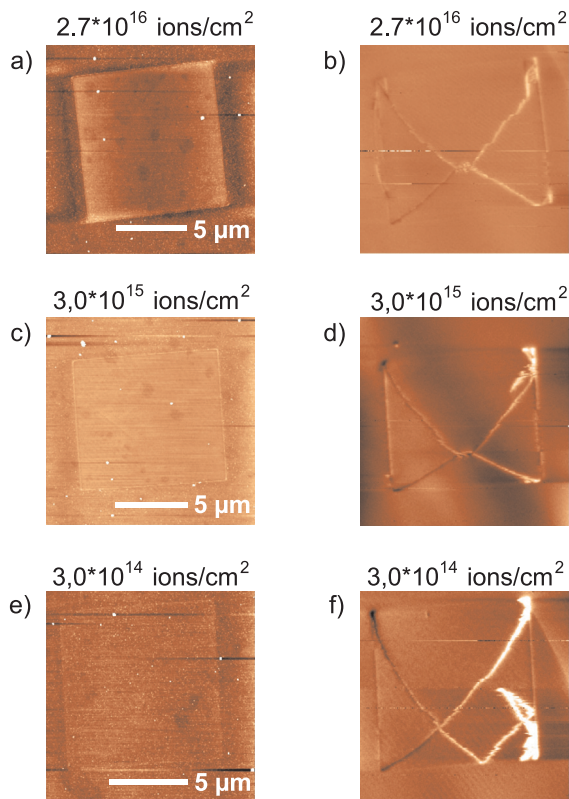


Fig. 1:

Atomic Force Microscopy (AFM) and Magnetic Force Microscopy (MFM) images of irradiated squares for different ion doses. a), c) and e) show AFM images of elements which were irradiated with $2.7 \cdot 10^{16}$ ions/cm², $3 \cdot 10^{15}$ ions/cm² and $3 \cdot 10^{14}$ ions/cm², respectively. The corresponding magnetic contrast images are shown in b), d) and f). All three ion doses lead to a Landau domain configuration typical for square ferromagnetic elements of this size. Some distortions from the fourfold symmetry can be observed which can be attributed to stray field effects of the MFM tip.

Because antiferromagnetically coupled areas will not exhibit visible domain walls due to compensation of the stray fields, the formation of such Landau domains is a proof for ferromagnetic coupling in the irradiated regions. Note that for the lowest ion dose the topographic exposure between irradiated and non-irradiated areas is below the noise level.

¹In collaboration with B. Reuscher, A. Zeuner (IFOS Kaiserslautern); S. Pofahl, R. Schäfer (IFW Dresden).

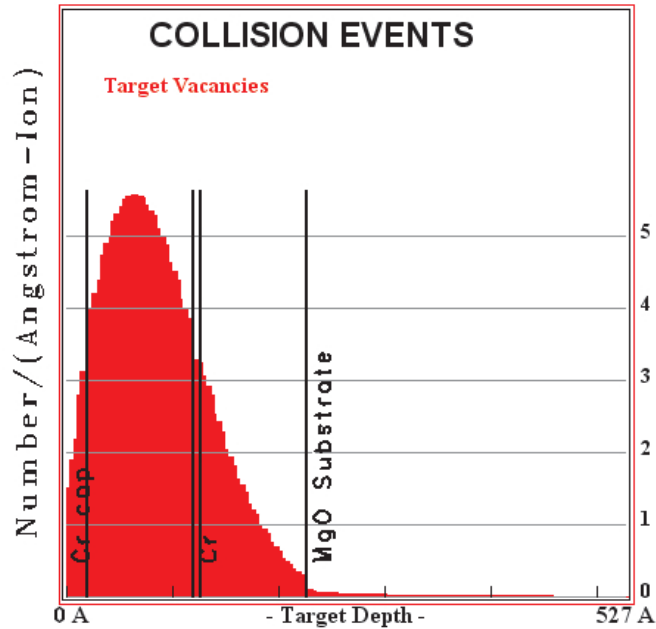


Fig. 2: Number of generated vacancies per ion and penetration depth, as calculated by SRIM. For the Cr interlayer a value of about 3.3 vacancies/Å · ion yields a total of 23 vacancies per ion in the interlayer.

and [4]). It was proven that ion irradiation yields the desired results. Also the limitations of the procedure were elaborated, and especially it was found that independent elements must have a distance of at least $1\text{ }\mu\text{m}$. We show here that this limitation can be overcome by choosing a much smaller ion dose.

In a first step, we determined the minimum ion dose still revealing the desired change in the interlayer coupling behavior. The results are summarized in Fig. 1. For this purpose, $20 \times 20\text{ }\mu\text{m}^2$ squares were irradiated by FIB with different doses and analyzed with Magnetic Force Microscopy (MFM). Ferromagnetic elements of this size show a typical (slightly distorted) Landau pattern in zero field (see Fig. 1). The Landau pattern is still persistent for ion doses as low as $3 \cdot 10^{14}\text{ ions/cm}^2$ and vanishes only if the dose is chosen even lower. Note that the topography is nearly unchanged for this low ion dose (see Fig. 1c), sputtering and implantation effects are negligible in this case.

The result obtained for the minimum dose is in excellent agreement with numerical calculations and other experimental observations. The SRIM software ("The Stopping and Range of Ions in Matter", see [5]) was used to estimate the damage caused by the ion beam. This was done by numerically computing the target vacancies per penetration depth (see Fig. 2). It was assumed that a change in the coupling behavior requires a significant damaging of the interlayer. By integrating the collision curve over the interlayer we obtain a value of about 23 collisions per ion leading to vacancies. For calculation purposes we assumed that every collision hits a different atom, which is well justified for low ion doses. In a $1 \times 1 \times 0.7\text{ nm}^3$ cuboid there are 84 Cr atoms. Thus an ion dose of $3 \cdot 10^{14}\text{ ions/cm}^2$ leads to a 80% destruction of the interlayer. Since this is not a low ion dose anymore, the true value will be somewhat lower, but it is obvious that with our applied ion dose of $3 \cdot 10^{14}\text{ ions/cm}^2$ we are indeed in the critical regime. On the other hand, an applied dose of $2.7 \cdot 10^{16}\text{ ions/cm}^2$ as used in earlier works leads to a massive overkill in the interlayer region.

Rettnner et al. (see Ref. [6]) have analyzed the effect of 30 keV Ga^+ -ion beams on a different system, but derived a similar critical ion dose. This is not surprising, since their reported effect is also based on a significant damage and intermixing of the layer structure. Of course the used

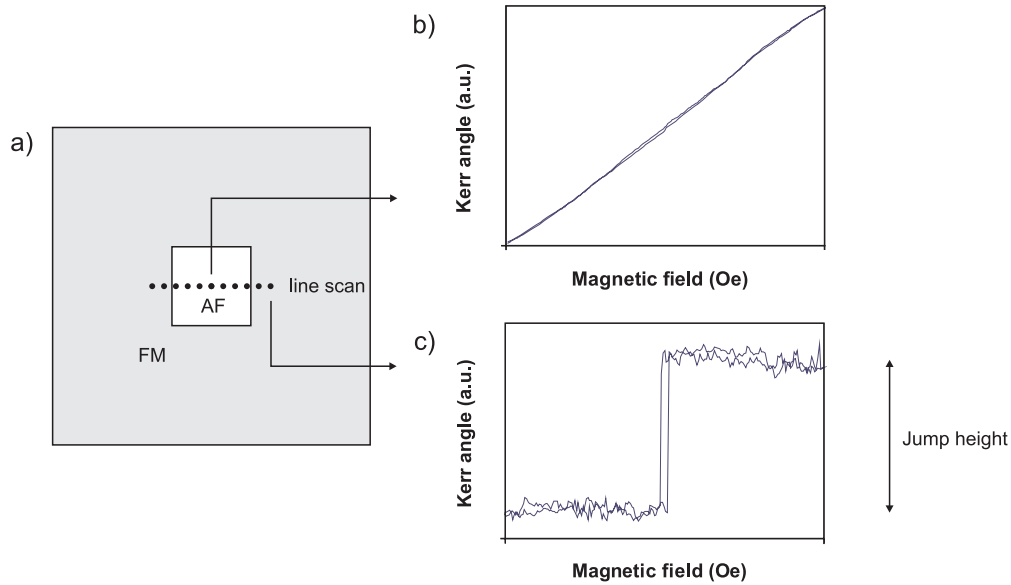


Fig. 3: a) Sketch of a MOKE linescan across an antiferromagnetic area embedded into a surrounding ferromagnetic area. Typical hysteresis curves for the ferromagnetic (FM) and antiferromagnetic (AF) case, as well as the parameter "jump height" are shown in b) and c). In the border region between FM and AF areas, the hysteresis curve will be a mixture of FM and AF curves, and the jump height can be used to deduce the corresponding fractions.

materials have different properties to a certain extent, but the order of magnitude is comparable.

The most important measure for practical applicability of this technique is the minimum distance between two independent, irradiated elements. Below this distance two elements influence each other and cannot be treated separately. For a large ion dose of $2.7 \cdot 10^{16}$ ions/cm² this distance was determined to be about 1 μ m (see [4] for details). Such a distance limits possible application to a great extent.

In order to determine the limits of size reduction, we created antiferromagnetic elements in a ferromagnetic environment. This was made by irradiating a large area (typically $50 \times 50 \mu\text{m}^2$), while leaving a non-irradiated square of $10 \times 10 \mu\text{m}^2$ in the center of the area. We realized these samples employing the FIB as well as the mask technique, but due to brevity here only the results of the mask technique are presented. Three different ion doses were used: $2.7 \cdot 10^{16}$ ions/cm², $3 \cdot 10^{15}$ ions/cm² and $3 \cdot 10^{14}$ ions/cm². Unfortunately, it is difficult to determine the kind of coupling using the MFM, because the stray fields of antiferromagnetically coupled layers compensate each other, resulting in no measurable signal. So we chose another approach: By applying Magneto-Optical Kerr Effect microscopy (MOKE-microscopy) we were able to measure the local hysteresis curves and from their shape to determine the coupling behavior. Curves from the ferromagnetic area show a strong jump of the Kerr angle around zero field, while antiferromagnetic curves show a gradual increase of the Kerr angle with the external field (see Fig. 3b, c for a sketch of typical curves in ferromagnetic and antiferromagnetic areas).

A line scan (see Fig. 3a) enabled us to deduce the true size of the antiferromagnetic area from the measured hysteresis curves. For this purpose, the finite laser spot size of the MOKE microscope must also be taken into account, since at the border the signals of the inner antiferromagnetic as well as the outer ferromagnetic region will overlap in the hysteresis curve. As a quantity to be measured the jump height around zero field was chosen. Since this height is always maximal for pure ferromagnetic coupling and zero for antiferromagnetic coupling, the overlap effect can thus

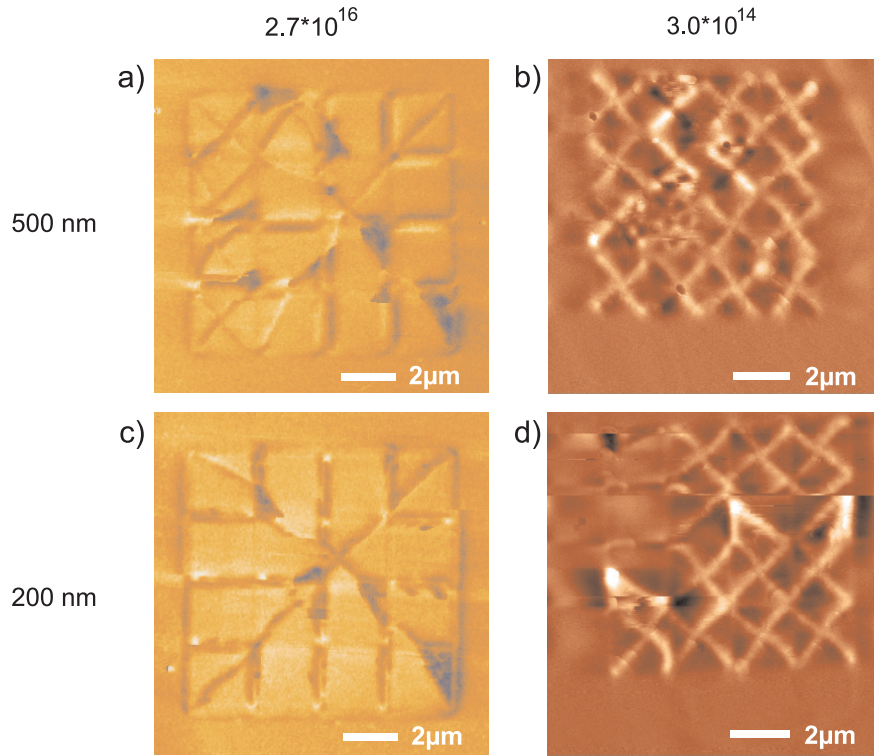


Fig. 4: Different 4×4 arrays compared with MFM imaging. Images a) and c) were taken from Ref. [4] and show arrays irradiated with $2.7 \cdot 10^{16}$ ions/cm², images b) and d) show arrays irradiated with $3 \cdot 10^{14}$ ions/cm². For arrays a) and b) the distance between the squares is 500 nm, for arrays c) and d) it is 200 nm. It is clearly visible that coupling over the whole array is only present for the large ion dose. For the small ion dose, the elements behave independently even if brought together very close.

be eliminated. The concrete mathematical computations are omitted here due to brevity.

For the largest ion dose, the earlier results could be reproduced, but with a different interpretation. The true width of the antiferromagnetic area is about $1 \mu\text{m}$ smaller than it should be according to the mask used for irradiation, as it was similarly observed in [4]. However, there it was attributed to the influence of exchange coupling. If this is correct, then we expect the same result for lower ion doses as well. But the obtained results are different: For the two lower doses, the narrowing effect vanishes, and the true width of the antiferromagnetic area coincides (within the measurement accuracy) with that of the non-irradiated region. Therefore, in contrast to former assumptions, we conclude that the irradiation itself must be the reason for this effect.

Now the advantage of the resist mask technique in this case becomes clear: With the FIB technique similar results were obtained, but there the effects of the long range beam tail (like higher order diffraction discs) might have had an influence. This is not possible with the resist mask technique, since now all areas which must not be irradiated are covered by a thick mask impenetrable to the beam. So the explanation of minor irradiation in the vicinity of the ferromagnetic areas is ruled out. Instead, we propose that secondary effects like surface channeling are responsible for the observed narrowing effect. However, this explanation is difficult to test due to the low doses involved.

The obtained results imply another conclusion: If the broadening of the ferromagnetic areas arises only due to minor irradiation of the vicinity and not due to exchange coupling, then the observed fact that elements closer than $1 \mu\text{m}$ influence each other should vanish for lower ion doses.

We have corroborated this conclusion with the following setup: Arrays of 4×4 identical squares

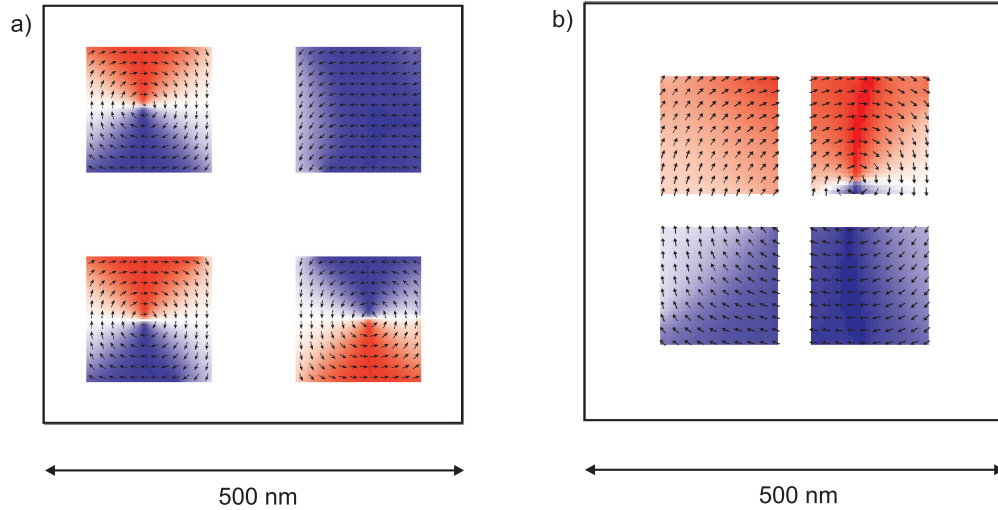


Fig. 5: OOMMF Simulation of arrays of 2×2 identical ferromagnetic square elements with dimensions of $150 \times 150 \text{ nm}^2$ and a distance of a) 100 nm and b) 40 nm. The squares are embedded into an antiferromagnetically coupled environment (the large white square). The colors (or levels of gray) and the arrows represent the magnetization direction of the sample. [8]

It is clearly visible that no coupling takes place between the elements for a distance of 100 nm. This changes for a distance of 40 nm.

with dimensions of $2 \times 2 \mu\text{m}^2$ were fabricated with a certain distance between each square using the FIB technique. These distances were decreased subsequently until coupling between the squares was visible. The results are shown exemplarily in Fig. 4 and compared to those obtained for higher doses [4]. Without coupling, all squares should show separate Landau structures; if they couple with each other, the whole array should exhibit one common Landau structure (see Fig. 4). As expected, for low ion doses no coupling is visible even for distances as low as 200 nm. Only for the smallest distance of 100 nm the array behaves as a whole (not shown here). This is a consequence of two effects: The finite size of the ion beam, together with a short-range coupling of the patterned elements. In our case, the intensity of the beam has dropped to a factor of one half at about 20 nm, so that in an additional area of 40 – 50 nm between two squares the interlayer is sufficiently damaged to destroy the antiferromagnetic coupling. Thus the remaining 50 nm should be a consequence of the intrinsic magnetic coupling between the elements.

We have tested this hypothesis using the micromagnetic simulation software OOMMF ("Object Oriented MicroMagnetic Framework", [7]). An array of 2×2 identical ferromagnetic squares with dimensions of $150 \times 150 \times 5 \text{ nm}^2$ and distances of 100 nm was embedded into an antiferromagnetically coupled environment with dimensions of $500 \times 500 \times 5 \text{ nm}^2$. The result (without the environment) can be seen in Fig. 5a. It is obvious that the four squares do not couple to each other. However, for distances of 40 nm or less, a mutual influence between the squares can be observed (see Fig. 5b). Adding up the coupling and the irradiation effects, a minimum distance of 100 – 150 nm between two independent elements must be maintained. This coincides with our observations.

Comparison with Ref. [9] shows that the technique of ion irradiation can also compete with topographic methods if it comes to sub-micron-sized patterning. The minimum distance of independent topographic elements roughly coincides with the minimum distance of embedded elements created by ion beam irradiation.

In summary we have shown that it is possible to create ferromagnetically coupled elements in an

antiferromagnetically coupled environment by low ion dose irradiation. This irradiation does not alter the topography, thereby creating elements which are truly embedded into the surrounding. In contrast to high ion dose irradiation, the elements can be brought together as close as 200 nm without coupling to each other. The limiting factors are the ion beam diameter and the intrinsic magnetic coupling of the elements, which could be demonstrated by micromagnetic simulations.

Financial support by the Deutsche Forschungsgemeinschaft (HI 380/18-3) and the Graduiertenkolleg 792 is gratefully acknowledged.

References

- [1] S.O. Demokritov, C. Bayer, S. Poppe, M. Rickart, J. Fassbender, B. Hillebrands, D.I. Kholin, N.M. Kreines; O.M. Liedke, *Control of interlayer exchange coupling in Fe/Cr/Fe trilayers by ion beam irradiation*, Phys. Rev. Lett. **90**, 097201 (2003).
- [2] S. Blomeier, P. Candeloro, B. Hillebrands, B. Reuscher, A. Brodyanski, M. Kopnarski, *Micromagnetism and magnetization reversal of embedded ferromagnetic elements*, Phys. Rev. B **74**, 184405 (2006).
- [3] S. Blomeier, B. Hillebrands, V.E. Demidov, S.O. Demokritov B. Reuscher, A. Brodyanski, M. Kopnarski, *Magnetic patterning of Fe/Cr/Fe(001) trilayers by Ga⁺ ion irradiation*, J. Appl. Phys. **98**, 093503 (2005).
- [4] S. Blomeier, B. Hillebrands, B. Reuscher, A. Brodyanski, M. Kopnarski, R.L. Stamps, *Exchange interaction and magnetic domain formation in periodically inhomogeneous magnetic media*, Phys. Rev. B **77**, 094405 (2008).
- [5] <http://www.srim.org>
- [6] C.T. Rettner, S. Anders, J.E.E. Baglin, T. Thomson, B.D. Terris, *Characterization of the magnetic modification of Co/Pt multilayer films by He⁺, Ar⁺ and Ga⁺ ion irradiation*, Appl. Phys. Lett. **80**, 279 (2002).
- [7] M.J. Donahue, D.G. Porter, Report NISTIR 6376, National Institute of Standards and Technology, Gaithersburg, MD (1999)
- [8] Used parameters: uniform exchange constant $A = 2.1 \cdot 10^{-12}$, cubic anisotropy constant $K_1 = 4.5 \cdot 10^4$, saturation magnetization $M_S = 1.7 \cdot 10^6$, bilinear coupling constant $\sigma = -1.5 \cdot 10^{-3}$, biquadratic coupling constant $\sigma_2 = -1.5 \cdot 10^{-4}$, cellsize $2.5 \cdot 10^{-9} \times 2.5 \cdot 10^{-9} \times 1 \cdot 10^{-9}$, damping parameter $\alpha = 0.2$.
- [9] M. Bolte, R. Eiselt, G. Meier, D.-H. Kim, P. Fischer, *Real space observation of dipolar interaction in arrays of Fe microelements*, J. Appl. Phys. **99**, 08H301 (2006).

4.15 Microscopic magnetic structuring of a spin-wave waveguide by ion implantation in a $\text{Ni}_{81}\text{Fe}_{19}$ layer

*B. Obry, T. Meyer, P. Pirro, T. Brächer, R. Neb, and B. Hillebrands*¹

The ability of magnetic patterning has contributed considerably to advancing the field of magnetization dynamics onto the microscopic scale. In particular, investigations on the quantization and propagation of spin waves have benefited from the fabrication of microscopic waveguides, dots and rings with lateral dimensions in the order of the spin waves' wavelength [1–7]. Usually, the patterning process consists of the deposition of a magnetic layer and the selective removal of those regions which are not part of the considered structure. As a consequence, the boundaries of the magnetic material imply variations of the sample's topography. This can lead to difficulties in the design of magnetic multilayers, e.g. at two crossing waveguides, where the additional topography can cause undesirable stray fields. Furthermore, if small magnetic objects are exposed to intense microwave fields (excitation of spin waves) or investigated by laser spectroscopy (Brillouin light scattering), heating effects have to be taken into account. Thus a method to tailor the magnetic structure of a material without major changes of its topography will find a large number of applications.

Ion beam irradiation or ion implantation of ferromagnetic films has proven to be a promising tool for the fabrication of fully planar samples with a microscopic magnetic substructure [8,9]. The different contributions to the change of the magnetic structure due to ion implantation have been the subject of several studies over the past few years. Fassbender et al. have shown that the implantation of Cr^+ ions into a $\text{Ni}_{81}\text{Fe}_{19}$ layer modifies its magnetic properties via several mechanisms [10]: besides the doping of Cr^+ ions into the $\text{Ni}_{81}\text{Fe}_{19}$, a lattice expansion and an increasing amorphization with increasing ion fluence can be observed. Additionally, the ion irradiation induces the formation of a magnetic dead layer at the surface of the $\text{Ni}_{81}\text{Fe}_{19}$. Upon Cr^+ implantation, the saturation magnetization M_s of the $\text{Ni}_{81}\text{Fe}_{19}$ is reduced and an increase of the damping constant α can be observed. As these are important parameters in the description of spin waves, it is obvious that a fabrication of spin-wave conduits by ion implantation in a ferromagnetic layer is possible.

This Report presents the observation of a waveguide-like propagation of spin waves in a $\text{Ni}_{81}\text{Fe}_{19}$ film that has been patterned by locally doping the layer with Cr^+ ions. It will be shown that the formation of a waveguide in the $\text{Ni}_{81}\text{Fe}_{19}$ film strongly depends on the ion implantation fluence. This technique is a new way to manipulate the propagation of spin waves in thin ferromagnetic films yielding several advantages with respect to heat dissipation especially for nanoscopic structures.

For the fabrication of the spin-wave waveguides a $\text{Ni}_{81}\text{Fe}_{19}$ film with a thickness of $t = 20\text{ nm}$ has been deposited on a Si/SiO (200 nm) substrate by molecular beam epitaxy (MBE). Subsequently, magnetic patterning has been made using a mask of polymethyl methacrylate (PMMA) which has been exposed to e-beam lithography revealing a stripe of resist with a width $w = 4.5\text{ }\mu\text{m}$ and a length $L = 75\text{ }\mu\text{m}$ on top of the $\text{Ni}_{81}\text{Fe}_{19}$ layer. Ion implantation into the uncovered region of the $\text{Ni}_{81}\text{Fe}_{19}$ has been performed at the Helmholtz-Zentrum Dresden-Rossendorf by exposing the sample to a homogeneous irradiation of Cr^+ ions with an energy of 30 keV. The result after removing the resist is a $\text{Ni}_{81}\text{Fe}_{19}$ film with decreased saturation magnetization M_s and increased

¹In collaboration with J. Osten, T. Strache, and J. Fassbender, Institut für Ionenstrahlphysik und Materialforschung, Helmholtz-Zentrum Dresden-Rossendorf.

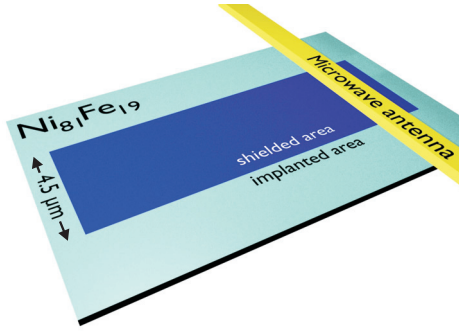


Fig. 1: Illustration of the sample setup. Into a 20nm thick $\text{Ni}_{81}\text{Fe}_{19}$ film a $4.5\mu\text{m}$ wide stripe region is patterned by shielding it from ion implantation of 30keV Cr^+ ions. Afterwards, a Cu microwave antenna is fabricated on top for the excitation of spin waves in the ferromagnetic layer.

damping constant α containing a stripe with unchanged magnetic properties that is supposed to act as a waveguide. This is illustrated in Fig. 1. In order to excite spin waves in the $\text{Ni}_{81}\text{Fe}_{19}$ film, a Cu antenna with a thickness of 500nm and a width of $1\mu\text{m}$ is produced using a lift-off technique and electron beam evaporation. It is placed perpendicular to the long axis of the stripe in the $\text{Ni}_{81}\text{Fe}_{19}$ film in order to excite spin waves in the ferromagnetic film. For a quantitative analysis of the influence of the ion implantation on the magnetic properties of the $\text{Ni}_{81}\text{Fe}_{19}$ several samples are irradiated with varying Cr^+ ion fluences between $2.2 \cdot 10^{15} \text{ ions/cm}^2$ and $1.1 \cdot 10^{16} \text{ ions/cm}^2$. The absolute values of the saturation magnetization M_s are obtained using reference samples with the same $\text{Ni}_{81}\text{Fe}_{19}$ film and a homogeneous ion implantation, i.e. without any stripe structure. The measurements of M_s have been achieved using polar magneto-optical Kerr effect (MOKE) measurements according to Markó et al. [11]. Here, the detected Kerr rotation is a measure of the magnetization component that is perpendicular to the film plane. Since the crystalline anisotropy of $\text{Ni}_{81}\text{Fe}_{19}$ is negligible, $\mu_0 M_s$ can be obtained from the shape anisotropy field $\mu_0 H_s$. Figure 2b shows that the latter can be determined from the intercept of the two fits of the saturation and reversal region, respectively. The measured polar MOKE loops are shown in Fig. 2a. It is obvious that with increasing ion fluence saturation is achieved with lower field values indicating a decrease in M_s . The experimentally determined values of M_s are listed in Tab. 1. For the highest applied ion fluence a reduction of the saturation magnetization to half of its original value is observed. The decrease in M_s is also reflected in the spin-wave resonance spectra, where a shift of the resonance spectrum to lower frequencies is detected. Besides this frequency shift, also a strong reduction of the spin-wave intensity appears in the implanted regions. This reduction by a factor of up to ten indicates a strong increase of the magnetic damping constant α .

| Cr^+ fluence (ions/cm^2) | $M_s(\text{kA/m})$ | M_s/M_s^0 |
|--|--------------------|--------------|
| $2.2 \cdot 10^{15}$ | — | $0.9^{[10]}$ |
| $4.4 \cdot 10^{15}$ | 651 | 0.76 |
| $6.6 \cdot 10^{15}$ | 565 | 0.66 |
| $8.8 \cdot 10^{15}$ | 486 | 0.57 |
| $1.1 \cdot 10^{16}$ | 446 | 0.52 |

Table 1: Measured saturation magnetization values for varying intensities of the ion implantation. With increasing ion fluence M_s decreases. The last column indicates the change of M_s with respect to its original value $M_s^0 = 860 \text{ kA/m}$. The sample with an ion fluence of $2.2 \cdot 10^{15} \text{ ions/cm}^2$ has not been measured, its value of M_s/M_s^0 is adapted from [10].

The observation of the spin-wave propagation in the implanted $\text{Ni}_{81}\text{Fe}_{19}$ films that contain a stripe with unchanged magnetic properties has been realized using Brillouin light scattering microscopy. Spin waves are excited by the dynamic Oersted field of the microwave antenna and propagate along the long axis of the stripe. An external magnetic field is applied parallel to the short axis

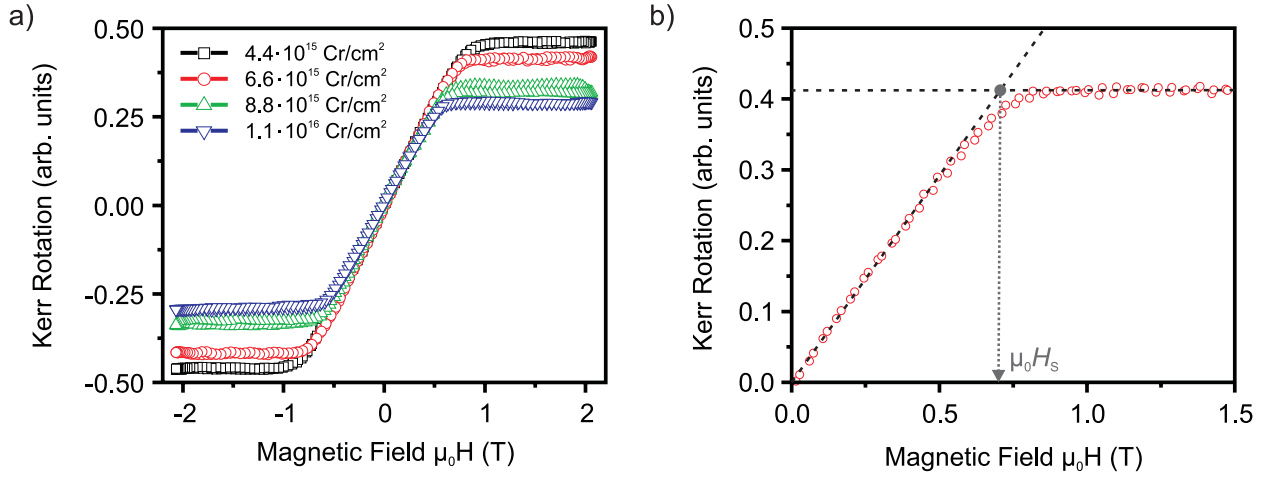


Fig. 2: a) Polar magneto-optical Kerr effect (MOKE) measurements on $\text{Ni}_{81}\text{Fe}_{19}$ films with prior exposition to ion implantation with different fluences. From the out-of-plane magnetization reversal loops, it is possible to determine the absolute value of the saturation magnetization of the ferromagnetic layer [11]. b) In the case of $\text{Ni}_{81}\text{Fe}_{19}$ the saturation magnetization can be obtained from the shape anisotropy field $\mu_0 H_s$, which is the x coordinate of the intercept between the fit lines to the reversal region and the saturation region, respectively.

of the stripe, ensuring a perpendicular relative orientation of the spin-wave wavevector and the magnetization direction (Damon-Eshbach geometry). The spatial distribution of the locally excited spin waves within the film can be mapped by scanning the BLS laser focus across the sample with a spatial resolution of 300 nm. Figure 3 shows the results for two different samples, which differ in the degree of ion implantation. Figure 3a depicts the measurement on a $\text{Ni}_{81}\text{Fe}_{19}$ film, where the ion implantation with the lowest fluence of $2.2 \cdot 10^{15} \text{ ions/cm}^2$ has been performed. The intensity graph shows a color-coded map of the Brillouin light scattering intensity, which is proportional to the spin-wave intensity, as a function of the lateral position on the film. White (black) color indicates high (low) spin-wave intensities. From the position of the antenna at $x = 0 \mu\text{m}$ the measured spin-wave intensity decays exponentially with increasing x . The position of the stripe which has been shielded from implantation is indicated by the white dashed lines. It is obvious that the spin-wave propagation length inside the stripe area significantly exceeds the decay length in the irradiated outer regions. This can be attributed to the smaller value of the damping parameter α . However, a clear channeling of the spin-wave intensity inside the stripe area cannot be observed. The sample which has been irradiated by a high fluence of $8.8 \cdot 10^{15} \text{ ions/cm}^2$ is shown in Fig. 3b. Within the irradiated region, this corresponds to a decrease of the saturation magnetization to a value of $M_s = 486 \text{ kA/m}$. In comparison to the original saturation magnetization of $\text{Ni}_{81}\text{Fe}_{19}$, $M_s^0 = 860 \text{ kA/m}$, this is a reduction to $M_s/M_s^0 = 0.57$. The Brillouin light scattering measurement clearly shows that there is a visible spin-wave intensity inside the stripe region only. The outer region, where the implantation has caused a decrease in M_s and where the damping is increased, does not exhibit any pronounced spin-wave signal. Thus, the stripe with unchanged magnetic properties can be considered as a spin-wave waveguide.

Obviously, the implantation of Cr^+ ions into the $\text{Ni}_{81}\text{Fe}_{19}$ layer has affected the spin-wave propagation in the film. The mechanisms by which ion implantation influences the magnetization dynamics have been identified. The two main contributions are given by the drop of the saturation magnetization M_s as well as the increase of the damping constant α . While the change in α causes a faster decay of spin waves and hence decreases the propagation length, the decrease of M_s gives rise to a shift of the dispersion relation to lower frequencies. For the given geometry and as the spin-wave frequency remains constant, this will result in a larger spin-wave wavevector. As

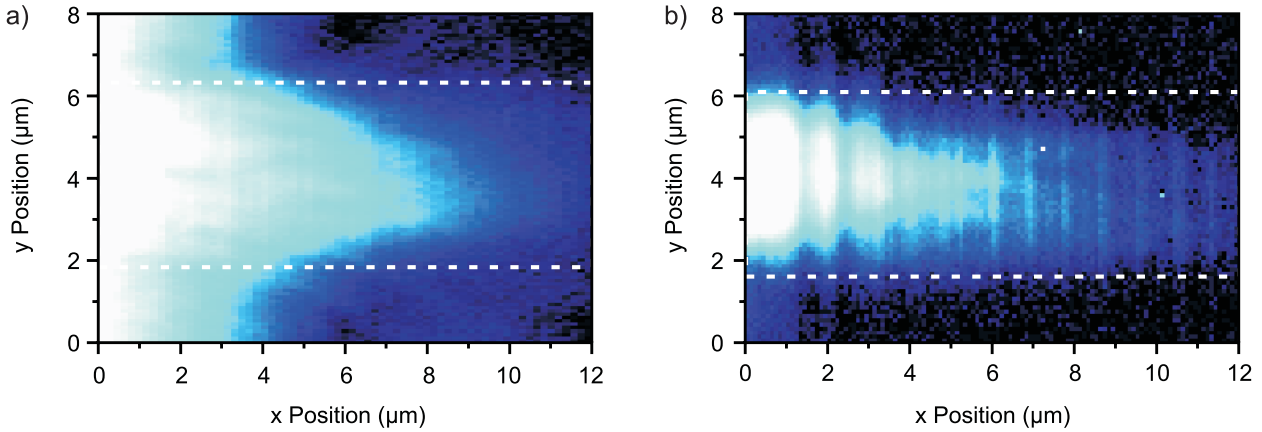


Fig. 3: Brillouin light scattering microscopy measurements of the spin wave intensity distribution of two $\text{Ni}_{81}\text{Fe}_{19}$ films exposed to different ion implantation fluences. Red (blue) color indicates high (low) spin-wave intensity. Spin waves are excited by the microwave antenna at the position $x = 0\mu\text{m}$. The stripe region which has been shielded from the ion irradiation is indicated by the dashed lines. The spin-wave intensity distribution is shown for Cr^+ fluences of a) $2.2 \cdot 10^{15} \text{ ions/cm}^2$ and b) $8.8 \cdot 10^{15} \text{ ions/cm}^2$.

a consequence, the excitation of spin waves by the microwave antenna becomes less efficient [12]. Thus, M_s and α both contribute to the formation of a quasi spin-wave waveguide. Yet the underlying processes which result in the formation of a spin-wave beam inside the unirradiated stripe are not fully understood. It is apparent that the excitation of spin waves by the microwave antenna in the irradiated regions outside the stripe is less efficient in the case of Fig. 3b. This enables a well-defined spin-wave propagation inside the stripe borders only and hence motivates the picture of a spin-wave waveguide. However, other waveguide properties like the reflection of spin waves at the stripe borders still have to be proven and require further investigations.

Besides the decrease of the saturation magnetization and the increase of the damping, also the sputtering effect due to the ion irradiation has to be taken into account. Atomic force microscopy measurements confirm a drop of the film thickness by up to 4 nm in the implanted regions. Calculations of the spin-wave dispersion relation indicate that the reduction in film thickness and the magnetization decrease both contribute to a downshift of the dispersion and hence affect the magnetization dynamics in the same direction. However, the reduced film thickness has a small influence only and for small spin-wave wavevectors, i.e. for frequencies close to the ferromagnetic resonance, its effects are negligible in comparison to the change due to the drop in saturation magnetization. However, a quantitative analysis of the different contributions of the mentioned parameters to the spin-wave behavior still has to be made. In comparison to the film thickness the reduction due to the sputtering effect is significant. Nevertheless, the advantages of patterning a waveguide into a film by pure magnetic structuring with respect to a topographic fabrication of a waveguide are still obvious, since, e.g., there is still a good heat conductivity present in the film.

In conclusion, it has been shown that it is possible to spatially confine spin-wave propagation in a $\text{Ni}_{81}\text{Fe}_{19}$ film by ion implantation using a lithographically produced resist mask. The formation of a waveguide-like spin-wave conduit is due to a reduction of the saturation magnetization in the irradiated region in combination with an increase of the damping constant, which make a propagation and excitation of spin waves inside this area very ineffective. By controlling the magnitude of the saturation magnetization by variation of the ion fluence it has been possible to show the transition of an unchanged region from a mere stripe with different damping properties at low ion fluences to an effective spin-wave waveguide for high ion fluences. Further investigations

are intended to quantify this transition more precisely. This technique of patterning waveguides into ferromagnetic films by ion implantation is very promising for future applications. In the case of nanoscopic structures of a metallic ferromagnet it will ensure an efficient heat dissipation. Moreover, the fabrication of multilayers made from several structured magnetic materials will be easier compared to pure topographic sample fabrication.

The authors would like to thank the Nano+Bio Center of the TU Kaiserslautern for assistance in sample preparation. Financial support by the Graduiertenkolleg (GRK) 792 is gratefully acknowledged.

References

- [1] K. Vogt, H. Schultheiss, S.J. Hermsdoerfer, P. Pirro, A.A. Serga, B. Hillebrands, *All-optical detection of phase fronts of propagating spin waves in a $\text{Ni}_{81}\text{Fe}_{19}$ microstripe*, Appl. Phys. Lett. **95**, 182508 (2009).
- [2] P. Clausen, K. Vogt, H. Schultheiss, S. Schäfer, B. Obry, G. Wolf, P. Pirro, B. Leven, B. Hillebrands, *Mode conversion by symmetry breaking of propagating spin waves*, Appl. Phys. Lett. **99**, 162505 (2011).
- [3] P. Pirro, T. Brächer, K. Vogt, B. Obry, H. Schultheiss, B. Leven, B. Hillebrands, *Interference of coherent spin waves in micron-sized ferromagnetic waveguides*, Phys. Stat. Solidi B **248**, 2404-2408 (2011).
- [4] M. Buess, R. Höllinger, T. Haug, K. Perzlmaier, U. Krey, D. Pescia, M.R. Scheinfein, D. Weiss, C.H. Back, *Fourier transform imaging of spin vortex eigenmodes*, Phys. Rev. Lett. **93**, 77207 (2004).
- [5] M. Buess, T.P.J. Knowles, R. Höllinger, T. Haug, U. Krey, D. Weiss, D. Pescia, M.R. Scheinfein, C.H. Back, *Excitations with negative dispersion in a spin vortex*, Phys. Rev. B **71**, 104415 (2005).
- [6] G. Gubbiotti, M. Madami, S. Tacchi, G. Carlotti, H. Tanigawa, T. Ono, L. Giovannini, F. Montoncello, F. Nizzoli, *Splitting of spin excitations in nanometric rings induced by a magnetic field*, Phys. Rev. Lett. **97**, 247203 (2006).
- [7] H. Schultheiss, S. Schäfer, P. Candeloro, B. Leven, B. Hillebrands, A.N. Slavin, *Observation of coherence and partial decoherence of quantized spin waves in nanoscaled magnetic ring structures*, Phys. Rev. Lett. **100**, 47204 (2008).
- [8] J. Fassbender, J. McCord, *Magnetic patterning by means of ion irradiation and implantation*, J. Magn. Magn. Mater. **320**, 579-596 (2008).
- [9] L. Folks, R.E. Fontana, B.A. Gurney, J.R. Childress, S. Maat, J.A. Katine, J.E.E. Baglin, A.J. Kellock, *Localized magnetic modification of permalloy using Cr^+ ion implantation*, J. Phys. D : Applied Physics **36**, 2601 (2003).
- [10] J. Fassbender, J. von Borany, A. Mücklich, K. Potzger, W. Möller, J. McCord, L. Schultz, R. Mattheis, *Structural and magnetic modifications of Cr-implanted permalloy*, Phys. Rev. B **73**, 184410 (2006).
- [11] D. Markó, T. Strache, K. Lenz, J. Fassbender, R. Kaltofen, *Determination of the saturation magnetization of ion irradiated Py/Ta samples using polar magneto-optical Kerr effect and ferromagnetic resonance*, Appl. Phys. Lett. **96**, 022503 (2010).
- [12] V.E. Demidov, M.P. Kostylev, K. Rott, P. Krzysteczko, G. Reiss, S.O. Demokritov, *Excitation of microwaveguide modes by a stripe antenna*, Appl. Phys. Lett. **95**, 112509 (2009).

F. Applied Spintronics

A substantial part of our research is devoted to fields that have a close relation to applications. Our group is aiming to intensify the communication flow between the academic and the industrial world in order to promote the necessary transfer of technology and know-how. Until beginning of the year 2011 we took part in the industrial collaboration project MultiMag funded by the BMBF jointly with the industrial partner Sensitec, Mainz, and the universities of Bielefeld and Mainz. In this project we contributed with to the design of new sensor concepts by micromagnetic simulations, the material characterization, especially of Heusler thin films and in other subjects.

In Report 4.16 the development and the characterization of tunneling magnetoresistance (TMR) based memory cells for low-cost, low-density memory is presented. The influence of the size and the shape of the TMR elements on the reliability of the switching process of the memory cell is discussed.

In Report 4.17 measurements of slow (range of hours) magnetization dynamics of circular dot $\text{Ni}_{81}\text{Fe}_{19}$ arrays in in-plane magnetic fields are shown. This process is relevant for the design of magnetic memory devices because it determines the long-term stability of the stored data.

Report 4.18 addresses a study of magnetic vortex dynamics near vortex state nucleation in $\text{Ni}_{81}\text{Fe}_{19}$ dots.

F. Angewandte Spin Dynamik

Ein wesentlicher Teil unserer Aktivitäten ist auf das Gebiet der anwendungsorientierten Forschung gerichtet. Unsere Gruppe ist daran beteiligt Brücken zwischen der akademischen und der industriellen Welt zu bauen, um den Technologietransfer und den Ideenaustausch zu fördern. Bis Anfang 2011 haben wir am vom BMBF geförderten Industriekooperationsprojekt MultiMag teilgenommen. Dieses Projekt war eine Kollaboration zwischen der TU Kaiserslautern, den Universitäten Mainz und Bielefeld und dem Industriepartner Sensitec, Mainz. Unsere Aufgabe bestand unter anderen darin, das Design neuer Sensoren mit mikromagnetischen Simulationen zu begleiten und die magnetische Charakterisierung von Heusler-Dünnschichten durchzuführen.

In Bericht 4.16 wird die Charakterisierung von auf dem TMR basierenden Speicherzellen für Anwendungen im Niedrigkostenbereich und kleiner Speicherdichte gezeigt. Der Einfluss der Dimensionen der TMR-Elemente auf die Funktion der Speicherzellen wird diskutiert.

In Bericht 4.17 werden Untersuchungen zum Langzeitverhalten der Magnetisierungsdynamik von kreisförmigen $\text{Ni}_{81}\text{Fe}_{19}$ -Mikrostrukturierungen diskutiert. Diese Prozesse haben eine große Relevanz für die langfristige Stabilität von Information in magnetischen Speichern.

Bericht 4.18 stellt eine Studie zur Vortexdynamik nahe des Nukleationspunktes des Vortexzustandes in kreisförmigen $\text{Ni}_{81}\text{Fe}_{19}$ -Strukturen vor.

4.16 Determination of dynamic switching fields of TMR structures

G. Wolf, B. Leven, and B. Hillebrands

Tunneling-Magneto-Resistance (TMR) structures are a promising solution for new types of memory cells due to their non-volatility and fast operation speed. The most famous application is the magnetic random access memory (MRAM) [1–3]. Not only the high end technology for computer systems is a field of application for TMR structures, they may be also useful for industrial standard devices such as micro controllers for robotics or small machines. TMR structures are of interest because they can be used to build an embedded memory system with low density, but fast operation speed for micro controllers in order to store and read small amounts of information on processor speed. The fast magnetization reversal process of the free magnetic layer is a crucial aspect for high speed operation [4, 5].

Finding a stable working point for the writing process is essential for reliable operation of an industrial device. The cell size is ought to be in the μm -range, due to limitations in standard lithography methods in industrial production lines. This study aims at a memory cell in the classical MRAM geometry, where the TMR elements are arranged in an array and the magnetic state of one element can be switched by applying two perpendicular field pulses in the low nanosecond time scale. The geometrical arrangement and the temporal sequence is illustrated in Fig. 1a. The transversal magnetic field pulse H_t excites the magnetization in the magnetic hard axis. After a delay time the longitudinal pulse H_l reverses the magnetization to the opposite state. Variations of the switching parameters due to unavoidable properties distribution shall not disturb the functionality of the device. Finding proper parameters for a stable and reliable switching is a crucial aspect for industrial production.

The structure under investigation is a TMR layer stack fabricated in an industrial sputtering system in collaboration with Singulus Technologies. The layer stack consists of Ta 5nm/MnIr 12nm/CoFe 3nm/Ru 0.85nm/CoFeB 3.5nm/MgO 1.1nm/CoFeB 2.5nm/Ta 5nm/Ru 5nm. The magnetization of the lower magnetic reference layer is fixed via an exchange bias mechanism to the antiferromagnetic MnIr layer, so that only the upper CoFeB layer can be affected by the magnetic field pulses. The magnetic field pulses are generated by electrical voltage pulses applied to a system of crossed coplanar waveguides (CPW) [6], situated under the TMR layer stack. Figure 1b shows a schematic overview of the sample structure. The layer stack was structured by electron beam lithography and ion milling into elliptically shaped elements, situated in the crossing points of the waveguides. The

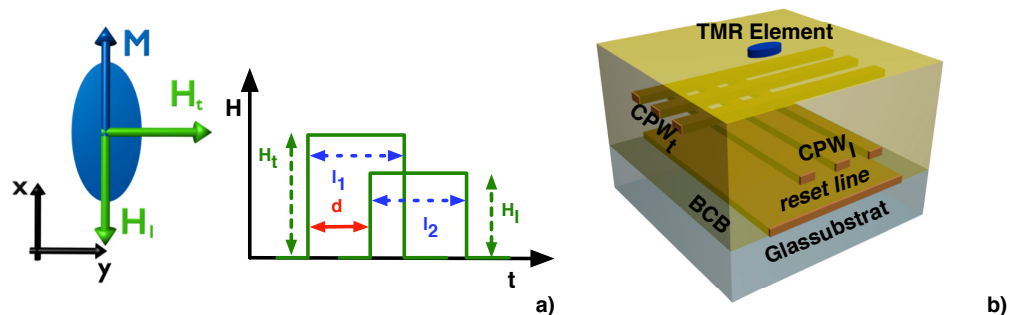


Fig. 1: a) Temporal sequence of the magnetic field pulses. b) Schematic drawing of the sample structure. A TMR-Element is structured on a system of crossed coplanar waveguides (CPW), which generate magnetic field pulses.

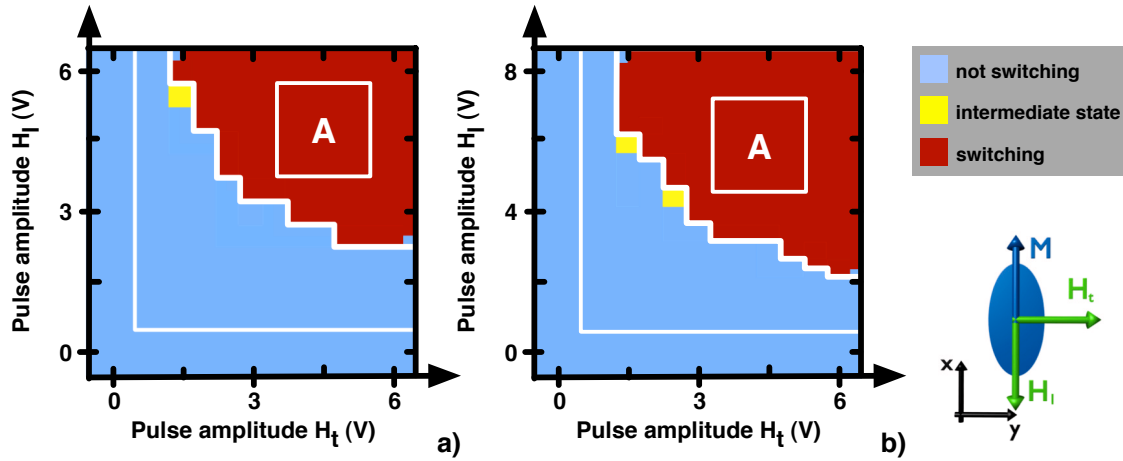


Fig. 2: Switching chart for an elliptical structure with size $4.0\mu\text{m} \times 2.0\mu\text{m}$. The color code (gray scale) represents the final magnetization state after the pulses were applied, blue (light gray) represents the original state and red (dark gray) the switched state. The pulse length is set to a) 2 ns and b) 1 ns. The delay is set in both cases to $d = 0.5$ ns. The white frame labeled A marks a possible working area for ns-switching.

elliptical shape provides a uniform demagnetization field. The magnetic easy axis is induced along the long axis of the ellipse. Three different sizes are prepared, $4.0\mu\text{m} \times 2.0\mu\text{m}$, $4.5\mu\text{m} \times 1.5\mu\text{m}$, and $3.6\mu\text{m} \times 1.2\mu\text{m}$. The magnetization reversal process is monitored by time-resolved Kerr effect microscopy, which gives direct access to the magnetization dynamics with spatial resolution in the low μm -range and additionally the required ps-time-resolution.

The parameter space is set up by the field strength of the pulses H_t and H_l , the duration of the pulses l_1 and l_2 and their relative delay d (see also Fig. 1a). In order to reduce the volume of the parameter space we predefined the pulse length to be equal for both pulses. The duration is set to 2 ns and 1 ns, while the delay between the pulses can still be varied.

In the favored concept for the writing process of the memory cell, only a combination of the two pulses should be able to reverse the magnetization. One field pulse alone shall not switch the magnetization to avoid the *half select* problem [1]. This is the most important restriction to the parameter space. The field strength of the pulses can only be chosen in a range, where a single pulse cannot switch the element. All structures were tested with respect to this restriction and a range of possible field pulse amplitudes has been defined individually for all sizes. Figure 2 shows two exemplary switching charts for a structure of the size $4.0\mu\text{m} \times 2.0\mu\text{m}$, where all possible combinations of field pulse amplitudes H_t and H_l were tested. In Fig. 2a the pulse length is set to 2 ns and in b) to 1 ns, the delay is $d = 0.5$ ns in both cases. The color code (gray scale) represents the final magnetization state after the field pulses were applied, where red (dark gray) corresponds to the switched state and blue (light gray) to the original state. The field axes are in units of the nominal voltage of the electrical pulses applied to the waveguides. The voltage is directly proportional to the field strength, but it can only be estimated from the impedance of the waveguide and the distance to the magnetic layer.¹ Both pulse length show a sharp transition between combinations of field pulses, that lead to a magnetization reversal, and those, which do not. This will be further referred as switching line (white line in Fig. 2). For the shorter pulse length of 1 ns pulses (Fig. 2b)) the allowed voltage range for the longitudinal pulse H_l is larger and also the switching

¹The same voltage value for H_t and H_l does not imply the same field value, due to different distances and impedances of the waveguides. $H_t(\text{V}) \neq H_l(\text{V})$

line is shifted slightly towards higher voltage values compared to the the line of the 2 ns pulse. The shorter pulse length requires a higher field amplitude to switch the magnetization.

The white rectangular frame indicates a possible working range, where small variations in the field amplitude of the pulses still lead to a reversal of the magnetization of the element. The working point must be set in an appropriate distance to the switching line, so that a small variation in the pulse amplitude does not disturb the switching event. In the same way the working point must be set apart from pulse amplitudes, of which a single pulses can switch the element, to avoid a *half select* of the other elements in the array.

Additional overview charts have been reproduced for several values of the delay d between the two field pulses and for the other structure sizes. For each delay value the switching line has been extracted and plotted in Fig. 3.

For the $4.0\mu\text{m} \times 2.0\mu\text{m}$ element and a pulse length of 2 ns (Fig. 3a) the switching lines for the different delays show only small variations from each other, except for a small temporal overlap of the pulses ($d = 1.8\text{ ns}$ and $d = 2.0\text{ ns}$). A small temporal overlap causes higher pulse amplitudes to switch the magnetization. However, such a large delay is not favorable because a variation in the timing might lead to no overlap of the pulses and no switching might be reached. On the other hand a small delay does not affect significantly the position of the switching line but reduces the operation time of the writing process. The situation is similar for the pulse length of 1 ns, but the shorter pulse length moves the switching lines towards combinations with higher pulse amplitude, as already seen in Fig. 2.

The $3.6\mu\text{m} \times 1.2\mu\text{m}$ element shows a similar result for both pulse length (Fig. 3c and d). The switching lines for the different delay values lie close to each other, but in comparison to the $4.0\mu\text{m} \times 2.0\mu\text{m}$ structure they are shifted to higher pulse amplitudes. The smaller size and the higher aspect ratio lead to a higher demagnetizing field. As a consequence higher pulse amplitudes are necessary to switch the magnetization, especially along the short axis of the ellipse.

The $4.5\mu\text{m} \times 1.5\mu\text{m}$ structure reveals a different picture (Fig. 3e and f). In particular for the pulse length of 2 ns the switching lines show strong variations from each other. For the longitudinal pulse H_{\parallel} larger pulse amplitudes are allowed, which is contrary to the expected demagnetizing fields. The larger dimensions should lead to smaller pulse amplitudes to switch the element. It seems, that this element shows special conditions for the magnetization reversal process. A complex combination of nucleation, movement, and pinning of domain walls could be a possible explanation of these results. Further more it can not be excluded that the electrical contact between the electrical pulse generators and the waveguides varied slowly over the measurement time. This would generate varying field amplitudes, and thus reveal different results for the different measurements. The exact cause of this behavior is still unclear and needs to be explored in further investigations. However, this example demonstrates the necessity of finding a stable working point for an operating device, as variations in the pulse amplitudes or the element properties cause different switching properties.

In summary we were able to determine a working area for all structures sizes, where the magnetization can be switched with a combination of two pulse amplitudes, that do not lead to a *half select*. Furthermore it could be identified, that in general the delay between the pulses does not play a significant role. As a consequence the delay is not a crucial parameter, which is in contrast to the expectations of a simple macrospin model, where the phase of the excitation during the magnetization precession is important in order to realize a switching of the magnetization [4]. On the other hand this allows for a certain variation of the timing, without disturbing the functionality of the memory, i.e. a robustness for application purposes. However, the delay should be set to

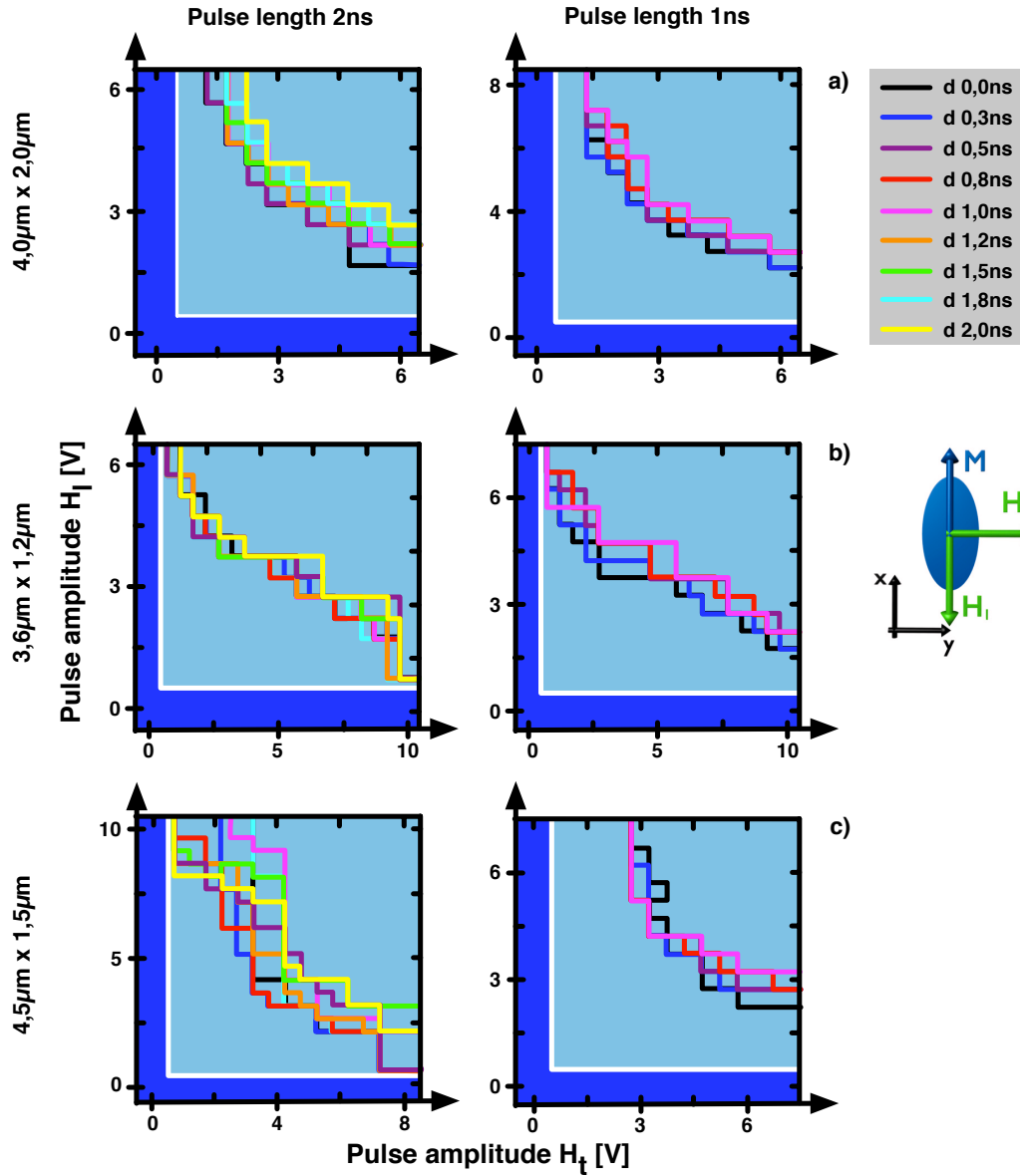


Fig. 3: Switching chart for elliptical sizes a) the $4.0\mu\text{m} \times 2.0\mu\text{m}$, b) $3.6\mu\text{m} \times 1.2\mu\text{m}$ and c) $4.5\mu\text{m} \times 1.5\mu\text{m}$ each for a pulse length of 2 ns and 1 ns and different delay d .

a small value, in order to reduce the operation time of the memory cell. When operation time should be further reduced by using the 1 ns pulse length, higher field amplitudes are necessary to switch the element a reliable way, but still the delay does only effect in a small range the switching properties.

The authors thank Dr. J. Langer from Singulus Technologies for providing the TMR layer stack. The BMBF project *Heuspin* (13N9434) is gracefully acknowledged for financial support.

References

- [1] J.M. Slaughter, R.W. Dave, M. DeHerrera, M. Durlam, B.N. Engel, J. Janesky, N.D. Rizzo, S. Tehrani, *Fundamentals of MRAM technology*, Jour. of Supercond.: Incorporating Novel Magnetism **15**, 19 (2002).

- [2] B.N. Engel, J. Åkerman, B. Butcher, R.W. Dave, M. DeHerrera, M. Durlam, G. Grynkewich, J. Janesky, S.V. Pietambaram, N.D. Rizzo, J.M. Slaughter, K. Smith, J.J. Sun, S.Tehrani, *A 4-Mb toggle MRAM based on a novel bit and switching method*, IEEE Trans. Magn. **41**, 132 (2005).
- [3] W.J. Gallagher, S.S.P. Parkin, *Development of the magnetic tunnel junction MRAM at IBM: From first junctions to a 16-Mb MRAM demonstrator chip*, IBM Journal of Research and Development **50**, 5 (2006).
- [4] M. Bauer, J. Fassbender, B. Hillebrands, *Switching behavior of a Stoner particle beyond the relaxation time limit*, Phys. Rev. B **61**, 3410 (2000).
- [5] C. Maunoury, T. Devolder, C.K Lim, P. Crozat, C. Chappert, *Precessional direct-write switching in micrometer-sized magnetic tunnel junctions*, J. Appl. Phys. **97**, 074503 (2005).
- [6] P. Martin-Pimentel, S.J. Hermsdoerfer, H.T. Nembach, B. Leven, B. Hillebrands, S. Trellenkamp, S. Wolff, *A crossed coplanar waveguide design for ultrafast magnetization switching utilizing polymer insulation layers*, J. Appl. Phys. **88**, 122510 (2006).

4.17 Characterization of a TMR-based magnetic memory cell with elliptically shaped elements for moderate switching speed

A. Ruiz Calaforra, A. Conca, B. Leven, and B. Hillebrands¹

A very promising application of magnetic tunneling junctions (MTJ) is the construction of magnetic random access memories (MRAM). They consist of an array of MTJs in which each single junction stores a bit since the two possible magnetic states can code a logic '0' or '1'. The two possible magnetic states correspond to the situation in which both magnetic electrodes are magnetized in the same direction (parallel configuration) and the one in which the magnetization points in opposite directions (antiparallel configuration). Due to the tunneling magnetoresistance (TMR) effect, this two configurations are translated into a change of the resistance of the junction. First MRAM chips have already reached the market [1, 2] although the total storage capacity is still small. This technology fulfills the necessity of non-volatility and stability, high read and write speed, and can be easily integrated with semiconductor electronics. Although the advantages over other types of existing memories are clear, the technical problems to overcome are still challenging. Characteristics such as reliability, reproducibility and low power consumption are crucial for these types of devices and are the focus of the current efforts in research.

The aim of the research presented here is not to compete in speed or storage capacity with well established MRAM techniques, but to proportionate a small storage capacity for many moderate-speed industrial applications (for instance, storage of important production details or calibration parameters of industrial machinery). The main goal is, thus, to achieve a high reproducibility and reliability with the advantages of non-volatility and low power consumption. In accordance with the MRAM design a 4×4 bit memory cell system based on a quasi-static switching process was produced in an industrial environment in collaboration with Sensitec GmbH [3], Mainz, in the framework of the MultiMag project. In this Report, we present a systematic study of the magnetic

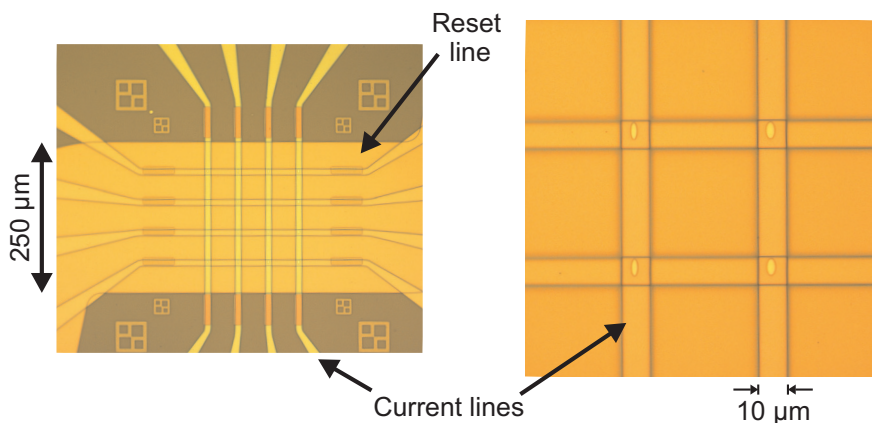


Fig. 1: Micrographs of one of the arrays. The image in a) was taken before structuring the elliptical elements, while b) shows a magnified view of the array after structuring.

¹In collaboration with Sensitec GmbH, Mainz, Germany; B. Lägél, S. Wolff, Nano+Bio Center, Technische Universität Kaiserslautern, Germany.

switching behavior of the magnetic bits depending on the geometrical parameters.

The sample design is based on the MRAM concept, where the basic unit consists of two perpendicularly crossing copper current lines and a MTJ lying on the intersection. To be able to define an antiparallel or parallel configuration, the magnetization of the bottom magnetic layer is pinned via exchange-bias with an additional antiferromagnetic layer and the top magnetic layer acts as free electrode. The switching of the MTJ free electrode is achieved by two independent microsecond field pulses, generated by current pulses sent through the current lines. Due to the important role that the shape anisotropy plays in the magnetic behavior of the element [4], micron-sized elliptical elements with different dimensions have been studied.

The current lines have been structured by UV-lithography and etching techniques on an industrial Si-substrate wafer covered with amorphous Al_2O_3 . The current lines are $10\mu\text{m}$ wide with a thickness of 300nm (see Fig. 1). An additional $250\mu\text{m}$ wide current line is added to reset the magnetization to allow the initialization of the whole array system. All metallized layers are separated by a 800nm thick insulating Al_2O_3 layer. After depositing and structuring the copper lines, a series of 8 different micron-sized elliptical elements separated in 2 sets of 4×4 arrays was structured using standard electron beam lithography and a lift-off process. Ellipses with long axis sizes of $6\mu\text{m}$, $4\mu\text{m}$ and $3\mu\text{m}$ with aspect ratios (AR) 2, 3 and 4 were defined. The left side of Fig. 1 shows a top view microscope image of one array before structuring the elliptical elements, while at the right side the intersection area with the larger ellipses processed is shown in an enlarged scale. As one can see, the elements are oriented so that the symmetry axes of the elliptical elements are parallel to the current lines. Since for this study an optical access to the elements is required, the process was designed so that the elliptical elements were placed on top of the current lines. An important disadvantage of this approach is the presence of an increased surface roughness for the deposition of the elliptical elements in comparison with a deposition of the elements below the current lines, i. e. directly on the Si-wafer surface.

As well as the shape and size of the MTJ, the material chosen for the free layer is of major importance. A good candidate for this is the ferromagnetic compound CoFeB which is known to provide large TMR values in combination with MgO tunneling barriers [5, 6]. In a real tunneling junction the magnetic coupling between the two electrodes (via dipolar coupling or orange-peel coupling) represents an additional complication in order to study the switching properties of the elements. For this reason, in order to isolate the effect of the dimension - dependence, a single magnetic layer system resembling only the free electrode has been used. Therefore, the elements consist of a layer of Ta (15nm), a $\text{Co}_{40}\text{Fe}_{40}\text{B}_{20}$ layer (6nm) and a Ta capping layer (4nm) which are deposited via RF sputter deposition. An external magnetic field was applied during the growth process in order to induce an easy axis along the long axis direction of the ellipses.

The switching of the magnetization of a selected ellipse is accomplished by applying a field pulse perpendicular to the long axis direction followed by a second field pulse applied in the parallel direction. These pulses should be high enough that the combination of both switches the magnetization. But at the same time it should be guaranteed that the rest of the half-selected elements in the same row is not switched with a single pulse. In our study and due to demand from the industry project partner the duration of all field pulses is set to $1\mu\text{s}$. The overlap between the perpendicular and the parallel pulse is $0.5\mu\text{s}$. In the work shown here, the amplitude of these two pulses is varied in order to identify the working area for each ellipse dimension. Since all applied pulses are in the microsecond regime, the impedance matching of the current lines is not crucial.

The investigation on the dynamic switching process was performed employing a time resolved magneto-optical Kerr microscope with a laser spot diameter of 400nm . A stroboscopic technique

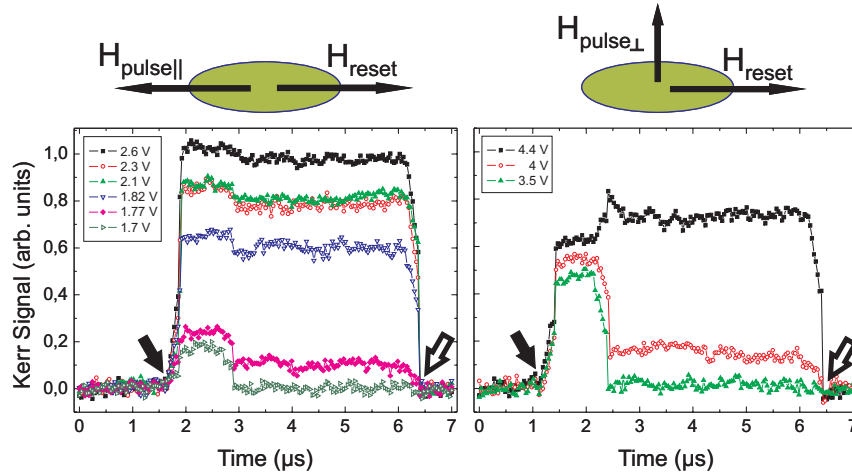


Fig. 2: Time resolved MOKE measurements for a $6\mu\text{m} \times 2\mu\text{m}$ CoFeB elliptical element excited by $1\mu\text{s}$ long pulses with different amplitudes. Left: The exciting pulse is parallel to the long axis; right: The exciting pulse is perpendicular to the long axis. The black full arrows indicate the beginning of the parallel (perpendicular) pulse. The empty arrows point to the arrival of the reset pulse.

was used in which the signal is a result of an averaging process over a large number of identical switching cycles. In order to define the magnetization of the element at the start of each cycle, a reset pulse is used. The amplitude of this pulse is always kept constant and large enough to assure an initial homogeneously magnetized state. The measured Kerr signal is proportional to the magnetic component along the ellipse's long axis. In a first set of measurements single pulses are applied either parallel or perpendicular to the long axis direction to identify the area where a single pulse does not affect the magnetization state. An example of these measurements can be seen in Fig. 2. The Kerr rotation has been normalized to the value corresponding to a complete switching. The black full arrows indicate the beginning of the parallel (perpendicular) pulse in Fig. 2 left (right). The empty arrows point to the arrival of the reset pulse. These results correspond to an ellipse of dimensions $6\mu\text{m} \times 2\mu\text{m}$ (AR 3). In order to have a reliable device it is important to know what is happening after the pulse ends and into which state the magnetization relaxes. For the chosen ellipse three different states can be distinguished. If the ellipse is excited with a parallel pulse with an amplitude of 2.6 V or larger the magnetization switches completely with the pulse and stays so after the ending of the pulse. For smaller amplitudes, between 2.3 V and 1.82 V the element relaxes into some intermediate state, i. e. some domain configuration is formed after the end of the pulse. Only for voltages smaller or equal to 1.7 V the magnetization relaxes back into the initial magnetized state. For the perpendicular pulse excitation, two different cases can be observed. Either the magnetization relaxes into an intermediate state, with pulses over 4 V , or it relaxes back to its initial state.

Following, the switching behavior caused by the combination of the two pulses - perpendicular and parallel - has been studied while varying the amplitude of both pulses. The amplitude of the pulses spans a two-dimensional parameter space. The results are displayed color coded in Fig. 3 depending on the final magnetization state: switched, intermediate, and not switched. The result for all ellipses' dimensions are shown. White color represents non-measured points due to the fact that certain voltage values are technically not available.

As already mentioned before, the desired switching scheme occurs when single pulses do not switch the magnetization, but the combination of two pulses achieves this. This area is shown in the figures by a white dashed box and represents the working area. As one can immediately

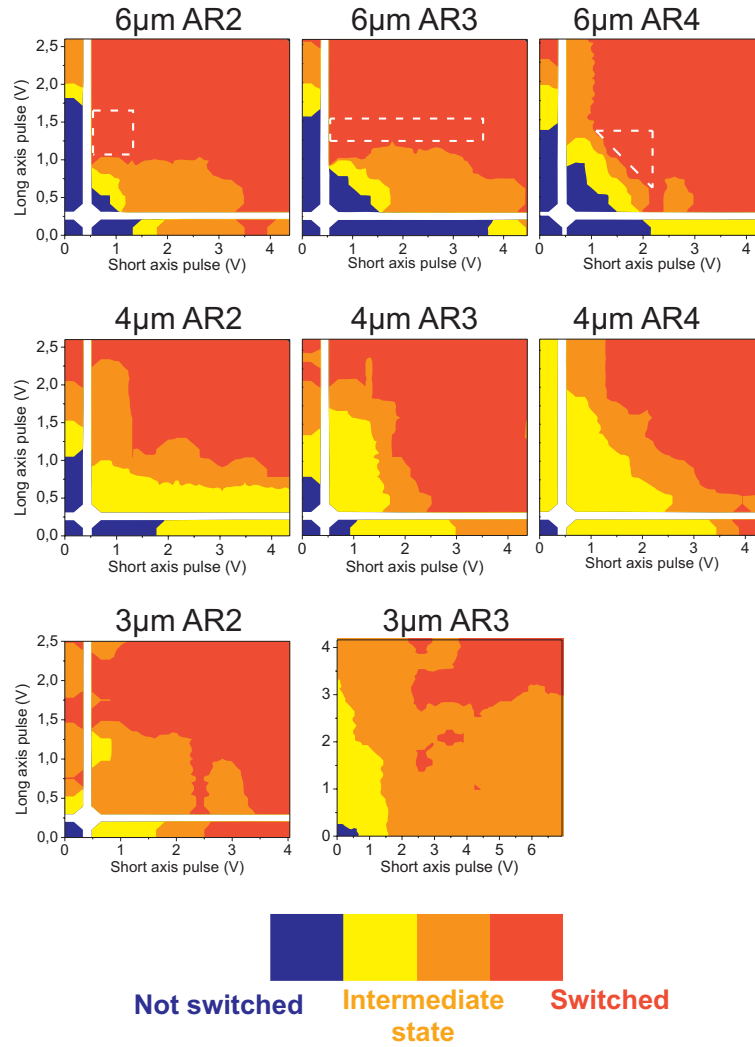


Fig. 3: Parameter space of CoFeB elements of different dimensions excited by two $1\mu\text{s}$ long pulses with an overlap of $0.5\mu\text{s}$. A color code scale is used to classify the magnetization state of the element into: not switched, intermediate state, or switched. The regions separated by the white gaps represent the single pulse excitation. The dashed boxes mark the working areas.

recognize, the only elements showing such an area are the ellipses with a size of $6\mu\text{m}$. It can also be observed that for the ellipse with the dimension $6\mu\text{m}$ AR4, single perpendicular pulses with lower amplitudes excite the magnetization into an intermediate state, although the AR is the largest of all elements studied and therefore a higher stability along the long axis is expected. Furthermore, as the dimensions of the ellipse decrease, the fully switched area also does so, showing a larger area for the intermediate state. Actually, single pulses, both parallel and perpendicular, of very low voltages are able to excite the magnetization in ellipses with the dimensions $4\mu\text{m}$ AR4 and $3\mu\text{m}$ AR 2 and 3. For the ellipse with the dimension $3\mu\text{m}$ AR3 the measured area has been enlarged in order to measure a region where a complete switching of the magnetization occurs. These results differ from the expected ones, in the sense that smaller dimensions and larger ARs are expected to show less probability of domain formation. An explanation for this discrepancy could be the influence of a high surface roughness that was indicated by atomic force microscopy measurements performed on the sample. As explained before, the elements have been deposited on top of many layers which add up irregularities. In addition, edge roughness produced by the combination of

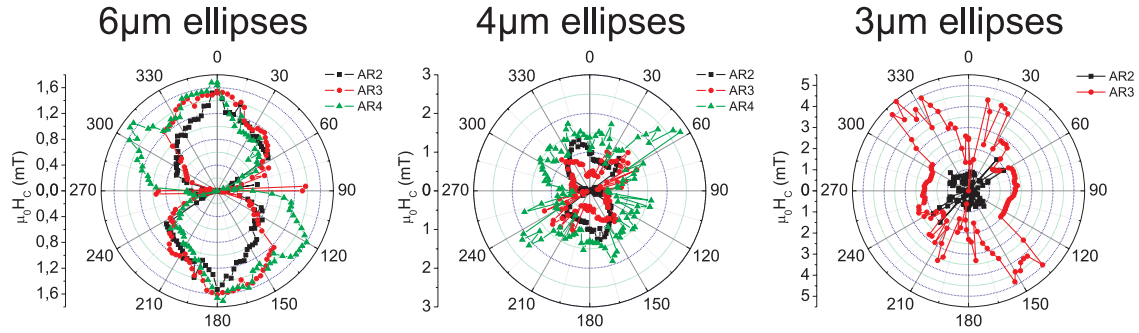


Fig. 4: Angular dependence of the the coercive field of CoFeB elliptical elements with a long axis of $6\mu\text{m}$, $4\mu\text{m}$ and $3\mu\text{m}$ and variable aspect ratio (AR). An orientation of $\phi = 0^\circ$ or $\phi = 180^\circ$ corresponds to a hysteresis loop measured along the long axis of the element.

lift-off and sputtering processes could also contribute.

In order to understand these results, investigations on the anisotropy have been carried out with an alternative microfocused MOKE setup [4] provided with a rotational unit. They are shown in Fig. 4. The coercive field is plotted as a function of the sample's in-plane angle between the long axis and the applied field direction and is useful to establish the role played by the shape anisotropy in our measurements. Ellipses of $6\mu\text{m}$ with AR 2 and 3 show an uniaxial anisotropy in the direction of the long axis as expected from an elliptical magnetic structure where the shape anisotropy dominates over the material's crystalline anisotropy (negligible for CoFeB). The ellipse of $6\mu\text{m}$ AR4, shows a non uniform easy axis parallel to the long axis which explains the small not switched area in single perpendicular pulses. In comparison, the $4\mu\text{m}$ and $3\mu\text{m}$ ellipses show a not clearly defined anisotropy. These results explain the tendency of the magnetization to relax into intermediate states mentioned before. Most probably this is a consequence of the surface roughness present in the elements.

In summary, the production of a small memory array could be achieved in an industrial environment. The fabricated set of ellipses with different sizes and ARs was analyzed with respect to its switching behavior with microsecond pulse excitation. The functionality of the ellipses as switching elements in a memory cell was qualitatively demonstrated. However, it was observed that the roughness has a big impact on the switching behavior leading to undesired domain formation and intermediate states. This influence becomes more pronounced for smaller element dimensions, implicating that high quality elements with low roughness are necessary for a reliable device.

Financial support by the state Rhineland-Palatinate in the project Technologieplattform Spintronik in Rheinland-Pfalz and the BMBF project *MultiMag* (VDI- TZ 13N9913) is gratefully acknowledged.

References

- [1] B.N. Engel, J. Åkerman, B. Butcher, R.W. Dave, M. DeHerrera, M. Durlam, G. Grynkewich, J. Janesky, S.V. Pietambaram, N.D. Rizzo, J.M. Slaughter, K. Smith, J.J. Sun, S. Tehrani, *A 4-Mb toggle MRAM based on a novel bit and switching method*, IEEE Trans. Magn. vol. **41**, no. 1, pp. 132-136 (2005).
- [2] Press release of Toshiba and NEC Corporation:
<http://www.nec.co.jp/press/en/0602/0702.html>
- [3] www.sensitec.com
- [4] T. Sebastian, A. Conca, G. Wolf, H. Schultheiß, B. Leven, and B. Hillebrands, *Magneto-optical investigation of the shape anisotropy of individual micron-sized magnetic elements*, J. Appl. Phys. , **110**, 083909 (2011).

- [5] D. D. Djayaprawira, K. Tsunekawa, M. Nagai, H. Machara, S. Yamagata, and N. Watanabe, *230% room-temperature magnetoresistance in CoFeB/MgO/CoFeB magnetic tunnel junctions*, Appl. Phys. Lett. **86**, 092502 (2005).
- [6] R.W. Dave, G. Steiner, J.M. Slaughter, J.J. Sun, B. Craigo, S. Pictambaram, K. Smith, G. Grynkewich, M. De-Herrera, J. Åkerman, and S. Tehrani, *MgO-based tunnel junction material for high-speed toggle magnetic random access memory*, IEEE Trans. Magn. **42**, 1935 (2006).

4.18 Magnetic dynamics near vortex state nucleation in $\text{Ni}_{81}\text{Fe}_{19}$ dots

A.A. Serga, A.V. Chumak, and B. Hillebrands¹

The thermally induced magnetization decay of the vortex and single domain states, i.e., overcoming of energy barriers as a function of time for the given field and temperature, was not studied for circular magnetic dots so far. Meanwhile, this process is of paramount importance for the design of magnetic memory devices because it determines the long-term stability of the stored data. Here we present measurements of slow (range of hours) magnetization dynamics of $\text{Ni}_{81}\text{Fe}_{19}$ circular dot array applying in-plane magnetic fields close to the vortex nucleation in the temperature range 200 – 400 K. Overcoming the energy barrier of individual dots as a function of the observation time is essentially a random process, and its parameters can be found from the statistics of many repeated experiments with the same dot. Therefore, measurements of an integral signal of the whole array of uncoupled dots rather than of an individual element (as in Refs. [1–3]) allow to obtain the natural statistical averaging of the over-barrier jumps and extract magnetization decay parameters during one measurement.

A square array of $\text{Ni}_{81}\text{Fe}_{19}$ dots (2000×2000 elements) with radii $R = 250\text{nm}$ and thickness $L = 40\text{nm}$ was prepared on a Si wafer with an oxidized surface by means of electron-beam lithography and a lift-off technique using a Raith 150 electron-beam writer. The interdot center-to-center distance was equal to $4R = 1000\text{nm}$ to exclude the influence of interdot magnetostatic interactions on the results. $\text{Ni}_{81}\text{Fe}_{19}$ films were deposited using molecular-beam epitaxy in a vacuum of 10^{-8}mbar . To improve the magnetic film quality, a 2 nm Cr underlayer was deposited on Si/SiO₂ prior to the $\text{Ni}_{81}\text{Fe}_{19}$ growth. To protect the patterned samples from oxidation they were covered by a 2 nm thick Al layer. After removing the resist, the quality of the dots was checked by scanning electron microscopy (see inset to Fig. 1). The saturation magnetization of the $\text{Ni}_{81}\text{Fe}_{19}$ reference continuous film (prepared in the same deposition run) was found to be $M_s = 785\text{emu/cm}^3$ taken from the continuous-wave Ferromagnetic Resonance measurements (see Ref. [4] for a procedure description) using a Bruker ELEXYS 500 spectrometer operating at a frequency of 9.85 GHz. Hysteresis loops at different temperatures in the 200 – 375 K temperature range were measured by a Quantum Design Physical Property Measurement System equipped with a Vibrating Sample Magnetometer option.

A set of hysteresis loops for temperatures 200, 305 and 375 K is shown in Fig. 1. Typical for the vortex circular dots a double-lobe shape of the hysteresis loops with a pronounced nucleation field H_n and annihilation field H_{an} was observed, confirming the high quality of the patterned array, and similarity of all the dots. We note that the value of H_n is almost the same for all measured temperatures and is equal approximately to $\simeq 290\text{Oe}$ (defined as an instability of the saturated state with respect to a magnetic vortex formation [3]), whereas the field H_{an} gradually increases with temperature decrease from 750 to 840 Oe. Unlike the measurements by Mihajlović et al. [1] for larger $\text{Ni}_{81}\text{Fe}_{19}$ dots, the sharp magnetization decreases below H_n ($H_1 = 250\text{Oe}$ for all the measured temperatures). This means that a stable vortex state develops almost immediately from

¹In collaboration with G.N. Kakazei, Dpto. de Física da Faculdade de Ciencias, IFIMUP and IN-Institute of Nanoscience and Nanotechnology, Universidade do Porto, Rua Campo Alegre 687, Porto 4169-007, Portugal; M. Ilyn, J. Gonzalez, and K.Y. Guslienko, Dpto. de Física de Materiales, Universidad del País Vasco, Donostia-San Sebastian 20018, Spain; O. Chubykalo-Fesenko, Instituto Ciencia de Materiales de Madrid, Madrid 28049, Spain; B. Laegel, Nano-Bio Center, Technische Universität Kaiserslautern, Kaiserslautern, Germany.

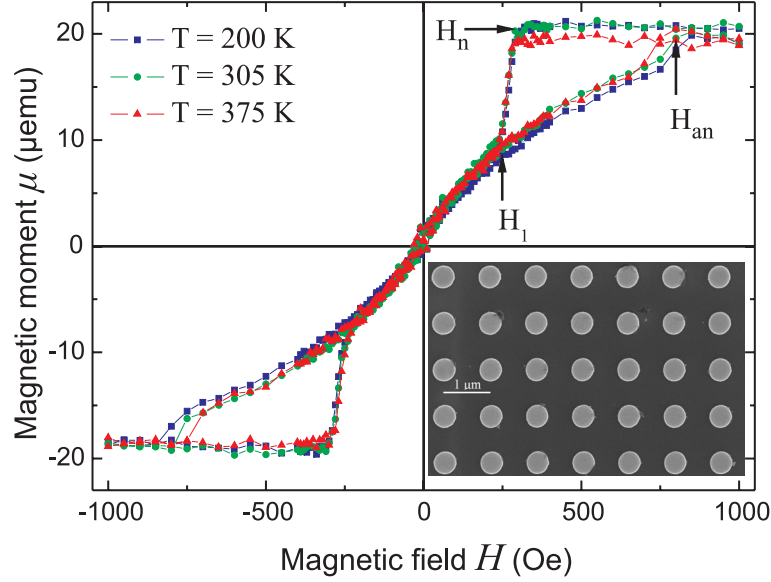


Fig. 1: Magnetization hysteresis loops for a square array of circular Permalloy dots at different temperatures. The dot radius is $R = 250\text{nm}$ and the thickness is $L = 40\text{nm}$. Inset: Scanning electron microscope image of the dot array.

the saturated state and quasi-uniform C- and S-states play a minor role in the nucleation process.

To study the slow magnetization dynamics of our samples, the following algorithm was implemented. First, the samples were saturated applying an in-plane field of up to 1000 Oe. Then, the field was decreased in the non-overshoot regime to a value in the vicinity of the vortex nucleation field (230 – 320 Oe). Immediately after this the recording of the magnetic moment of the dot array $\mu(t)$ as function of time was started. The total observation time for all the measurements was fixed at 5000 s (83 min). These measurements were performed for the same set of temperatures as the hysteresis loops $M(H)$ studies. Since the time between measurements was kept at $\simeq 1\text{ s}$ (to observe possible fast changes at the beginning of the process) and the total magnetic moment of the array is $\simeq 2 \cdot 10^{-5}\text{ emu}$, the measured $\mu(t)$ dependencies were noisy. Therefore, their averaging was performed and results for $T = 300\text{ K}$ are presented in Fig. 2. We note that around $H = 270\text{ Oe}$ the total decrease of magnetic moment with elapsing time was as big as 7 % of its initial value.

The measured time-dependent magnetic properties of an ensemble of isolated $\text{Ni}_{81}\text{Fe}_{19}$ dots were interpreted in terms of the energy barrier and relaxation time. The nucleation process in each dot is independent and corresponds to a different value of the energy barrier and probability to nucleate the vortex core within the dot. In our case, the resulting signal is an average over an ensemble of $\simeq 4 \cdot 10^6$ dots. The nucleation has two stages: (1) fast continuous transition from the single domain state to an intermediate quasi-uniform C- (S-) state for several tens of seconds and (2) slow magnetization time decay related to the energy barriers. The thermally induced long-time magnetization dynamics of the dot array assuming an uniform statistical distribution of the energy barriers within the interval $[0, E_m]$ can be described by the equation [5, 6]:

$$\mu(t) = \mu(t_0) - S \ln(t/t_0) \quad (1)$$

This equation was used to find the magnetic viscosity S from the fitting of the experimental $\mu(t)$ -dependences presented in Fig. 2. One can see good correspondence of the measured and calculated data of the magnetization time decay $\mu(t)$ of the dot array. Here, within a simple model,

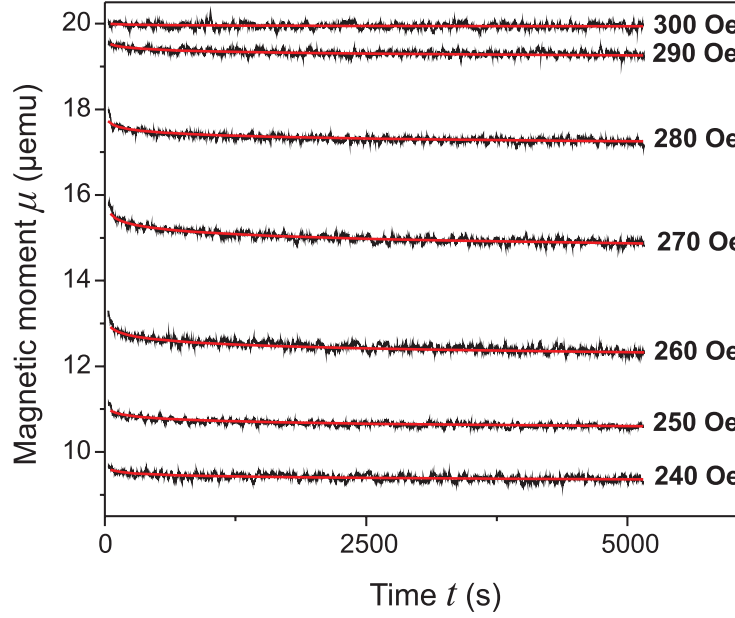


Fig. 2: Evolution of the magnetic moment of the square array of circular Permalloy dots with time after initial saturation followed by magnetic field decrease to the value close to the nucleation field H_n for $T = 305$ K (black lines). The solid red lines are fittings by Eq. (1).

the viscosity is $S(T, H) = k_B T V \Delta M(H) / E_m(H)$, where V is the volume of the magnetic material in the dot arrays, $\Delta M(H) = M_{qu}(H) - M_v(H)$ is the difference of equilibrium magnetizations in the metastable quasi-uniform and the stable vortex state, $E_m(H)$ is the maximum barrier for the transition from the quasi-uniform to vortex state. We use the equilibrium magnetization approximate values $M_{qu}(H) \approx \mu_s / V$ because the nucleation is quite abrupt, and $M_v(H) \approx \mu_s / (H_{an} V)$, where μ_s is the measured saturation magnetic moment ($\mu_s = 2 \cdot 10^{-5}$ emu) for the dot array with $R = 250$ nm). Therefore, the energy barriers extracted from the magnetic moment decay curves can be found from the equation:

$$E_m(H) = \frac{k_B T \mu_s (1 - H/H_n)}{S(T, H)} \quad (2)$$

The magnetic viscosity S plotted in Fig. 3 as function of H for different temperatures reveals a well defined maximum at $H \approx 270$ Oe. The energy barriers rapidly increase and $S(H)$ decreases with H increasing within the interval 270 – 320 Oe according to Eq. (2). $H_n^0(T) \approx 270$ Oe has sense of a critical field for the transition from the C-(S-) state to the vortex state decreasing H . The viscosity $S(H)$ decreases at $H \leq H_n^0$ because a fraction of the dots having $H > H_n^0(\text{local})$ is decreasing with decreasing H . Here we assume that the field dependence of the energy barrier $E_m(H)$ near the vortex nucleation field can be represented as power series decomposition

$$E_m(H) = E_0 + a(H/H_n^0 - 1)^n. \quad (3)$$

The dependence $\lg(E_m(H) - E_0)$ on $H - H_n^0$ is very close to a straight line that allows to find the model parameters E_0 , a , n and refine the parameter H_n^0 from fitting this equation to the experimentally determined energy barriers via Eq. (1). We find the following parameters $(E_0, a, n, H_n^0) = (4.25 \cdot 10^{-12} \text{ erg}, 5.54 \cdot 10^{-17} \text{ erg}, 3.56, 269 \text{ Oe}), (4.19 \cdot 10^{-12} \text{ erg}, 5.93 \cdot 10^{-17} \text{ erg}, 3.55, 262 \text{ Oe}), (3.70 \cdot 10^{-12} \text{ erg}, 4.39 \cdot 10^{-17} \text{ erg}, 3.96, 261 \text{ Oe})$ for the temperatures $T = 200, 305$, and 375 K,

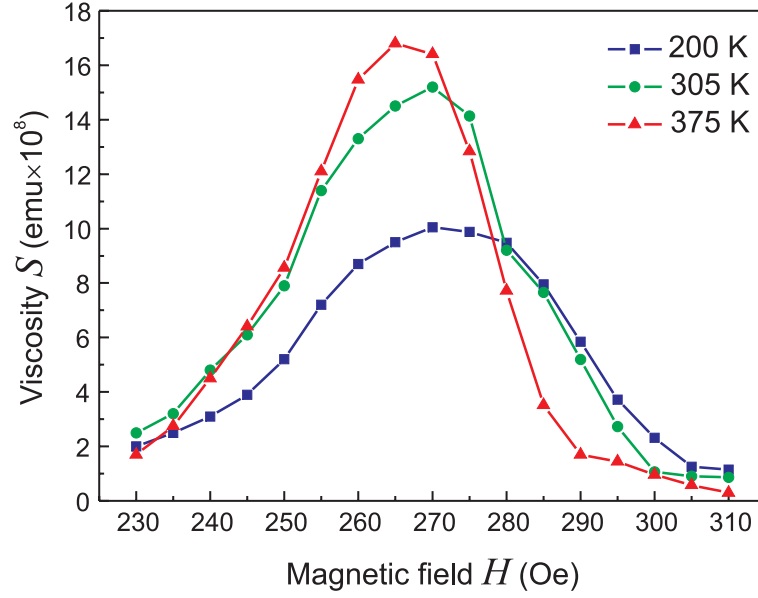


Fig. 3: Magnetic viscosity of the Permalloy dot array vs. in-plane magnetic field extracted from the experimental magnetization time decay dependencies by using Eq. (1): blue squares ($T = 200$ K), green circles ($T = 305$ K) and red triangles ($T = 375$ K). The solid lines are for eye guide only.

respectively. All the values in the sets (E_0, a, n, H_n^0) are very close to each other at different temperatures that justifies the use of the power approximation for the $E_m(H)$ dependence.

A typical value of the energy barrier $E_m(H)$ is 10^{-11} erg, and the energy density per unit of the dot volume V_0 is $E_m/V_0 \simeq 1.2 \times 10^3$ erg/cm³, a reasonable value. Note that $E_m \ll M_s^2 V_0$ ($M_s^2 V_0$ determining the dot magnetostatic energy scale is 4.5×10^{-9} erg for a dot with $R = 250$ nm). However, this does not mean that we need to introduce an extremely small activation volume V_a or radius $R_a = 4.3$ nm of the nucleation process to reproduce the value of $E_m(H)$ like it was done in Ref. [2]. We consider that the vortex nucleation occurs via developing the bending of C-state when an imaginary vortex centered outside the dot approaches to the dot border, i.e. the non-uniform nucleation mode is not localized. The nucleation radius, determined according to the equations $E_m = M_s^2 V_a$, $V_a = \pi R_a^2 L$, is $R_a = 11$ nm. R_a is comparable with the vortex core radius $R_c = 0.68 L_c (L/L_c)^{1/3} \simeq 16$ nm determined from the variational model in Ref. [7] ($L_c = \sqrt{2A}/M_s$ is the material exchange length, A is the exchange stiffness, $L_c = 18$ nm for Ni₈₁Fe₁₉). This is reasonable because the vortex nucleation is related to the vortex core formation within the dot. The exponent $n = 3/2$ found in Ref. [2] from fitting of the field sweep rate dependencies of H_n differs essentially from $n = 3.6 - 4.0$ found in the present work from the long-time magnetization decay measurements. This is a challenge for future theory of the magnetic vortex state energy barriers. The estimation of the thermal stability parameter at room temperature yields $E_m(H)/k_B T \simeq 100 \gg 1$, that justifies the use of the high barrier approximation [5] in deriving the equation for $\mu(t)$ on the basis of the Neel-Arrhenius expression for the over barrier relaxation time $\tau(E) = \tau_0 \exp(E/k_B T)$. Using the above approach based on Eqs. (1) - (2) we calculated the magnetization time decay of the dot array and extracted information about the energy barriers and their field dependence.

To conclude, the effect of the in-plane magnetic field and temperature on the vortex nucleation in 2D Permalloy dot arrays was investigated both experimentally and theoretically. Our measurements demonstrate the essential role of the field dependent energy barriers in the long time vortex nucleation dynamics. The obtained results can serve as a basis for understanding of the magneti-

zation reversal and thermal stability in the vortex state magnetic dot arrays.

This work was recently published in Applied Physics Letters [8].

The German and Portuguese groups acknowledge support from a DAAD-FCT collaborative grant.

References

- [1] G. Mihajlović, M.S. Patrick, J.E. Pearson, V. Novosad, S.D. Bader, M. Field, G.J. Sullivan, A. Hoffmann, *Temperature dependent nucleation and annihilation of individual magnetic vortices*, Appl. Phys. Lett. **96**, 112501 (2010).
- [2] J.P. Davis, D. Vick, J.A.J. Burgess, D.C. Fortin, P. Li, V. Sauer, W.K. Hiebert, M.R. Freeman, *Observation of magnetic supercooling of the transition to the vortex state*, New J. Phys. **12**, 093033 (2010).
- [3] J.A.J. Burgess, D.C. Fortin, J.E. Losby, D. Grombacher, J.P. Davis, M.R. Freeman, *Thermally activated decay of magnetic vortices*, Phys. Rev. B **82**, 144403 (2010).
- [4] G.N. Kakazei, P.E. Wigen, K.Y. Guslienko, R.W. Chantrell, N.A. Lesnik, V. Metlushko, H. Shima, K. Fukamichi, Y. Otani, V. Novosad, *In-plane and out-of-plane uniaxial anisotropies in rectangular arrays of circular dots studied by ferromagnetic resonance*, J. Appl. Phys. **93**, 8418 (2003).
- [5] P. Gaunt, *Magnetic viscosity and thermal activation energy*, J. Appl. Phys. **59**, 4129 (1986).
- [6] A. Lyberatos, R.W. Chantrell, *The fluctuation field of ferromagnetic materials*, J. Phys.: Condens. Matter **9**, 2623 (1997).
- [7] N.A. Usov, S.E. Peschany, *Magnetization curling in a fine cylindrical particle*, J. Magn. Magn. Mater. **118**, L290 (1993).
- [8] G.N. Kakazei, M. Ilyn, O. Chubykalo-Fesenko, J. Gonzalez, A.A. Serga, A.V. Chumak, P.A. Beck, B. Laegel, B. Hillebrands, K.Y. Guslienko, *Slow magnetization dynamics and energy barriers near vortex state nucleation in circular Permalloy dots*, Appl. Phys. Lett. **99**, 052512 (2011).

Chapter 5: Publications

Most publications can be downloaded from <http://www.physik.uni-kl.de/hillebrands>.

5.1 published

1. *Magneto-optical observation of four-wave scattering in a 15 nm Ni₈₁Fe₁₉ film during large angle magnetization precession*
H.T. Nembach, K.L. Livesey, M.P. Kostylev, P. Martin-Pimentel, S. Hermsdoerfer, B. Leven, J. Fassbender, R.L. Stamps, and B. Hillebrands
Phys. Rev. B **84**, 184413 (2011).
2. *Temporal evolution of inverse spin Hall effect voltage in a magnetic insulator-nonmagnetic metal structure*
M.B. Jungfleisch, A.V. Chumak, V.I. Vasyuchka, A.A. Serga, B. Obry, H. Schultheiss, P.A. Beck, A.D. Karenowska, E. Saitoh, and B. Hillebrands
Appl. Phys. Lett. **99**, 182512 (2011).
3. *Magneto-optical investigations of the shape anisotropy of individual micron sized magnetic elements*
T. Sebastian, A. Conca, G. Wolf, H. Schultheiss, B. Leven, and B. Hillebrands
J. Appl. Phys. **110**, 083909 (2011).
4. *Mechanisms of nonlinear spin-wave emission from a microwave driven nanocontact*
F. Ciubotaru, A.A. Serga, B. Leven, L. Lopez Diaz, and B. Hillebrands
Phys. Rev. B **84**, 144424 (2011).
5. *Mode conversion by symmetry breaking of propagating spin waves*
P. Clausen, K. Vogt, H. Schultheiss, S. Schäfer, B. Obry, G. Wolf, P. Pirro, B. Leven, and B. Hillebrands
Appl. Phys. Lett. **99**, 162505 (2011).
6. *Mode selective parametric excitation of spin waves in a Ni₈₁Fe₁₉ microstripe*
T. Brächer, P. Pirro, B. Obry, B. Leven, A.A. Serga, and B. Hillebrands
Appl. Phys. Lett. **99**, 162501 (2011).
7. *Long-range spin Seebeck effect and acoustic spin pumping*
K. Uchida, H. Adachi, T. An, T. Ota, M. Toda, B. Hillebrands, S. Maekawa, and E. Saitoh
Nature Materials **10**, 737-741 (2011).
8. *Quadratic magneto-optical Kerr effect in Co₂MnSi*
G. Wolf, J. Hamrle, S. Trudel, T. Kubota, Y. Ando, and B. Hillebrands
J. Appl. Phys. **110**, 043904 (2011).
9. *Slow magnetization dynamics and energy barriers near vortex state nucleation in circular Permalloy dots*
G.N. Kakazei, M. Ilyn, O. Chubykalo-Fesenko, J. Gonzalez, A.A. Serga, A.V. Chumak, P.A. Beck, B. Laegel, B. Hillebrands, and K.Y. Guslienko
Appl. Phys. Lett. **99**, 052512 (2011).

10. *Employing magnonic crystals to dictate the characteristics of auto-oscillatory spin-wave systems*
A.D. Karenowska, A.V. Chumak, A.A. Serga, J.F. Gregg, and B. Hillebrands
J. Phys.: Conf. Ser. **303** 012007 (2011).
11. *Spin information transfer and transport in hybrid spinmechatronic structures*
A.D. Karenowska, J.F. Gregg, A.V. Chumak, A.A. Serga, and B. Hillebrands
J. Phys.: Conf. Ser. **303** 012018 (2011).
12. *Interference of coherent spin waves in micron-sized ferromagnetic waveguides*
P. Pirro, T. Brächer, K. Vogt, B. Obry, H. Schultheiss, B. Leven, and B. Hillebrands
Phys. Status Solidi B **248**, 2404–2408 (2011).
13. *Optical detection of spin transport in non-magnetic metals*
F. Fohr, Y. Fukuma, S. Kaltenborn, L. Wang, J. Hamrle, H. Schultheiss, A.A. Serga, H.C. Schneider, Y. Otani, and B. Hillebrands
Phys. Rev. Lett. **106**, 226601 (2011).
14. *Spin pumping by parametrically excited exchange magnons*
C.W. Sandweg, Y. Kajiwara, A.V. Chumak, A.A. Serga, V.I. Vasyuchka, M.B. Jungfleisch, E. Saitoh, and B. Hillebrands
Phys. Rev. Lett. **106**, 216601 (2011).
15. *Variable damping and coherence in a high-density magnon gas*
S. Schäfer, V. Kegel, A.A. Serga, B. Hillebrands, and M.P. Kostylev
Phys. Rev. B **83**, 184407 (2011).
16. *Radiation of caustic beams from a collapsing bullet*
M.P. Kostylev, A.A. Serga, and B. Hillebrands
Phys. Rev. Lett. **106**, 134101 (2011).
17. *Effect of annealing on $\text{Co}_2\text{FeAl}_{0.5}\text{Si}_{0.5}$ thin films: A magneto-optical and x-ray absorption study*
S. Trudel, G. Wolf, J. Hamrle, B. Hillebrands, P. Klaer, M. Kallmayer, H.J. Elmers, H. Sukegawa, W. Wang, and K. Inomata
Phys. Rev. B **83**, 104412 (2011).

5.2 in press

1. *Interplay of energy dissipation, ion-induced mixing, and crystal structure recovery, and surface effects in ion-irradiated magnetic Fe/Cr/Fe trilayers*
A. Brodyanski, S. Blomeier, H. Gnaser, W. Bock, B. Hillebrands, M. Kopnarski, and B. Reuscher
Phys. Rev. B., in press.
2. *Oscillatory energy exchange between waves coupled by a dynamic artificial crystal*
A.D. Karenowska, V.S. Tiberkevich, A.V. Chumak, A.A. Serga, J.F. Gregg, A.N. Slavin, and B. Hillebrands
Phys. Rev. Lett., in press.

5.3 submitted

1. *Storage-recovery phenomenon in magnonic crystal*
A.V. Chumak, V.I. Vasyuchka, A.A. Serga, M.P. Kostylev, and B. Hillebrands
submitted to Phys. Rev. Lett..
2. *Near- and far-field excitation of lateral standing spin waves in a magnetic microstripe*
K. Vogt, H. Schultheiss, S. Schäfer, B. Leven, and B. Hillebrands
submitted to Appl. Phys. Lett..

5.4 Ph.D. theses

1. *Untersuchung parametrisch gepumpter Magnonengase*
Christian Werner Sandweg, TU Kaiserslautern, April 2011.
2. *Spin dynamics in non-magnetic metals*
Jan Frederik Fohr, TU Kaiserslautern, März 2011.

Chapter 6: Conferences, Workshops, Schools, Seminars

(shown in chronological order; if not indicated otherwise the contributions were presented by the first author)

6.1 Conferences

6.1.1 Conference Organization

B. Hillebrands:

Conference Co-Chair, International Conference on Nanomaterials and Nanotechnology (Nano 2010)

Namakkal, India, December 2010

6.1.2 Invited talks

B. Hillebrands:

Magnonic Crystals (opening plenary talk)

Magnet 2011, Turin, Italy, February 2011

B. Hillebrands:

Magnonen für den Computer von übermorgen?

Akademie Vortrag, Akademie der Wissenschaften und der Literatur, Mainz, Germany, April 2011

B. Hillebrands:

Magnonic crystal devices

INTERMAG Taipei, Taiwan, April 2011

B. Hillebrands:

Magnon crystal devices

Recent Trends in Nanomagnetism, Spintronics and their Applications, Ordizia, Spain, June 2011

B. Hillebrands:

The concept of magnon spintronics

Magnetic North II - Competing Interactions in Magnetic Materials, Newfoundland, Canada, June 2011

B. Hillebrands:

Magnon crystal devices

2011 Canadian Association of Physics Annual Congress, Memorial University of Newfoundland, Canada, June 2011

B. Hillebrands:

The concept of magnon spintronics

JSPS York-Tohoku Research Symposium on "Magnetic Materials and Spintronics", York, United Kingdom, June 2011

A.V. Serga:

Collapsing bullet and subwavelength spin-wave beams

International Symposium on Spin Waves 2011, St. Petersburg, Russia, June 2011

A.V. Chumak:

Frequency inversion and time reversal via a dynamic magnonic crystal

Moscow International Symposium on Magnetism MISM, Russia, August 2011

B. Hillebrands:

Magnon Spintronics

2nd International Workshop on Magnonics, Recife, Brasil, August 2011

A.A. Serga:

Magnon gases and condensates

2nd International Workshop on Magnonics, Recife, Brasil, August 2011

B. Hillebrands:

Concept of magnon spintronics

SFB 491, Abschlusskonferenz, Bochum, September 2011

A.A. Serga:

Time-resolved spin pumping by sub-micron wavelength magnons from a magnetic insulator

56th Annual Conference on Magnetism and Magnetic Materials, Scottsdale, USA, November 2011

6.1.3 Contributed talks and posters

V.I. Vasyuchka, A.V. Chumak, A.A. Serga, M.P. Kostylev, B. Hillebrands:

Parametrical recovery of a spin-wave signal stored in a magnonic crystal

55th MMM Conference, Atlanta, USA, November 2010

M.B. Jungfleisch, A.V. Chumak, C.W. Sandweg, V.I. Vasyuchka, A.A. Serga, B. Obry, E. Saitoh, B. Hillebrands:

Temporal evolution of spin pumping from a magnetic insulator detected by the inverse spin Hall effect

55th MMM Conference, Atlanta, USA, November 2010

G.N. Kakazei, S.A. Bunyavev, V.O. Golub, N.A. Sobolev, N. Santos, B.A. Ivanov, E.V. Tartakovskaya, A.A. Serga, A.V. Chumak, P.A. Beck, B. Laegel, B. Hillebrands:

Splitting of magnetostatic spin-wave modes of circular magnetic dots upon small deviation of magnetic field from the normal

55th MMM Conference, Atlanta, USA, November 2010

A.V. Chumak, V.S. Tiberkevich, A.D. Karenowska, A.A. Serga, J.F. Gregg, A.N. Slavin, B. Hillebrands:

All-linear frequency inversion and time reversal via a dynamic magnonic crystal

55th MMM Conference, Atlanta, USA, November 2010

- K. Vogt, H. Schultheiss, S.J. Hermsdoerfer, P. Pirro, A.A. Serga, B. Hillebrands:
Phase patterns of laterally standing spin waves on the micrometer scale
 55th MMM Conference, Atlanta, USA, November 2010
- G. Wolf, J. Hamrle, B. Leven, B. Hillebrands, D. Ebke, A. Thomas, G. Reiss, T. Kubota, Y. Ando, H. Sukegawa, W. Wang, K. Inomata:
Quadratic magneto-optical Kerr effect on Co-based Heusler compounds
 IEEE International Magnetic Conference 2011, Taipei, Taiwan, April 2011
- P. Pirro, A.V. Chumak, F. Ciubotaru, A.A. Serga, H. Schultheiss, K. Vogt, M.P. Kostylev, B. Hillebrands:
Propagating spin waves in a microstructured magnonic crystal
 IEEE International Magnetic Conference 2011, Taipei, Taiwan, April 2011
- M.B. Jungfleisch, A.V. Chumak, V.I. Vasyuchka, A.A. Serga, B. Obry, H. Schultheiss, P.A. Beck, B. Hillebrands, A.D. Karenowska, E. Saitoh:
Temporal behavior of the inverse spin Hall voltage in a magnetic insulator - nonmagnetic metal structure
 IEEE International Magnetic Conference 2011, Taipei, Taiwan, April 2011
- C.W. Sandweg, A.V. Chumak, V.I. Vasyuchka, A.A. Serga, M.B. Jungfleisch, B. Hillebrands, Y. Kajiwara, E. Saitoh:
Spin pumping by exchange-dominated magnons
 IEEE International Magnetic Conference 2011, Taipei, Taiwan, April 2011
- A.D. Karenowska, J.F. Gregg, A.V. Chumak, A.A. Serga, B. Hillebrands, V.S. Tiberkevich, A.N. Slavin:
Oscillatory energy exchange between spin waves coupled by a dynamic magnonic crystal
 IEEE International Magnetic Conference 2011, Taipei, Taiwan, April 2011
- V.I. Vasyuchka, B. Obry, T. Langner, A.A. Serga, B. Hillebrands:
Magnon mediated heat and spin transport in magnetic insulators
 Spin Caloritronics III, Leiden, The Netherlands, May 2011
- M.B. Jungfleisch, A.V. Chumak, V.I. Vasyuchka, A.A. Serga, B. Obry, H. Schultheiss, P.A. Beck, A.D. Karenowska, E. Saitoh, B. Hillebrands:
Temporal behavior of the inverse spin Hall voltage in a magnetic insulator - nonmagnetic metal structure
 Spin Caloritronics III, Leiden, The Netherlands, May 2011
- A.D. Karenowska, A.V. Chumak, V.S. Tiberkevich, A.A. Serga, J.F. Gregg, A.N. Slavin, B. Hillebrands:
Oscillatory energy exchange between spin wave modes coupled by a dynamic magnonic crystal
 International Symposium Spin Waves, Saint Petersburg, Russia, June 2011
- T. Sebastian, A. Conca Parra, G. Wolf, B. Leven, B. Hillebrands:
Magneto-optical investigation of the shape anisotropy of individual elliptical microstructures
 JSPS York-Tohoku Research Symposium on "Magnetic Materials and Spintronics", York, UK, June 2011

A.V. Chumak, C.W. Sandweg, Y. Kajiwara, V.V. Vasyuchka, A.A. Serga, M.B. Jungfleisch, E. Saitoh, B. Hillebrands:

Spin pumping by short-wavelength exchange-dominated excited by parametric pumping

Recent Trends in Nanomagnetism, Spintronics and their Applications, Ordizia, Spain, June 2011

K. Vogt, H. Schultheiss, P. Pirro, B. Hillebrands:

All-optical investigation of propagating and standing spin waves in magnetic micro-waveguides

2nd International Workshop on Magnonics, Recife, Brasil, August 2011

A. Karenowska, A.V. Chumak, V. Tiberkevich, A.A. Serga, J.F. Gregg, A.N. Slavin, B. Hillebrands:

The dynamic magnonic crystal: a window into new wave phenomena

2nd International Workshop on Magnonics, Recife, Brasil, August 2011

G. Melkov, Y. Koblyanskiy, V. Novosad, K. Gusliencko, A. Slavin, A. Chumak, B. Hillebrands:

Nonlinear magnonic crystal based on a planar array of magnetic dots

2nd International Workshop on Magnonics, Recife, Brasil, August 2011

V.I. Vasyuchka, P. Clausen, A.A. Serga, B. Hillebrands:

Evolution of parametrical driven magnon gas

Annual Retreat SFB/TR 49, Alzey, September 2011

G.N. Kakazei, M. Ilyn, O. Chubykalo-Fesenko, J.M. Gonzalez, A.A. Serga, A.V. Chumak, B. Hillebrands, K.Y. Gusliencko:

Magnetization relaxation in circular magnetic dots near vortex state nucleation

56th Annual Conference on Magnetism and Magnetic Materials, Scottsdale, USA, November 2011

A.V. Chumak, M.B. Jungfleisch, A.A. Serga, R. Neb, B. Hillebrands:

Direct detection of magnon spin transport by the inverse spin Hall effect

56th Annual Conference on Magnetism and Magnetic Materials, Scottsdale, USA, November 2011

6.1.4 Contributions to the DPG Frühjahrstagung

16 contributions: DPG Frühjahrstagung, Dresden, March 2011

6.2 Workshops and Schools

6.2.1 Invited lectures

B. Hillebrands:

Fundamentals of spin waves and Brillouin light scattering

ASPI-MATT Workshop and Summerschool, Kaiserslautern, Germany, August 2011

A.A. Serga:

Nonlinear spin-wave dynamics and radiation properties of small Heusler devices
3rd Meeting of Strategic Japanese-German Joint Research Program “ASPIMATT”: Advanced spintronic materials and transport phenomena, Diemerstein/Kaiserslautern, Germany, August 2011

A.A. Serga:

Influence of a photon field on temporal dynamics of Bose-Einstein magnon condensate
Annual Retreat of the SFB/TRR49, Kaiserslautern, September 2011

6.2.2 Contributed talks and posters

M. Agrawal, F. Fohr, A.A. Serga, B. Hillebrands, Y. Fukuma, L. Wang, Y. Otani:

Optical detection of spin transport in non-magnetic metals
IEEE Magnetic Society Summer School, New Orleans, USA, May 2011

M.B. Jungfleisch, A.V. Chumak, V.I. Vasyuchka, A.A. Serga, B. Obry, H. Schultheiss, P.A. Beck, A.D. Karenowska, E. Saitoh, B. Hillebrands:

Temporal behavior of the inverse spin Hall voltage in a magnetic insulator - nonmagnetic metal structure
IEEE Magnetic Society Summer School, New Orleans, USA, May 2011

M. Agrawal, F. Fohr, A.A. Serga, B. Hillebrands, Y. Fukuma, L. Wang, Y. Otani:

Optical spin transport detection: A new aspect of Brillouin light scattering
ASPIMATT Workshop and Summerschool, Kaiserslautern, Germany, August 2011

T. Sebastian:

Brillouin light scattering and its application to $\text{Co}_2\text{Mn}_{0.6}\text{Fe}_{0.4}\text{Si}$
ASPIMATT Workshop and Summerschool, Kaiserslautern, Germany, August 2011

M.B. Jungfleisch, C.W. Sandweg, Y. Kajiwara, A.V. Chumak, V.I. Vasyuchka, A.A. Serga, B. Obry, H. Schultheiss, P.A. Beck, A.D. Karenowska, E. Saitoh, B. Hillebrands:

Inverse spin Hall voltage in a magnetic insulator - nonmagnetic metal structure
ASPIMATT Workshop and Summerschool, Kaiserslautern, Germany, August 2011

6.3 Other meetings and trade fairs

B. Hillebrands:

INNOMAG, Jena, March 2011

A. Conca Parra, A. Ruiz Calaforra, B. Leven, B. Hillebrands:

Presentation of MULTIMAG project
Hannover Messe 2011, Hannover, Germany, April 2011

6.4 Invited seminar talks and colloquia

K. Vogt:

Optical detection of propagating spin waves in a $\text{Ni}_{81}\text{Fe}_{19}$ microstripe
Colorado State University, Fort Collins, USA, July 2011

6.5 Seminars

P. Clausen:

Magnon gases and condensates
Student Seminar Summer Term, Riezlern, Austria, July 2011

6.6 Awards and Fellowships

B. Hillebrands:

“APS Fellow” for contributions to the understanding of dynamic magnetic excitations in confined magnetic structures, linear and nonlinear spin-wave propagation phenomena, and his pioneering work on the development of space- and time-resolved Brillouin light scattering technique,
November 2010

H. Schultheiss:

Preis der Kreissparkassen-Stiftung
June 2011

H. Schultheiss:

Preis der Prof. Dr. Jürgen Geiger-Stiftung, TU Kaiserslautern
October 2011

Appendix: Impressions from 2011



Ph.D. defense Dr. Christian Sandweg



Ph.D. defense Dr. Frederik Fohr



Group excursion